School of Civil and Mechanical Engineering

Structural Analysis and Design of Fibre-reinforced Ambient-cured Geopolymer Concrete Beams under Static and Dynamic Loading

Thanh Tung Tran

This thesis is presented for the Degree of
Doctor of Philosophy
of
Curtin University

Nov 2020

Declaration

To the best of my knowledge and belief, this thesis contains no material previously published by any other person except where due acknowledgment has been made.

This thesis contains no material which has been accepted for the award of any other degree or diploma in any university.

Signature: (**Thanh Tung Tran**)

Date: 13/11/2020

Dedication

To my beloved family: my father, my mother, and my sister!

To my thesis advisors (Professor Hong Hao and Dr. Thong Pham)!

Abstract

Ordinary Portland concrete (OPC) has imposed an increasing environmental problem due to the synthesis process of Portland cement emitting a large amount of Carbon dioxide (CO_2) into the atmosphere. Therefore, developing an alternative low carbon binder to replace the conventional but non-environmentally friendly Portland cement is a hot research topic in the last three decades. Ambient-cured geopolymer concrete (GPC), which is a result of the chemical reactions between Aluminosilicate minerals and an alkaline solution, is a promising material to replace Portland cement. The existing studies demonstrated that ambient-cured GPC could be manufactured with superior characteristics such as excellent acid and heat resistance when compared with OPC. However, a significantly brittle response due to inferior fracture energy may be a real challenge of employing ambient-cured GPC into practice since the structural elements made from this material may fail in a brittle manner without appropriate warning signs, which should always be avoided in structural design. To overcome this issue, fibres can be incorporated in the GPC matrix to improve the tensile strength, flexural strength, and ductility of this brittle material. The mechanical properties of fibre reinforced GPC material have been intensively investigated but no study has been conducted to unveil the performance of structures made of this material until now. For the application of fibre reinforced ambient-cured GPC material in construction, a systematic investigation into the response of fibre reinforced GPC structures is required.

On the other hand, maintaining long-term performance and extending the service life of concrete structures remain a challenge in the construction industry for engineering asset owners due to corrosion of steel reinforcements. The use of non-corrosive materials such as basalt fibre reinforced polymer (BFRP) bars to replace the conventional steel bars to reinforce concrete structures can be an effective approach in terms of cost-efficiency for life-cycle maintenance. Nevertheless, the lower axial stiffness and no yielding behaviour of BFRP bars may lead to the lower capacity and brittle failure of the structures. The inclusion of fibres is a rational solution to improve the strength and ductility of structures using BFRP reinforcements. Through the combination of BFRP bars and fibre reinforced ambient-cured GPC, it is expected to create an innovative structure that not only is highly durable and sustainable but also provides good ductility and load-carrying capacity.

During the service life, concrete structures may be subjected to extreme cases of loadings such as impact load by a vehicle collision and falling objects or blast load from an explosion. Those incidents may result in catastrophic consequences like the collapse of structures which may lead to human casualties. Therefore, it is essential to investigate the dynamic response of concrete structures under extreme events including impact and blast loads. The existing studies indicated that the failure manners of structures against dynamic loads can be governed by local or global modes, which are strongly dependent on the loading rate. For example, reinforced concrete beams against impact load can fail locally by a punching shear mode at the impact area in case of high impact velocity even though those beams are designed with much higher shear strength and would fail by pure flexural mode under static loading. This implies that the use of equivalent static analysis to estimate and design the dynamic capacities of concrete structures may lead to unreliable and unconservative outcomes. For this reason, the impact response of conventional reinforced OPC beams has received substantial research attention in recent years. Nevertheless, the studies related to GPC structures subjected to impact loads are very limited. Thus, investigations on the dynamic response of GPC structures are deemed necessary.

From the aforementioned motivations, the study presented in this dissertation aims to investigate the structural response of fibre reinforced ambient cured GPC beams under static and impact loads. Due to differences in mechanical properties of GPC and OPC, the study presented in Chapter 2 was first conducted to indicate an overestimation in estimating the loading capacity of ambient cured GPC members when using rectangular stress-block parameters from available OPC standards. In that chapter, new sets of parameters for obtaining an accurate prediction that can be used in the design of GPC beams were proposed. After that, the experimental and analytical investigations through four-point bending, three-point bending, and drop-weight tests were carried out in this study. In particular, Chapter 3 investigates experimentally and analytically the flexural static behaviour of fibre reinforced GPC beams via four-point bending tests and unveils the effects of fibre dosage and length of macro steel fibres (SF) on the performance of the beams. To predict the load-deflection response of fibre reinforced GPC beams, an analytical procedure based on the sectional analysis combining with several modifications of concrete models were developed and presented in Chapter 3. The performance of GPC beams reinforced with BFRP bars subjected to static and impact loads were investigated and compared with those of the OPC beams reinforced with steel bars in Chapters 4, 5, and 6. The shear response of fibre reinforced GPC beams under static loads and the

influence of different volume fractions of fibres were presented in Chapter 4. Different fibre combinations were used to enhance the shear capacity of the beams, including (1) single type of macro-steel fibre (SF), (2) macro-synthetic polypropylene fibres (PF), (3) hybridization of SF and micro-polyvinyl alcohol fibres (PVF), and (4) PF and micro- carbon fibres (CF). From those investigations, an optimal design for fibre reinforcement to enhance the shear performance of GPC beams were recommended. Furthermore, Chapter 4 also proposes three models based on ACI 440-1R-06 guideline and modified compression field theory (MCFT) to predict the shear capacity of fibre reinforced GPC with BFRP reinforcements. The proposed models indicated that the shear strength of fibre reinforced GPC beams could be estimated based on the theory developed for OPC beams with appropriate modifications in concrete material models.

The dynamic response of fibre reinforced GPC beams against impact loads is presented in Chapters 5 and 6. In Chapter 5, the effectiveness of fibre reinforcement in improving the flexural performance of the GPC beams using BFRP stirrups was examined. Moreover, the residual strength of the beams after the impact tests was determined by using static three-point bending tests. Through those results, the effect of fibre incorporation on reducing the impact damage was evaluated. Meanwhile, the influence of different types of fibre reinforcement on the shear failure of GPC beams without using stirrups was investigated in Chapter 6. It should be noted that the impact force profiles were affected strongly by contact properties of the impacted area owing to varying contact stiffness. Since only very few studies in the literature have investigated the effect of contact conditions on impact responses of reinforced concrete beams, the influence of two different types of contact conditions including direct contact and rubber pad contact on the impact response of beams was also investigated in Chapter 6. Finally, the key findings and recommendations for designing the fibre reinforced GPC beams against static and impact loads were summarized in Chapter 7.

Acknowledgment

First and foremost, I would like to express my heartfelt gratitude and respect to my supervisor Professor Hong Hao and co-supervisor Dr. Thong Pham for enlightening guidance, patience, kindness, and belief throughout my PhD journey. Without their tremendous support, I would not complete the comprehensive work done for this thesis. For me, they are great supervisors with extraordinary scientific and human qualities, which is an honour for me to be one of their PhD students. Their encouragement and lessons are also an inspiration and motivation for me to pursue a research career after PhD journey. Once again, I would like to sincerely thank my supervisors for believing in me and giving me the chance to become their student.

I would like to deeply thank Curtin University for providing me with the full scholarship for the Ph.D. study. Without these scholarship awards from Curtin University, it would have been impossible for me to participate in a Higher Degree by Research in Australia. I am also grateful to the Australian Research Council for supporting this research project.

I would like to express gratitude to all the administrative support staff at School of Civil and Mechanical Engineering, especially to Ms. Cheryl Cheng for helping me complete the paper works during my PhD course. I would also like to extend a deep appreciation to all the lab technicians in Civil Engineering Laboratory at Curtin University including Mr. Mick Elliss (former lab technician), Mr. Luke English (former lab technician), Mr. Ashely Hughes, Mr. Rob Cutter, Dr. Arnie Bredin, Mr. Kevin Reilly, Mr. Gary Woodward, and Mr. Darren Isaac for their support in experimental work. I would like to send special gratefulness to the lab manager, Mr. Mark Whittaker, who always responds quickly to my problems related to experimental work and also gives great solutions.

Furthermore, I would like to extend my appreciation to all the students, research associates, and staff members in Professor Hao's research group at Curtin University for their great friendship and support during PhD. I would especially thank Dr. Wensu Chen for his kindness and valuable advice. I am also grateful to my colleagues and friends, especially Dr. Tan Le, Dr. Tin Do, Mr. Tuan Ngo, Mr. Huawei Li, Mr. Zhixing Li, Mr. Zhijie Huang, Dr. Cheng Yuan, Mr. Yan Qiang, Mr. Nhi Vo, Mr. Duong Tran, and Mr. Emad Pournasiri for the supports and share of knowledge during my research.

In the end, I would like to express my special gratitude to my family for their unconditional love and constant encouragement. I would like to send my deepest appreciation and love to my parents because of their enormous sacrifices to bring the best education for me. I also express my gratefulness to my sister who is always willing to encourage and believes in me.

LIST OF PUBLISHED WORKS AND WORK PREPARED FOR PUBLICATION

The list of published papers and work prepared for publication, with the full bibliographic citations in the order they appear in the dissertation, are outlined below.

Chapter 2:

Tran TT, Pham TM, Hao H. Rectangular Stress-block Parameters for Fly-ash and Slag Based Geopolymer Concrete. *Structures*. 2019;19:143-55.

DOI: https://doi.org/10.1016/j.istruc.2019.01.006

Chapter 3:

Tran TT, Pham TM, Hao H. Experimental and analytical investigation on flexural behaviour of ambient cured geopolymer concrete beams reinforced with steel fibers. *Engineering Structures*. 2019;200:109707

DOI: https://doi.org/10.1016/j.engstruct.2019.109707

Chapter 4:

Tran TT, Pham TM, Hao H. Effect of hybrid fibers on shear behaviour of geopolymer concrete beams reinforced by basalt fiber reinforced polymer (BFRP) bars without stirrups. *Composite Structures*. 2020;243:112236

DOI: https://doi.org/10.1016/j.compstruct.2020.112236

Chapter 5:

Tran TT, Pham TM, Huang Z, Chen W, Hao H, Elchalakani M. Impact response of fibre reinforced geopolymer concrete beams with BFRP bars and stirrups. Eng Struct. 2021;231:111785.

Chapter 6:

Tran TT, Pham TM, Huang Z, Chen W, Ngo TT, Hao H, Elchalakani M. Effect of Fibre Reinforcements on Shear Capacity of Geopolymer Concrete Beams subjected to Impact Loads. *International Journal of Impact Engineering*. 2020;Under review.

Statement of Contribution of Others

This research project was initiated by Prof. Hong Hao as a primary supervisor, who defined the overall scope and objectives of this study, supervised the research scheme through the instructions of the research approach and feasible research methodologies, and supported the research funding. As a co-supervisor, Dr. Thong Pham helped significantly supervise the investigations of this study including suggesting, contributing, and advising the aims, conceptual ideas, and methods for each publication. Under the supervision and guidance of Prof. Hong Hao and Dr. Thong Pham, the candidate (Thanh Tung Tran) who was also the first author of each publication was responsible for conducting the literature review, plan experimental schemes, carrying out the tests, analysing, interpreting the experimental findings, deriving analytical solutions, and writing the manuscript drafts. Dr. Thong Pham and Prof. Hong Hao then revised, edited each manuscript, and provided intellectual input towards the data processing, analysis, and discussions of the results. In the publications of Chapters 5 and 6, Dr. Wensu Chen and Mr. Zhijie Huang supported and advised several intellectual suggestions for experimental schemes and data collection. Dr. Wensu Chen also helped revise and give intellectual input towards discussions in the manuscripts formed Chapters 5 and 6. Moreover, Dr. Mohamed Elchalakani helped revise the manuscripts of Chapters 5 and 6. Finally, the experimental works and the process of data collection for Chapter 6 were supported and advised by Mr. Tuan Ngo. The attribution of the authorship is signed by co-authors and attached in the appendix.

List of Relevant Supplemental Publications

The list of additional publications relevant to the dissertation, but not being part of it with the full bibliographic citations, is given below

1. T.T. Ngo, **T.T. Tran**, T.M. Pham, H. Hao, Performance of geopolymer concrete in monolithic and non-corrosive dry joints using CFRP bolts under cyclic loading, Compos. Struct. 258 (2021) 113394.
2. Z. Huang, W. Chen, H. Hao, Z. Chen, T.M. Pham, **T.T. Tran**, M. Elchalakani, Flexural behaviour of ambient cured geopolymer concrete beams reinforced with BFRP bars under static and impact loads, Compos. Struct. (2020) 113282.
3. Z. Huang, W. Chen, H. Hao, Z. Chen, T.M. Pham, **T.T. Tran**, M. Elchalakani, Shear behaviour of ambient cured geopolymer concrete beams reinforced with BFRP bars under static and impact loads, Eng. Struct. 231 (2021) 111730.
4. Z. Huang, W. Chen, **T.T. Tran**, T.M. Pham, H. Hao, Z. Chen, M. Elchalakani, Experimental and numerical study on concrete beams reinforced with Basalt FRP bars under static and impact loads, Compos. Struct. 263 (2021) 113648.

Table of Contents

List of figures

List of tables

Chapter 1. Introduction

1. 1. Preamble

Although ordinary Portland concrete (OPC) is the primary material in constructional areas, it has imposed enormous burdens on the environment. It should be noted that the process of Portland cement production results in adverse effects on non-renewable natural resources such as limestone and clay. Furthermore, one of the most critical issues is that the synthesis process of Portland cement emits a large amount of Carbon dioxide (CO_2) into the atmosphere, which has contributed 5-7% of global greenhouse gases [1]. Therefore, a further increase in OPC production may lead to adverse consequences for the environment, e.g, global warming and climate change. Due to those reasons, many governments have made enormous efforts to diminish CO_2 emission from concrete manufacture and the construction industries are now constrained strictly to sustainable policies. In this context, a new type of building material, namely "geopolymer", was invented based on the chemical reaction between alkaline solutions and aluminosilicate materials which can be obtained from industrial by-products (for example, fly ash, slag, or rice-husk ash) [2]. Due to the similarity of chemical components, this material has been alternatively referred to as the alkali-activated materials [3]. However, the consistent definition to distinguish geopolymer and alkali-activated materials has been still a controversial topic among researchers. Such an issue related to the chemical and material aspect is beyond the scope and also not the purpose of this study. Therefore, the common term "geopolymer" which was known as fly ash and slag-based concrete mixtures in the previous studies [4, 5] was adopted in this dissertation. After the advent of geopolymer cement, many investigations demonstrated that the usage of geopolymer concrete (GPC) to replace OPC can reduce significantly greenhouse gas emissions [6, 7]. As can be seen from Figure 1-1, the manufacture of 1 m^3 GPC required the lowest carbon footprint intensity which is only half of the requirement for producing 1 m^3 OPC [8]. This indicates that GPC is a promising solution for developing sustainable construction industry.

Apart from the environmental issues, the deterioration in the long-term performance and service life of concrete structures due to the corrosion of steel reinforcements is also a major consideration for reinforced concrete. Corrosion of steel reinforcements can lead to deterioration of the capacity of structures or even catastrophic failures. Moreover, corrosion issues may increase the budget for infrastructure maintenance because of the cost of corrosion prevention. For example, it is reported that in the United States of America, the annual cost for

maintenance and improvement of bridge condition can reach $5.8 billion for the 20-year period of 1998-2017 [9]. Since the technical, financial, and societal requirement to deal with damage from steel corrosion is considerable, it is imperative to seek a replacement of steel reinforcement to develop new systems of infrastructure with long-term durability and requiring less maintenance cost. Fortunately, fibre reinforced polymer (FRP) material invented with beneficial characteristics such as lightweight, high tension capacity, and especially non-corrosion and excellent chemical resistance can be an effective solution. Despite the high initial cost of manufacturing FPR reinforcement, the repair and maintenance cost of infrastructures adopting FRP reinforcements can be reduced significantly owing to its non-corrosive characteristics. Additionally, FRP reinforcements can be chemically recycled to be used as fillers and reinforcing materials for other products. Generally, the adoption of FRP reinforcements not only overcomes the deterioration in long-term performance and the increase in maintenance cost of infrastructures due to steel corrosion, but also provides an alternatively sustainable option compared to steel reinforcements.

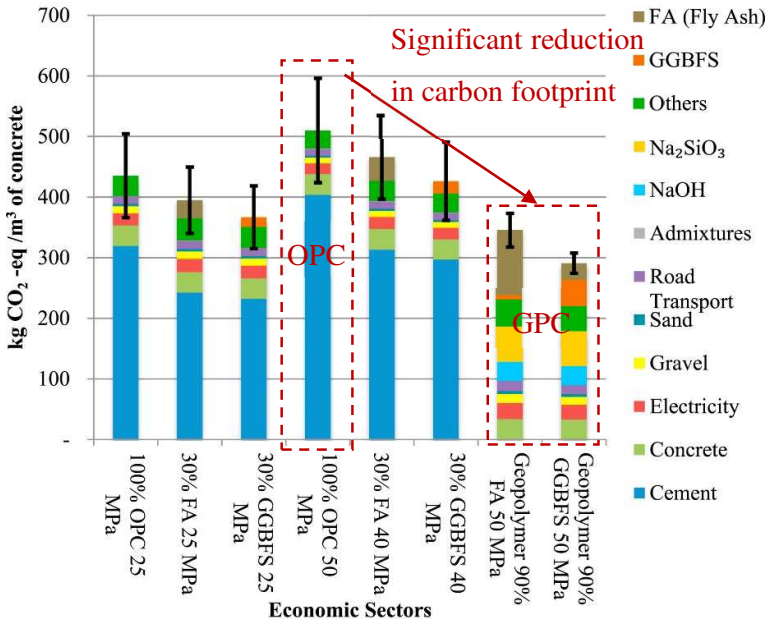

Figure 1-1. Comparison of carbon footprint intensities of GPC and OPC [8]

In recent decades, infrastructure has frequently suffered from extreme loads including impact and blast loads due to an increase in unexpected human errors and terrorism activities such as vehicle collision, chemical explosions, or bomb attacks. According to statistics, 15% of bridge failures in the United States from 1951 to 1988 were due to vehicle collisions [10, 11]. Meanwhile, from 1989 to 2000 it is reported that there were 14 cases of damaged bridges in

the United States because of vehicle impact. In 2002, the I-40 bridge in the southeast of Webbers Falls, Oklahoma, United States collapsed (see in Figure 1-2a) under a collision between freight barges and the bridge piers, which led to 14 deaths and 11 injuries [12]. Moreover, infrastructure has a risk to suffer from extreme loads due to natural disasters, e.g., hailstone impact or rock falling during a landslide. As can be seen from Figure 1-2b, a part of the house was devastated after being smashed by a rock boulder during a landslide in Italy [13]. From the aforementioned review, it is worth noting that traditional designs for reinforced concrete (RC) structures under impact load are vulnerable and usually exhibit catastrophic failures which can cause considerable economic and human life losses. This can be attributed to the distinct difference between the quasi-static and dynamic response of concrete structures. The previous findings indicated that RC structures failed by a sudden and brittle shear failure under extreme events such as impact loads even though those structures were designed with sufficient static shear capacity and failed in a ductile manner under quasi-static loads [14-16]. Consequently, using conventional designs based on equivalent static assumptions for RC structures subjected to extreme loads might not be appropriate and might yield unconservative results. Therefore, it is vital to develop resilient structures owning the ability to minimize damage and functionality disruptions during extreme events.

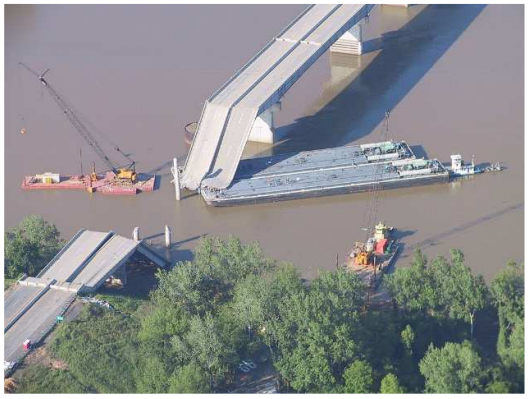

(a) Bridge collapsed due to barge collision [12]

(b) Rock smashed a house [13]

Figure 1-2. The devastation of infrastructure or houses due to extreme events

Due to the aforementioned issues, the desire for developing not only sustainable but also resilient structures was a motivation of this dissertation. A potential solution to obtain such structures is using the combination of GPC and fibre reinforcement. It should be noted that GPC can be synthesized under heat-cured or ambient-cured conditions. However, the heat curing process is not appropriate for the in-situ structures and also a large contributor to CO_2 emission [4]. Meanwhile, ambient-cured GPC with sufficient compressive strength can be a more suitable option for large-scale cast-in-situ applications [17, 18]. Moreover, the incorporation of fibres can improve significantly both the quasi-static and dynamic properties of GPC including the dynamic compressive and splitting tensile strengths [19, 20]. Consequently, fibre reinforced concrete structures can be applied to resist extreme events like impact or blast loading due to their high impact and blast resistance capacity. This indicates a great potential of fibre reinforced ambient-cured GPC for various protective and resilient applications in the infrastructure industry. Nonetheless, until now there has been no investigation to unveil the structural performance of fibre reinforced ambient-cured GPC. Therefore, guidelines and recommendations for designing this type of structure have been still questionable. To fulfil this research gap, this dissertation investigated the response of fibre reinforced ambient-cured GPC against both static and impact loads. The corrosion issues mentioned previously were solved by adopting basalt FRP (BFRP) bars as longitudinal and transverse reinforcements. BFRP was selected among other FRP materials since it has been one of the most state-of-the-art FRP technologies with considerably better cost-efficiency compared to CFRP and greater mechanical properties compared with GFRP [16]. Through the findings of this dissertation, it would lead to the better understandings of the performances of

GPC structures reinforced with FRP bars under static and dynamic loadings, and the establishments of the design guides of such structures to meet the multi-requirements for structural designs as presented in Figure 1-3.

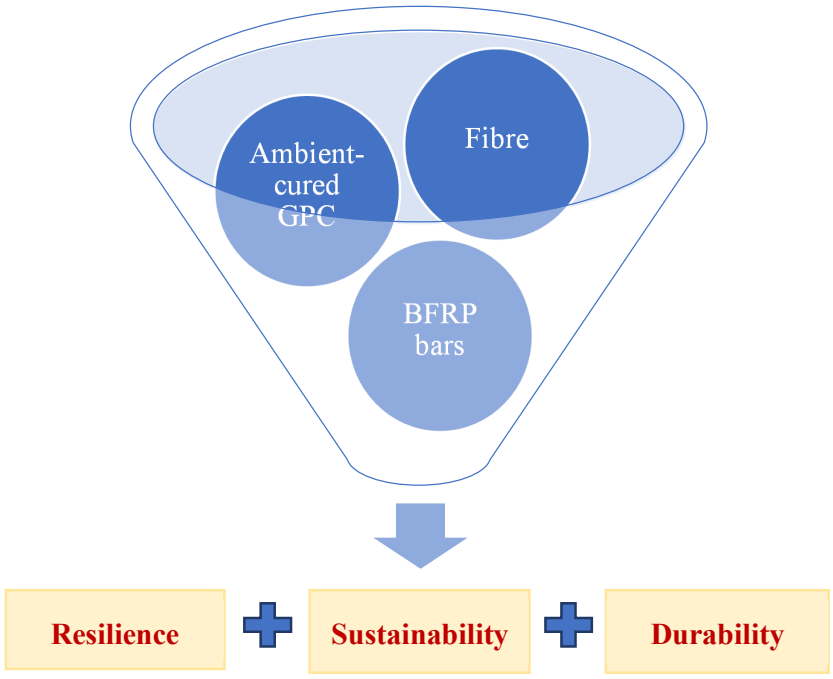

Figure 1-3. Advantages of the proposed structure

1. 2. Research objectives

The objective of this study is to investigate the structural response of fibre reinforced ambient-cured GPC beams subjected to static and impact loads. Through experimental tests and analytical derivations, the current design analysis models for normal concrete beams are modified by taking into consideration the mechanical properties of fibre reinforced GPC to develop new design procedures for fibre reinforced GPC beams. To achieve these goals, the following specific research tasks had been defined and carried out:

- The static flexural and shear behaviour of fibre reinforced ambient-cured GPC beams were investigated via the four-point and three-point bending tests. Based on test data, the effects of critical parameters such as fibre dosage, fibre length, and types of fibre on the flexural capacity, ductility, and shear strength of the beams were unveiled. The recommendations for obtaining an effective design analysis of fibre reinforced GPC beams were proposed.

- The impact response of fibre reinforced ambient-cured GPC beams was studied through the drop-weight test system. The dynamic failure modes including flexure and shear of the beams were examined. The influence of volume fraction of fibres and types of fibres on the impact behaviour of the beams was investigated and explained. Different kinds of contact conditions (direct contact and rubber pad contact) were also employed during the tests to investigate the effect of contact conditions on the dynamic response of the beams.
- Based on the test data in the literature and this study, appropriate modifications were made to available design procedures intended for OPC to design ambient-cured GPC structures. An analytical procedure based on sectional analysis was also proposed to predict the load-deflection curves of fibre reinforced ambient-cured GPC beams. Analytical models to estimate the shear capacity of the beams were also developed.

1. 3. Research outline

This dissertation consists of seven chapters. The contents of six chapters following the introduction are presented as follows:

Chapter 2 presents a review of differences in mechanical properties between GPC and OPC. This chapter indicates that due to such differences, the rectangular stress-block parameters in current design codes intended for OPC could not predict well the strength of ambient-cured GPC structures. The new sets of stress-block parameters were proposed and verified with available test data collected in the literature.

Chapter 3 exhibits an experimental and analytical analysis of the flexural behaviour of fibre-reinforced ambient-cured GPC beams under static loads. The differences in the behaviour of OPC and GPC beams were examined and discussed. The influences of fibre dosage and fibre length on the flexural capacity and ductility of GPC beams were investigated. An analytical model was derived to predict the load-deflection curve of the tested beams with a good correlation with the test data.

Chapter 4 presents the experimental and analytical analyses of the static shear behaviour of fibre-reinforced ambient-cured GPC beams using longitudinal basalt FRP (BFRP) bars without stirrups. Different types of fibre reinforcement were adopted to improve the shear performance of the beams, including (1) mono macro-steel fibres (SF), (2) mono macro-synthetic polypropylene fibres (PF), (3) hybridization of SF and micro-polyvinyl alcohol fibres (PVF),

and (4) PF and micro- carbon fibres (CF). The comparison of the shear response between the fibre reinforced GPC and OPC beams was conducted. The effectiveness of different fibre reinforcements was also evaluated in this chapter. Three analytical models based on current codes or modified compression field theory (MCFT) were proposed to predict the shear capacity of the SF reinforced ambient-cured GPC beams.

Chapter 5 presents an experimental investigation into the impact behaviour of ambient-cured GPC beams reinforced with various kinds of fibres and longitudinal and transverse reinforcing BFRP bars. All the beams were tested under a drop-weight system. After the impact tests, the damaged beams were monotonically loaded under three-point bending tests to determine the residual capacity. Based on the experimental results, the differences in the dynamic response of GPC and OPC beams were examined. The effect of both the volume fraction of fibres and types of fibres on the beam response, including the failure modes, dynamic loads, midspan displacement, energy absorption, and residual load-carrying capacity, were also examined and discussed.

Chapter 6 investigates the shear failure mechanism of fibre reinforced ambient-cured GPC beams without stirrups subjected to impact loads. During the impact tests, two types of contact interlayers including rubber pad contact and direct contact between projectile and load cell were employed. The influences of fibre incorporation on the dynamic loads, midspan displacement, failure modes, and cracking patterns of the beams were examined and discussed. The fast Fourier transform (FFT) analysis was also conducted to investigate the effect of the contact conditions on the impact force profiles. The methods for estimating the imparted and absorbed energy were proposed and evaluated to quantify the impact performance.

Chapter 7 summarizes the main findings, draws conclusions, and recommends some future works.

Overall, this dissertation is compiled from the technical papers prepared for publications during the PhD studies. Each chapter from Chapter 2 to Chapter 6 is comprised of one technical paper. The technical papers in the chapters are formatted according to the rules from Curtin University. References cited by each technical paper are included at the end of each chapter.

1. 4. References

[1] Benhelal E, Zahedi G, Shamsaei E, Bahadori A. Global strategies and potentials to curb CO2 emissions in cement industry. J Cleaner Prod. 2013;51:142-61.

[2] Davidovits J. Geopolymers: inorganic polymeric new materials. J Therm Anal Calorim. 1991;37:1633-56.

[3] van Deventer JSJ, Provis JL. Alkali Activated Materials: State-Of-the-Art Report, RILEM TC 224-AAM. 2014 ed. Dordrecht: Dordrecht: Springer Netherlands; 2013.

[4] Khan MZN, Shaikh FUA, Hao Y, Hao H. Synthesis of high strength ambient cured geopolymer composite by using low calcium fly ash. Constr Build Mater. 2016;125:809-20.

[5] Nath P, Sarker PK. Effect of GGBFS on setting, workability and early strength properties of fly ash geopolymer concrete cured in ambient condition. Constr Build Mater. 2014;66:163-71.

[6] Turner LK, Collins FG. Carbon dioxide equivalent (CO2-e) emissions: A comparison between geopolymer and OPC cement concrete. Constr Build Mater. 2013;43:125-30.

[7] McLellan BC, Williams RP, Lay J, van Riessen A, Corder GD. Costs and carbon emissions for geopolymer pastes in comparison to ordinary portland cement. J Cleaner Prod. 2011;19:1080-90.

[8] Teh SH, Wiedmann T, Castel A, de Burgh J. Hybrid life cycle assessment of greenhouse gas emissions from cement, concrete and geopolymer concrete in Australia. J Cleaner Prod. 2017;152:312-20.

[9] Ngo TT, Pham TM, Hao H. Effects of steel fibres and prestress levels on behaviour of newly proposed exterior dry joints using SFRC and CFRP bolts. Eng Struct. 2020;205:110083.

[10] Chen L, Wu H, Liu T. Vehicle collision with bridge piers: A state-of-the-art review. Adv Struct Eng. 2020:1369433220953510.

[11] Wu M, Jin L, Du X. Dynamic responses and reliability analysis of bridge double-column under vehicle collision. Eng Struct. 2020;221:111035.

[12] https://en.wikipedia.org/wiki/I-40_bridge_disaster.

[13] https://www.bbc.com/news/world-europe-25975251.

[14] Pham TM, Hao H. Behavior of fiber-reinforced polymer-strengthened reinforced concrete beams under static and impact loads. International Journal of Protective Structures. 2017;8:3-24.

[15] Zhao D-B, Yi W-J, Kunnath Sashi K. Shear Mechanisms in Reinforced Concrete Beams under Impact Loading. J Struct Eng. 2017;143:04017089.

[16] Pham TM, Chen W, Elchalakani M, Karrech A, Hao H. Experimental investigation on lightweight rubberized concrete beams strengthened with BFRP sheets subjected to impact loads. Eng Struct. 2020;205:110095.

[17] Tran TT, Pham TM, Hao H. Experimental and analytical investigation on flexural behaviour of ambient cured geopolymer concrete beams reinforced with steel fibers. Eng Struct. 2019;200:109707.

[18] Tran TT, Pham TM, Hao H. Effect of hybrid fibers on shear behaviour of geopolymer concrete beams reinforced by basalt fiber reinforced polymer (BFRP) bars without stirrups. Compos Struct. 2020;243:112236.

[19] Khan MZN, Hao Y, Hao H, Shaikh FUA. Experimental evaluation of quasi-static and dynamic compressive properties of ambient-cured high-strength plain and fiber reinforced geopolymer composites. Constr Build Mater. 2018;166:482-99.

[20] Khan MZN, Hao Y, Hao H, Shaikh FuA. Mechanical properties and behaviour of high-strength plain and hybrid-fiber reinforced geopolymer composites under dynamic splitting tension. Cem Concr Compos. 2019;104:103343.

Chapter 2. Mechanical Properties and Differences in Structural Design of Ambient-cured Geopolymer Concrete

Abstract[1]

Although there has been a large number of studies investigating the mechanical properties of geopolymer concrete (GPC), parameters for designing GPC structures are still not systematically investigated and carefully justified. ACI rectangular stress-block parameters can predict well the strength of conventional concrete structures but their applicability for GPC is questionable. This chapter aims to establish new sets of rectangular stress-block parameters for GPC with a broad range of compressive strength up to 66 MPa. The proposed rectangular stress-block parameters are based on two analytical concrete stress-strain models and measured curves from previous studies of GPC materials. The results show that the use of ACI recommendations for concrete structure in designing GPC beams is still acceptable with high accuracy. However, the axial load-carrying capacity of GPC columns computed by ACI parameters deviates significantly from the experimental results while the proposed parameters provide a good correlation with these experimental data. The significant difference is mainly due to the modification of k_3, which is the ratio of concrete strength in real structures to standard cylinder samples. It is suggested that the assumption of k_3=0.9 in previous studies for conventional Portland concrete is not suitable for use in deriving the stress-block parameters of GPC. In some cases, this ratio should be reduced to 0.7 depending on the curing condition.

2.1. Introduction

The process of synthesizing Portland cement which is emitting a large amount of carbon dioxide (CO2) into the atmosphere [1] is one of the main factors contributing to global warming. In this context, it is necessary to find a new material to replace the conventional but non-environmentally friendly Portland cement. Currently, geopolymer concrete (GPC), which

[1] This chapter was extracted from the paper published in Structures, but the tittle of the chapter and subsections were modified to follow the flow of the thesis. The full bibliographic citation of the paper is as follows:
Tran TT, Pham TM, Hao H. Rectangular Stress-block Parameters for Fly-ash and Slag Based Geopolymer Concrete. Structures. 2019;19:143-55.
https://doi.org/10.1016/j.istruc.2019.01.006

is produced from industrial by-products such as fly ash and slags [2], is regarded as a promising solution.

Until now most studies have focused on investigating the mixture design and mechanical properties of GPC [3]. It is demonstrated that GPC has some superior characteristics such as low creep, little drying shrinkage, excellent sulphate and acid sulfuric resistance [4], and better bonding as well as flexural strength [5, 6]. Furthermore, by adjusting the ratio of sodium silicate and sodium hydroxide solution when mixing GPC, the bond strength between GPC and steel reinforcement could increase up to 36% [7]. In contrast, some available studies also specified the disadvantages of the mechanical characteristics of GPC. The experimental findings of these studies reported the lower elastic modulus of GPC compared to those of ordinary Portland concrete (OPC) with the same compressive strength [8-10]. Therefore, the equations for estimating the elastic modulus of OPC in current standards tend to overestimate the actual elastic modulus of GPC [8]. In addition, a more brittle response in the mechanical behaviour of GPC than OPC was observed in the experimental tests [11-13]. Most studies investigating the compressive stress-strain behaviour of GPC also reported significant differences between GPC and OPC [10, 14, 15]. Due to such distinction of the material behaviour between GPC and OPC, it is essential to examine the suitability of applying the current design methods of OPC for GPC.

In contrast to the number of previous studies on the mechanical properties of GPC, investigations of the behaviours of structures made of GPC are still limited and contrary findings were reported. The behaviour of GPC beams was investigated in several experimental studies [16-22] while other studies examined the structural performance of GPC columns [23-26]. In general, these studies showed the structural response of the GPC beams and columns was almost identical to that of OPC and thus concluded that the current design codes and models for OPC structures can be applied to calculate the strength of GPC beams and columns. Nevertheless, a recent investigation on the behaviour of ambient cured GPC columns subjected to axial load and uniaxial bending demonstrated that the sectional analysis procedure based on AS3600 standards considerably overestimated the strength of these columns compared to test results [27]. This variation indicates that the design procedures in available standards for OPC structures are inaccurate in estimating the capacity of GPC structures.

To estimate the load-carrying capacity of reinforced OPC beams and columns, the ACI 318-11 building code [28] recommended rectangular stress-block parameters that can be derived from

the tests of eccentrically loaded columns [29] or an analytic stress-strain curve [30]. From the obvious difference of compressive stress-strain relationship between GPC and OPC, it is evident that the stress-block parameters of GPC cannot be the same as OPC. Hence this paper aims to formulate the equations of rectangular stress-block parameters for GPC. The proposed equations are used to estimate the bending moment capacity of GPC beams and the axial load-moment interaction diagrams of GPC columns. The analytical estimations are verified against the test results from the previous studies in the literature [16, 23, 27].

2.2. Research significance

There has been a limited number of studies evaluating and proposing the equivalent stress-block parameters for fly ash-based GPC until now [31, 32]. In the first study, the Popovics's stress-strain curve for modelling the stress-strain relationship of fly ash-based GPC was calibrated by Prachasaree et al. [31] to derive a set of equivalent stress-block parameters. Meanwhile, a combined axial-flexural test proposed by Hognestad et al. [29] was conducted in the second study to determine experimentally equivalent stress-block parameters of GPC. Although the results calculated by those parameters demonstrated a good prediction of the moment capacity of GPC beams, there has been no verification of the reliability of these parameters in calculating the strength of GPC columns. Moreover, a drastic difference in stress-strain behaviour of GPC made of ground granulated blast furnace slag (GGBFS) and fly ash with OPC was reported in the previous study [10] and illustrated in Figure 2-1. The performance of GPC after the peak stress is extremely brittle compared to OPC. The same phenomenon has been observed in previous experiments and has been attributed to the high prevalence of micro-cracking in GPC made of GGBFS [13]. Owing to such differences, it is apparent that the use of stress-block parameters in current design codes for OPC likely leads to unsafe predictions for GPC as reported in the aforementioned study [27]. With this motivation, a set of rectangular stress-block parameters for GPC columns and beams is proposed in the study of this chapter. In literature, the rectangular stress-block parameters were derived from an analytical stress-strain model [30, 33]. Therefore, the study in this chapter adopts the two modified-Popovics stress-strain curves for GPC in the previous studies [10, 24] to establish two sets of rectangular stress-block parameters. Furthermore, based on measured curves from the published experimental results [8, 10, 13, 34] which were summarized in Table 2-1, the third set of rectangular stress-block parameters is also derived. Then, the three sets of

rectangular stress-block parameters are compared and the most suitable set for GPC design is determined.

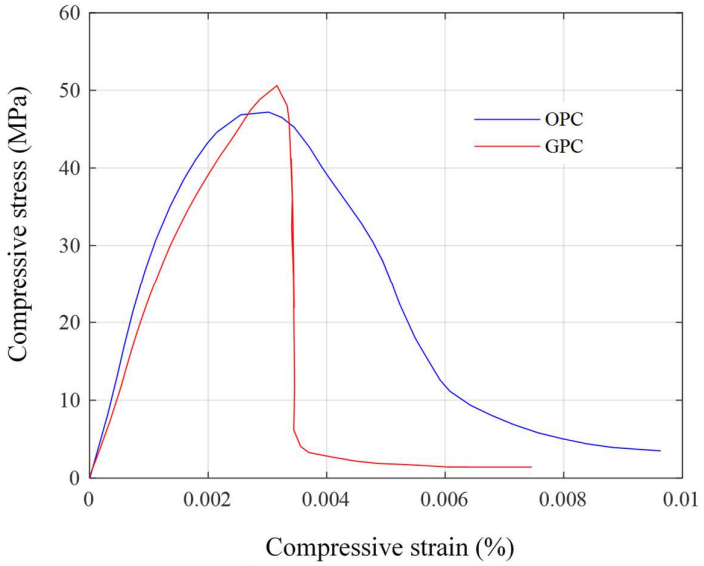

Figure 2-1. Comparison of stress-strain curves of cylinder tests of GPC and OPC

Table 2-1. Summary of experimental data of compressive cylinder tests

Specimen designation	Curing		f_c' (MPa)	E_c(GPa)	Reference
	Temp (°C)	Length (hour)			
Mixture-23	90	24	64	30.6	[8]
Mixture-24	90	24	61	30.8	[8]
Mixture-26	60	24	41	24.7	[8]
GPC-SAC	22	-	41.7	19.3	[10]
GPC-HC-1	60	8	27.4	13.5	[10]
GPC-HC-2	60	12	37.8	16.6	[10]
GPC-HC-3	60	18	45.6	20.3	[10]
GPC-HC-4	60	24	50	22.9	[10]
GPC-HC-5	75	8	44.8	20.4	[10]
GPC-HC-6	75	12	53.9	22.8	[10]
GPC-HC-7	75	18	60	24.4	[10]

GPC-HC-8	75	24	62.3	25.9	[10]
GPC-HC-9	90	8	52.2	23.5	[10]
GPC-HC-10	90	12	58.6	23.9	[10]
GPC-HC-11	90	18	59.8	25.1	[10]
GPC-HC-12	90	24	60.7	25.8	[10]
FC1-22 °C	22	-	28.9	21.5	[13]
FC1-50 °C	50	48	47.7	26	[13]
GGBFS5-22 °C	22	-	45.7	22.4	[13]
GGBFS5-50 °C	50	48	48.7	22.9	[13]
S-25	22	-	42.2	31.5	[34]
S-30	22	-	28.5	25.3	[34]
C-28	22	-	37.1	29.9	[34]
C-30	22	-	24.2	21.6	[34]

Note: Temp= curing temperature (if temp=22, the specimens were cured in temperature room until the test day), length= the period of time for curing, f_c'= compressive strength at 28 days, E_c=modulus of elasticity.

2.3. Review of stress-block parameters

The assumptions for the simplification of designing the concrete members subjected to bending moment are described in Figure 2-2. The strain distribution (Figure 2-2b) on the whole section is linear and the tensile stress of concrete is neglected. Concrete stress in the compressive zone is distributed according to the measured stress-strain curve that can be expressed mathematically by three parameters, i.e., k_1, k_2, and k_3 (Figure 2-2c) or is assumed having a rectangular shape in which the stress-block parameters are defined by two parameters α and β (Figure 2-2d). To determine these parameters, a comprehensive test program of eccentrically loaded C-shaped columns was conducted by Hognestad et al. [29] and the results had been adopted by the ACI 318 building code and recommended for concrete structure design until today. Currently, ACI 318-11 standard [28] recommends 0.85 for the parameter α while β has a value of 0.85 when the concrete compressive strength is less than 28 MPa and decreases by 0.05 for each 7 MPa but is limited by 0.65.

Although the research by Hognestad et al. [29] was comprehensive and provided a relatively accurate design calculation, it had just considered the concrete with normal strength under 60 MPa. In terms of high strength concrete, Ibrahim and MacGregor conducted 20 tests of eccentrically loaded columns to obtain parameters k_1, k_2, and k_3 and then derived the equivalent rectangular stress-block parameters α and β [35, 36]. Their research indicated the ACI value of 0.85 for parameter α was too high and not conservative to calculate the column capacity of high strength concrete. This can be explained by the fact that the actual stress-strain relationship of high strength concrete approaches to a triangular shape when the compressive strength increases. As a result, the value of α reduced considerably until reaching 0.725. In addition, the lower bound value of β derived from the ACI equation is too small for high strength concrete. Hence, the internal level arm becomes too big and the moment capacity is overestimated. Based on experimental data and findings from regression analysis, they suggested that the parameters α and β could be expressed as follows:

$$\alpha = 0.85 - \frac{f_c^{'}}{800} \geq 0.725 \tag{2-1}$$

$$\beta = 0.95 - \frac{f_c^{'}}{400} \geq 0.7 \tag{2-2}$$

where $f_c^{'}$ (MPa) is the compressive strength of concrete.

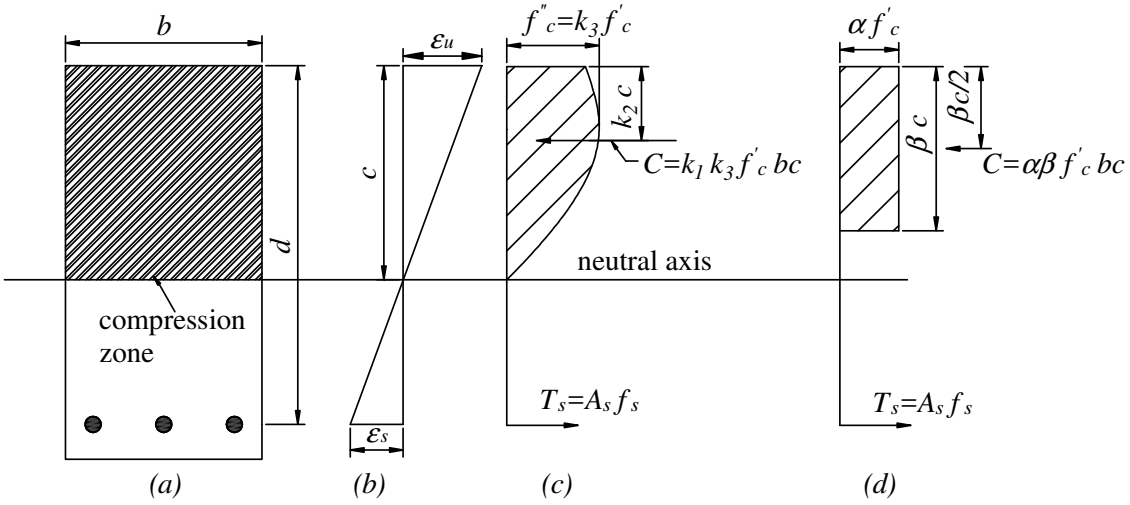

Figure 2-2. Assumptions for concrete structure designs

Moreover, the premature cover spalling in high strength concrete columns was recorded in the previous studies [35, 37]. Such a phenomenon leads to a strength loss in the columns. To ensure the safety in design, some researchers proposed new sets of stress-block parameters

incorporating the early cover spalling of high strength concrete for calculating the column capacity. Ozbakkaloglu and Saatcioglu [38] introduced the effect of cover spalling through multiplying k_3 by a parameter k_4 to predict the strength of the high strength concrete column under axial load.

$$k_4 = \gamma + (1-\gamma)\frac{A_c}{A_g} \leq 0.95 \tag{2-3}$$

$$\gamma = 1.1 - 0.007 f_c^{'} \leq 0.8 \tag{2-4}$$

where A_c is the area of core concrete and A_g is the gross area of concrete sections. Nevertheless, in the case of eccentrically loaded columns, they assumed that the cover spalling of the columns under bending is not likely to happen and thus the parameter k_4 in Eq. (2-3) becomes 1. In contrast, the results in the previous study by Bae and Bayrak [39] demonstrated a capacity reduction of high strength concrete columns under eccentric loads due to the early cover spalling and then proposed a new set of equivalent rectangular stress-block parameters considering this phenomenon [40]. Their stress-block parameters are relatively accurate to calculate the axial load-carrying capacity of high strength concrete columns.

A previous study also indicated transverse reinforcement ratio influences the capacity of high strength concrete columns [41]. From the tests in that study, it is noted that the flexural strength of columns confined with the reasonable transverse reinforcement ratio exceeded the calculated capacity based on rectangular stress-block parameters derived by Ibrahim and MacGregor [36]. For that reason, a set of rectangular stress-block parameters for unconfined and confined concrete has been proposed by Karthik and Mander [30]. In order to obtain the rectangular stress-block model, they suggested a new and simplified analytical stress-strain curve for a wide range of concrete strengths and confining stresses. Recently, a rectangular stress-block model was proposed to calculate the flexural strength of steel fibre reinforced concrete beams [42]. By using that model, the calculated moment capacity of beams was fairly accurate compared to the experimental findings.

In spite of a large number of studies on the rectangular stress-block parameters for conventional Portland concrete with a wide range of compressive strength, only a few studies on stress-block parameters for fly ash-based GPC under heated curing condition has been reported in the literature [31, 32]. Those studies proposed new sets of parameters defining the equivalent rectangular stress-block. Their results gave a better prediction for the flexural capacity of GPC

beams. However, they suggested that it is reasonable to use the parameters from the ACI 318-11 building code [28] since it still provided a conservative estimation. In contrast, it seems that the strength of GPC columns calculated by the stress-block parameters from ACI 318-11 code [28] is not conservative. An aforementioned study indicated a significant overestimation of the load-carrying capacity of GPC columns when using the current design codes [27]. In addition, in their experiments, the early cover spalling of columns was observed in most cases even though the normal-strength concrete of about 35 MPa was used. It is worth mentioning that this phenomenon has been only recorded in high-strength Portland concrete columns. Owing to such a distinction in structural performance, it is evident that the rectangular stress-block parameters in the current design codes for Portland concrete are not necessarily suitable for designing GPC structures. With this observation, this research intends to develop a new and rational set of equivalent rectangular stress-block parameters for GPC structures. The equations of these parameters are established based on integrating the analytical stress-strain curves obtained from previous studies with GPC [10, 24] or measured curves from the published experimental results [8, 10, 13, 34].

2.4. Analytical stress-strain curves for geopolymer concrete

Based on a review of stress-strain models of GPC, the following two constitutive models are adopted to derive rectangular stress block parameters for GPC structures [10, 24]. According to the previous studies by Hardjito and Sarker, a modified Popovics model of stress-strain relationship for conventional concrete can predict accurately the compressive behaviour of GPC [8, 24]. This model is expressed mathematically by Eq. (2-5)

$$f_c = f(\varepsilon_c) = f_c' \frac{\varepsilon_c}{\varepsilon_c'} \frac{n}{n-1+\left(\frac{\varepsilon_c}{\varepsilon_c'}\right)^{np}} \tag{2-5}$$

where f_c is concrete compressive stress, ε_c is the compressive strain of concrete, f_c' (in MPa) is the concrete cylinder strength, ε_c' is the concrete strain at f_c which is calculated by Eq. (2-8), the curve fitting factors n and p are presented in Eqs. (2-6) and (2-7), and the elastic modulus of GPC is calculated by using the empirical Eq. (2-9) proposed by Hardjito [24] as follows:

$$n = 0.8 + \frac{f_c'}{12} \tag{2-6}$$

$$p = 0.67 + \frac{f_c^{'}}{62} \text{ when } \frac{\varepsilon_c}{\varepsilon_c^{'}} > 1 \text{ and } p = 1 \text{ when } \frac{\varepsilon_c}{\varepsilon_c^{'}} \le 1 \tag{2-7}$$

$$\varepsilon_c^{'} = \frac{f_c^{'}}{E_c} \frac{n}{n-1} \tag{2-8}$$

$$E_c = 2707\sqrt{f_c^{'}} + 5300 \text{ (MPa)} \tag{2-9}$$

Similarly, in an effort to establish a stress-strain relationship for GPC Noushini et al. [10] developed a new model through calibrating the curve-fitting parameters of the Popovics stress-strain curve based on the cylinder compressive test results of 13 GPC specimens. The model is presented in Eqs. (2-10)-(2-16), where the modulus of elasticity and strain at peak of GPC is calculated by Eqs. (2-17) and (2-18).

$$f_c = f(\varepsilon_c) = f_c^{'} \frac{\varepsilon_c}{\varepsilon_c^{'}} \frac{n}{n-1+\left(\frac{\varepsilon_c}{\varepsilon_c^{'}}\right)^n} \tag{2-10}$$

$$n = n_1 = \left[1.02 - 1.17(E_{\text{sec}} / E_c)\right]^{-0.45} \text{ if } \varepsilon_c \le \varepsilon_c^{'} \tag{2-11}$$

$$n = n_2 = n_1 + (\varpi + 28\zeta) \text{ if } \varepsilon_c > \varepsilon_c^{'} \tag{2-12}$$

$$\varpi = C\left(12.4 - 0.015 f_c^{'}\right)^{-0.5} \tag{2-13}$$

$$\zeta = 0.83 \times \exp(-911 / f_c^{'}) \tag{2-14}$$

$$C = 17 \text{ for heat-cured GPC} \tag{2-15}$$

$$E_{\text{sec}} = f_c^{'} / \varepsilon_c^{'} \tag{2-16}$$

$$E_C = -11470 + 4712\sqrt{f_c^{'}} \tag{2-17}$$

$$\varepsilon_c^{'} = \frac{2.23 \times 10^{-7} \left(E_c\right)^{1.74}}{\left(f_c^{'}\right)^{1.98}} \tag{2-18}$$

where the curve fitting factor n is represented by two modified parameters n_1 at the ascending branch (Eq. (2-11)) and n_2 at the descending branch (Eq. (2-12)), ϖ and ζ are the necessary coefficients to determine n_1 and n_2, C is the curing parameter which is equal to 17 for GPC

under heat curing condition, E_c (Eq. (2-17) is the modulus of elasticity of GPC in MPa and E_{sec} (Eq. (2-16)) is the secant modulus. The strain ε_c' at peak stress is calculated by Eq. (2-18).

The method to establish rectangular stress-block parameters based on analytical stress-strain curves was developed in previous studies for Portland concrete [30, 33, 40, 43]. This method is also adopted in the study of this chapter to derive the rectangular stress-block parameters for GPC. In addition, the study also proposes a method to obtain the rectangular stress-block parameters directly from experimental stress-strain curves measured in uniaxial compression tests of cylinder samples. These methods will be presented in the next section.

2.5. Derivation of rectangular stress-block parameters

2.5.1. Establishing equations for rectangular stress-block parameters

For the compression zone with the width b and depth to neutral axis c in Figure 2-2, the resultant compressive force is

$$C = k_1 f_c^{''} bc = k_1 \left(k_3 f_c^{'} \right) bc \tag{2-19}$$

where the parameter k_3 is a ratio of the real maximum stress f_c'' in the compression zone of structural elements to concrete strength of cylinder samples f_c', the parameter k_1 is the ratio of the average compressive stress to the maximum stress f_c'' and the parameter k_2 is the ratio of the distance between the extreme compression fibre and the internal compressive force C to the depth of the neutral axis.

According to Wight and MacGregor [44], the value of k_1 is determined by dividing the stress-block by the area of the rectangle (as illustrated in Figure 2-3b). The stress-block area and the area of the rectangle are presented mathematically in Eqs. (2-20) and (2-21) as follows:

$$\text{Stress-block area} = \int_0^c f_c(\varepsilon_c) dy = \frac{c}{\varepsilon_{cu}} \int_0^{\varepsilon_{cu}} f_c(\varepsilon_c) d\varepsilon_c \tag{2-20}$$

$$\text{Area of rectangle} = f_c^{''} c = k_3 f_c^{'} c \tag{2-21}$$

where ε_{cu} is the ultimate strain at extreme compression strip (Figure 2-3a) and $f_c(\varepsilon_c)$ (Figure 2-3c) is the function that represents the compressive stress-strain relationship for concrete. $f_c(\varepsilon_c)$ can be estimated based on the measured stress-strain curves obtained from concrete cylinder tests or the available analytical stress-strain models. However, Wight and MacGregor

[44] suggested that the peak stress f_c' in stress-strain models or curves adopted to calculate stress-block parameters should be $f_c'' = k_3 f_c'$ because there are differences of strengths between the cylinder samples and structural members in real scale (the suitable values of k_3 will be discussed below). Therefore, k_3 diminishes in the equation to determine k_1 by combining Eqs. (2-20) and (2-21) as follows:

$$k_1 = \frac{\text{Stress-block area}}{\text{Area of rectangle}} = \frac{\int_0^{\varepsilon_{cu}} f_c(\varepsilon_c)\, d\varepsilon_c}{f_c' \varepsilon_{cu}} \tag{2-22}$$

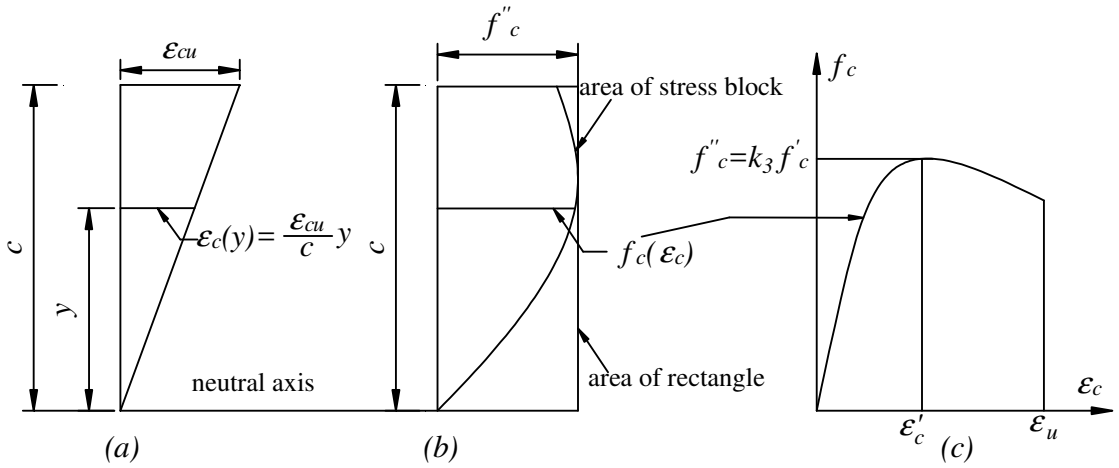

Figure 2-3. Illustrations for k_1 determination

With a stress-block illustrated in Figure 2-4, the parameter k_2 is calculated by

$$k_2 = \frac{c - \bar{y}}{c} \tag{2-23}$$

where $\bar{y}$ is the distance from the neutral axis to the centroid of the stress-block and can be expressed as follows:

$$\bar{y} = \frac{\int_0^c y f(y)\, dy}{\int_0^c f(y)\, dy} = \frac{c\int_0^{\varepsilon_{cu}} \varepsilon_c f_c(\varepsilon_c)\, d\varepsilon_c}{\varepsilon_{cu}\int_0^{\varepsilon_{cu}} f_c(\varepsilon_c)\, d\varepsilon_c} \tag{2-24}$$

After substituting $\overline{y}$ in Eq. (2-24) into Eq. (2-23), the integral formula of k_2 is

$$k_2 = 1 - \frac{\int_0^{\varepsilon_{cu}} \varepsilon_c f_c(\varepsilon_c) d\varepsilon_c}{\varepsilon_{cu} \int_0^{\varepsilon_{cu}} f_c(\varepsilon_c) d\varepsilon_c} \tag{2-25}$$

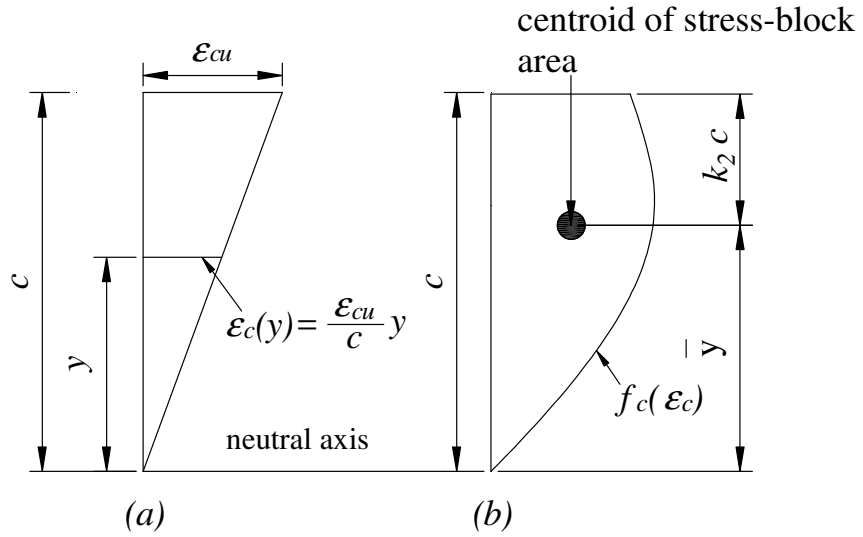

Figure 2-4. Relationship of k_2 and centroid of stress-block area $\overline{y}$

If the stress-strain relationship $f_c(\varepsilon_c)$ is known, the parameters k_1 and k_2 can be determined from Eqs. (2-22) and (2-25). In this chapter, two analytical models of GPC in Eq. (2-5) and Eq. (2-10) are adopted to represent the stress-strain relationship of concrete. In addition, $f_c(\varepsilon_c)$ can be obtained from measured stress-strain curves in cylinder tests, which were reported in the published studies in the literature [8, 10, 13, 34].

The integrals in Eq. (2-22) and Eq. (2-25) depend on the value of the ultimate concrete compressive strain ε_{cu}, so the determination of this parameter is significantly important. In ACI 318-11 standard [28], the value of ε_{cu} is recommended as 0.003 while in the modified Hognestad stress-strain curve, it has a value of 0.0038. Another way to estimate ε_{cu} is based only on the unit moment $\overline{M}$ caused by compressive stress-block [33], which is expressed by Eqs. (2-26) and (2-27). Figure 2-5 illustrates the function $\overline{M}$ of variable ε_{cu} when using the Popovics stress-strain curve. By differentiating $\overline{M}$ at the maximum $\overline{M}_{max}$ value, the value of

ε_{cu} can be calculated as shown in Eq. (2-28). This value is used to calculate integrals in Eqs. (2-22) and (2-25).

$$M = k_1(k_3 f_c^{'})cb\left(c - k_2 c\right) \tag{2-26}$$

$$\overline{M} = \frac{M}{\left(k_3 f_c^{'}\right)c^2 b} = k_1\left(1 - k_2\right) = \frac{\int_0^{\varepsilon_{cu}} \varepsilon_c f\left(\varepsilon_c\right) d\varepsilon_c}{\varepsilon_{cu}^2 f_c^{'}} \tag{2-27}$$

$$\frac{d\overline{M}}{d\varepsilon_{cu}} = \frac{\varepsilon_{cu}^2 f_c\left(\varepsilon_{cu}\right) - 2\int_0^{\varepsilon_{cu}} \varepsilon_c f\left(\varepsilon_c\right) d\varepsilon_c}{\varepsilon_{cu}^3 f_c^{'}} = 0 \tag{2-28}$$

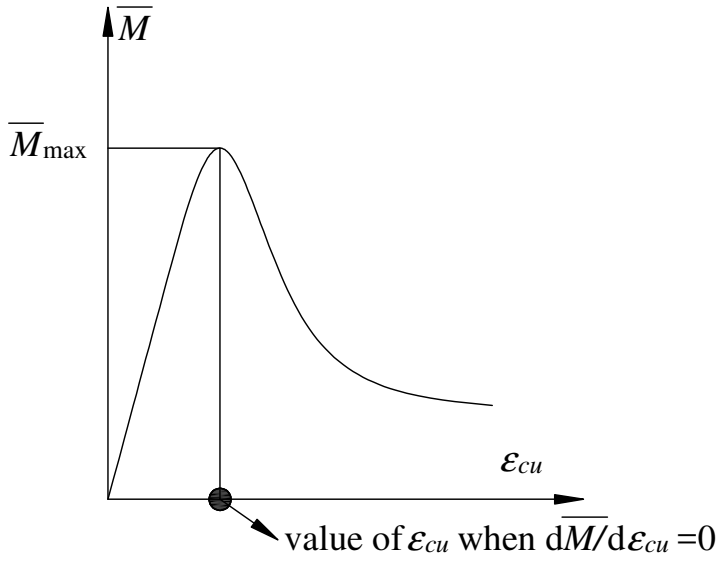

Figure 2-5. The relationship between $\overline{M}$ and ε_{cu}

For the stress-block with the rectangular shape depicted in Figure 2-2b, the resultant compressive force caused by rectangular stress-block parameters α and β can be expressed as follows:

$$C = \alpha\beta f_c^{'} bc \tag{2-29}$$

Since the resultant compressive force in Eq. (2-29) must be equal to the value resulted from the real stress-block in Eq. (2-19), the equation for α and β can be written as follows:

$$\alpha\beta = k_1 k_3 \tag{2-30}$$

Moreover, the rectangular stress-block gives the same internal level arm of real stress-block and thus β is expressed as follows:

$$\beta = 2k_2 \tag{2-31}$$

By combining Eq. (2-30) and Eq. (2-31), α can be expressed as:

$$\alpha = \frac{k_1 k_3}{2k_2} \tag{2-32}$$

To sum up, the rectangular stress-block parameters α and β can be calculated straightforwardly if the parameters k_1, k_2, and k_3 of real stress-block are known. In order to determine the parameters k_1 and k_2, the integration of Eqs. (2-22) and (2-25) must be carried out. The analytical procedures to obtain the solution for these integrals will be described in Section 2.5.3. The value of k_3 will be discussed in Section 2.5.2.

2.5.2. Assumption of the value of parameter k_3

According to ACI 318-11 standard [28], the pure ultimate axial load of concrete columns can be computed based on the value of k_3 as follows:

$$P_0 = k_3 f_c^{'}(A_g - A_s) + f_y A_s \tag{2-33}$$

where P_0 is the ultimate pure axial load, A_g is the gross area of column section, A_s is the total area of longitudinal steel reinforcement steel and f_y is the yield strength of steel reinforcement. The parameter k_3 represents the difference between the concrete compressive strength of a structural element and that of a cylinder sample owing to the change in the shape, size, and random factors such as curing condition, vibration during casting, and loading rate, etc. In the ACI 318-11 standard [28], k_3 is recommended to be 0.85. Until now, this parameter has been mainly determined from concentrically loaded column tests [45, 46] and the tests on eccentrically loaded C-shaped columns [35]. Based on these recorded data, Ibrahim and MacGregor [36] recommended that the value of 0.85 for k_3 from the ACI standard was conservative compared to the test findings of eccentrically loaded columns. However, except for columns subjected to pure axial load, the ACI code does not recommend using k_3 for concrete structures under both high axial load and bending moment. Therefore, Wight and MacGregor [44] proposed the use of $k_3 = 0.9$ according to the previous studies by Pfrang et al. [47] when calculating the combined axial and bending strength of a column section.

In terms of GPC, Sarker [24] used the value $k_3 = 0.9$ to analyse the structural performance of columns under axial load and bending moment. The correlation between the results of his analysis and experiment data was quite good. In contrast, Albitar et al. [27] indicated that the use of $k_3 = 0.85$ according to the current standards overestimates the axial load of geopolymer concrete columns by 30%. This difference is attributed to the variation of mixtures and the curing condition. In his study, the content of the mixture for GPC consisted of fly ash and granulated lead smelter slag (GLSS) and the columns were cured in ambient condition. It should be noted that the adoption of high content of slag and ambient curing condition can lead to the increase of shrinkage cracks and thereby reducing the fracture energy of GPC [12-13]. Meanwhile, Sarker [24] used fly ash-based geopolymer concrete columns, which were manufactured in a heat curing condition. This indicates that the use of $k_3 = 0.9$ might be suitable for heat-cured fly ash-based GPC columns. For GPC containing another material such as slag and cast in ambient condition, this parameter tends to be smaller than that of the conventional concrete.

From Eq. (2-33) the parameter k_3 can be estimated by the following expression:

$$k_3 = \frac{P_0 - f_y A_s}{f_c^{'}(A_g - A_s)} \tag{2-34}$$

where the value of P_0 can be obtained for the concentrically loaded columns. Based on experimental data from column tests in the study by Albitar et al. [27], the authors suggested that k_3 should be 0.7 for the ambient cured GPC. Obviously, it is essential that more studies should be conducted to investigate the factors that govern parameter k_3.

To sum up, regarding the heat-cured fly ash-based GPC, k_3 is assumed to be 0.9 for determining the parameter α in Eq. (2-32) while the value k_3=0.7 is employed in the case of fly ash and slag-based GPC which is cured under ambient condition.

2.5.3. Analytical solutions of stress-block equations

This section presents the procedures to obtain analytical solutions for equations of rectangular stress-block parameters based on the two aforementioned stress-strain models or experimental curves from cylinder tests. Initially, the analytical stress-strain model by Sarker [24] in Eq. (2-5) is employed in Eq. (2-22) and Eq. (2-25), and hence the formulas of parameters k_1 and k_2 become

$$k_1 = \frac{1}{f_c^{'}\varepsilon_{cu}} \int_0^{\varepsilon_{cu}} f_c^{'} \frac{\varepsilon_c}{\varepsilon_c^{'}} \frac{n}{n-1+\left(\varepsilon_c/\varepsilon_c^{'}\right)^{nk}} d\varepsilon_c = \frac{1}{\varepsilon_{cu}} \int_0^{\varepsilon_{cu}} \frac{n\left(\varepsilon_c/\varepsilon_c^{'}\right)}{n-1+\left(\varepsilon_c/\varepsilon_c^{'}\right)^{nk}} d\varepsilon_c \tag{2-35}$$

$$k_2 = 1 - \frac{\int_0^{\varepsilon_{cu}} f_c^{'} \frac{\varepsilon_c^2}{\varepsilon_c^{'}} \frac{n}{n-1+\left(\varepsilon_c/\varepsilon_c^{'}\right)^{nk}} d\varepsilon_c}{\varepsilon_{cu} \int_0^{\varepsilon_{cu}} f_c^{'} \frac{\varepsilon_c}{\varepsilon_c^{'}} \frac{n}{n-1+\left(\varepsilon_c/\varepsilon_c^{'}\right)^{nk}} d\varepsilon_c} = 1 - \frac{\varepsilon_c^{'} \int_0^{\varepsilon_{cu}} \frac{n\left(\varepsilon_c/\varepsilon_c^{'}\right)^2}{n-1+\left(\varepsilon_c/\varepsilon_c^{'}\right)^{nk}} d\varepsilon_c}{\varepsilon_{cu} \int_0^{\varepsilon_{cu}} \frac{n\left(\varepsilon_c/\varepsilon_c^{'}\right)}{n-1+\left(\varepsilon_c/\varepsilon_c^{'}\right)^{nk}} d\varepsilon_c} \tag{2-36}$$

To facilitate later calculation, Eq. (2-35) and Eq. (2-36) are rewritten as follows:

$$k_1 = \frac{\varepsilon_c^{'} A}{\varepsilon_{cu}} \tag{2-37}$$

$$k_2 = 1 - \frac{\varepsilon_c^{'} B}{\varepsilon_{cu} \cdot A} \tag{2-38}$$

Where

$$A = \int_0^{\varepsilon_{cu}/\varepsilon_c^{'}} \frac{nX}{n-1+\left(X\right)^{nk}} dX \text{ with } X = \frac{\varepsilon_c}{\varepsilon_c^{'}} \tag{2-39}$$

$$B = \int_0^{\varepsilon_{cu}/\varepsilon_c^{'}} \frac{nX^2}{n-1+\left(X\right)^{nk}} dX \text{ with } X = \frac{\varepsilon_c}{\varepsilon_c^{'}} \tag{2-40}$$

It is noted that integral expressions in Eqs. (2-39) and (2-40) are very complex and it is too difficult to be achieved by analytical solutions. Consequently, a Newton-Cotes numerical integration with the trapezoidal rule [48] is adopted to calculate integrals A (Eq. (2-39)) and B (Eq. (2-40)). Figure 2-6 illustrates the application of the trapezoidal rule to calculate an integration of an arbitrary stress-strain function. The area is divided into *m* equal segments ($\varepsilon_0 = 0, \varepsilon_1, \varepsilon_2, \ldots, \varepsilon_{m-1}, \varepsilon_m = \varepsilon_{cu}$) and hence, the equal width of each segment is

$$\Delta\varepsilon = \frac{\varepsilon_{cu}}{m} \tag{2-41}$$

then the total integral can be represented as follows:

$$I \approx \Delta\varepsilon\left(f_c(\varepsilon_0) + 2\sum_{1}^{m-1} f_c(\varepsilon_i) + f_c(\varepsilon_{cu}) \right) \tag{2-42}$$

By solving Eq. (2-42), the integrals A (Eq. (2-39)) and B (Eq. (2-40)) will be determined analytically. The error for the application of the trapezoidal rule will become negligible if the number of divided segments is large enough. In this chapter, the number of segments is chosen as m =100 to ensure the error of numerical integration is smaller than 1%.

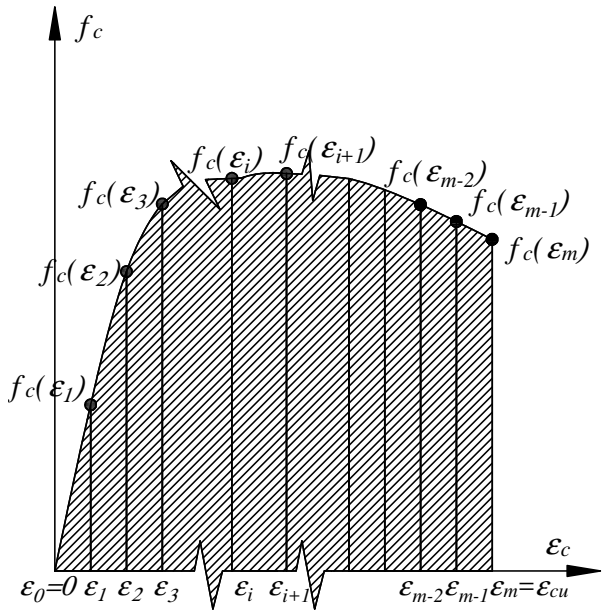

Figure 2-6. Illustration of numerical integration by using the trapezoidal rule

Similarly, the same method to derive parameters k_1 and k_2 will be applied for the stress-strain model by Noushini et al. [10] in Eq. (2-10). However, when the compressive strength of cylinders $f_c^{'}$ is greater than 66 MPa, the value of curve fitting factor n_1 in Eq. (2-11) becomes invalid and then the function cannot be solved. As a result, the solution based on the model by Noushini et al. [10] is only obtained for GPC with compressive strength smaller than 66 MPa. This method can be also employed for measured stress-strain curves with some modifications. Since it is almost impossible to determine an analytical function for an arbitrarily measured stress-strain curve, the calculation of parameters k_1 and k_2 is now conducted by Eq. (2-22) and Eq. (2-25) instead of using integrals A (Eq. (2-39)) and B (Eq. (2-40)). The use of the trapezoidal rule to calculate the integrals $\int_0^{\varepsilon_{cu}} f_c(\varepsilon_c)\,d\varepsilon_c$ of Eq. (2-22) and the integrals

$\int_0^{\varepsilon_{cu}} \varepsilon_c f_c(\varepsilon_c) d\varepsilon_c$ of Eq. (2-25) is based on the value of strain points ($\varepsilon_0 = 0, \varepsilon_1, \varepsilon_2, \ldots, \varepsilon_{m-1}, \varepsilon_m = \varepsilon_{cu}$) and stress points ($f_c(\varepsilon_0), f_c(\varepsilon_1), f_c(\varepsilon_2), \ldots, f_c(\varepsilon_{m-1}), f_c(\varepsilon_m) = f_c(\varepsilon_{cu})$) which are obtained directly from the experiment data of cylinder tests [8, 10, 13, 34]. Then Eq. (2-42) is adopted to derive the parameters k_1 and k_2.

The problem when solving the integrals is that the value of ε_{cu} must be known. To determine ε_{cu}, Eq. (2-28), which also contains the integrals in the mathematical expression of parameters k_1 and k_2, must be solved. For that reason, an iterative procedure developed to calculate ε_{cu}, k_1 and k_2 is presented (Figure 2-7) as follows:

Step 1: The area of the whole stress-strain curve is divided into *m* segments, with the value of divided strain points ($\varepsilon_0 = 0, \varepsilon_1, \varepsilon_2, \ldots, \varepsilon_{m-1}, \varepsilon_m = \varepsilon_{cu}$) and stress points (($f_c(\varepsilon_0), f_c(\varepsilon_1), f_c(\varepsilon_2), \ldots, f_c(\varepsilon_{m-1}), f_c(\varepsilon_m)$)from analytical models or experimental data;

Step 2: Assign $\varepsilon_{cu} = \varepsilon_i$ (initially, *i* is equal to 0);

Step 3: Calculate k_1 and k_2 based on Eqs. (2-37)-(2-40) (if using the analytical stress-strain models) or Eq. (2-22) and Eq. (2-25) (if using the measured curves). The derivative $\frac{d\overline{M}}{d\varepsilon_{cu}}$ is obtained from Eq. (2-28);

Step 4: Check condition $\frac{d\overline{M}}{d\varepsilon_{cu}} < 0$. If this condition is not satisfied, return to step 2 with new value *i=i+1*;

Step 5: Output the results ε_{cu}, k_1, and k_2.

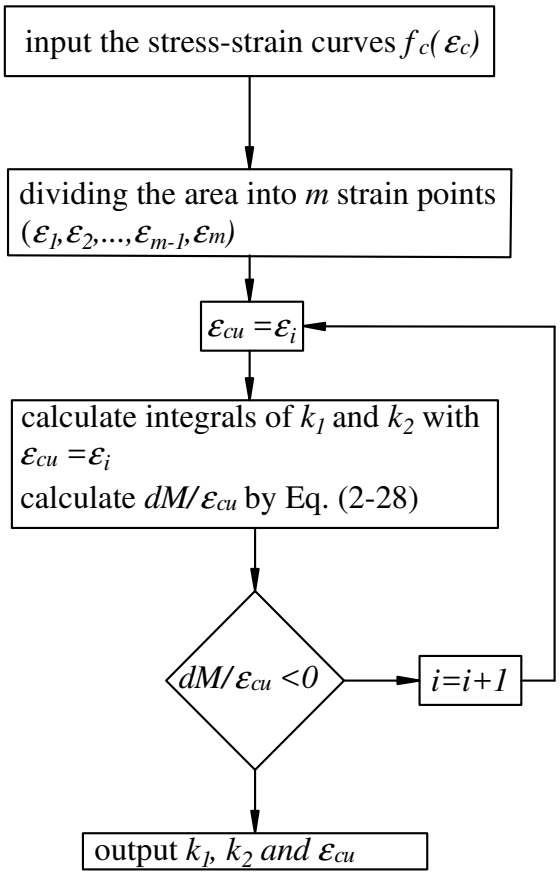

Figure 2-7. Flow chart for the analytical procedure to determine ε_{cu}, k_1, and k_2

Once the parameters k_1 and k_2 are determined, the rectangular stress-block parameters α and β are calculated straightforwardly from Eq. (2-31) and Eq. (2-32) associated with the assumption of k_3 discussed in Section 2.5.2 of this chapter. The proposed rectangular stress-block parameters are presented in the next section.

2.6. Proposed rectangular stress-block parameters

An analytical algorithm based on the procedures presented in the previous section is developed using Matlab programming [49] to derive the rectangular stress-block parameters α and β. The results of α and β are shown in Figure 2-8 through Figure 2-10. Figure 2-8 shows the variation of α versus the concrete strength in the case of k_3=0.9 for the heat-cured fly ash-based GPC while Figure 2-9 illustrates the equations of α for ambient-cured fly ash and slag-based GPC with k_3=0.7. From these figures, the proposed parameter α tends to decrease with the increase of concrete strength instead of being a constant as recommended by ACI 318-11 standard [28]. As a result, this may lead to a more conservative estimation when using ACI 318-11 standard.

The variation of β and ε_{cu} is plotted in Figure 2-10 and Figure 2-11, respectively. It should be noted that the equations of β and ε_{cu} are the same for both the cases of heat-cured fly ash-based GPC and ambient cured fly ash and slag-based GPC because they are independence of k_3. As can be seen from Figure 2-10, the values of β according to ACI 318-11 standard [28] are smaller than those estimated from the proposed equations when the concrete compressive strength exceeds 45 MPa. It is worth mentioning that if the value of β is too low, the internal level arm will be too high. Therefore, the design procedure in ACI 318-11 standard likely overestimates the bending moment capacity of GPC structures. However, this does not mean ACI always gives unsafe prediction since the strength estimation of a concrete section still depends on the value of ε_{cu}. ACI 318-11 standard recommends the value of $\varepsilon_{cu} = 0.003$ which is almost the lower bound of analytical results derived from the measured curves [28] (Figure 2-11). The common values of ε_{cu} calculated from the measured stress-strain curves vary considerably from 0.0025 to 0.0045. The mean value of regression analysis is about 0.0035 with a standard deviation of 8.9634e-04. These results demonstrate that the range of ε_{cu} for GPC is relatively similar to that of OPC. Meanwhile, the equation of ε_{cu} formulated from the modified Popovics model by Sarker [24] is relatively close to the value $\varepsilon_{cu} = 0.003$. The stress-strain model proposed by Noushini et al. [1] yields the highest value of ε_{cu}. This is mainly due to the overestimation of strain at peak stress ε_c' in Eq. (2-18).

In addition, the proposed parameters α and β derived from the modified Popovics model by Sarker [24] are likely to be the average values from measured curves while the proposed parameters calculated from the model of Noushini et al. [10] tend to be the upper bound. Due to the considerable variation of results between two analytical stress-strain models, the study in this chapter proposes the equations for α and β by using regression analysis for values obtained from measured curves. These equations are expressed in Eqs. (2-43)-(2-45) and depicted in Figures 2-8 to 2-10. By taking the mean of all values of ε_{cu} in Figure 2-11, Eq. (2-46) is proposed. Eq. (2-43) is used for the case of heat-cured fly ash-based GPC while the calculation for the ambient cured fly ash and slag-based GPC is based on Eqs. (2-44)- (2-46).

$$\alpha = -4.039\times10^{-6}\left(f_c^{'}\right)^2 - 0.001194\, f_c^{'} + 0.8542 \quad \text{with } k_3=0.9 \tag{2-43}$$

$$\alpha = -3.142\times10^{-6}\left(f_c^{'}\right)^2 - 0.0009284\, f_c^{'} + 0.6644 \quad \text{with } k_3=0.7 \tag{2-44}$$

$$\beta = -0.002537\, f_c^{'} + 0.8675 \tag{2-45}$$

$$\varepsilon_{cu} = 0.0035 \tag{2-46}$$

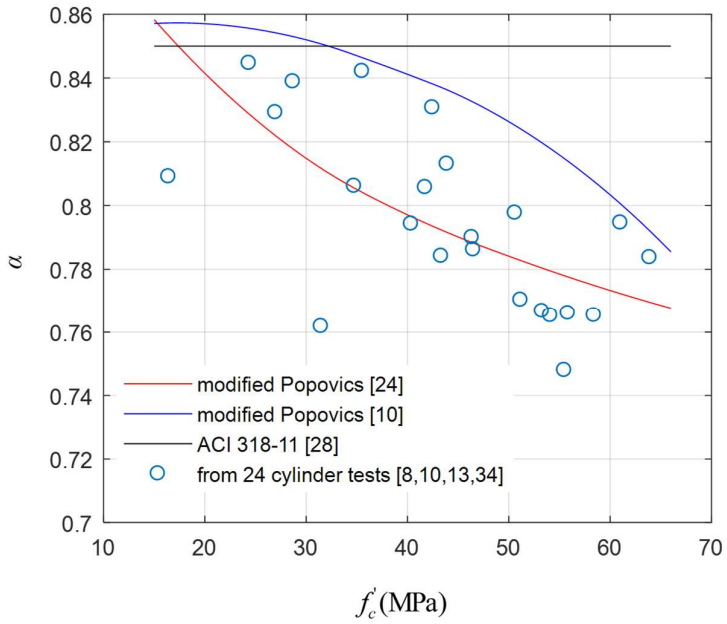

Figure 2-8. Stress-block parameter α in the case of k_3=0.9

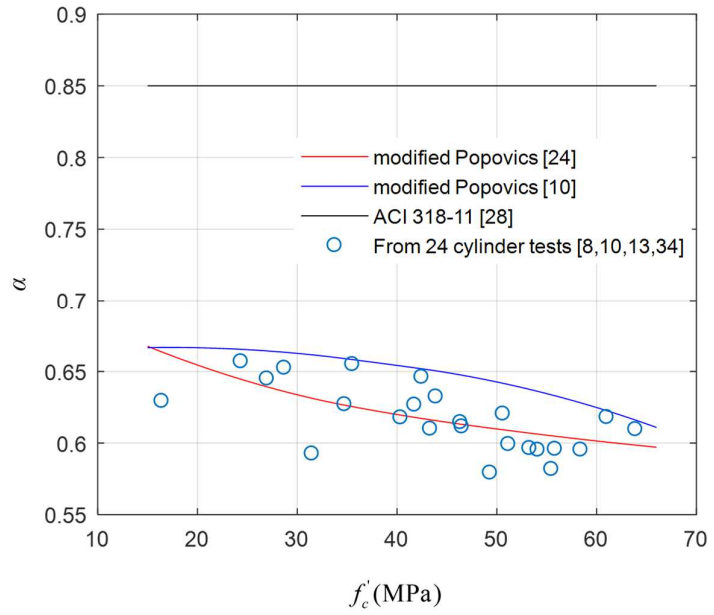

Figure 2-9. Stress-block parameter α in the case of k_3=0.7

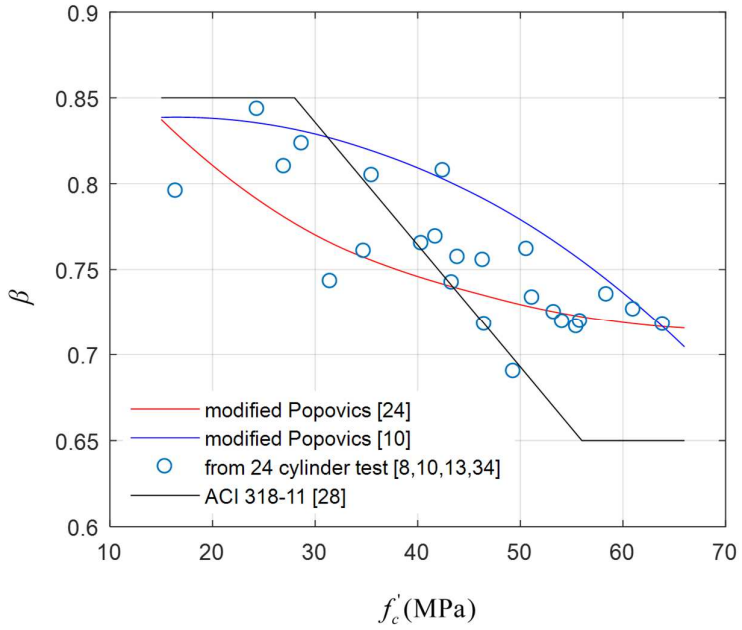

Figure 2-10. Stress-block parameter β

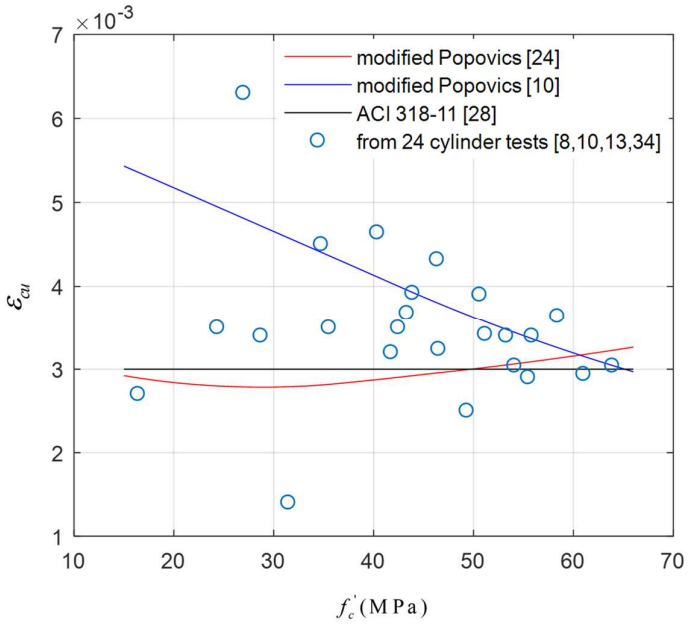

Figure 2-11. Ultimate concrete strain ε_{cu}

2.7. Experimental verification and discussion

2.7.1. Flexural capacity of beams

The moment capacity of 15 heat-cured fly ash-based GPC beams reported in the previous studies [16, 17] is calculated with the proposed rectangular stress-block parameters from Eqs. (2-43), (2-45) and (2-46). The results are compared with calculations based on ACI 318-11 standard [28] and the other stress-block parameters of the aforementioned studies [31, 32] (summarized in Table 2-2). The calculated moment capacity M_{cal} is verified against the experimental data (M_{cal}) reported in those studies. Figure 2-12 shows the error δ_b between the M_{cal} and M_{exp}, where $\delta_b = \frac{M_{\text{cal}} - M_{\text{exp}}}{M_{\text{exp}}} \times 100\%$. In general, the calculated moment capacity indicates a conservative estimation. Despite that both the ACI parameters and parameters proposed by Prachasaree et al. [31] and Tempest et al. [32] differ from the proposed rectangular stress-block parameters of the study in this chapter, there is no significant difference in the findings of these beams. Therefore, it seems that the calculation of ultimate moment capacity is not sensitive to the variation in the stress-block model. A similar observation is also drawn in [33]. In order to clarify this phenomenon, the mathematical relationship between the relative change of moment capacity and the relative difference of parameters α and β needs to be derived.

Table 2-2. Analytical moment capacity and experimental data

Specimen	Reference	f_c' (MPa)	ρ_s(%)	Bending moment capacity M (MPa)				
				ACI 318-11	Prachasaree et al. [31]	Brett et al. [50]	Proposed	Test
GBI-1	[16]	37	0.64	47.56	49.27	47.41	46.24	56.3
GBI-2	[16]	42	1.18	78.08	79.35	78.89	77.71	87.65
GBI-3	[16]	42	1.84	115.52	117.73	117.56	114.81	116.85
GBI-4	[16]	37	2.69	145.97	156.14	145.67	148.10	162.5
GBII-1	[16]	46	0.64	50.92	52.62	51.64	50.48	58.35
GBII-2	[16]	53	1.18	79.49	80.56	80.80	79.22	90.55
GBII-3	[16]	53	1.84	118.74	120.05	121.48	117.54	119
GBII-4	[16]	46	2.69	156.98	160.34	161.53	155.47	168.7
GBIII-1	[16]	76	0.64	61.46	63.41	54.60	59.63	64.9

GBIII-2	[16]	72	1.18	81.78	83.97	83.09	80.60	92.9
GBIII-3	[16]	72	1.84	122.3	123.22	125.47	120.81	126.8
GBIII-4	[16]	76	2.69	168.39	170.30	175.07	165.60	179.95
FAB-1	[17]	17	1.95	9	9.53	8.72	9.05	8.44
FAB-2	[17]	49	2.92	14.94	15.20	15.39	14.78	19.07
FAB-3	[17]	52	3.53	17.07	17.36	17.67	16.83	20.21

Note: all specimens GBI-1 to GBIII-4 of reference [16] were kept at room temperature for three days and then and cured at 60 ^{o}C for 24 hours, specimens FAB-1 to FAB-3 of reference [17] were cured at room temperature for 28 days.

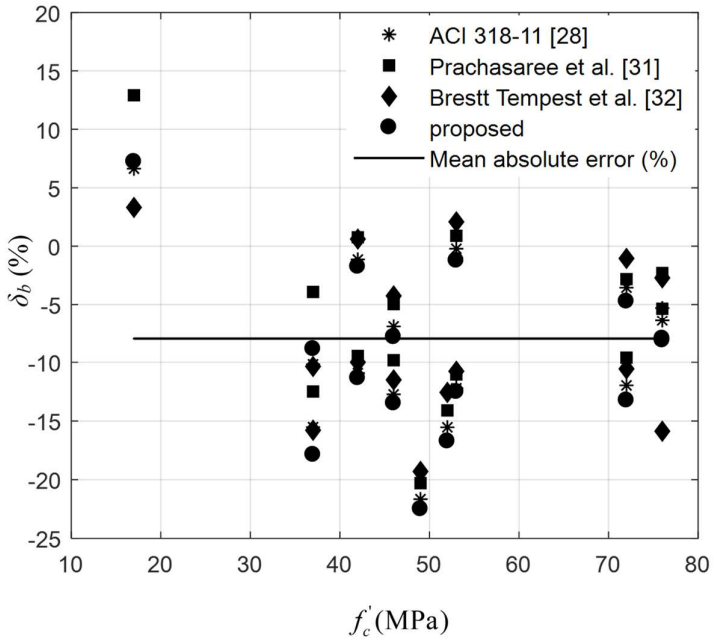

Figure 2-12. Error between calculated and experimental moment capacity

It is noted that the bending moment of the beams is estimated based on the equilibrium condition as follows (Figure 2-2):

$$T = A_s f_s = \alpha\beta f_c^{'} bc \tag{2-47}$$

$$M = T\left(d - \frac{\beta c}{2}\right) \tag{2-48}$$

By combining Eqs. (2-47) and (2-48), the bending moment capacity can be calculated by Eq. (2-49). If the balance condition is achieved, the tension force in the section is a constant so that the bending moment is a function of solely α.

$$M = M(\alpha) = T\left(d - \frac{T}{2\alpha f_c' b}\right) \tag{2-49}$$

The relative change of moment capacity is expressed mathematically as follows:

$$\frac{\Delta M}{M} = \frac{M(\alpha+\Delta\alpha) - M(\alpha)}{M} = \frac{\Delta\alpha}{(\alpha+\Delta\alpha)\left(\frac{2d\alpha f_c' b}{T} - 1\right)} \tag{2-50}$$

By substituting the tensile force T in Eq. (2-47) into Eq. (2-50), the relative change of moment $\frac{\Delta M}{M}$ is reformulated following Eq. (2-51) as

$$\frac{\Delta M}{M} = \frac{\Delta\alpha}{\alpha+\Delta\alpha}\frac{1}{\frac{2d}{\beta c} - 1} \tag{2-51}$$

In Eq. (2-51), the relative change of the bending moment capacity $\frac{\Delta M}{M}$ is proportional to the relative variation of α through a reduced magnitude $\frac{1}{\left(\frac{2d}{\beta c} - 1\right)}$. If the balanced failure happens, that means the strain of longitudinal steel is equal to yield strain, the value of $\frac{d}{c}$ is about 2.5 according to the previous study [2] and then $\frac{1}{\left(\frac{2d}{\beta c} - 1\right)}$ is equal to approximately 0.2. In particular, when the proposed parameter α varies up to 20% as observed in Figure 2-13, the value of the bending moment capacity only changes by 4%. From the relationship of $\frac{\Delta M}{M}$ and the ratio of $\frac{d}{c}$ plotted in Figure 2-13, it is noted that the ultimate bending moment capacity may change considerably if the ratio $\frac{d}{c}$ becomes smaller. It means that the section of beam is over-reinforced and the compression failure happens. Nevertheless, in design procedures, the longitudinal reinforcement ratio of beam is kept less than or equal to 0.75 times balanced reinforcement ratio [28]. As a result, the bending moment capacity will be relatively insensitive to the change of stress-block models if the ratio of reinforcement steel is selected reasonably.

Hence it is suggested that the stress-block parameters of ACI 318-11 standard are acceptable to be used for designing the flexural strength of GPC beams. However, the error in estimating the capacity of GPC structures may become significant for columns, which will be discussed in the following section.

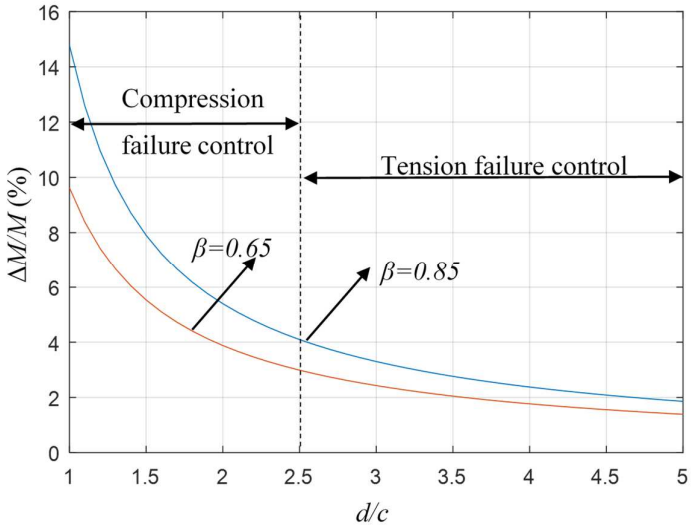

Figure 2-13. Relationship between $\frac{\Delta M}{M}$ and d/c with relative variation of α = 20%

2.7.2. Strength of columns under axial load and bending

As mentioned in the previous section, the moment capacity will be more sensitive to the variation of stress-block parameters when the compression failure controls. Therefore, it is likely that the capacity calculation of eccentrically loaded columns will be influenced considerably by the selection of stress-block models. The experimental data of 21 GPC columns collected from the previous studies [23, 27] are presented in Table 2-3. The interaction diagrams of axial load and bending moment for heat-cured GPC columns are shown in Figure 2-14. Those diagrams are computed by the proposed rectangular stress-block parameters of the study in this chapter, together with those suggested by ACI 318-11 [28] and Karthik and Mander [30]. It is worth mentioning that the load-carrying capacity of heat-cured GPC is very different from ambient-cured GPC at the same compressive strength. The distinguished behaviour of the ambient-cured GPC column is shown in Figure 2-15. The expression for the error δc between calculated column capacity and experimental values is illustrated in Figure 2-16. Accordingly, Figure 2-17 shows the comparison of errors as calculated by the proposed rectangular stress-block parameters and the other models for OPC as suggested by ACI 318-

11 [28] and Karthik and Mander [30]. In the case of heat-cured fly ash-based GPC columns, those parameters provided relatively similar interaction diagrams and the errors δ_c among three models were not significantly distinguishable. The results indicated that the assumption of k_3=0.9 is reasonable and the stress-block distribution of heat-cured fly ash-based GPC columns is not much different from conventional concrete columns.

Table 2-3. Experimental data for GPC columns

Column	Reference	b (mm)	$f_c^{'}$ (MPa)	e (mm)	Δ_{mid} (mm)	P_u (kN)	M_u (kN.m)
GCI	[23]	175	42	15	5.44	940	19.21
GCI	[23]	175	42	35	8.02	674	29.00
GCI	[23]	175	42	50	10.31	555	33.47
`GCII	[23]	175	43	15	6.24	1237	26.27
GCII	[23]	175	43	35	9.08	852	37.56
GCII	[23]	175	43	50	9.40	666	39.56
GCIII	[23]	175	66	15	4.94	1455	29.01
GCIII	[23]	175	66	35	7.59	1030	43.87
GCIII	[23]	175	66	50	10.70	827	50.20
GCIV	[23]	175	59	15	5.59	1559	32.1
GCIV	[23]	175	59	30	7.97	1057	45.42
GCIV	[23]	175	59	50	9.18	810	47.94
SHC	[27]	150	35	0	0.73	776	0.57
SHC	[27]	150	35	10	3.58	545	7.40
SHC	[27]	150	35	35	6.16	355	14.61
SHC	[27]	150	35	50	8.52	272	15.94
SHC	[27]	150	35	85	10.83	170	16.32
SLC	[27]	150	30	0	0.5	597	0.3

SLC	[27]	150	30	30	9.69	303	12.01
SLC	[27]	150	30	125	20.48	92	13.37
SLC	[27]	150	30	145	19.66	76	12.56

Note: all specimens GCI to GCIV of reference [23] were cured at 60 ºC for 24 hours while specimens SHC and SLC of reference [27] were ambient cured for 56 days prior to testing.

With regard to the ambient cured fly ash and slag-based GPC columns, however, all the parameters for conventional concrete suggested by ACI 318-11 [28] and Karthik and Mander [30] overestimate the capacity of column significantly. Particularly, the calculations based on ACI parameters and the model of Karthik and Mander [30] are higher than test results, up to 30% (specimen SLC as shown in Figure 2-17f). The proposed parameters with the assumption of k_3=0.9 also gave an unsafe prediction because it does not consider the early spalling of brittle concrete cover in ambient cured GPC columns. In contrast, the proposed parameters with the assumption of k_3=0.7 provided a better estimation with the highest error δ_c=15%. These evidences demonstrate that the value of k_3=0.85 recommended by ACI 318-11 standard [28] or k_3=0.9 from the previous studies of Portland concrete is not accurate to predict the strength of ambient cured fly ash and slag-based GPC columns in real scale at which k_3 of 0.7 should be adopted. Such a loss of strength can be attributed to the cover spalling which was observed in the experiment of Albitar et al. [27]. This phenomenon is likely caused by drying shrinkage of the cover concrete [51] which is greatly influenced by the curing condition. Moreover, several previous studies indicated that the performance of GPC using the slag mortar was very brittle since it performed a very high drying shrinkage, up to six times compared to OPC [13, 52]. Therefore, the ambient cured fly ash and slag-based GPC structures are likely to perform more poorly than those made from heat-cured fly ash-based GPC. The premature spalling of concrete cover in ambient-cured GPC columns is thus attributed to the reduction in the axial loading capacity. The spalling of concrete cover was observed in 11 different ambient-cured GPC columns with various eccentricities as presented in the previous study by Albitar et al. [27]. Due to a considerable distinction between those two cases, it is suggested that only the parameter α with the assumption of k_3=0.7 in Eq. (2-44) is applied for designing GPC structures to get conservative predictions. Despite that, it is evidently necessary to conduct more experiments of GPC columns with the same consistent test methods of OPC columns to acquire a reliable correlation between cylinder strength and the real compressive strength in GPC column.

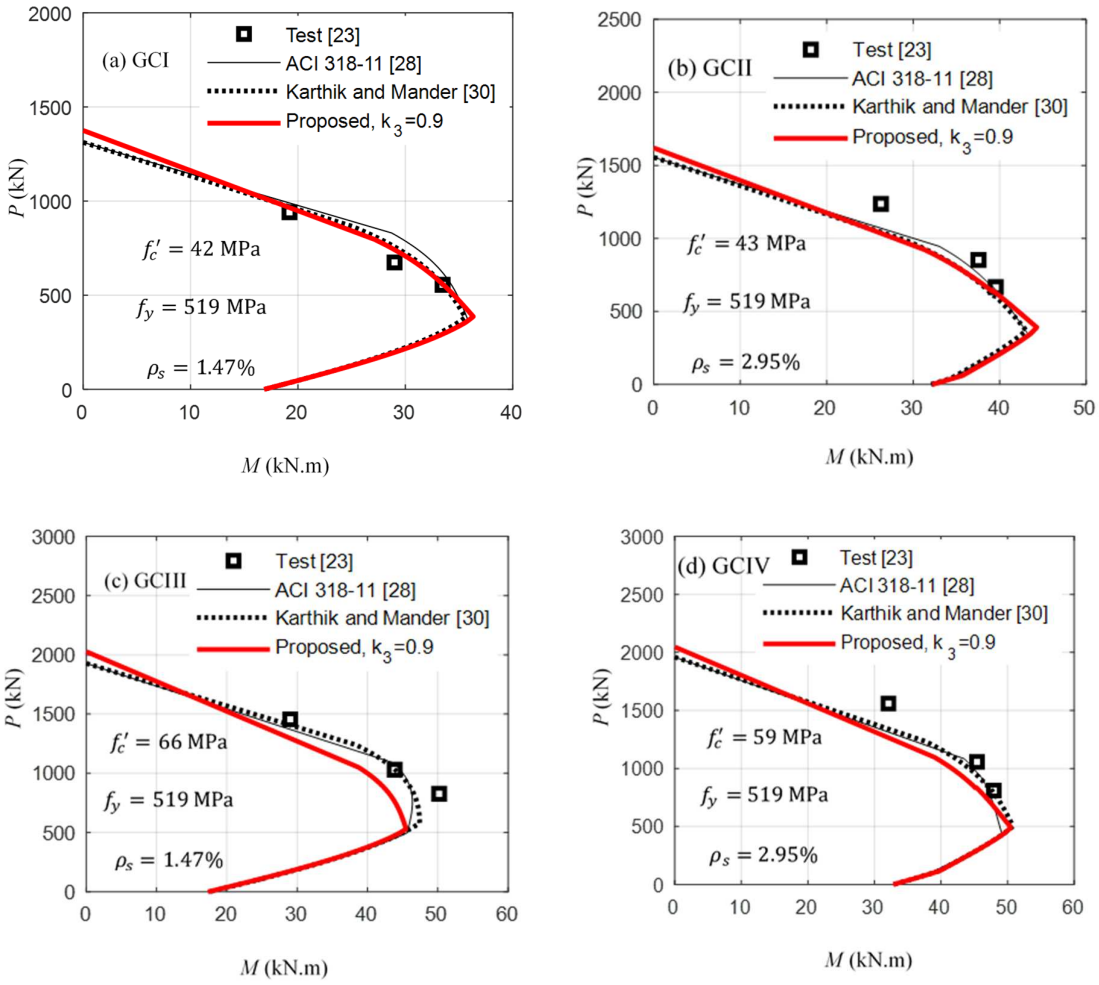

Figure 2-14. Interaction diagrams of heat-cured fly ash-based GPC columns

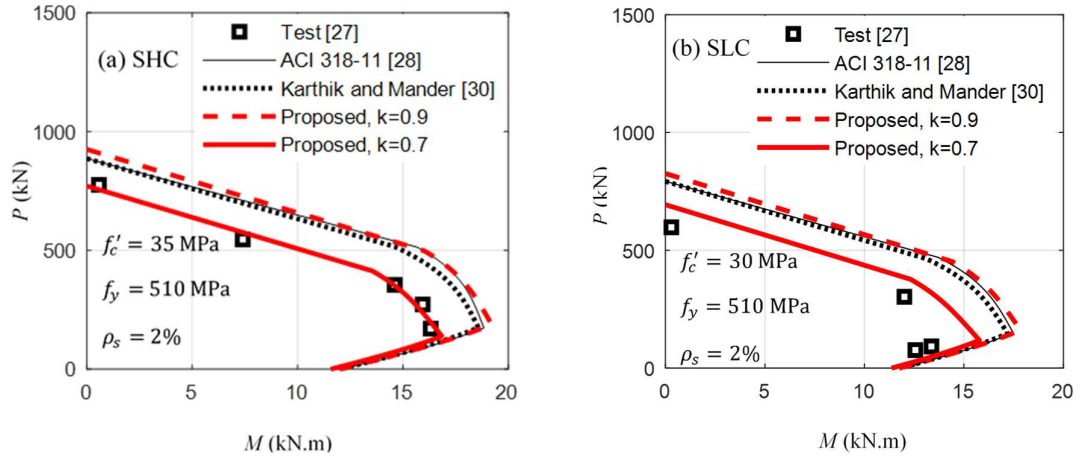

Figure 2-15. Interaction diagrams of ambient cured fly ash and slag-based GPC columns

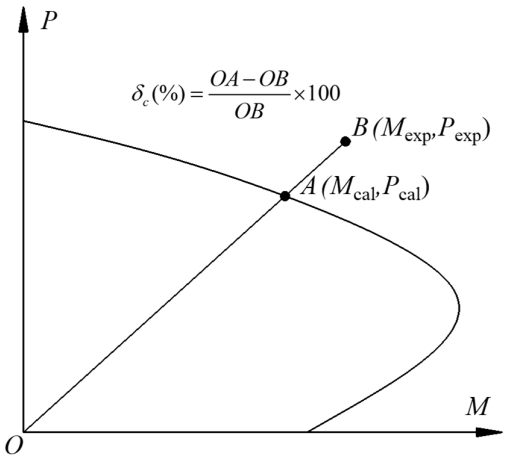

Figure 2-16. Error δ_c between calculated capacity of column and experimental value

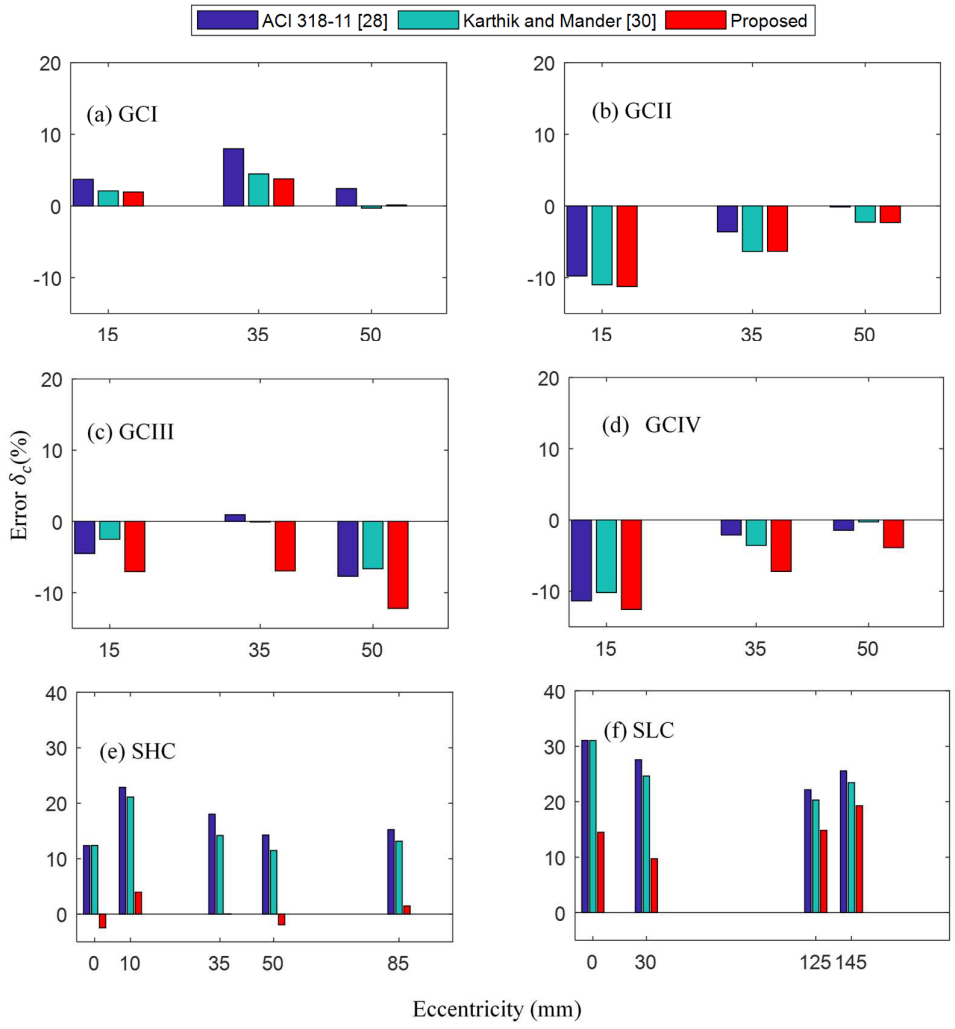

Figure 2-17. Comparison of δ_c calculated from proposed rectangular stress-block parameters and other parameters

2.8. Conclusion

An analytical procedure to determine rectangular stress-block parameters and ultimate strain ε_{cu} is proposed. Based on the proposed method, a set of rectangular stress-block parameters for GPC with the range of compressive strength up to 66 MPa is established. The load-carrying capacities of GPC beams and columns are calculated by using the proposed parameters together with available stress-block models for OPC. The results were then compared with the test data available in the literature. Based on the discussion and findings from the study in this chapter, the following conclusions can be drawn:

1. The moment capacity of beams is not sensitive to the variation of rectangular stress-block parameters. With the balanced reinforcement ratio as recommended in current codes, the moment capacity of beams insignificantly changes when stress-block parameters vary up to 20%. Hence, in designing the flexural capacity of GPC beams, the use of current codes for OPC is still acceptable.
2. The column capacity is sensitive to the variation of the rectangular stress-block parameters which are mainly influenced by k_3. For heat-cured fly ash-based GPC columns, the assumption k_3=0.9 is still acceptable. The calculation results indicated that the stress-block distribution of heat-cured fly ash-based GPC is fairly similar to OPC.
3. In the case of ambient cured fly ash and slag-based GPC columns, the value of k_3 should reduce to 0.7 due to primarily toa significant strength loss in real scale structure compared to cylinder strength. The load-carrying capacity calculated based on stress-block parameters for OPC is not conservative compared to the test data. In some cases, it overestimates the capacity of columns up to 23%.
4. Based on the comparison of the calculated capacity of columns and experimental data, the proposed rectangular stress-block parameters yield better estimations of the column capacities.

In general, the rectangular stress-block parameters for OPC can be used for GPC beams because the bending capacity is not sensitive to these parameters. However, those for OPC columns cannot be utilized for ambient-cured GPC columns, which are more brittle and exhibited a greater strength loss in real scale columns than OPC. Therefore, in order to acquire a better reliable correlation between the compressive strength of real scale column and cylinder strength, it is suggested that more GPC column tests need to be conducted.

Notation

A_c = area of core concrete

A_g = gross area of concrete section

A_s = area of longitudinal reinforced steel

α,β = rectangular stress-block parameters

b = breadth of rectangular section for beam and square section for column

c = neutral axis depth

C = internal compressive force

d = effective depth of concrete section

E_c = elastic modulus of concrete

ε_c = compressive strain of concrete in stress-strain model

ε_c' = concrete compressive strain at peak stress

ε_{cu} = ultimate strain at extreme compression fibre

ε_y = yield strain of longitudinal steel

e = the eccentricity of the axial load

f_c' = concrete cylinder compressive strength

f_c = concrete compressive stress in stress-strain model

f_s = tensile stress in longitudinal steel

f_y = yield stress of longitudinal steel

k_1 = ratio that represents the difference between the area of real and rectangular stress distribution

k_2 = ratio of the distance between the extreme compression fibre and the internal compressive force C to the depth of the neutral axis c

k_3 = ratio that represents the difference between in-place and cylinder strengths

k_4 = ratio that considers strength loss owing to the cover spalling

ρ_s = steel reinforcement ratio

T_s = internal tensile stress

References

[1] Benhelal E, Zahedi G, Shamsaei E, Bahadori A. Global strategies and potentials to curb CO2 emissions in cement industry. J Cleaner Prod. 2013;51:142-61.

[2] Khan MZN, Shaikh FUA, Hao Y, Hao H. Synthesis of high strength ambient cured geopolymer composite by using low calcium fly ash. Constr Build Mater. 2016;125:809-20.

[3] Ding Y, Dai J-G, Shi C-J. Mechanical properties of alkali-activated concrete: A state-of-the-art review. Constr Build Mater. 2016;127:68-79.

[4] Wallah SE, Rangan BV. Low-calcium fly ash-based geopolymer concrete: long-term properties, research report GC 2. Perth (Australia): Faculty of Engineering Curtin University of Technology; 2006.

[5] Nath P, Sarker PK. Flexural strength and elastic modulus of ambient-cured blended low-calcium fly ash geopolymer concrete. Constr Build Mater. 2017;130:22-31.

[6] Fernandez-Jimenez AM, Palomo A, Lopez-Hombrados C. Engineering properties of alkali-activated fly ash concrete. ACI Mater J. 2006;103:106-12.

[7] Al-Azzawi M, Yu T, Hadi MNS. Factors Affecting the Bond Strength Between the Fly Ash-based Geopolymer Concrete and Steel Reinforcement. Structures. 2018;14:262-72.

[8] Hardjito D. Studies of fly ash-based geopolymer concrete, PhD Thesis [Thesis (Ph D)]. Perth, Australia: Curtin University of Technology; 2005.

[9] Sofi M, van Deventer JSJ, Mendis PA, Lukey GC. Engineering properties of inorganic polymer concretes (IPCs). Cem Concr Res. 2007;37:251-7.

[10] Noushini A, Aslani F, Castel A, Gilbert RI, Uy B, Foster S. Compressive stress-strain model for low-calcium fly ash-based geopolymer and heat-cured Portland cement concrete. Cem Concr Compos. 2016;73:136-46.

[11] Pan Z, Sanjayan JG, Rangan BV. Fracture properties of geopolymer paste and concrete. Mag Concr Res. 2011;63:763-71.

[12] Sarker PK, Haque R, Ramgolam KV. Fracture behaviour of heat cured fly ash based geopolymer concrete. Mater Des. 2013;44:580-6.

[13] Thomas RJ, Peethamparan S. Alkali-activated concrete: Engineering properties and stress–strain behavior. Constr Build Mater. 2015;93:49-56.

[14] Ganesan N, Abraham R, Deepa Raj S, Sasi D. Stress–strain behaviour of confined Geopolymer concrete. Constr Build Mater. 2014;73:326-31.

[15] Haider GM, Sanjayan JG, Ranjith PG. Complete triaxial stress–strain curves for geopolymer. Constr Build Mater. 2014;69:196-202.

[16] Sumajouw MDJ, Rangan BV. Low-Calcium Fly Ash-Based Geopolymer Concrete: Reinforced Beams and Columns, Research Report GC. Perth(Australia): Curtin University of Technology; 2006.

[17] Dattatreya J K RN, Sabitha D, Ambily P S, Nataraja MC. Flexural behaviour of reinforced Geopolymer concrete beams. Int J Civ Struct Eng. 2011;2:138–59.

[18] Yost JR, Radlinska A, Ernst S, Salera M, Martignetti NJ. Structural behavior of alkali activated fly ash concrete. Part 2: structural testing and experimental findings. Mater Struct. 2012;46:449-62.

[19] Ng TS, Amin A, Foster SJ. The behaviour of steel-fibre-reinforced geopolymer concrete beams in shear. Mag Concr Res. 2013;65:308-18.

[20] Maranan GB, Manalo AC, Benmokrane B, Karunasena W, Mendis P. Evaluation of the flexural strength and serviceability of geopolymer concrete beams reinforced with glass-fibre-reinforced polymer (GFRP) bars. Eng Struct. 2015;101:529-41.

[21] Un CH, Sanjayan JG, San Nicolas R, van Deventer JSJ. Predictions of long-term deflection of geopolymer concrete beams. Constr Build Mater. 2015;94:10-9.

[22] Nguyen KT, Ahn N, Le TA, Lee K. Theoretical and experimental study on mechanical properties and flexural strength of fly ash-geopolymer concrete. Constr Build Mater. 2016;106:65-77.

[23] Sumajouw DMJ, Hardjito D, Wallah SE, Rangan BV. Fly ash-based geopolymer concrete: study of slender reinforced columns. J Mater Sci. 2006;42:3124-30.

[24] Sarker PK. Analysis of geopolymer concrete columns. Mater Struct. 2008;42:715-24.

[25] Elchalakani M, Karrech A, Dong M, Mohamed Ali MS, Yang B. Experiments and Finite Element Analysis of GFRP Reinforced Geopolymer Concrete Rectangular Columns Subjected to Concentric and Eccentric Axial Loading. Structures. 2018;14:273-89.

[26] Farhan NA, Sheikh MN, Hadi MNS. Experimental Investigation on the Effect of Corrosion on the Bond Between Reinforcing Steel Bars and Fibre Reinforced Geopolymer Concrete. Structures. 2018;14:251-61.

[27] Albitar M, Mohamed Ali MS, Visintin P. Experimental study on fly ash and lead smelter slag-based geopolymer concrete columns. Constr Build Mater. 2017;141:104-12.

[28] ACI Committee 318. Building Code Requirements for Structural Concrete (ACI 318-11). 2011.

[29] Hognestad E, Hanson NW, McHenry D. Concrete distribution in ultimate strength design. ACI Journal Proceedings. 1955;52:455-80.

[30] Karthik M, Mander J. Stress-Block Parameters for Unconfined and Confined Concrete Based on a Unified Stress-Strain Model. J Struct Eng. 2011;137:270-3.

[31] Prachasaree W, Limkatanyu S, Hawa A, Samakrattakit A. Development of Equivalent Stress Block Parameters for Fly-Ash-Based Geopolymer Concrete. Arab J Sci Eng. 2014;39:8549-58.

[32] Tempest B, Gergely J, Skipper A. Reinforced geopolymer cement concrete in flexure: A closer look at stress-strain performance and equivalent stress-block parameters. PCI Journal. 2016;61:30-43.

[33] Attard MM, Stewart MG. A two parameter stress block for high-strength concrete. ACI Struct J. 1998;95:305-17.

[34] Yang K-H, Cho A-R, Song J-K. Effect of water–binder ratio on the mechanical properties of calcium hydroxide-based alkali-activated slag concrete. Constr Build Mater. 2012;29:504-11.

[35] Ibrahim HHH, MacGregor JG. Tests of eccentrically loaded high-strength concrete columns. ACI Struct J. 1996;93:585-94.

[36] Ibrahim HHH, MacGregor JG. Modification of the ACI rectangular stress black for high-strength concrete. ACI Struct J. 1997;94:40-8.

[37] Jae-Hoon L, Hyeok-Soo S. Failure and Strength of High-Strength Concrete Columns Subjected to Eccentric Loads. ACI Struct J. 2000;97:75-85.

[38] Ozbakkaloglu T, Saatcioglu M. Rectangular stress block for high-strength concrete. ACI Struct J. 2004;101:475-83.

[39] Bae S, Bayrak O. Early Cover Spalling in High-Strength Concrete Columns. J Struct Eng. 2003;129:314-23.

[40] Sungjin B, Oguzhan B. Stress Block Parameters for High-Strength Concrete Members. ACI Struct J. 2003;100:626-36.

[41] Hwang S-K, Yun H-D. Effects of transverse reinforcement on flexural behaviour of high-strength concrete columns. Eng Struct. 2004;26:1-12.

[42] van Zijl GPAG, Mbewe PBK. Flexural modelling of steel fibre-reinforced concrete beams with and without steel bars. Eng Struct. 2013;53:52-62.

[43] Oztekin E, Pul S, Husem M. Determination of rectangular stress block parameters for high performance concrete. Eng Struct. 2003;25:371-6.

[44] Wight JK, MacGregor JG. Reinforced concrete : mechanics and design. 6th ed. Boston: Pearson; 2012.

[45] Saatcioglu M, Razvi Salim R. High-Strength Concrete Columns with Square Sections under Concentric Compression. J Struct Eng. 1998;124:1438-47.

[46] Cusson D, Paultre P. High-Strength Concrete Columns Confined by Rectangular Ties. J Struct Eng. 1994;120:783-804.

[47] Pfrang EO, Siess CP, Sozen MA. Load-Moment-Curvature Characteristics of Reinforced Concrete Cross Sections. ACI Journal Proceedings. 1964;61:763-78.

[48] Chapra SC, Canale RP. Numerical methods for engineers. 5th ed. Boston: McGraw-Hill Higher Education; 2006.

[49] Matlab. Matlab R2017a [Computer sofware]. Natick, MA, United States: The Mathworks Inc; 2017.

[50] Brett T, Janos G, Ashley S. Reinforced geopolymer cement concrete in flexure: A closer look at stress-strain performance and equivalent stress-block parameters. PCI J. 2016;61:30-43.

[51] Collins MP, Mitchell D, MacGregor JG. Structural Design Considerations for High-Strength Concrete. Concrete International. 1993;15:27-34.

[52] Duran Atiş C, Bilim C, Çelik Ö, Karahan O. Influence of activator on the strength and drying shrinkage of alkali-activated slag mortar. Constr Build Mater. 2009;23:548-55.

Chapter 3. Effect of Fibres on Flexural Response of Ambient-Cured Geopolymer Concrete Beams under Static Loading

Abstract[2]

This chapter investigates the flexural behaviour of geopolymer concrete (GPC) beams reinforced with steel fibres. The effects of the volume fraction and fibre length on the flexural behaviour of GPC beams are investigated. The distinctive behaviour of GPC beams versus ordinary Portland Concrete (OPC) beams is identified and discussed. Based on the experimental results, the GPC beams reinforced with steel fibres showed great improvement in the cracking resistance, serviceability, and ductility compared to the reference beams. The GPC beam without steel fibres failed in a very brittle manner while those reinforced with steel fibres experienced ductile failure. The load-carrying capacity of the GPC beams increased with the volume fraction of steel fibre up to 0.75%. Further increasing the fibre content to 1.5% showed a deterioration in the flexural behavior due to poor workability of GPC leading to worse fibre dispersion and orientation. The increase of fibre length up to 60 mm did not improve the moment capacity of the GPC beams owing to premature fibre fracture. An analytical procedure was proposed to estimate the load-deflection curve of the tested beams with a good correlation between predictive and experimental results.

3.1. Introduction

Nowadays, due to environmental issues, the application of sustainable materials in the construction industry is desired and has become more popular. For example, recycled aggregates can be a possible solution for replacing conventional aggregates in precast components [1]. Another solution is to use geopolymer concrete (GPC) to replace ordinary Portland concrete (OPC), which has been one of the largest contributors to carbon dioxide emission [2]. This can bring about a promising and environmentally friendly solution for

[2] This chapter was extracted from the paper published in Engineering Structures, but the tittle of the chapter and subsections were modified to follow the flow of the thesis. The full bibliographic citation of the paper is as follows: Tran TT, Pham TM, Hao H. Experimental and analytical investigation on flexural behaviour of ambient cured geopolymer concrete beams reinforced with steel fibres. Eng Struct. 2019;200:109707. https://doi.org/10.1016/j.engstruct.2019.109707

building materials. There have been numerous studies investigating the mechanical properties of GPC with good characteristics including excellent acid resistance [3, 4], high bond strength with steel reinforcements [5, 6], and high flexural strength [7]. These good characteristics possibly make GPC an alternative and green solution for building materials in the construction industry.

However, GPC exhibits poor cracking resistance due to its high brittleness as compared to OPC [8, 9]. From the chemical point of view, the brittleness of GPC is intrinsic due to the highly cross-link framework of the geopolymeric mortar [10]. In addition, the ambient cured GPC with a high content of slag exhibits large autogenous and drying shrinkage, considerably higher than that of OPC [11, 12]. This may be attributed to the presence of alkali cations C-A-S-H (calcium-alumina-silicate-hydrate), which leads to a reduction of regularity in the stacking of C-A-S-H layers and induce easier collapse of the C-A-S-H layers and redistribute upon ambient drying process [13]. To deal with these problems, fibres can be added into GPC to improve its mechanical properties as demonstrated in previous studies [9, 14, 15]. The inclusion of steel fibres was reported to not only enhance significantly the fracture toughness, splitting tensile, and flexural strength of GPC but also improves the post-peak behaviour of the stress-strain response in compression from brittle to ductile [9, 15]. In addition, a previous study showed that the use of short polymer hybrid fibres reduced the cracking of GPC due to shrinkage [16]. A recent study, investigating the pull-out behaviour between the different kinds of steel fibres and GPC matrices, indicated a superior bond strength of GPC matrix compared to that of OPC counterpart [17]. As can be seen that GPC reinforced with fibres is a potential solution for structural applications with excellent performance.

In contrast to the abundance of studies investigating the engineering characteristics of GPC material such as the elastic modulus and the bonding behaviour with steel reinforcements [18], the splitting tensile strength and flexural strength [19], the compressive stress-strain curves [20], and the effect of curing condition on development of the compressive strength [21], investigations on the behaviours of structures made of GPC are still limited and inconsistent findings were reported. The flexural and shear responses of GPC beams were reported in several experimental studies [22-28] while other studies examined the structural behaviour of GPC columns [29-31]. The flexural behaviour and failure modes of heat-cured fly ash-based GPC beams under four-point bending tests were found to be identical to OPC beams [22, 27]. The analytical results for determining the capacity of the beams by applying current design codes for OPC showed a good agreement with experimental findings [22]. Nguyen et al. [27]

demonstrated that the load-deflection of heat-cured fly ash-based GPC beams can be simulated accurately based on the available models of OPC. In terms of the behaviour of GPC columns, the response of heat-cured fly ash-based GPC columns under axial loading and uniaxial bending were reported to be similar to that of OPC counterparts [29, 31]. Sarker [30] also showed that the analytical method to analyse the behaviour of OPC columns can predict well the load-deflection curve of heat-cured fly ash-based GPC columns. Generally, based on the results of those studies, it is reasonable to conclude the suitability in adopting the current design codes and analytical models of OPC structures for structures made of heat-cured fly ash-based GPC.

There were, however, some significant differences between GPC and OPC structures. Yost et al. [25] reported an unusual explosive concrete crushing failure in the compression zone of GPC beams which often do not happen in normal strength OPC beams. Similarly, low ductility of GPC beams was observed in a previous study [24]. Albitar et al. [32] indicated a considerable overestimation (up to 30%) in calculating the capacity of ambient cured GPC columns subjected to axial load and uniaxial bending by using AS3600 [33]. The inconsistency in those results may be attributed to the sensitivity of GPC to the different mixtures and curing conditions applied in those studies. As can be seen that the behaviour of fly ash-based GPC structures under heat-cured condition seems similar to OPC ones [22] while the behaviour of GPC structures with the high content of slag curing under ambient condition, which suffers from adverse effects such as high drying shrinkage and brittle behaviour, is still questionable.

In spite that GPC reinforced with steel fibres is a potential material for construction, the number of studies investigating its structural behaviour is very limited [34-36]. The study of this chapter, therefore, investigates the flexural behaviour of ambient cured geopolymer concrete beams reinforced with steel fibres. The effects of volume fraction and fibre length on the response of the tested beams are investigated. The distinctive behaviour of GPC beams versus OPC beams is specified and discussed. Furthermore, an analytical procedure to predict the load-deflection curves of these beams is proposed. A comparison between the analytical predictions and test results is used to verify the reliability of the proposed model.

3.2. Experimental programme

3.2.1. Material properties

All GPC beams were cast based on the mix design proposed by the previous studies [9, 37] and given in Table 3-1. The binder of the mixture constituted of low calcium fly ash (FA) and ground granulated blast furnace slag (GGBFS) as presented in Table 3-2. The alkaline activator (Aa) was a combination between 12M sodium hydroxide (NaOH) and D-grade sodium silicate (Na_2SiO_3) solution. Crushed stones with the maximum size of 7 mm and silica sand were used as coarse and fine aggregates. After casting, all the beams were demoulded after 3 days and then covered by plastic sheets at ambient conditions in the lab for two months before testing. 10 mm deformed steel bars were used for both transverse and longitudinal reinforcements. The yielding and ultimate stress of the steel bars determined from the tensile tests as per ASTM A370-18 [38] were 548 MPa and 675 MPa, respectively. The hook-ended steel fibres were supplied by TEXO Australasia Pty Ltd [39] with different dimensions (including fibre length, l_f, and diameter of fibre, d_f) as presented in Table 3-3.

Table 3-1. Mix proportion of 1 m^3 GPC

Materials	Quantity
Coarse aggregate (kg/m^3)	1100
Sand (kg/m^3)	630
FA (kg/m^3)	240
GGBFS (kg/m^3)	160
Aa/binder ratio	0.6
12 M NaOH solution (kg/m^3)	69
Na_2SiO_3 solution (kg/m^3)	172
Na_2SiO_3/NaOH ratio	2.5

Table 3-2. Chemical compositions of FA and GGBFS [37]

Composition (wt. %)	FA	GGBFS

SiO_2	51.1	32.5
Al_2O_3	25.6	13.6
Fe_2O_3	12.5	0.9
CaO	4.3	41.2
MgO	1.5	5.1
MnO	0.15	0.25
K_2O	0.7	0.35
Na_2O	0.8	0.3
P_2O_5	0.9	0.03
TiO_2	1.3	0.5
SO_3	0.24	3.2
Others	0.46	1.12
LOI[a]	0.6	1.1

[a]Loss on ignition.

Table 3-3. Characteristics of the hook-ended steel fibres (from the manufacturer [39])

Steel fibres	l_f (mm)	d_f (mm)	Aspect ratio (l/d)	Tensile strength (MPa)	Young's Modulus (GPa)
ReoCo 65/35	35	0.55	65	1350	210
ReoCo 65/60	60	0.9	65	1200	210

3.2.2. Design and fabrication of the beams

Five GPC beams and one OPC reference beam were fabricated and tested. The dimensions of the rectangular beams were 150 mm wide, 200 mm deep, and 1700 mm long. The cross-sectional geometry and reinforcement details of the beams are shown in Figure 3-1. All the beams were reinforced at top and bottom by two 10 mm diameter-deformed steel bars. The

reinforcement ratio was 0.68% which corresponds to under-reinforced beams. Two leg stirrups with 10 mm diameter were placed at 100 mm spacing in the shear spans to provide sufficient shear resistance and avoid premature shear failure of the beams. The volume fraction of steel fibres (35 mm and 60 mm length) varied from 0%, 0.375%, 0.75% to 1.5% is used to investigate its effect on the behaviours of the beams. The labels and classification of all the beams are summarized in Table 3-4.

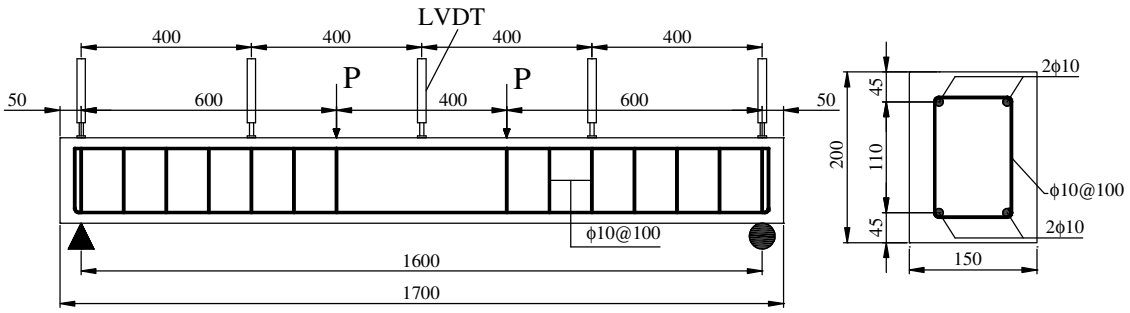

Figure 3-1. Geometry of the beams and cross-section

Table 3-4. Beam design

Beam	A_s (mm^2)	ρ_s (%)	V_f (%)	l_f (mm)	d_f (mm)	f_c' (MPa)	E_c (GPa)	f_{ct} (MPa)
OPC	157	0.68	0	-	-	33	27.0	3.4
GPC	157	0.68	0	-	-	44	19.9	3.7
GPC-0.375-35	157	0.68	0.375	35	0.55	70	28.0	6.0
GPC-0.75-35	157	0.68	0.750	35	0.55	61	25.4	7.4
GPC-1.5-35	157	0.68	1.500	35	0.55	62	25.7	9.3
GPC-0.375-60	157	0.68	0.375	60	0.90	64	26.3	5.8

The mechanical properties of all the beams are summarized in Table 3-4. The compressive strength, f_c', and splitting tensile strength, f_{ct}, of the beams were experimentally measured according to ASTM C496-17 and ASTM C39-18 [40, 41]. The elastic moduli of OPC and GPC are determined based on Eq. (3-1) recommended by ACI 318 [42] and Eq. (3-2) proposed by Noushini et al. [20], respectively.

$$E_{OPC} = 4700\sqrt{f_c'} \tag{3-1}$$

$$E_{GPC} = -11400 + 4712\sqrt{f_c'} \quad (3\text{-}2)$$

where E_{OPC} and E_{GPC} are the elastic moduli of OPC and GPC in MPa, respectively, and f_c' (MPa) is the mean compressive strength measured from cylinder tests.

3.2.3. Testing procedure

The static four-point bending test was adopted to investigate the flexural response of the simply supported beams. The load was applied by two independent hydraulic jacks with the load rate at approximately 1mm/min until failure. Five linear variable differential transformers (LVDTs) were placed at different positions of the beams to measure the deflections as shown in Figures 3-1 and 2. Furthermore, a strain gauge was attached at mid-span on the top of the beam to monitor the compressive strain of concrete. The flexural and shear spans of the beams were 400 mm and 600 mm, respectively.

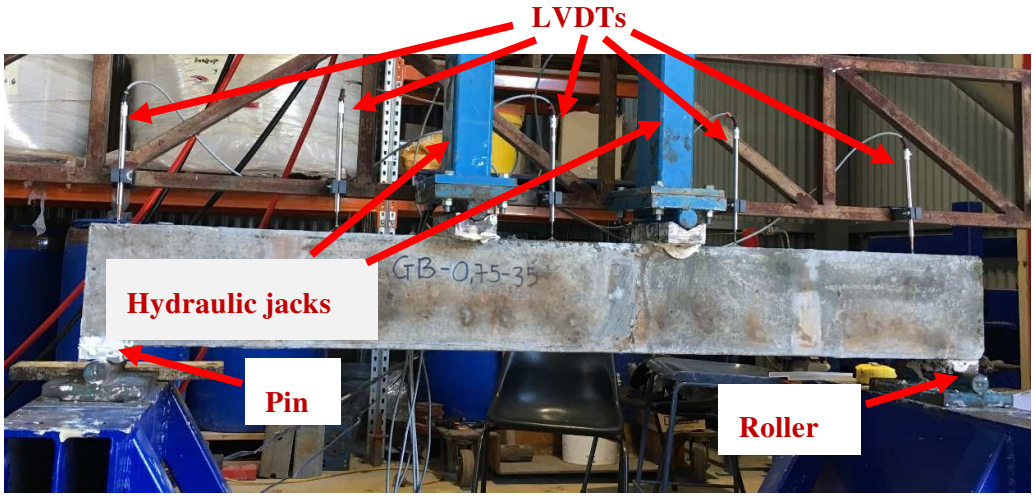

Figure 3-2. Test setup system

3.3. Experimental results and discussion

The experimental results including the load-deflection relationship, failure modes, ductility index, cracking pattern, and cracking space of the beams are presented and discussed in this section. Accordingly, the distinctions between the GPC and OPC beams reinforced with steel fibres are discussed.

3.3.1. Load-deflection relationship

The experimental results of the tested beams are analysed based on the general knowledge of reinforced concrete beams and compared to those from previous studies [43, 44]. Hence, the general flexural behaviour of reinforced concrete beam is summarized in this section.

Generally, the typical load-deflection behaviour of an under-reinforced OPC beam includes three stages as illustrated in Figure 3-3 [43, 44]. Initially, the beam exhibits a linear load-deflection relation and no cracking occurs in the beam (O-A) until the moment the mid-span zone reaches the cracking moment and the first crack happens (represent by cracking point A). When a section cracks, the moment of inertia of the beam reduces and thus causes a decrease in the beam's stiffness [44]. Then the beam undergoes the post-cracked stage (A-B) [43]. In the post-cracked stage, even though the reinforcing bars are assumed to carry entirely tensile force, concrete is still able to transfer tension through the bond between reinforcing bars and concrete [45]. The contribution of concrete to transfer tensile stress, which makes the change of beam stiffness gradually from cracking point to yielding point, is considered as the tension stiffening effect of reinforced concrete [46]. Once reinforcing bars yield (represent by yielding point B), the stiffness of the beam drops significantly. This stage (B-C) is considered as the post-yielded stage [43] and governed mainly by reinforcing bars. In this stage, the beam continues to carry more load due to the hardening of steel bars until reaching its moment capacity (represent by peak point C).

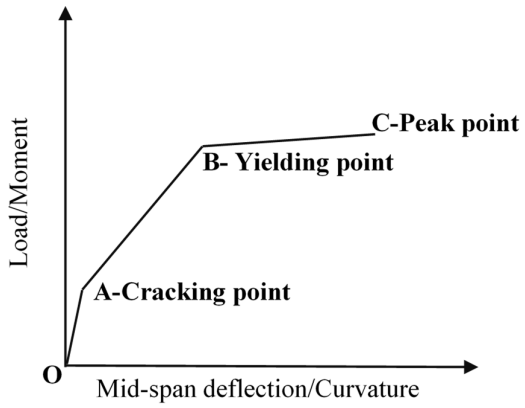

Figure 3-3. Typical load-deflection behaviour of an under-reinforced concrete beam [3]

a. Uncracked stage and cracking point

Figure 3-4 shows the experimental load-deflection curves of all the tested beams. Generally, the load–deflection behaviour of the GPC beams experienced the same three stages as the OPC

beam. However, the stiffness of each stage and the critical points including cracking, yielding and peak points are quite different between the OPC and GPC beams.

The cracking moment of the beams obtained from tests and the analytical estimations are summarized in Table 3-5, where f_r is the flexural strength taken as $0.62\sqrt{f_c'}$ based on the recommendation by ACI 318-11 [42], in which $M_{cr(exp)}$ is the experimental cracking moment and $M_{cr(theo)}$ is the cracking moment determined from Eq. (3-3) in case the top and bottom reinforcement is symmetric.

$$M_{cr(theo)} = \frac{f_r I_g}{y_t} \text{ (kN.m)} \quad (3\text{-}3)$$

where $I_g = \frac{bh^3}{12} + 2nA_s(\frac{h}{2} - d')$ (m^4) is the moment of inertia of uncracked concrete section with n which is the ratio between elastic modulus of steel (E_s) and concrete (E_c), A_s is the area of top or bottom reinforcement, d' is the distance from the bottom surface to the centre of bottom reinforcement bars and y_t is the distance from the centroid axis of the gross section to the tension face. In some cases where the load-deflection curves of the GPC beams with a high volume fraction of fibres do not exhibit a clear cracking point, a definition of the cracking point is proposed and presented in Figure 3-5. The cracking point is determined as the intersection between the initial slope of the uncracked stage and the tangent slope of the post-cracked stage [47]. The discussion on the cracking point requires a closer observation at the transition between uncracked and post-cracked stage as shown in Figure 3-6, in which the load-deflection response of the OPC and plain GPC beams is presented up to the deflection of 6 mm. As seen in the figure, GPC beams showed a lower cracking moment as compared to Beam OPC even though the compressive strength of the first one was higher than those of the later one. This phenomenon is opposite to the common performance of reinforced OPC beams that the cracking moment increases with the compressive strength [48, 49]. Moreover, the previous studies indicated that GPC has a higher flexural strength than OPC with the same compressive strength [7, 19], which leads to a higher cracking moment. Such a phenomenon has not been reported in previous studies investigating the flexural performance of GPC beams [22, 24-27]. This poor performance of the cracking resistance can be attributed to the significantly high drying shrinkage of the GPC beam. It is well-known that the drying shrinkage might lead to a reduction of the cracking moment of reinforced OPC structures due to an appearance of shrinkage restraint stresses induced by shrinkage strain [50, 51]. Meanwhile, GPC with a high content of GGBFS under ambient curing condition has been reported to exhibit a considerably

higher shrinkage than OPC [11, 12]. Therefore, the severe shrinkage cracks and strain may be the cause of the decreased cracking moment reported in this chapter.

On the other hand, as can be seen in Table 3-5, the GPC beams reinforced with steel fibres demonstrated a better cracking resistance since the presence of fibres is effective to counteract the drying shrinkage tendency of GPC [16, 52]. The table shows that the cracking moment of the GPC beams increased with the flexural strength. However, there is no clear correlation between the fibre content and the cracking moment of the GPC beams. The cracking moments, $M_{cr(theo)}$, calculated by Eq. (3-3) are lower than the experimental values. This variation can be resulted from the underestimation of the actual flexural strength of the GPC beams by using ACI 318-11 [42]. Moreover, the comparison between the estimated deflection at cracking point, $\delta_{cr(theo)}$ (as calculated by Eq. (3-4)) and the experimental results, $\delta_{cr(exp)}$ are shown in Table 3-5. The comparison of theoretical calculation and experimental results indicates the deflections of the GPC beams are underestimated. This might be due to the overestimation of elastic modulus of GPC by using the Eq. (3-2). Therefore, there should be more studies conducted to provide a reasonable empirical equation for predicting the modulus of elasticity of GPC.

$$\delta_{cr} = \frac{M_{cr(exp)}}{6E_c I_g}\left(\frac{3L^2}{4} - a^2\right) \tag{3-4}$$

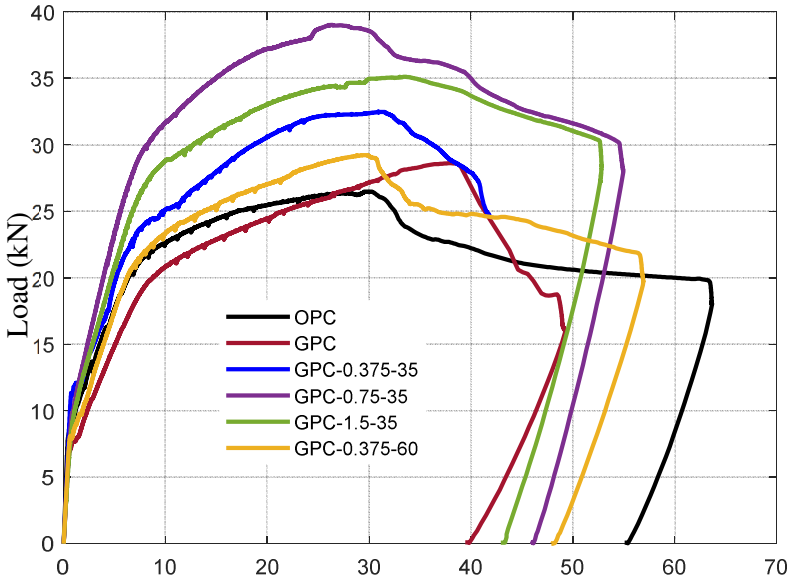

Figure 3-4. Load-deflection curves of all the specimens

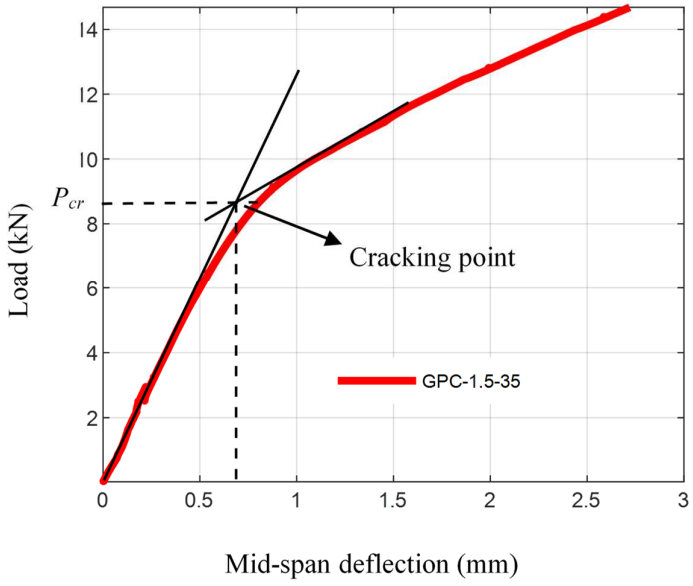

Figure 3-5. The definition of cracking point for beam reinforced with fibres

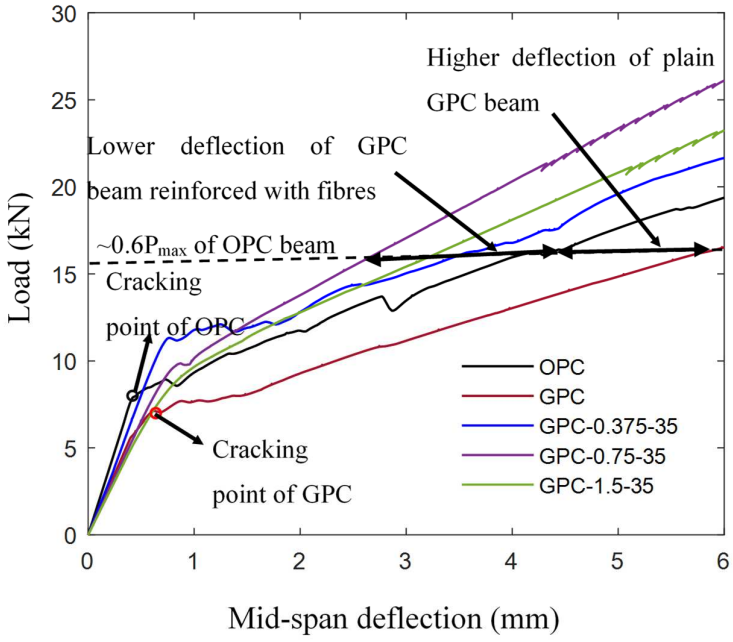

Figure 3-6. Load-deflection curves of plain OPC and GPC beams

Table 3-5. Experimental and theoretical cracking moments

Beams	f_r (MPa)	$M_{cr(exp)}$ (kN.m)	$M_{cr(theo)}$ (kN.m)	$\delta_{cr(exp)}$ (mm)	$\delta_{cr(theo)}$ (mm)	$\frac{M_{cr(theo)}}{M_{cr(exp)}}$	$\frac{\delta_{cr(theo)}}{\delta_{cr(exp)}}$
OPC	3.6	4.74	3.85	0.41	0.43	0.81	1.04
GPC	4.1	4.26	4.49	0.63	0.51	1.05	0.81
GPC-0.375-35	5.2	6.78	5.55	0.76	0.59	0.82	0.78
GPC-0.75-35	4.8	5.88	5.16	0.87	0.56	0.88	0.64
GPC-1.5-35	4.9	5.28	5.26	0.83	0.50	1.00	0.60
GPC-0.375-60	5.0	4.86	5.36	0.67	0.45	1.10	0.67

* *exp*: experimental results; *theo* : theoretical values

b. Post-cracked stage and serviceability stage

In the post-cracked stage, the stiffness of the plain GPC beam was still lower than that of the OPC beam as can be seen in Figure 3-6. This observation can be explained by two reasons: (1) the elastic modulus of GPC (19.9 GPa) is significantly smaller than that of OPC (27.0 GPa) and (2) the severe drying shrinkage of the GPC beams resulted in a significant loss of tension stiffening, which leads to a reduction in stiffness in the post-cracked stage of reinforced concrete members [50, 53]. In contrast, the GPC beams with steel fibres showed higher stiffness in the post-cracked stage due to the ability to transfer the tensile force at cracks [54] and better control of shrinkage cracks and strain [55] as shown in Figure 3-6.

The experimental loads vs mid-span deflections at the serviceability condition ($\delta_{s(exp)}$) are presented in Table 3-6. In this chapter, the benchmark of the service load for under-reinforced concrete beams suggested by Bischoff [45] is adopted. In his study, the service load was recommended to be approximately 0.6 of the load capacity of the beams (P_{max}). As can be seen from Table 3-6, the GPC beam without steel fibre demonstrated the largest serviceability mid-span deflection (more than 40% of the deflection of OPC beam at the same level) owing to the poor performance of the tension stiffness as explained previously. Meanwhile, the addition of steel fibres improved the structural performance of the GPC beams at the serviceability condition, their mid-span deflections reduced by roughly 21% as compared to that of the GPC

beam without fibres. This improvement indicates that the addition of steel fibres can be an effective method to reduce the adverse effect of drying shrinkage and improve the performance of GPC beams in the post-cracked stage. Furthermore, the theoretical service deflections of the beams calculated based on ACI 318-11 [42], $\delta_{s(ACI)}$ were verified with the experimental results and presented in Table 3-6. The comparison indicated the considerable underestimation of the service deflection in the case of the plain GPC beam and GPC reinforced with a low volume fraction of fibres (V_f = 0.375%). The reason for this might be that the calculation based on ACI 318-11 cannot capture the reduction of tension stiffness caused by severe shrinkage cracks of GPC and the low elastic modulus of GPC cannot be accurately estimated by using Eq. (3-2). Hence, it is essential that there should be more studies to investigate those issues.

c. Post-yielded stage and load-carrying capacity

As can be seen from Figure 3-4, the post-yielded stage of Beams OPC and GPC were relatively similar with an almost linear behaviour. Meanwhile, the behaviour of the GPC beams reinforced with steel fibres in the post-yielded stage was more nonlinear. The failure modes, maximum load, yielding load, and corresponding deflections of all the tested beams are also summarized in Table 3-6. The flexural capacity of the GPC beams improved as the volume fraction of steel fibre increased. For example, the maximum load of the GPC beams increased from 28.6 kN to 39 kN (increasing by roughly 40%) when the volume fraction of steel fibres increased from 0% to 0.75%. However, Beam GPC-1.5-35 showed a reduction in the load-carrying capacity with the volume fraction of steel fibres of 1.5%. This reduction might result from poor distribution and orientation of steel fibres to the tension force direction, which leads to a decrease in the strengthening effect of the fibres as also observed in a previous study [56]. It is known that good fibre dispersion and fibre orientation depend on the good workability of the mixture [57]. The optimal volume fractions of steel fibres for OPC mixes should be from 0.5% to 2.5% to ensure good workability as reported in a previous study [58]. Nevertheless, the rheology of a GPC mixture is generally distinct from an OPC mixture. A previous study indicated that a GPC mixture with high content of GGBFS showed low concrete slump and poor workability performance [59]. Additionally, the inclusion of steel fibres further reduced the workability of GPC mixtures [60]. Therefore, it is suggested that a volume fraction of steel fibre about 0.75% might be employed to achieve an optimal flexural capacity.

In addition, as can be seen from Table 3-6 Beam GPC-0.375-60 showed a decrease in the load-carrying capacity when comparing with Beam GPC-0.375-35. Meanwhile, Figure 3-7 indicates

rupture of a steel fibre at the critical crack at the midspan of Beam GPC-0.375-35. This observation indicated that 35-mm steel fibres provide the sufficient embedded length so that a pull-out failure did not occur. As a result, an increase in the fibre length more than 35 mm did not improve the load-carrying capacity of the GPC beams but even causes adverse effects such as poor fibre dispersion and fibre balling which lead to a decrease in the load-carrying capacity [61]. In brief, the experimental results have proven that Beam GPC-0.375-35 exhibited a higher load-carrying capacity than that of Beam GPC-0.375-60. The reasons for this variation are attributed to the sufficient embedded length of 35-mm fibres and the worse distribution of using longer fibres as also observed for OPC beams [61, 62].

Figure 3-7. Fibre ruptured at the crack at the soffit of Beam GPC-0.375-35

d. Further discussion about critical fibre length for fibre fracture

Figure 3-8 illustrates a fibre in the equilibrium condition under induced pull-out force at a crack. A fibre will fracture when its length exceeds the critical length, l_c , which must satisfy the equilibrium condition in Eq. (3-5) as shown below:

$$0.5\tau_b \pi d_f l_c = 0.25\sigma_{fu}\pi(d_f)^2 \quad (3\text{-}5)$$

where τ_b and σ_{fu} are the bond strength and tensile strength of steel fibre in MPa, respectively, and d_f is the fibre diameter in mm. The Eq. (3-5) can be expressed in another form shown in Eq. (3-6) as follows:

$$\frac{l_c}{d_f} = \frac{\sigma_{fu}}{2\tau_b} \quad (3\text{-}6)$$

The bond strength of hook-ended steel fibres with OPC, τ_b, can be taken as $0.68\sqrt{f_c'}$ proposed by Khuntia et al. [63] and thus Eq. (3-6) can be rewritten as follows:

$$\frac{l_c}{d_f} = \frac{\sigma_{fu}}{1.36\sqrt{f_c'}} \tag{3-7}$$

By using Eq. (3-7) with the mechanical properties of steel fibres in Table 3-3, the effective fibre length to prevent premature pull-out failure of fibres is 70 mm for fibres with 0.55 mm diameter and 111 mm for fibres having 0.9 mm diameter. Those calculated fibre lengths are twice as long as the values of fibre length reported in the previous section. This can be explained by a better adhesive bonding between geopolymer mortar and steel fibres which leads to higher bond strength. Previous studies investigating the pull-out behaviour of fibres in geopolymer mortars reported a significantly high peak bond strength of steel hook-ended fibres and geopolymer mortar which was approximately two times more than that of ordinary Portland mortar [17, 64]. According to those studies, the bond strength of hook-ended steel fibres with GPC, τ_b, can be assumed as $1.36\sqrt{f_c'}$ and then by combining with Eq. (3-7) the critical length of fibre l_c is now calculated as follows:

$$\frac{l_c}{d_f} = \frac{\sigma_{fu}}{2.72\sqrt{f_c'}} \tag{3-8}$$

As a result, the effective fibre lengths to prevent premature pull-out failure of fibres are now recalculated as 35 mm and 56 mm for 0.55 mm and 0.90 mm diameter fibres, respectively. Therefore, the fibre length of 35 mm used in the study of this chapter is sufficient to totally utilize their tensile strength before pull-out happens. In fact, the optimistic assumption of fibre located symmetrically at crack surface (as shown in Figure 3-8) can cause an underestimation of the critical fibre length. However, due to the lack of study investigating the effect of fibre length on GPC reinforced with fibres, Eq. (3-8) is adopted to calculate the critical fibre length for fibre fracture until more studies on this problem are available.

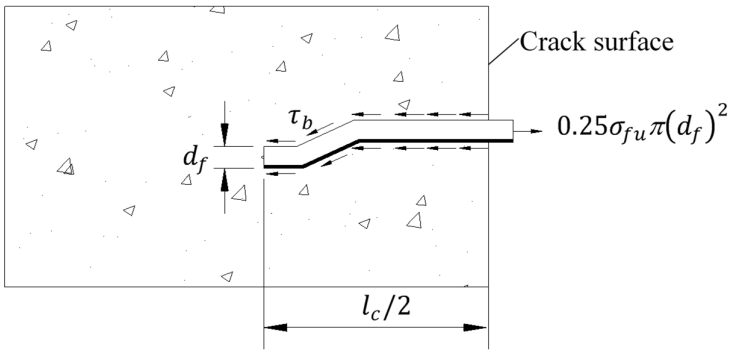

Figure 3-8. Equilibrium diagram for a fibre subjected to a pull-out force at a crack surface

3.3.2. Failure modes, ductility, and cracking behavior

The observed failure modes of the tested beams are presented in Table 3-6 and Figure 3-9. All the beams failed in flexure owing to reinforcing bars yielding in the tension zone following by concrete crushing in the compression zone, which is also the typical failure of under-reinforced OPC beams. The obvious difference among these beams was that the failure of the OPC and GPC beams reinforced with steel fibre happened due to gradual concrete crushing whereas Beam GPC underwent a sudden and explosive concrete crushing with low residual deflection (Figure 3-4). It is noted that a similar failure mode as Beam GPC was also reported in a previous study [25]. This phenomenon can be attributed to the high brittleness of GPC as compared to OPC [8]. On the other hand, the addition of steel fibres significantly improved the post-peak behavior of the compressive concrete zone due to the enhancement of toughness [65]. As a result, the failure of the GPC beams with fibres was more ductile and their concrete crushing zone was still intact compared to the plain GPC beam as shown in Figure 3-9c. As can be seen from Figure 3-4, after the peak load, the residual deflections of the GPC beams reinforced with steel fibres were higher than the plain GPC beam.

The ductility index, μ_δ, is defined as the ratio between the ultimate deflection δ_u and the deflection at the yield point δ_y. The ultimate deflection, δ_u, in the case of ductile concrete structures is conventionally considered as a deflection corresponding to a decreased load equal to 85% of the peak load [66, 67]. The definition of the yield deflection proposed by Park [66] is adopted in this chapter and the detailed yielding points and ultimate points of all beams are presented in Figure 3-10. Table 3-6 shows that Beam GPC without fibres exhibited the lowest ductility and the ductility increased with the volume fraction of steel fibres. For example, Beam GPC-1.5-35 with 1.5% fibres showed the highest ductility with an improvement up to 49% as compared to Beam GPC. The experimental results have shown that steel fibre reinforcement can reduce the brittleness of the failure mode of GPC beams.

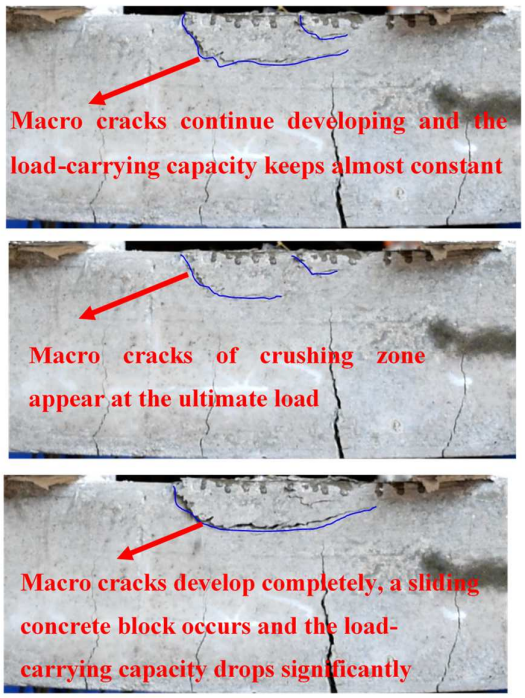

(a) A progressive failure of OPC beam

(b) Failure of plain GPC beam

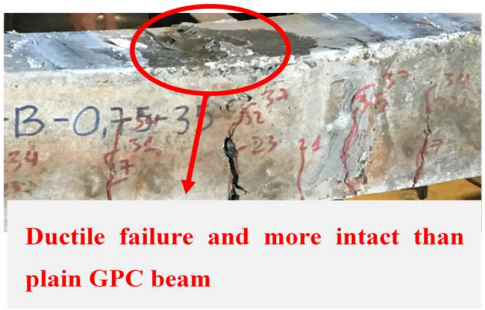

(c) Failure of Beam GPC-0.75-35

Figure 3-9. Typical failures of OPC and GPC beams

Table 3-6. Failure modes, peak loads, mid-span deflections, and ductility of the beams

Beams	$P_{\max}$ (kN)	$0.6P_{max}$ (kN)	$\delta_{s(exp)}$ (mm)	$\delta_{s(ACI)}$ (mm)	$\frac{\delta_{s(ACI)}}{\delta_{s(exp)}}$	δ_y (mm)	δ_u (mm)	μ_δ	Failure modes
OPC	26.3	15.6	3.8	3.64	0.96	9.3	38.0	4.1	Pcc
GPC	28.6	17.2	6.4	4.39	0.69	12.1	42.0	3.5	Ecc
GPC-0.375-35	32.5	19.5	5.0	3.95	0.79	11.0	40.5	3.7	Pcc
GPC-0.75-35	39.0	23.4	6.0	6.03	1.00	9.4	43.0	4.6	Pcc
GPC-1.5-35	35.1	21.1	4.4	5.00	1.14	10.1	52.5	5.2	Pcc
GPC-0.375-60	29.2	17.5	5.1	3.38	0.66	10.3	37.7	3.7	Pcc

*Pcc: Progressive concrete crushing; E_{cc}: Explosive concrete crushing

*$\delta_{s(exp)}$: experimental service deflection; $\delta_{s(ACI)}$: calculated service deflection based on ACI 318- 11

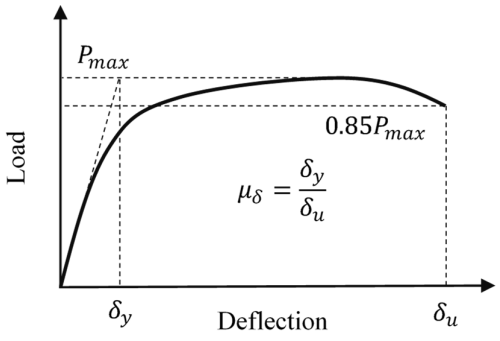

(a) Definitions of ductility

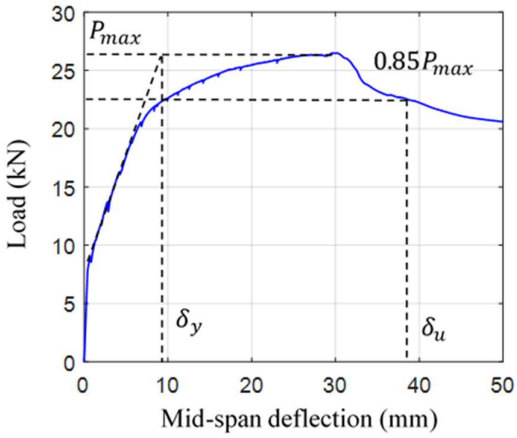

(b) OPC

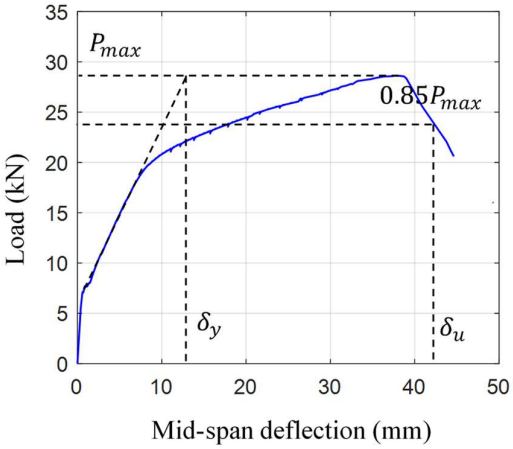

(c) GPC

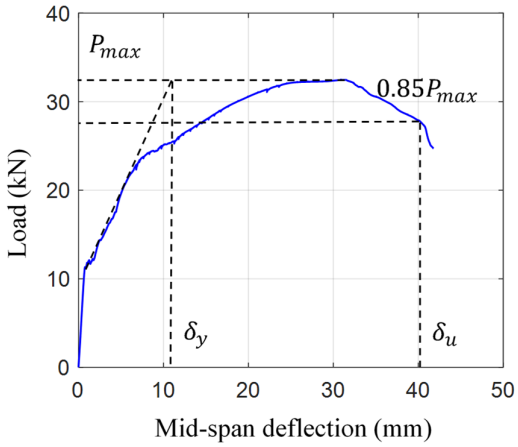

(d) GPC-0.375-35

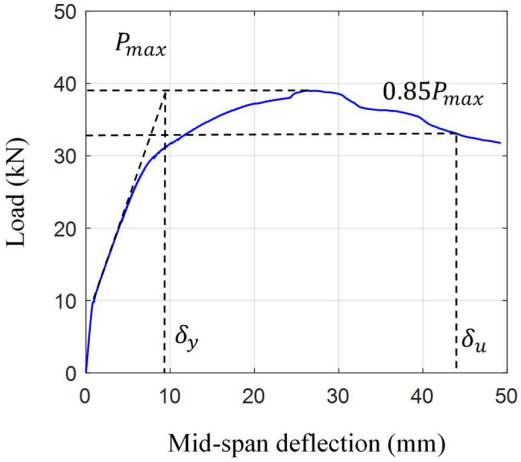

(e) GPC-0.75-35

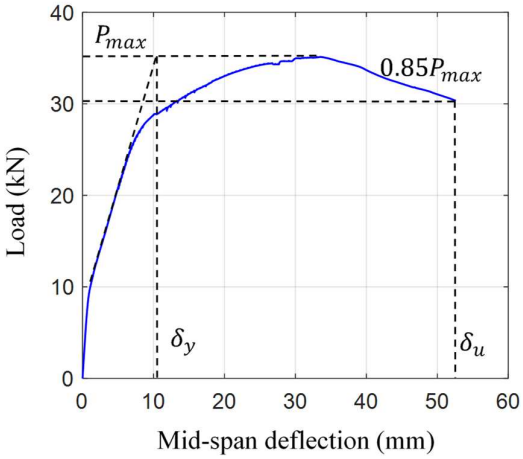

(f) GPC-1.5-35

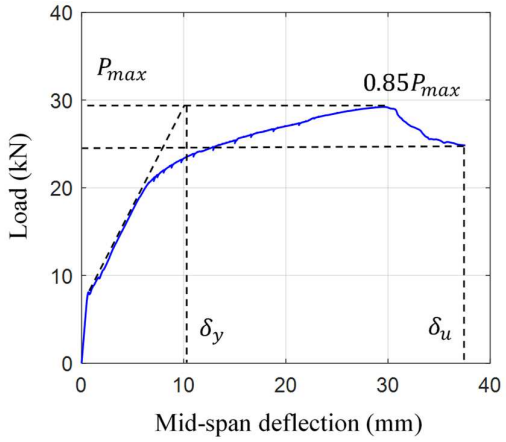

(g) GPC-0.375-60

Figure 3-10. Detailed plots with specific yielding and ultimate points of tested beams

For all the tested beams, only vertical flexural cracks occurred and no inclined cracks appeared even in the shear spans as shown in Figure 3-11. There were approximately 6 cracks distributed quite uniformly along the flexural span of all the beams, with an average crack spacing of 100 mm for plain GPC and OPC. In general, the crack development and patterns of the plain GPC beams were almost identical to cracking behavior of reinforced OPC beams reported in the literature [22]. All the GPC beams with steel fibres showed a smaller crack width and slower crack development as compared to the OPC and plain GPC beams. The addition of steel fibres narrows the crack width and slows the crack development but did not affect the number of cracks. This is mainly due to the contribution of steel fibres in improving the tensile behavior of concrete which was discussed in the previous sections.

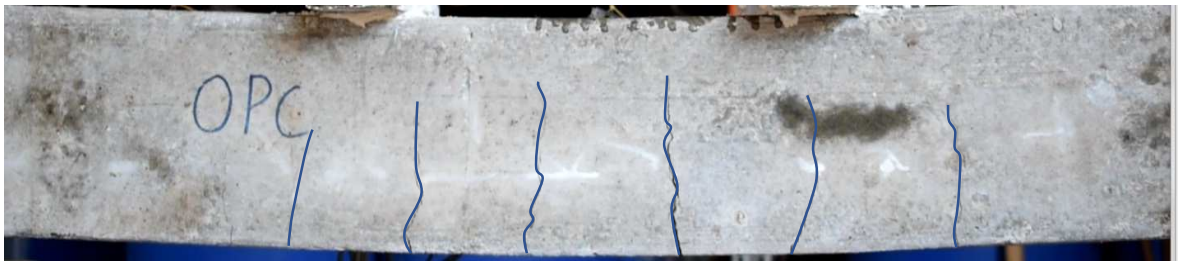

(a) OPC

(b) GPC

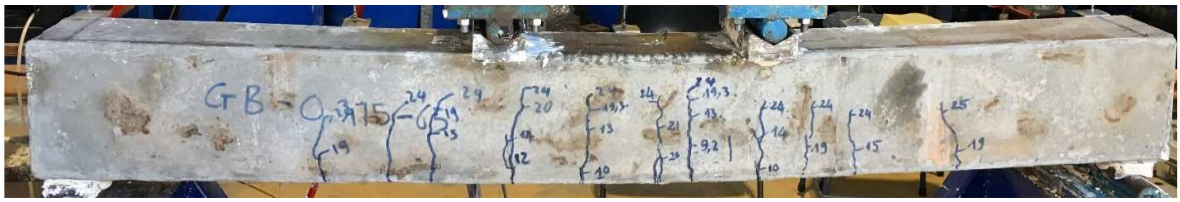

(c) GPC-0.375-65

(d) GPC-0.75-35

(e) GPC-1.5-35

Figure 3-11. Cracking patterns of the tested beams

3.3. Analytical solution to estimate load-deflection relation ship

In this section, an analytical procedure to estimate the load-deflection response of steel fibre reinforced GPC beams is developed based on the method of the simplified trilinear moment curvature which is similar to the typical load-deflection curve presented in Figure 3-3. The cracking point (Φ_{cr}, M_{cr}), the yield point (Φ_y, M_y) and the peak point (Φ_p, M_p) are determined through the sectional analysis. The initial assumptions for the section analysis are summarized as follows:

a. The Bernoulli theory for the flexural behaviour of beams is adopted, meaning the cross-section remains plane.
b. The bond of reinforcing steel bars and concrete is perfect, no slip occurs.
c. The compressive behaviour of OPC, GPC and steel fibre reinforced GPC is calibrated from the stress-strain curves proposed by Carreira and Chu [68].
d. The tension model for stress-strain behaviour of steel fibre reinforced GPC is calibrated from the simplified model suggested by Mobasher et al. [47].
e. The ultimate strain of the extreme top concrete fibre, ε_{cu}, is conventionally the value of strain corresponding to the 85% of post-peak stress in the stress-strain curve [44, 69].
f. The material model of reinforcing bars is assumed as a bilinear isotropic hardening model.

3.4.1. Material Models

a. Compressive stress-strain relationship of concrete

The stress-strain curve for concrete in compression proposed by Carreira and Chu [68] is adopted as follows:

$$\sigma_c = f_c' \frac{\beta_f(\varepsilon_c/\varepsilon_c')}{\beta_f - 1 + (\varepsilon_c/\varepsilon_c')^{\beta_f}} \tag{3-9}$$

where σ_c is the compressive stress of concrete, ε_c is the compressive strain in the concrete, ε_c' is the strain at peak stress (corresponding to the compressive strength of concrete, f_c' in MPa), and β_f is the curve-fitting parameter. For OPC, β_f can be calculated by solving Eq. (3-10) proposed by Carreira and Chu [68].

$$\left(\alpha \frac{f_c'}{E_c \varepsilon_c'}\right)^{\beta_f} - \beta_f \left(\frac{f_c'}{E_c \varepsilon_c'} - 1\right) - 1 = 0 \tag{3-10}$$

where E_c is calculated by Eq. (3-1) and ε_c' is estimated by Eq. (3-11) which was proposed by Attard and Setunge [70] as follows:

$$\varepsilon_c' = \frac{f_c'}{E_c} \frac{4.26}{\sqrt[4]{f_c'}} \qquad \text{where } f_c' \text{ and } E_c \text{ in MPa} \tag{3-11}$$

In the case of plain GPC and GPC reinforced with steel fibres, due to a lack of study proposing the compressive stress-strain relationship, it is assumed that the effect of fibres on the modulus

of elasticity, strain at peak stress and the curve-fitting parameter of GPC is similar to OPC. Hence, those parameters for plain GPC and GPC reinforced with steel fibres are respectively estimated by using Eqs. (3-12) ,(3-13) and (3-14), proposed for steel fibre reinforced OPC by Ezeldin and Balaguru [71].

$$E_{cf} = E_c + 9.315\left(V_f \frac{l_f}{d_f}\right) \tag{3-12}$$

$$\varepsilon'_{cf} = \varepsilon'_c + 1338 \times 10^{-6}\left(V_f \frac{l_f}{d_f}\right) \tag{3-13}$$

$$\beta_f = \begin{cases} 1.093 + 7.4818\left(3V_f \dfrac{l_f}{d_f}\right)^{-1.387} & with\ V_f > 0 \\ (0.031 f'_c)^3 + 1.55 & with\ V_f = 0 \end{cases} \tag{3-14}$$

where ε'_{cf} is the strain corresponding to peak stress of steel fibre reinforced GPC, ε'_c is the strain at peak stress of plain GPC determined by Eq. (3-15) [20], E_{cf} is the modulus of elasticity of steel fibre reinforced GPC in MPa, and E_c is the modulus of elasticity of plain GPC (presented in Eq. (3-2)). The curve-fitting parameter β_f for both plain and fibre reinforced GPC is directly calculated from Eq. (3-14) instead of solving Eq. (3-10).

$$\varepsilon'_c = \frac{2.23 \times 10^{-7}(E_c)^{1.74}}{(f'_c)^{1.98}} \quad \text{where } f'_c \text{ and } E_c \text{ in MPa} \tag{3-15}$$

The ultimate strain, ε_{cu}, is determined by solving Eq. (3-9) when the compressive stress of concrete is settled to $0.85f'_c$. The equations to determine ε_{cu} for plain OPC and GPC are presented in Eq. (3-16). In order to determine ε_{cu} for GPC reinforced with steel fibres, the value of ε'_c is replaced by ε'_{cf} in Eq. (3-13) as follows:

$$0.85\left(\frac{\varepsilon_{cu}}{\varepsilon'_c}\right)^{\beta_f} - \beta_f\left(\frac{\varepsilon_{cu}}{\varepsilon'_c}\right) + 0.85\beta_f - 0.85 = 0 \qquad \text{with } \varepsilon_{cu} > \varepsilon'_c \tag{3-16}$$

By solving Eq. (3-16) for each case of plain OPC and GPC, and GPC with steel fibre reinforcement, the relationship between the ultimate strain, ε_{cu}, and compressive strength, f'_c, is plotted in Figure 3-12. As can be seen from the figure, ε_{cu} of OPC varies from 0.0035 to 0.0038 in the range of compressive strength from 30 MPa to 70 MPa. Those values are similar to the value proposed by Hognestad for OPC beams [44]. By comparison, plain GPC shows a higher ε_{cu} due to the higher strain at peak stress, ε'_c, which is resulted from the low modulus

of elasticity. While the ultimate strain of plain GPC decreases rapidly with an increase in the compressive strength, the ultimate strain of GPC reinforced with steel fibre is enhanced significantly due to the improvement in the post-peak behavior.

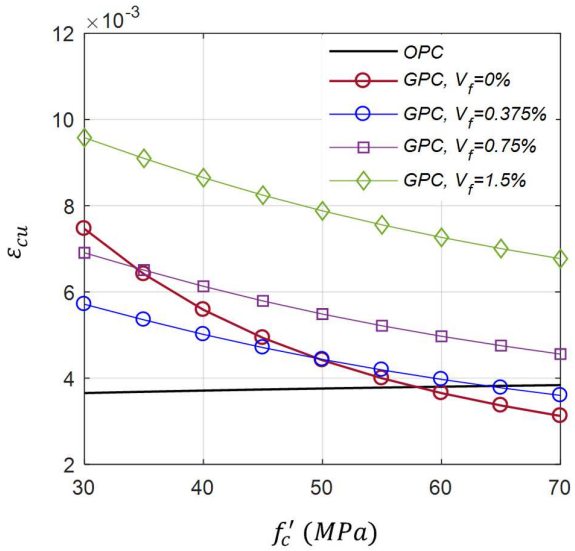

Figure 3-12. Ultimate strain ε_{cu}

b. Tension model for GPC reinforced with steel fibres and reinforcing bars

When designing OPC structures, the tensile resistance of concrete is often neglected in estimating the flexural behavior of reinforced concrete beams since the tensile strength of plain OPC is much less than its compressive strength. However, concrete reinforced with steel fibre reinforcement can resist considerable tensile forces through the bonding of steel fibres and the concrete matrix. Accordingly, the tensile response of steel fibre reinforced GPC must be taken into consideration in the analysis. Nevertheless, there has been no study proposing a tension model for GPC reinforced with steel fibres. In this chapter, an idealized tension model of steel fibre reinforced OPC proposed by Mobasher et al. [47] and illustrated in Figure 3-13 is adopted for analyzing the GPC beams with steel fibres. The mathematical formulation for the model is expressed as follows:

$$\sigma_c(\varepsilon_c) = \begin{cases} E_c\varepsilon_c & 0 \le \varepsilon_c \le \varepsilon_{cr} \\ \sigma_p & \varepsilon_{cr} \le \varepsilon_c \le \varepsilon_{tu} \\ 0 & \varepsilon_{tu} \le \varepsilon_c \end{cases} \tag{3-17}$$

where E_c is the elastic modulus of steel fibre reinforced GPC, ε_{cr} is the first cracking tensile strain ($\varepsilon_{cr} = f_r/E_c$, f_r is the flexural strength in Eq. (3-3)), ε_{tu} is the ultimate tensile strain

which can be taken as 0.02 [47], σ_p is the residual tensile stress after peak stress due to the bridging effect of hooked-end steel fibres on macro cracks. When the fibres pulled out from the matrix ($l_f < l_c$), f_p can be determined from Eq. (3-18) suggested by Naaman [72]:

$$\sigma_p = \lambda_1 \lambda_2 \lambda_3 V_f \left(\frac{l_f}{d_f}\right) \tau_b \qquad \text{(in MPa) with } l_f < l_c \tag{3-18}$$

where τ_b is the bond strength of a single fibre embedded in concrete, in the case of GPC, it was proposed in the previous section and now is presented in Eq. (3-19); λ_1 is the expected pull-out length ratio; λ_2 is the efficiency factor of orientation in cracked state; λ_3 is the group reduction factor associated with number of fibres pulling out per unit area. In the previous study of OPC reinforced with steel fibres, those coefficients were taken as $\lambda_1 = 0.25, \lambda_2 = 1.2, \lambda_3 = 1$ [69, 73] and thus those values are adopted in this chapter.

$$\tau_b = 1.36\sqrt{f_c'} \qquad \text{(in MPa)} \tag{3-19}$$

By substituting Eq. (3-19) and those coefficients into Eq. (3-18), the residual stress σ_p can be expressed as follows:

$$\sigma_p = 0.41\sqrt{f_c'} V_f \left(\frac{l_f}{d_f}\right) \qquad \text{(in MPa) with } l_f < l_c \tag{3-20}$$

In the case of $l_f \geq l_c$, which means the fibre fracture mode occurring, f_p is calculated based on the ultimate tensile strength of the fibres, σ_{fu}. By using the equilibrium condition in Eq. (3-8) with the fibre length embedded in concrete matrix, l_{emb}, the average bond stress τ_b at the crack surface of the fibre fracture is calculated as follows:

$$\tau_b = \sigma_{fu} \frac{d_f}{2l_{emb}} \qquad \text{(in MPa)} \tag{3-21}$$

The residual stress, f_p, in the case of fibre fracture mode is determined through substituting the bond stress τ_b of Eq. (3-21) into Eq. (3-18) as

$$\sigma_p = \lambda_1 \lambda_2 \lambda_3 \sigma_{fu} V_f \left(\frac{l_f}{2l_{emb}}\right) \qquad \text{(in MPa) with } l_f \geq l_c \tag{3-22}$$

where $\lambda_1, \lambda_2, \lambda_3$ are taken as the same values in Eq. (3-18). The fibre embedded length, l_{emb}, can be assumed as a half of fibre length $l_f/2$ and thus the residual stress, f_p can be expressed as follows:

$$\sigma_p = 0.3\sigma_{fu}V_f \quad \text{(in MPa) with } l_f \geq l_c \tag{3-23}$$

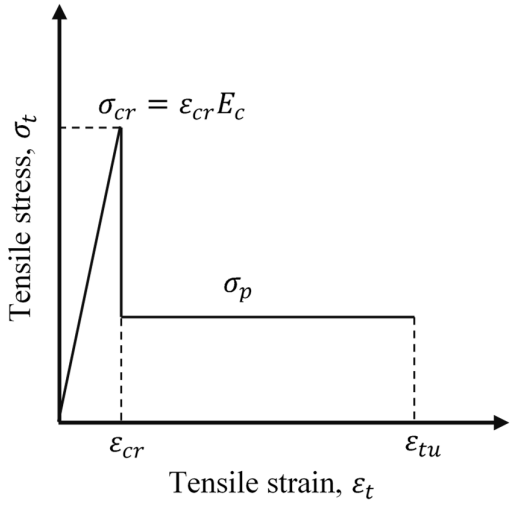

Figure 3-13. Tension model for steel fibre reinforced GPC

The reinforcing steel bars are modeled as an idealized isotropic hardening material with a bilinear curve illustrated in Figure 3-14. The yield strength of reinforcing steel bars, f_y is 548 MPa and the modulus of elasticity, E_s is 200 GPa. The hardening modulus of steel, E_{sh} can be assumed as $0.03E_s$ [74].

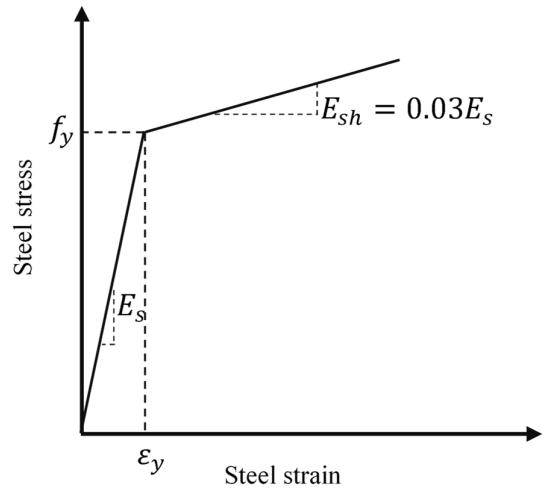

Figure 3-14. Stress-strain model for reinforcing bars

3.4.2. Solution for the moment-curvature diagram

In this section, a method to derive the trilinear moment-curvature diagram of the beams is proposed. By combining the Bernoulli assumption and the material models, shown in Eqs. (3-9) and (3-17), the linear strain profiles and stress distribution diagrams of a cross-section at the cracking point, yielding point, and peak point are presented in Figure 3-16. Based on those diagrams, the critical points of the moment-curvature diagram are determined.

The first crack of the beam appears when the extreme tensile strain at bottom of a certain section, ε_c^b reaches the cracking tensile strain, ε_{cr} (illustrated in Figure 3-15(a)). Because the section of the beams is symmetric, the neutral axis of the section at this stage is placed at the centre. The cracking curvature and moment are calculated by Eqs. (3-24) and (3-25), respectively.

$$\Phi_{cr} = \frac{2\varepsilon_{cr}}{h} = \frac{2f_r}{hE_c} \qquad \text{(rad/mm)} \tag{3-24}$$

where f_r is the modulus of rupture (flexural strength) in MPa (Eq. 3-3), E_c is the modulus of elasticity in MPa (Eq. (3-1) or (3-2)), h is the height of the cross-section in mm.

$$M_{cr} = \Phi_{cr}E_c\left(I_g + nA_s(h-2a)^2\right) \qquad \text{(N.mm)} \tag{3-25}$$

where I_g is the gross moment of inertia of cross-section equal to $bh^3/12$ (b is the width of section in mm), n is the ratio of the elastic moduli of steel and concrete (E_s/E_c), a is the distance from the bottom fibre of the section to the centre of the tensile longitudinal reinforcing bars in mm.

The calculation of the yielding curvature and the moment is implemented by considering the nonlinear distribution of compressive stresses based on the stress-strain curve in Eq. (3-9) and the bilinear distribution of tensile stresses based on the idealized model in Eq. (3-17) (the diagrams illustrated in Figure 3-15b). Accordingly, the yielding curvature, ϕ_y is calculated as follows:

$$\phi_y = \frac{\varepsilon_c^t - \varepsilon_y}{d} \tag{3-26}$$

where d is the effective depth of section in mm and ε_c^t is the concrete strain at the extreme top fibre of the section. Then the strain values of the section are determined by Eq. (3-27) as

$$\varepsilon_c = \phi_y(y-h) + \varepsilon_c^t = \frac{\varepsilon_c^t - \varepsilon_y}{d}(y-h) + \varepsilon_c^t \tag{3-27}$$

where y is the vertical coordinate illustrated in Figure 3-15. Once the strain profile of the section is known, the concrete stress distribution and the stresses in reinforcing bars are obtained based on the constitutive material relationships described in the previous sections. Then the internal forces such as yielding moment, M_y is attained through Eq. (3-28) as follows:

$$M_y = \int_0^h y\sigma_c(y)\,dy + \sigma_s' y_s' A_s' - \sigma_s y_s A_s \tag{3-28}$$

where $\sigma_c(y)$ is the stress of concrete, σ_s' is the stress in the top reinforcing bars corresponding to the area of A_s' and y_s' is the distance from the bottom fibre of the section to the centre of top reinforcing bars, σ_s is the stress in the bottom reinforcing bars (in case of yielding point, $\sigma_s = f_y$, yield strength of steel), A_s is the area of bottom reinforcing bars and y_s is the distance from the bottom fibre of the section to the centre of bottom reinforcing bars. To acquire totally the strain profile of the section, the value of ε_c^t is determined by solving the axial force equilibrium of the section which is presented as follows,

$$\sum F_x = 0 \Rightarrow \int_0^h \sigma_c(y)\,dy + \sigma_s' A_s' - \sigma_s A_s = 0 \tag{3-29}$$

However, the analytical integration of the stress distribution diagram across the section, $\int_0^h \sigma_c(y)\,dy$ is very complicated due to the complexity of constitutive material functions. Therefore, the entire section is divided into a number of layers with equal height, as shown in Figure 3-16. Concrete strain in each layer is assumed to be uniformly distributed and equal to the strain at the centre of the layer. Consequently, the axial force equilibrium of the section in Eq. (3-29) is rewritten under the numerical formulation as follows:

$$\sum F_x = 0 \Rightarrow \frac{bh}{n_l}\sum_1^{n_l} \sigma_{ci}(\varepsilon_c^t) + \sigma_s' A_s' - \sigma_s A_s = 0 \tag{3-30}$$

where n_l is the number of finite layers and σ_{ci} is the concrete stress at the centre of i^{th} layer. This nonlinear equation has only one unknown, ε_c^t, and thus the Newton-Raphson method is adopted. When ε_c^t is determined, all strain values, ε_{ci}, and stress values, σ_{ci}, of each layer is determined by using Eq. (3-27) and the constitutive material equations in Eqs. (3-9) and (3-17). Then the internal moment at yielding M_y is calculated as follows:

$$M_y = \frac{bh}{n_l}\sum_{1}^{n_l} y_i \sigma_{ci}(\varepsilon_c^t) + \sigma_s' y_s' A_s' - \sigma_s y_s A_s \tag{3-31}$$

where y_i is the vertical coordinates at the centre of the i^{th} layer (100 layers). It is worth to mention that Eq. (3-31) is the simplified form of Eq. (3-28). Similarly, the maximum moment M_p and corresponding curvature ϕ_p are determined based on the diagrams in Figure 3-15c and the layer method in Figure 3-16. The strain profile of the section at the ultimate stage is expressed as follows:

$$\varepsilon_c = \phi_p(y - h) + \varepsilon_{cu} \tag{3-32}$$

where ε_{cu} is the ultimate strain at the extreme top fibre of the section calculated from solving Eq. (3-16). To obtain the strain profile of sections and the stress of each layer, σ_{ci}, the ultimate curvature ϕ_p must be determined. The procedure to acquire ϕ_p is similar to that of ε_c^t mentioned above by solving the axial force equilibrium of section (Eq. (3-30)). Once ϕ_p is determined, the ultimate moment M_p is calculated similarly by using Eq. (3-31).

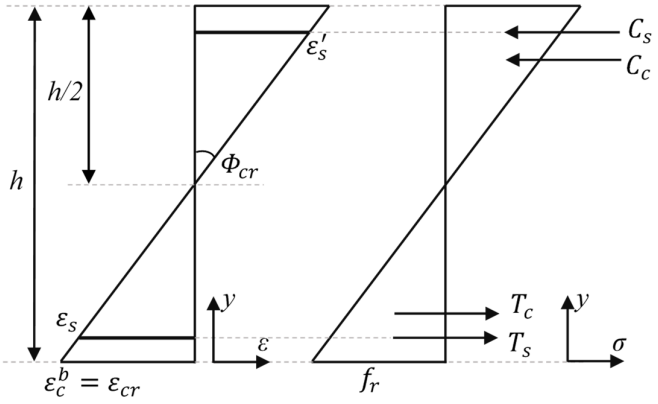

(a) cracking point

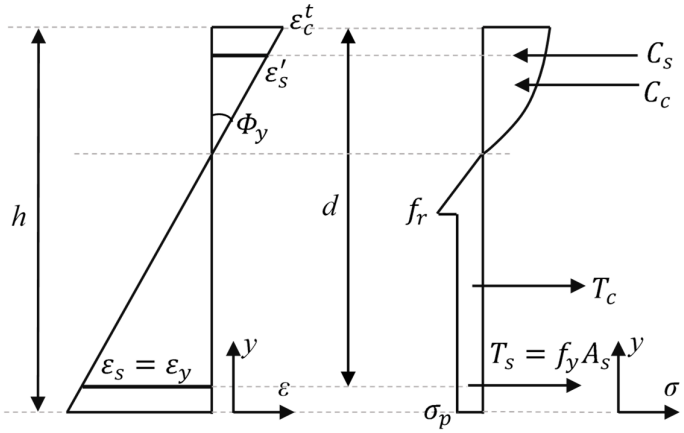

(b) yielding point

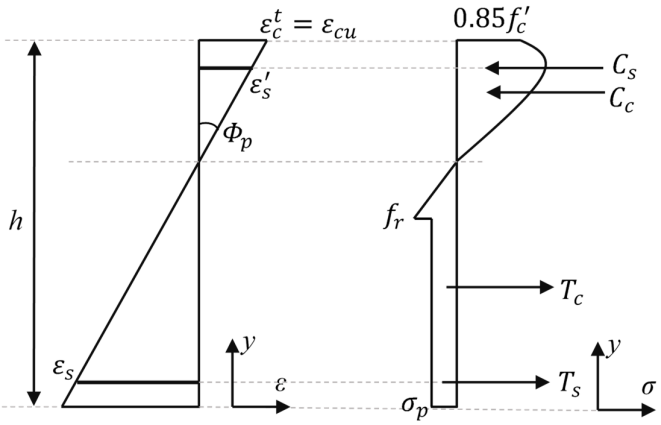

(c) peak point

Figure 3-15. Strain profile and stress distribution of cross-section at three stages

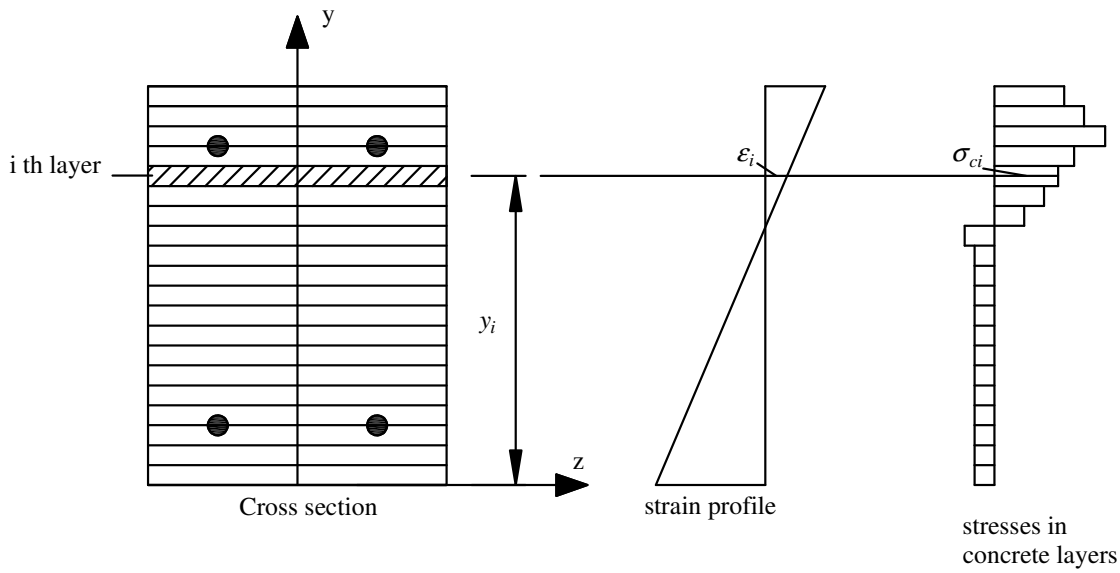

Figure 3-16. Layer method for the sectional analysis

3.4.3. Solution for the load-deflection curve

The deflection equation of a beam is obtained by integrating the function of curvature distributions along the beam axis as follows:

$$\delta(x) = \iint \phi(x)dx \tag{3-33}$$

where $\delta(x)$ and $\phi(x)$ are respectively the equations for the deflection and curvature at any point along the axis of the beam. Hence, the functions for curvature distribution along the beam axis, $\phi(x)$ need to be determined. Figures 3-17a and b show the beam subjected to four-point loading and the moment distribution obtained by static equilibrium. Three patterns of curvature distribution along the beam axis are illustrated in Figures 3-17c, d, and e. The mathematical equation for the curvature at any point along the axis of the beam, $\phi(x)$ is expressed as follows:

In the case of $M_{mid} \leq M_{cr}$ (M_{mid} is the constant moment in the pure bending zone),

$$\phi(x) = \begin{cases} x\dfrac{\phi_{mid}}{S_p}, & 0 \leq x \leq S_p \\ \phi_{mid}, & S_p \leq x \leq L - S_p \\ (L-x)\dfrac{\phi_{mid}}{S_p}, & L - S_p \leq x \leq L \end{cases} \tag{3-34}$$

where S_p is the shear span which is determined as a distance from the hinge support to the loading point and ϕ_{mid} is the curvature in the pure bending zone.

In the case of $M_{cr} \le M_{mid} \le M_y$,

$$\phi(x) = \begin{cases} x\dfrac{\phi_{cr}}{x_{cr}}, & 0 \le x \le x_{cr} \\ x\dfrac{\phi_{mid}-\phi_{cr}}{S_p-x_{cr}} + \dfrac{\phi_{cr}S_p-\phi_{mid}x_{cr}}{S_p-x_{cr}}, & x_{cr} \le x \le S_p \\ \phi_{mid}, & S_p \le x \le L-S_p \\ (L-x)\dfrac{\phi_{mid}-\phi_{cr}}{S_p-x_{cr}} + \dfrac{\phi_{cr}S_p-\phi_{mid}x_{cr}}{S_p-x_{cr}}, & L-S_p \le x \le L-x_{cr} \\ (L-x)\dfrac{\phi_{cr}}{x_{cr}}, & L-x_{cr} \le x \le L \end{cases} \quad (3\text{-}35)$$

where x_{cr} is the location of the cracking moment in the beam axis calculated in Eq. (3-36).

$$x_{cr} = \frac{M_{cr}}{M_{mid}} S_p \quad (3\text{-}36)$$

In the case of $M_y \le M_{mid} \le M_p$,

$$\phi(x) = \begin{cases} x\dfrac{\phi_{cr}}{x_{cr}}, & 0 \le x \le x_{cr} \\ x\dfrac{\phi_{y}-\phi_{cr}}{x_{y}-x_{cr}} + \dfrac{\phi_{cr}x_{y}-\phi_{y}x_{cr}}{x_{y}-x_{cr}}, & x_{cr} \le x \le x_{y} \\ x\dfrac{\phi_{mid}-\phi_{y}}{S_p-x_{y}} + \dfrac{\phi_{y}S_p-\phi_{mid}x_{y}}{S_p-x_{y}}, & x_{y} \le x \le S_p \\ \phi_{mid}, & S_p \le x \le L-S_p \\ (L-x)\dfrac{\phi_{mid}-\phi_{y}}{S_p-x_{y}} + \dfrac{\phi_{y}S_p-\phi_{mid}x_{y}}{S_p-x_{y}}, & L-S_p \le x \le L-x_{y} \\ (L-x)\dfrac{\phi_{y}-\phi_{cr}}{x_{y}-x_{cr}} + \dfrac{\phi_{cr}x_{y}-\phi_{y}x_{cr}}{x_{y}-x_{cr}}, & L-x_{y} \le x \le L-x_{cr} \\ (L-x)\dfrac{\phi_{cr}}{x_{cr}}, & L-x_{cr} \le x \le L \end{cases} \quad (3\text{-}37)$$

where x_{cr} is determined in Eq. (3-36) and x_y is the location of yielding moment in the beam axis calculated in Eq. (3-38).

$$x_y = \frac{M_y}{M_{mid}} S_p \quad (3\text{-}38)$$

The curvature in the pure bending zone, ϕ_{mid} is interpolated from the value of M_{mid} based on trilinear moment-curvature diagram determined in the previous section by using the following equation:

$$\phi_{mid} = \begin{cases} \dfrac{M_{mid}}{M_{cr}}\phi_{cr}, & 0 \le M_{mid} \le M_{cr} \\ M_{mid}\dfrac{\phi_y - \phi_{cr}}{M_y - M_{cr}} + \dfrac{M_y\phi_{cr} - M_{cr}\phi_y}{M_y - M_{cr}}, & M_{cr} \le M_{mid} \le M_y \\ M_{mid}\dfrac{\phi_p - \phi_y}{M_p - M_y} + \dfrac{M_p\phi_y - M_y\phi_p}{M_p - M_y}, & M_y \le M_{mid} \le M_p \end{cases} \quad (3\text{-}39)$$

To determine the load-deflection response of the beams, M_{mid} increases step by step from zero to the maximum moment, M_p. For a given M_{mid}, the corresponding ϕ_{mid} is estimated by using Eq. (3-39). With the determined ϕ_{mid}, the equation of curvature distribution along the beam axis is obtained based on Eqs. (3-34), (3-35) and (3-37). Then the deflection equation of the beam, $\delta(x)$ is determined by solving Eq. (3-33). In addition, Eq. (3-33) is not complicated to solve since it includes the integrations of linear functions. However, the determination of constants of integration, which needs to solve a large number of linear algebraic equations, is relatively complex. Therefore, in this chapter, an automatic procedure is developed by using the Matlab programming language to solve Eq. (3-33). The analytical results of the proposed procedure are verified with the experimental data in the next section. Details of this procedure and coding are presented in Appendix A for design purposes.

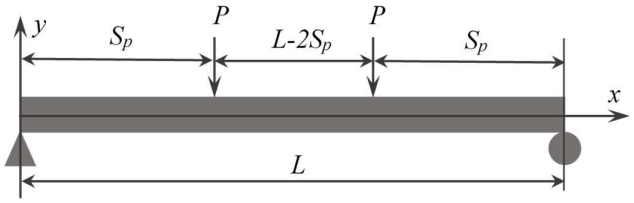

(a) Four-point bending test

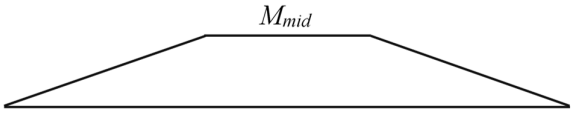

(b) Moment diagram

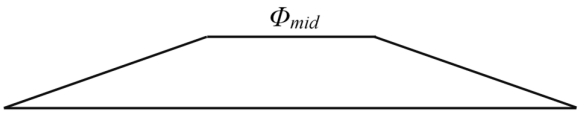

(c) Curvature distribution in case of $M_{mid} \leq M_{cr}$

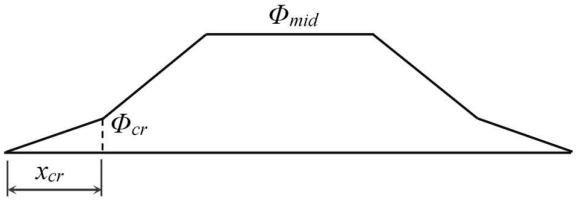

(d) Curvature distribution in case of $M_{cr} < M_{mid} \leq M_y$

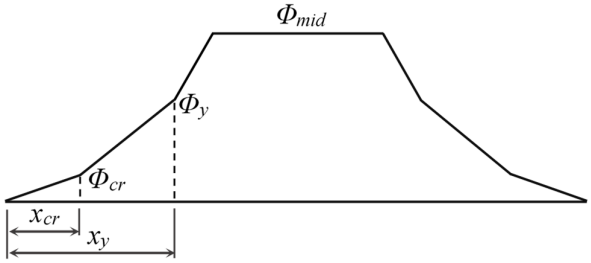

(e) Curvature distribution in case of $M_y < M_{mid} \leq M_p$

Figure 3-17. Moment and curvature distribution diagrams

3.4.4. Verification of analytical results with experimental data

The proposed procedure for load-deflection response is verified with the experimental data of the OPC and GPC beams obtained from the previous studies [22, 75] as shown in Figure 3-18. The details of each test specimen in the literature are presented in Table 3-7. Moreover, the comparison between the predicted curves with the test data is shown in Figure 3-19 and summarized in Table 3-8. It can be seen that there is a good correlation between the test results and predictions for most of the beams except for a slight overestimation of Beam GPC-1.5-35. The estimated load-carrying capacity of Beam GPC-1.5-35 was approximately 25% higher than the experimental result. This difference is due to the poor fibre distribution and orientation in the case of GPC reinforced with high fibre volume ($V_f = 1.5\%$) as discussed in the previous sections. Therefore, it is believed that the coefficients λ_1, λ_2 and λ_3 in Eq. (3-18) determined according to the previous studies of OPC reinforced with steel fibre [69, 73] seem to

overestimate the residual stress σ_p (in Eq. (3-23)) of GPC with a high volume of steel fibre reinforcement. In addition, the analytical prediction of Beam GPC-0.375-60 also shows a slight overestimation compared to the test results which is also attributed to poor fibre dispersion and fibre balling. The causes of those adverse effects were explained in Section 3.3.1.c. Generally, the proposed method demonstrates good predictions for the load-carrying capacity of GPC beams reinforced with steel fibres.

Based on Table 3-8, the estimated deflections at the peak load show a variation compared with the experimental outcomes. This variation is attributed to the estimation of the ultimate strain, ε_{cu} (from Eq. (3-16)) because of the direct use of Eqs. (3-13) and (3-14), which were proposed for steel fibre reinforced OPC, for estimating the strain at peak stress, ε_c', and the curve-fitting parameter, β, for GPC. Since the post-peak behavior of GPC is different from OPC, Eqs. (3-13) and (3-14) may not be able to capture the actual behavior of the descending part in the stress-strain relationship of GPC reinforced with steel fibres.

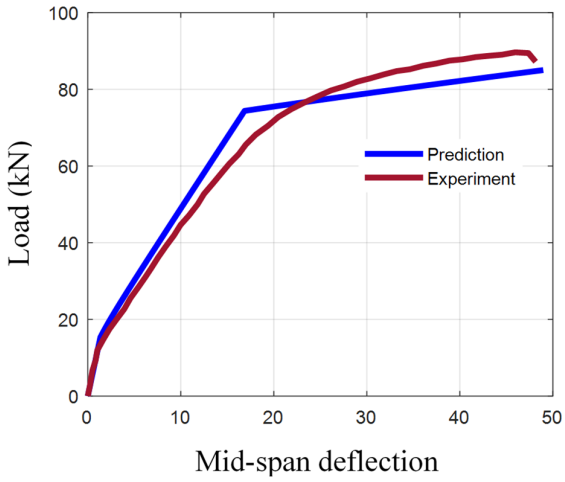

(a) GBII-2 [22]

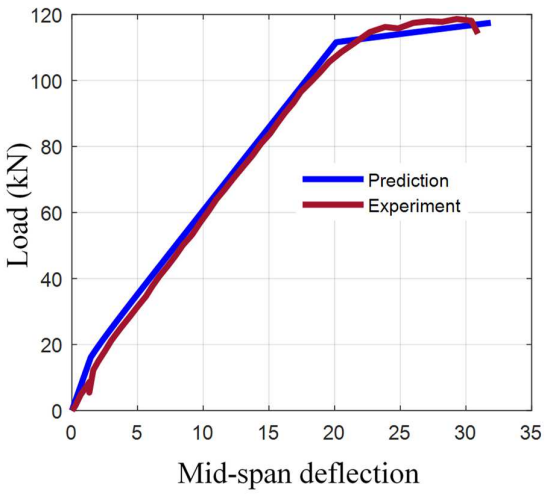

(b) GBII-3 [22]

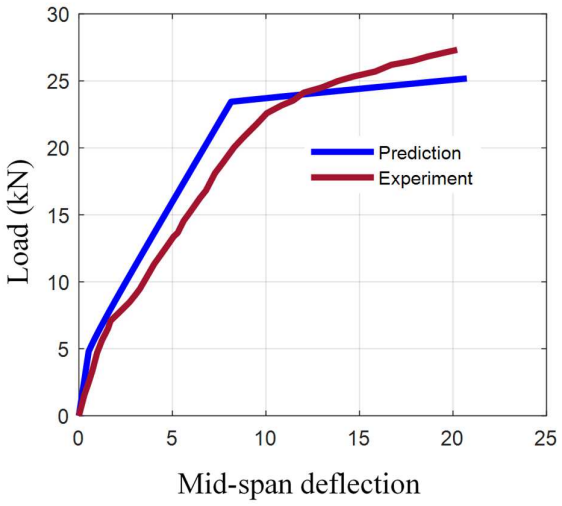

(c) OPC-B1 [75]

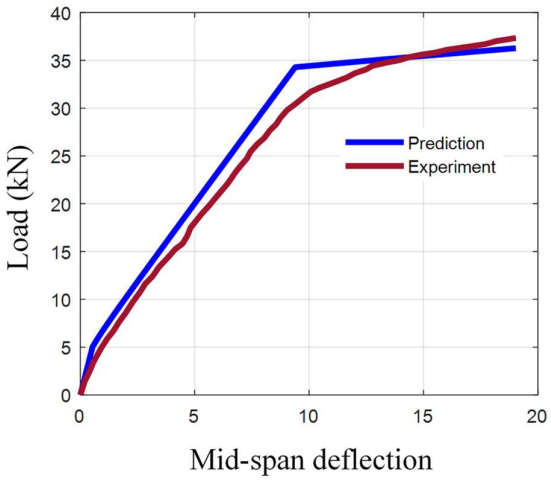

(d) OPC-B2 [75]

Figure 3-18. Comparison of predicted response and test data obtained from previous studies

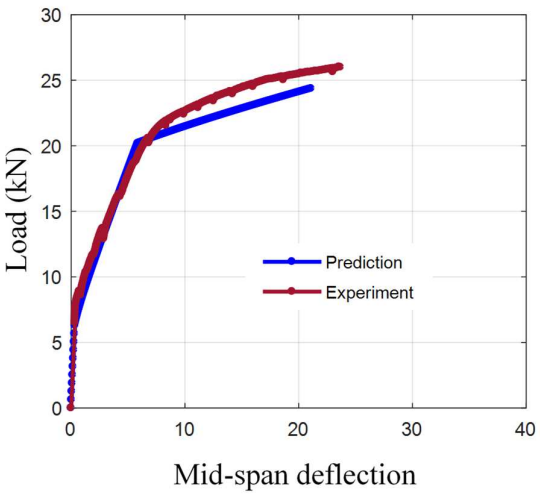

(a) OPC

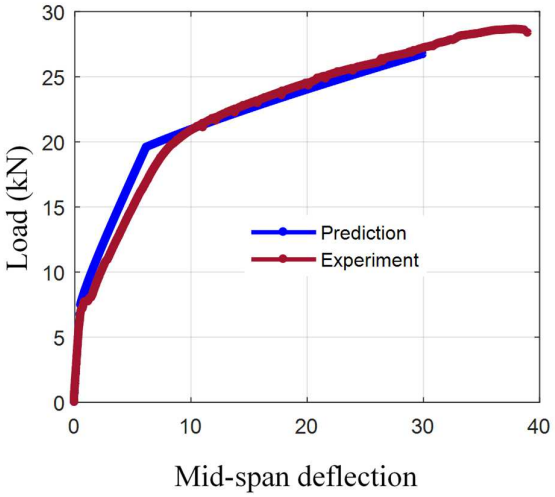

(b) GPC

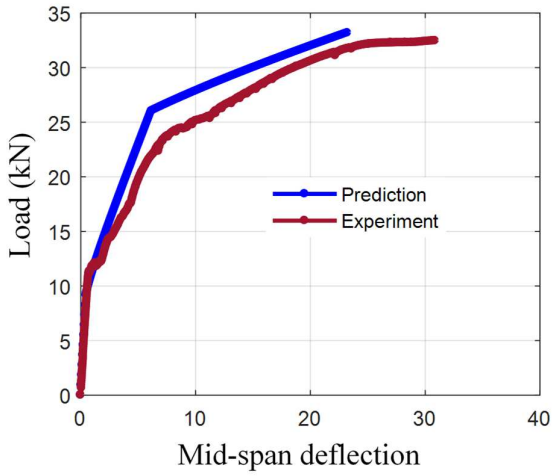

(c) GPC-0.375-35

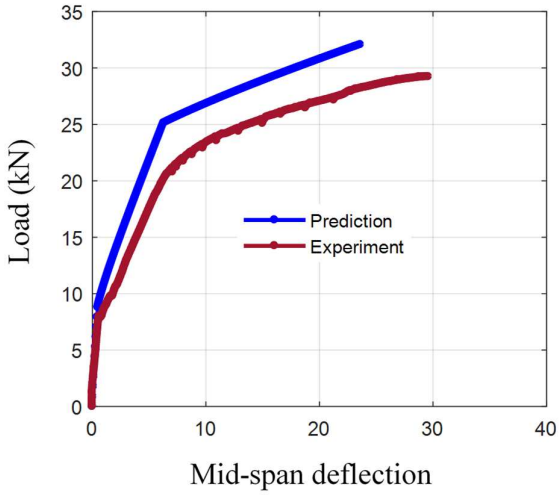

(d) GPC-0.375-60

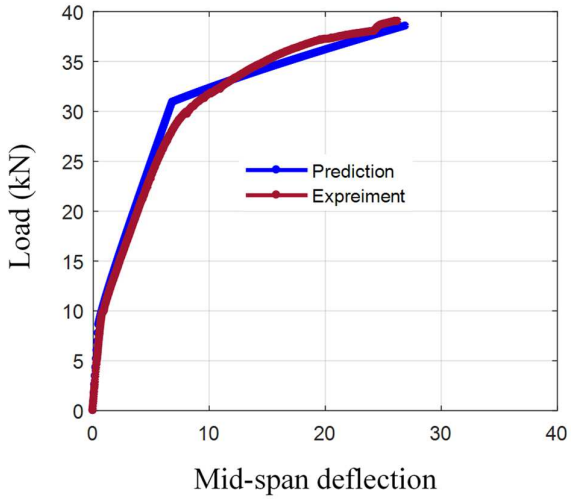

(e) GPC-0.75-35

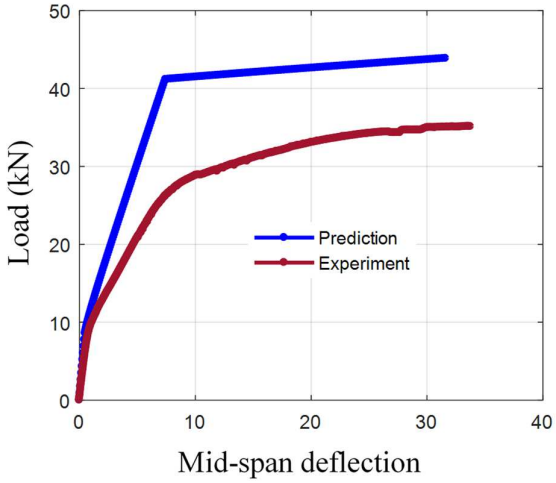

(f) GPC-1.5-35

Figure 3-19. Comparison of the predicted load-deflection curves and experimental results

Table 3-7. Details of specimens in the previous studies

Beam ID	b (mm)	h (mm)	l (mm)	a (mm)	A_s (mm^2)	A'_s (mm^2)	f_y (Mpa)	f'_c (Mpa)	V_f	l_f/d_f	Fibre types
GBII-2 [22]	200	300	3000	1000	603	226	560	53	-	-	-
GBII-3 [22]	200	300	3000	1000	942	226	560	53	-	-	-

OPC-B1 [75]	120	180	1800	600	253.4	-	420	43	1	57	Hook end
OPC-B2 [75]	120	180	1800	600	397.2	-	420	43	1	57	Hook end

Table 3-8. Experimental results versus analytical predictions

Beams	Estimation		Experiment		Estimated/test results	
	P_{max}^{est}(kN)	δ_p^{est} (mm)	P_{max}^{exp} (kN)	δ_p^{exp} (mm)	$P_{max}^{est}/P_{max}^{exp}$	$\delta_p^{est}/\delta_p^{exp}$
OPC	24.36	21.10	26.31	23.79	0.93	0.89
GPC	26.68	29.97	28.61	38.10	0.93	0.79
GPC-0.375-35	33.10	23.30	32.51	30.90	1.02	0.75
GPC-0.75-35	38.60	26.90	39.03	26.36	0.99	1.02
GPC-1.5-35	43.91	31.60	35.11	33.01	1.25	0.96
GPC-0.375-60	32.06	23.61	29.21	29.69	1.1	0.80
Mean					1.04	0.87
SD					0.12	0.11

Note: P_{max}^{est}, P_{max}^{exp} are the maximum load capacities respectively obtained from analytical estimation and experiment and δ_p^{est}, δ_p^{exp} are the corresponding deflections.

3.4. Conclusion

The flexural behavior of the ambient cured under-reinforced GPC beams with steel fibres is investigated and compared with that of the reference OPC beam. Based on the experimental and analytical results, the following conclusion can be drawn:

1. The plain GPC beam showed the lowest cracking moment and stiffness in the post-cracked stage due to high drying shrinkage and low modulus of elasticity. The serviceability displacement of the plain GPC was significantly large (40% more than the deflection of OPC beam). The serviceability deflections of plain GPC and GPC reinforced with a low volume of fibres were overestimated significantly by the ACI 318-11.
2. The failure of the GPC beam is very brittle with explosive concrete crushing on the top and then followed by a low residual deflection as compared to that of the OPC beam.

3. The addition of hooked-end steel fibres improved the cracking resistance, the stiffness in the post-cracked stage (decrease the service deflection by 21%), the flexural capacity (increase the maximum load by 40%) and the ductility (increase by 49%), owing to the enhancement in tension stiffening, the control of drying shrinkage and toughness and the improvement of post-peak behavior in the compressive zone.

4. An increase in the load-carrying capacity of the GPC beams increased with the volume fraction of steel fibres from 0 to 0.75%. However, the GPC beam with 1.5% fibre content showed the reduction of load-carrying capacity by 18% as compared to the GPC with 0.75% of volume fraction. Due to the poor workability performance of GPC, it is recommended to use the volume fraction of around 0.75% for GPC to ensure good fibre dispersion and orientation.

5. For the same fibre content, the GPC beams with the long fibre of 60 mm in length had a lower capacity (approximately 10%) than the GPC reinforced with shorter fibres (35 mm in length). The analytical estimation shows that the fibre length of 35 mm is sufficient to prevent premature pull-out of fibres from happening before fibres rupture. Therefore, increasing the fibre length does not improve the capacity of GPC beams but may cause adverse effects such as poor fibre dispersion and fibre balling.

6. The analytical predictions demonstrated a relatively good agreement with the experimental results in the case of GPC beams reinforced with short fibre ($l_f = 35mm$) and the low volume of fibre ($V_f < 0.75\%$). However, there was an overestimation in the case of the GPC beams with a high volume of fibres ($V_f = 1.5\%$) and using long fibres ($l_f = 35mm$).

Based on the obtained results, it can be concluded that the proposed analytical method is acceptable to estimate the load-deflection curve of fibre reinforced GPC beams with a volume fraction of about 0.75%. However, the variation in estimating deflections at peak load indicated unsuitability of using Eq. (3-13) and (3-14) to calculate the ultimate strain, ε_{cu} of GPC reinforced with steel fibres. Therefore, further study on this issue is deemed necessary.

Appendix. Procedures for analysing the load-deflection response of GPC beams reinforced with steel fibres

Step 1: Input all material properties of concrete (f_c'), reinforcing steel bars (f_y, E_s and E_{sh}), steel fibres (V_f, d_f and l_f) and geometry of beam cross-section.

Step 2: Calculate the cracking point (Φ_{cr}, M_{cr}) by using Eqs. (3-24) and (3-25).

Step 3: Divide the section into 100 layers. Determine all vertical coordinates at the centre of each layers, y_i.

Step 4: Choose the initial ε_c^t and then determine all strain values, ε_{ci}, and stress values, σ_{ci} of each layer by using Eq. (3-27).

Step 5: With the strain values in step 4, an iterative Newton-Raphson method is implemented to obtain a convergent value of ε_c^t which satisfies Eq. (3-30).

Step 6: The yielding point (ϕ_y, M_y) is determined by substituting the value ε_c^t into Eqs. (3-27) and (3-31).

Step 7: Determine ε_{cu} by solving Eq. (3-16).

Step 8: Choose the initial ϕ_p and combine with the value ε_{cu} of step 7 to determine all strain values, ε_{ci}, and stress values, σ_{ci} of each layer by using Eq. (3-32).

Step 9: With the strain values in step 8, an iterative Newton-Raphson method is implemented to obtain a convergent value of ϕ_p which satisfies Eq. (3-30).

Step 10: The peak point (ϕ_p, M_p) is determined by substituting the value ϕ_p of step 9 into Eq. (3-32).

Step 11: Assign $M_{mid} = M_{mid} + \Delta M$ ($\Delta M = M_p/100$, the initial value of $M_{mid} = 0$).

Step 12: Calculate the corresponding value of ϕ_{mid} by using Eq. (3-39) with the value of M_{mid} in Step 11 and the values of (Φ_{cr}, M_{cr}), (ϕ_y, M_y), (ϕ_p, M_p) determined from step 2 to step 10.

Step 13: Determine the function for curvature distribution along the beam axis, $\phi(x)$ by using Eqs. (3-34), (3-35) and (3-37).

Step 14: Integrating $\iint \phi(x)dx$ and solve constants of integration, the deflection equation of the beam, $\delta(x)$ is attained. The mid-span deflection δ_{mid} is obtained by substituting $x = L/2$ into deflection equation, $\delta(x)$.

Step 15: Repeat step 11 to 14 until M_{mid} reach the value M_p, the complete load-deflection response is obtained

Notation

A_s = area of bottom longitudinal reinforced steel

A'_s = area of top longitudinal reinforced steel

a = shear span of the beam

β_f = curve-fitting parameter of compressive stress strain curve of concrete

b = breadth of rectangular section of beam

d = effective depth of concrete section

d' = distance from the bottom surface of the section to the centre of bottom longitudinal reinforcement

d_f = fibre diameter

E_c = elastic modulus of plain concrete

E_{cf} = elastic modulus of concrete reinforced with steel fibres

E_s = elastic modulus of steel

E_{sh} = hardening modulus of steel

ε_c = compressive strain of concrete in the stress-strain model

ε'_c = concrete compressive strain at peak stress of plain concrete

ε'_{cf} = concrete compressive strain at peak stress of concrete reinforced with steel fibres

ε_{cu} = ultimate strain at extreme compression fibre

ε_y = yield strain of longitudinal steel

ε_{tu} = ultimate tensile strain of steel fibre reinforced concrete

f'_c = concrete cylinder compressive strength

f_{ct} = splitting tensile strength of the concrete cylinder

f_r = modulus of rupture of concrete

σ_p = the residual tensile strength of hooked-end steel fibre reinforced concrete

f_y = yield stress of reinforcing steel

h = height of rectangular section of beam

I_g = moment of inertia of the gross concrete section

L = total span of the beams

λ_1 = the expected pull-out length ratio

λ_2 = the efficiency factor of orientation in cracked state

λ_3 = the group reduction factor associated with number of fibres pulling out per unit area

M_{cr} = cracking moment

M_y = yielding moment

M_p = maximum moment

n = ratio of elastic modulus of steel reinforcement and concrete

ϕ_{cr} = curvature at cracking moment

ϕ_y = curvature at yielding moment

ϕ_p = curvature at maximum moment

P_{cr} = cracking load

σ_c = concrete compressive stress in stress-strain model

σ_s' = stress in top reinforcing steel bars

l_c = critical fibre length for fibre fracture

l_{emb} = the fibre length embedded in concrete matrix

l_f = fibre length

ρ_s = steel reinforcement ratio

τ_b = the bond strength of a single fibre embedded in the concrete

V_f = volume fraction of steel fibres

Reference

[1] López-Gayarre F, Blanco Viñuela R, Serrano-López MA, López-Colina C. Influence of the water variation on the mechanical properties of concrete manufactured with recycled mixed aggregates for pre-stressed components. Constr Build Mater. 2015;94:844-50.

[2] Benhelal E, Zahedi G, Shamsaei E, Bahadori A. Global strategies and potentials to curb CO2 emissions in cement industry. J Cleaner Prod. 2013;51:142-61.

[3] Bakharev T. Resistance of geopolymer materials to acid attack. Cem Concr Res. 2005;35:658-70.

[4] Ariffin MAM, Bhutta MAR, Hussin MW, Mohd Tahir M, Aziah N. Sulfuric acid resistance of blended ash geopolymer concrete. Constr Build Mater. 2013;43:80-6.

[5] Sarker PK. Bond strength of reinforcing steel embedded in fly ash-based geopolymer concrete. Mater Struct. 2010;44:1021-30.

[6] Castel A, Foster SJ. Bond strength between blended slag and Class F fly ash geopolymer concrete with steel reinforcement. Cem Concr Res. 2015;72:48-53.

[7] Nath P, Sarker PK. Flexural strength and elastic modulus of ambient-cured blended low-calcium fly ash geopolymer concrete. Constr Build Mater. 2017;130:22-31.

[8] Thomas RJ, Peethamparan S. Alkali-activated concrete: Engineering properties and stress–strain behavior. Constr Build Mater. 2015;93:49-56.

[9] Khan MZN, Hao Y, Hao H, Shaikh FUA. Mechanical properties of ambient cured high strength hybrid steel and synthetic fibers reinforced geopolymer composites. Cem Concr Compos. 2018;85:133-52.

[10] Pan Z, Sanjayan JG, Rangan BV. Fracture properties of geopolymer paste and concrete. Mag Concr Res. 2011;63:763-71.

[11] Collins F, Sanjayan JG. Cracking tendency of alkali-activated slag concrete subjected to restrained shrinkage. Cem Concr Res. 2000;30:791-8.

[12] Duran Atiş C, Bilim C, Çelik Ö, Karahan O. Influence of activator on the strength and drying shrinkage of alkali-activated slag mortar. Constr Build Mater. 2009;23:548-55.

[13] Ye H, Radlińska A. Shrinkage mechanisms of alkali-activated slag. Cem Concr Res. 2016;88:126-35.

[14] Shaikh FUA. Review of mechanical properties of short fibre reinforced geopolymer composites. Constr Build Mater. 2013;43:37-49.

[15] Farhan NA, Sheikh MN, Hadi MNS. Engineering Properties of Ambient Cured Alkali-Activated Fly Ash–Slag Concrete Reinforced with Different Types of Steel Fiber. J Mater Civ Eng. 2018;30:04018142.

[16] Kheradmand M, Abdollahnejad Z, Pacheco-Torgal F. Drying shrinkage of fly ash geopolymeric mortars reinforced with polymer hybrid fibres. Proceedings of the Institution of Civil Engineers - Construction Materials. 2017;0:1-13.

[17] Bhutta A, Farooq M, Zanotti C, Banthia N. Pull-out behavior of different fibers in geopolymer mortars: effects of alkaline solution concentration and curing. Mater Struct. 2017;50:80.

[18] Fernandez-Jimenez AM, Palomo A, Lopez-Hombrados C. Engineering properties of alkali-activated fly ash concrete. ACI Mater J. 2006;103:106-12.

[19] Sofi M, van Deventer JSJ, Mendis PA, Lukey GC. Engineering properties of inorganic polymer concretes (IPCs). Cem Concr Res. 2007;37:251-7.

[20] Noushini A, Aslani F, Castel A, Gilbert RI, Uy B, Foster S. Compressive stress-strain model for low-calcium fly ash-based geopolymer and heat-cured Portland cement concrete. Cem Concr Compos. 2016;73:136-46.

[21] Khan MZN, Shaikh FUA, Hao Y, Hao H. Effects of Curing Conditions and Sand-to-Binder Ratios on Compressive Strength Development of Fly Ash Geopolymer. J Mater Civ Eng. 2018;30:04017267.

[22] Sumajouw MDJ, Rangan BV. Low-Calcium Fly Ash-Based Geopolymer Concrete: Reinforced Beams and Columns, Research Report GC. Perth(Australia): Curtin University of Technology; 2006.

[23] Chang EH. Shear and Bond Behaviour of Reinforced Fly Ash-Based Geopolymer Concrete Beams [PhD thesis]: Curtin University of Technology; 2009.

[24] Dattatreya J K RN, Sabitha D, Ambily P S, Nataraja MC. Flexural behaviour of reinforced Geopolymer concrete beams. Int J Civ Struct Eng. 2011;2:138–59.

[25] Yost JR, Radlinska A, Ernst S, Salera M, Martignetti NJ. Structural behavior of alkali activated fly ash concrete. Part 2: structural testing and experimental findings. Mater Struct. 2012;46:449-62.

[26] Maranan GB, Manalo AC, Benmokrane B, Karunasena W, Mendis P. Evaluation of the flexural strength and serviceability of geopolymer concrete beams reinforced with glass-fibre-reinforced polymer (GFRP) bars. Eng Struct. 2015;101:529-41.

[27] Nguyen KT, Ahn N, Le TA, Lee K. Theoretical and experimental study on mechanical properties and flexural strength of fly ash-geopolymer concrete. Constr Build Mater. 2016;106:65-77.

[28] Visintin P, Mohamed Ali MS, Albitar M, Lucas W. Shear behaviour of geopolymer concrete beams without stirrups. Constr Build Mater. 2017;148:10-21.

[29] Sumajouw DMJ, Hardjito D, Wallah SE, Rangan BV. Fly ash-based geopolymer concrete: study of slender reinforced columns. J Mater Sci. 2006;42:3124-30.

[30] Sarker PK. Analysis of geopolymer concrete columns. Mater Struct. 2008;42:715-24.

[31] Rahman MM. Geopolymer Concrete Columns Subjected to Axial Load and Biaxial Bending [Master]: Curtin University; 2013.

[32] Albitar M, Mohamed Ali MS, Visintin P. Experimental study on fly ash and lead smelter slag-based geopolymer concrete columns. Constr Build Mater. 2017;141:104-12.

[33] Reinforced Concrete Design : in accordance with AS 3600-2009. Sydney, N.S.W: Cement & Concrete Aggregates Australia : Standards Australia; 2011.

[34] Ng TS, Amin A, Foster SJ. The behaviour of steel-fibre-reinforced geopolymer concrete beams in shear. Mag Concr Res. 2013;65:308-18.

[35] Devika C, Deepthi R. Study of flexural behavior of hybrid fibre reinforced geopolymer concrete beam. Int J Sci Res. 2015;4:130-5.

[36] Farhan NA, Sheikh MN, Hadi MNS. Behaviour of Ambient Cured Steel Fibre Reinforced Geopolymer Concrete Columns Under Axial and Flexural Loads. Structures. 2018;15:184-95.

[37] Khan MZN, Shaikh FUA, Hao Y, Hao H. Synthesis of high strength ambient cured geopolymer composite by using low calcium fly ash. Constr Build Mater. 2016;125:809-20.

[38] ASTM I. ASTM A370-18 Standard Test Methods and Definitions for Mechanical Testing of Steel Products. West Conshohocken, PA.2018.

[39] Ltd TAP. TEXO. http://texo.net.au/steel-fibre. 2016.

[40] ASTM I. ASTM C496/C496M-17 Standard Test Method for Splitting Tensile Strength of Cylindrical Concrete Specimens. West Conshohocken, PA. 2017.

[41] ASTM I. ASTM C39/C39M-18 Standard Test Method for Compressive Strength of Cylindrical Concrete Specimens. West Conshohocken, PA.2018.

[42] 318 AC. Building Code Requirements for Structural Concrete (ACI 318-11). 2011.

[43] Rasheed Hayder A, Charkas H, Melhem H. Simplified Nonlinear Analysis of Strengthened Concrete Beams Based on a Rigorous Approach. J Struct Eng. 2004;130:1087-96.

[44] Wight JK, MacGregor JG. Reinforced concrete: Mechanics and Design: Pearson; 2009.

[45] Bischoff PH. Rational model for calculating deflection of reinforced concrete beams and slabs. Can J Civ Eng. 2007;34:992-1002.

[46] Choi C-K, Cheung S-H. Tension stiffening model for planar reinforced concrete members. Comput Struct. 1996;59:179-90.

[47] Mobasher B, Yao Y, Soranakom C. Analytical solutions for flexural design of hybrid steel fiber reinforced concrete beams. Eng Struct. 2015;100:164-77.

[48] Ashour SA. Effect of compressive strength and tensile reinforcement ratio on flexural behavior of high-strength concrete beams. Eng Struct. 2000;22:413-23.

[49] Ashour SA, Wafa FF, Kamal MI. Effect of the concrete compressive strength and tensile reinforcement ratio on the flexural behavior of fibrous concrete beams. Eng Struct. 2000;22:1145-58.

[50] Bischoff PH. Effects of shrinkage on tension stiffening and cracking in reinforced concrete. Can J Civ Eng. 2001;28:363-74.

[51] Scanlon A, Bischoff PH. Shrinkage Restraint and Loading History Effects on Deflections of Flexural Members. ACI Struct J. 2008;105:498-506.

[52] Mesbah HA, Buyle-Bodin F. Efficiency of polypropylene and metallic fibres on control of shrinkage and cracking of recycled aggregate mortars. Constr Build Mater. 1999;13:439-47.

[53] Kaklauskas G, Gribniak V, Bacinskas D, Vainiunas P. Shrinkage influence on tension stiffening in concrete members. Eng Struct. 2009;31:1305-12.

[54] Bischoff PH. Tension Stiffening and Cracking of Steel Fiber-Reinforced Concrete. J Mater Civ Eng. 2003;15:174-82.

[55] Gribniak V, Kaklauskas G, Kliukas R, Jakubovskis R. Shrinkage effect on short-term deformation behavior of reinforced concrete – When it should not be neglected. Mater Des. 2013;51:1060-70.

[56] Kang ST, Lee BY, Kim J-K, Kim YY. The effect of fibre distribution characteristics on the flexural strength of steel fibre-reinforced ultra high strength concrete. Constr Build Mater. 2011;25:2450-7.

[57] Boulekbache B, Hamrat M, Chemrouk M, Amziane S. Flowability of fibre-reinforced concrete and its effect on the mechanical properties of the material. Constr Build Mater. 2010;24:1664-71.

[58] Yazıcı Ş, İnan G, Tabak V. Effect of aspect ratio and volume fraction of steel fiber on the mechanical properties of SFRC. Constr Build Mater. 2007;21:1250-3.

[59] Nath P, Sarker PK. Effect of GGBFS on setting, workability and early strength properties of fly ash geopolymer concrete cured in ambient condition. Constr Build Mater. 2014;66:163-71.

[60] Gao X, Yu QL, Brouwers HJH. Properties of alkali activated slag–fly ash blends with limestone addition. Cem Concr Compos. 2015;59:119-28.

[61] Yoo D-Y, Kang S-T, Yoon Y-S. Effect of fiber length and placement method on flexural behavior, tension-softening curve, and fiber distribution characteristics of UHPFRC. Constr Build Mater. 2014;64:67-81.

[62] Ma Y, Zhu B, Tan M. Properties of ceramic fiber reinforced cement composites. Cem Concr Res. 2005;35:296-300.

[63] Khuntia M, Stojadinovic B, Goel S. Shear Strength of Normal and High-Strength Fiber Reinforced Concrete Beams without Stirrups. ACI Struct J. 1999;96:282-9.

[64] Bhutta A, Borges PHR, Zanotti C, Farooq M, Banthia N. Flexural behavior of geopolymer composites reinforced with steel and polypropylene macro fibers. Cem Concr Compos. 2017;80:31-40.

[65] Bencardino F, Rizzuti L, Spadea G, Swamy RN. Stress-Strain Behavior of Steel Fiber-Reinforced Concrete in Compression. J Mater Civ Eng. 2008;20:255-63.

[66] Park R. Evaluation of ductility of structures and structural assemblages from laboratory testing. Bulletin of the New Zealand national society for earthquake engineering. 1989;22:155-66.

[67] Meda A, Minelli F, Plizzari GA. Flexural behaviour of RC beams in fibre reinforced concrete. Compos Part B: Eng. 2012;43:2930-7.

[68] Carreira DJ, Chu KH. Stress-Strain Relationship for Plain Concrete in Compression. ACI Journal Proceedings. 1985;82:797-804.

[69] Campione G, Mangiavillano ML. Fibrous reinforced concrete beams in flexure: Experimental investigation, analytical modelling and design considerations. Eng Struct. 2008;30:2970-80.

[70] Attard MM, Setunge S. Stress-Strain Relationship of Confined and Unconfined Concrete. ACI Mater J. 1996;93:432-42.

[71] Ezeldin AS, Balaguru PN. Normal- and High-Strength Fiber-Reinforced Concrete under Compression. J Mater Civ Eng. 1992;4:415-29.

[72] Naaman AE. Engineered Steel Fibers with Optimal Properties for Reinforcement of Cement Composites. J Adv Concr Technol. 2003;1:241-52.

[73] Campione G. Simplified Flexural Response of Steel Fiber-Reinforced Concrete Beams. J Mater Civ Eng. 2008;20:283-93.

[74] Dehestani M, Mousavi SS. Modified steel bar model incorporating bond-slip effects for embedded element method. Constr Build Mater. 2015;81:284-90.

[75] Oh BH. Flexural Analysis of Reinforced Concrete Beams Containing Steel Fibers. J Struct Eng. 1992;118:2821-35.

Chapter 4. Effect of Fibres on Shear Response of Ambient-Cured Geopolymer Concrete Beams under Static Loading

Abstract[3]

The shear response of twelve slender geopolymer concrete (GPC) beams and one control OPC beam reinforced with basalt fibre reinforced polymer (BFRP) bars as longitudinal reinforcements without stirrups was investigated. Different fibre combinations were used to enhance the shear capacity of the beams, including (1) single type of macro-steel fibres (SF) or (2) macro-synthetic polypropylene fibres (PF), (3) hybridization of SF and micro-polyvinyl alcohol fibres (PVF) or (4) PF and micro- carbon fibres (CF). The experimental results indicated that the presence of SF yielded the greatest improvement in the cracking behaviour, post-cracked stiffness, and shear capacity of the beams. The addition of 0.5% SF to the GPC and OPC beams increased the normalized shear strength most by 56% and 14%, respectively. The higher contribution of SF to the shear strength of GPC can be attributed to the superior adhesive bonding strength of fibre and GPC matrix. Despite being less effective than SF, adding PF also improves significantly the normalized shear strength up to 33% with 0.5% fibre content. The hybridization of SF and PVF showed a good synergy in enhancing the shear capacity. Meanwhile, the combination of PF and CF did not improve the shear strength but enhanced considerably the ductility of the beams. Furthermore, three analytical models were proposed to estimate the shear capacity of the SF reinforced concrete beams. The comparison of prediction and experimental results demonstrated the model derived from the modified compression field theory (MCFT) achieved the best correlation.

4. 1. Introduction

Due to the pressing environmental issues, geopolymer concrete (GPC) was introduced to replace the non-environmental friendly material like ordinary Portland concrete (OPC). Through increasing the content of slag, GPC can reach a sufficient compressive strength under

[3] This chapter was extracted from the paper published in Composite Structures, but the tittle of the chapter and subsections were modified to follow the flow of the thesis. The full bibliographic citation of the paper is as follows: Tran TT, Pham TM, Hao H. Effect of hybrid fibres on shear behaviour of geopolymer concrete beams reinforced by basalt fibre reinforced polymer (BFRP) bars without stirrups. Compos Struct. 2020;243:112236. https://doi.org/10.1016/j.compstruct.2020.112236

ambient curing conditions [1, 2]. Previous studies demonstrated GPC provides high bond performance with steel reinforcements [3], excellent acid resistance [4], and high flexural strength [5]. Meanwhile, the investigations at the structural level of beams and columns indicated a similarity in the general behaviour of heat-cured GPC and OPC [6, 7], and hence existing analytical models and current design codes of OPC structures are suitable to be applied for GPC structures [8]. In contrast, experimental and analytical investigations related to ambient-cured GPC structures are really limited and reported some adverse phenomena. The poor cracking resistance and low post-cracked stiffness were observed in ambient-cured GPC beams due to the severe dry shrinkage resulting from the presence of high slag content [1]. In addition, the failure of ambient-cured GPC structures including beams and beam-column joints was very brittle and their ductility was smaller compared to OPC counterparts [1, 9]. This can be attributed to the intrinsically brittle characteristic of a highly cross-link framework of geopolymeric matrix [10]. Such differences result in an overestimation when using existing design methods of OPC to estimate the capacity of ambient-cured GPC columns subjected to axial load and uniaxial bending [11]. Therefore, modifications to the rectangular stress-block parameters in current design codes were conducted and provided a closer capacity estimation of ambient-cured GPC columns [12]. Based on the review above, it can be concluded that the behaviour of heat-cured GPC structures seems similar to OPC ones whereas the behaviour of ambient-cured GPC structures needs further studies.

Another major concern in the construction industry is the reduction in the long-term performance and service life of concrete structures due to the corrosion of steel reinforcements. Some experimental and analytical studies indicated a significant reduction in bearing capacity of the beam owing to corrosion damage of stirrup and longitudinal reinforcement [13, 14]. Recently, fibre reinforced polymer (FRP) bars such as carbon FRP (CFRP) or glass FRP (GFRP) bars have been introduced as a rational approach to deal with this issue. The most common FRP bars applied in concrete structures are made of CFRP [15] or GFRP [16]. Meanwhile, basalt FRP (BFRP) has been a relatively new product and just introduced since the last decade. It, however, possesses enormous potential for being adopted as reinforcements due to its considerable better cost-efficiency in comparison with CFRP [17] and greater mechanical properties compared to GFRP in terms of tensile strength, elastic modulus, and chemical resistance [18]. Therefore, the concept of a system made from the combination of BFRP bars and GPC is expected to create not only highly durable and sustainable but also economical structures.

One of the most critical issues of using FRP reinforcements is a reduced contribution of the shear resistance of concrete in beams without stirrups. This phenomenon was firstly reported by Yost et al. [19] that beams reinforced with longitudinal FRP bars had a significantly lower shear capacity as compared to their OPC counterparts reinforced with traditional steel. The post-cracked stiffness of the beams was also significantly reduced by using longitudinal FRP bars [20]. The experimental results indicated a proportional ratio of the shear capacity of reinforced concrete beams without stirrups to axial stiffness of the longitudinal reinforcing bars, $E_f A_f$ (E_f, A_f are elastic modulus and the total cross-sectional area of FRP reinforcing bars, respectively) [21]. Empirical equations calibrated from the current design codes were proposed and then obtained a reasonable but rather conservative estimation of the shear strength of the FRP-reinforced beams [21]. Unlike those models, modified compression field theory (MCFT) can achieve a more reasonable prediction of the shear capacity of reinforced concrete beams regardless of the type of reinforcements as long as their strain is taken into account [22, 23].

In contrast to the studies of OPC beams, investigations on the shear behaviour related to GPC beams using FRP bars for longitudinal reinforcement are rare with only two experimental works conducted so far in literature [24, 25]. Those studies indicated the possibility of applying GFRP for transverse reinforcements of GPC beams. Meanwhile, the shear response of ambient-cured GPC beams using longitudinal BFRP bars has not been investigated yet, and thus this is the motivation of the study in this chapter. A previous study has stated that the shear behaviour of GPC and OPC was similar [26]. GPC beams using BFRP bars for longitudinal reinforcements are expected to have low shear resistance due to the low elastic modulus of BFRP bars, which leads to large shear cracks and thus losing the aggregate interlock effect [21]. Adding fibres to concrete to improve the shear capacity can be an effective solution [27]. Macro-steel fibre (SF) can enhance the shear capacity of GPC beams without stirrups [28] but not a durable solution due to their poor corrosion resistance. On the other hand, macro-synthetic polypropylene fibres (PF), which have high chemical resistance, are a sustainable alternative for SF [29]. Some existing experimental investigations also reported an increment in the shear capacity of conventionally reinforced OPC beams with 1% volume fraction of PF [30, 31]. Unfortunately, the influence of PF on the shear strength of GPC beams employing longitudinal BFRP bars has not yet been examined yet. Apart from using a single type of macro-fibre such as SF and PF, it has been suggested that the hybridization of different kinds of fibres can provide an increase in both strength and ductility far beyond what can be achieved from

individual fibres alone [32]. In particular, concrete composite using the combination of SF and micro- polyvinyl alcohol fibres (PVF) could obtain high ultimate strength, crack resistance and strain capacity [33] while those made of the hybrid PF and micro-carbon fibre (CF) yielded great synergy in toughness [34]. In terms of the performance at the structural level, only one study so far reported the influence of a combination between SF and micro-polypropylene fibres on the shear performance of OPC beams without stirrups [35]. Therefore, further studies are necessary to investigate the feasibility of applying fibre hybridization in the structural scales.

In this chapter, the shear response of OPC and GPC beams using longitudinal BFRP bars without stirrups was investigated through an experimental program. Different fibre combinations including SF, PF, hybridization of SF and PVF, and combination of PF and CF were adopted to enhance the shear capacity. Based on the experimental results, the effect of different kinds of fibre reinforcement on the shear response of the tested beams is discussed and explained. Afterward, shear models for GPC beams with SF were proposed based on existing theoretical models of OPC. Predictions from the proposed models were then compared with the experimental findings to verify their reliability.

4. 2. Material and experimental program

4.2.1. Test Specimens

A total of 13 concrete beams were cast and tested under static loads until failure. The configuration of all the beams is illustrated in Figure 4-1. The cross-section of all the beams was rectangular with a width (b) of 150 mm, depth (h) of 200 mm and length of 1250mm. All the beams were reinforced at top and bottom by two 16-mm diameter BFRP bars ($A_f = 402\ mm^2$) corresponding to reinforcement ratio, $\rho_f = 1.6\%$, to ensure an adequate flexural capacity so that all the beams fail in shear. Three stirrups with 4 mm in diameter were placed at two supports and the middle of the beam for easy fabrication of BFRP cages.

The classification of the beams shown in Table 4-1 was based on the usage of different kinds of fibres and their various volume fractions. Due to the poor workability of GPC mixture [36], all the beams contained the low fibre volume fraction (less than 0.5 %) except for the Beam GPC-1SF. Three control beams including a plain OPC and two plain GPC beams (GPC1 and GPC2) were used as references to investigate the contribution of various types of fibres to the

shear capacity of the beams. Beam GPC1 and GPC2 are different in terms of the compressive strengths of GPC which were 40 and 50 MPa, respectively.

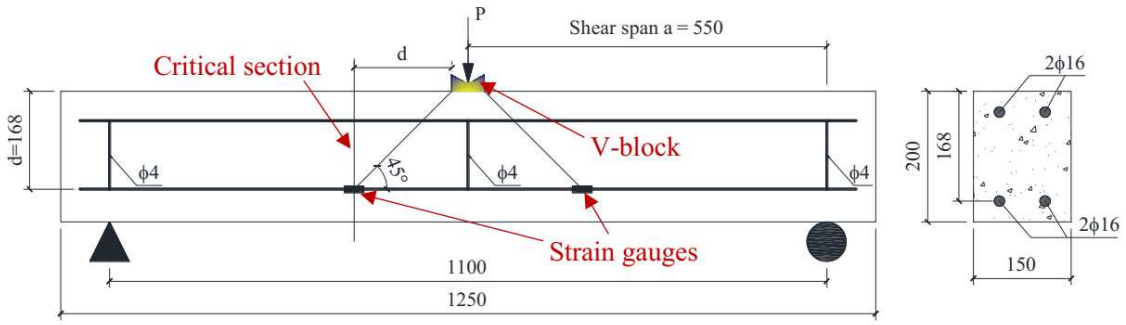

Figure 4-1. Specimen details and test setup (in mm)

Table 4-1. Fibre volume fraction of all the beams

Beam	Fibre volume fraction (%)			
	Steel	Synthetic	PVA	Carbon
OPC	-	-	-	-
OPC-0.5SF	0.5	-	-	-
GPC1	-	-	-	-
GPC2	-	-	-	-
GPC-0.25SF	0.25	-	-	-
GPC-0.5SF	0.5	-	-	-
GPC-1SF	1	-	-	-
GPC-0.25PF	-	0.25	-	-
GPC-0.5PF	-	0.5	-	-
GPC-0.4SF-0.1PVF	0.4	-	0.1	-
GPC-0.3SF-0.2PVF	0.3	-	0.2	-
GPC-0.4PF-0.1CF	-	0.4	-	0.1
GPC-0.3PF-0.2CF	-	0.3	-	0.2

- Not applicable

4.2.2. Material properties

The proportion of two GPC mixtures are outlined in Table 4-2 and based on the previous study using the same locally available materials [1]. Mixture 1 was used for casting all the GPC beams except for Beams GPC2 and GPC-1SF which adopted Mixture 2 to achieve higher compressive strength. The binder of the mixture is formed via a chemical reaction between low

calcium fly ash (FA) and ground granulated blast furnace slag (GGBFS) with a pre-mixture of 12M sodium hydroxide (NaOH) and D-grade sodium silicate (Na_2SiO_3) solution. Crushed stones with a maximum size of 10 mm and silica sand were used as coarse aggregates and fine aggregates, respectively. The mixing procedure to cast the GPC beams was conducted following the procedure adopted in the previous study [1]. 6 cylinders with the dimension of 100 mm x 200 mm were cast with the same batch of each GPC beams. After casting, all the beams and cylinder specimens were covered by plastic sheets and cured in the same ambient lab condition until testing dates.

Figure 4-2 shows the 16 mm BFRP bars which were used for longitudinal reinforcements [37]. According to the manufacturer, Young's modulus, tensile strength, and elongation at break of the BFRP bars are 55 GPa, 1100~1200 MPa, and 2%, respectively. The macro-fibres including hooked-end steel fibres (SF) and synthetic Vinyl Polypropylene fibres (PF) were supplied by BOSFA Pty Ltd [38] and BarChip Pty Ltd [39] while the micro-PVA fibres (PVF) and the micro-carbon fibre (CF) were purchased from Kuraray Co Ltd [40] and Beyond Materials Group Pty Ltd [41]. The visual demonstration and the relevant properties of fibres provided by manufacturers are presented in Figure 4-3 and Table 4-3.

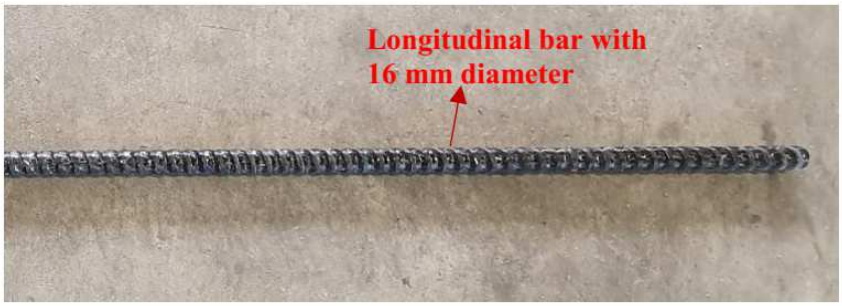

Figure 4-2. 16 mm BFRP bar for longitudinal reinforcements

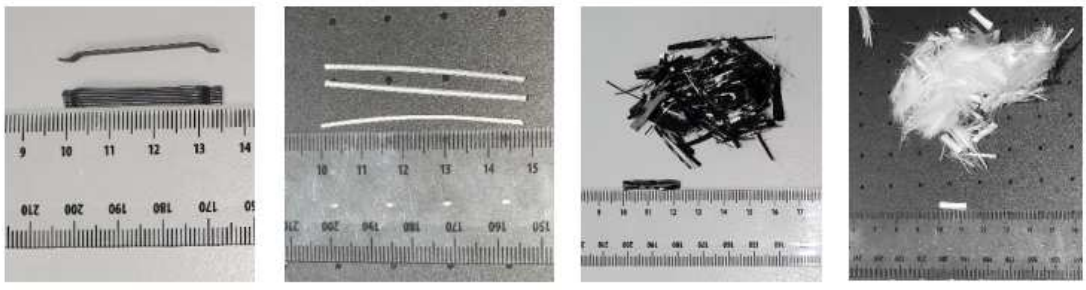

Figure 4-3. Images of adopted fibres: (a) hooked-end steel fibre; (b) synthetic fibres; (c) micro-carbon fibre; (d) micro-PVA fibres

Table 4-2. Mix proportion of GPC (kg/m^3)

Compositions	FA	GGBFS	Aggregates		NaOH Solution	Na_2SiO_3 solution
			Crushed stone	Sand		
Mixture 1	300	100	1100	630	69	172
Mixture 2	240	160	1100	630	69	172

Table 4-3. Characteristics of fibres

	Steel	Synthetic	PVA	Carbon
Length(mm)	35	48	12	24
Diameter(μm)	550	850	40	10
Density(g/cm^3)	7.8	0.9	1.3	1.78
Modulus (GPa)	210	12	66	230
Elongation at break (%)	-	-	5-6%	1.4%-1.6%
Tensile strength (MPa)	1345	640	1600	3400

4.2.3. Test set-up description

All the beams were simply supported and subjected to a symmetrical concentrated load at the midspan. The shear span (a) of all the beams was kept constant at 550 mm, giving the shear span-to-effective depth ratio (a/d) of 3.3. The applied load was controlled by a hydraulic jack with the load rate at approximately 1 mm/min until failure. Linear variable differential transformers (LVDTs) were placed at different positions of the beams to measure deflections as shown in Figures 4-1 and 4-4. Two electrical resistance strain gauges were attached to the bottom longitudinal bars with the symmetrical positions shown in Figure 4-1.

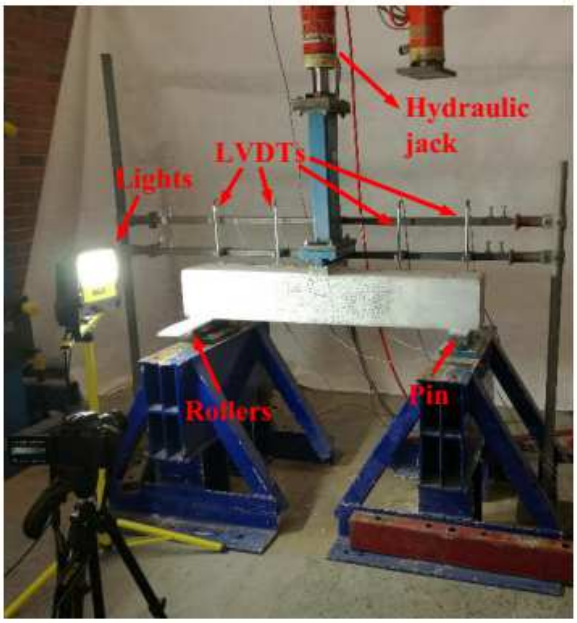

Figure 4-4. Test setup system

4. 3. Experimental results and discussion

The experimental results including the load-deflection response, crack pattern, shear capacity, and failure modes are presented and discussed in this section. Accordingly, the influence of different types of fibres on the shear behaviour of the beams is explained.

4.3.1. Crack pattern and failure modes

Firstly, the general cracking behaviour of the BFRP reinforced OPC and GPC beams was observed and described in Figure 4-5. As can be seen from the figure, the crack formation of all the beams initiated at the midspan. This flexural crack grew vertically due to the absence of shear stress. During the loading process, more flexural-shear cracks were formed within the shear span. Those flexural-shear cracks progressed in the inclined direction owing to the involvement of shear stress and propagated towards the load point. The critical diagonal cracks farthest from midspan led to a sudden failure of the beams. Such failure was defined as "diagonal tension failure" by ACI-ASCE Committee 426 [42].

In addition to the general behaviour, the primary differences in cracking patterns among the beams were also recorded. The plain OPC and GPC beams had the fewest number of flexural-shear cracks developing before failing by the first diagonal crack (as seen in Figure 4-5(a) and Figure 4-5(c)). Meanwhile, the beams reinforced with SF had developed more flexural-shear

cracks before failure (shown in Figure 4-5(b) and Figure 4-5(d)). This can be attributed to the presence of SF that helped transfer the tension stress across the shear cracks [43]. Hence, the stress can be redistributed to form multiple flexural-shear cracks. In addition, it is noticed that Beam GPC-0.5SF had the ability to develop additional inclined cracks after the formation of critical diagonal crack (as presented in Figure 4-5 (b)) while the OPC beams reinforced with the same volume fraction of fibre could not. This interesting phenomenon may stem from a better bonding of GPC composites and SF which leads to a better bridging action of fibres [44]. The better bridging effect provides slower propagation of the critical diagonal crack and thus achieve higher shear resistance owing to the aggregate interlock. Consequently, the SF reinforced GPC beams still retained the ability to redistribute the stresses to form multiple inclined cracks after the critical diagonal crack development. On the other hand, the poor performance of the cracking behaviour of GPC-0.5PF can be seen in Figure 4-5 (e). There were fewer flexural-shear cracks and no additional inclined crack recorded in this beam compared to Beam GPC-0.5SF. Such lesser effectiveness in controlling shear cracks is perhaps due to the low modulus of PF [45].

In terms of the beams with hybrid fibres, Beam GPC-0.3SF-0.2PVF exhibited the largest number of flexural and incline cracks as shown in Figure 4-5(f). This indicated the efficiency of hybrid fibre reinforcements of SF and PVF in the redistribution of stress due to the better fibre bridging effect [35]. By contrast, there was a fewer number of cracks recorded in Beams GPC-0.4PF-0.1CF and GPC-0.3PF-0.2CF (illustrated in Figure 4-5(g)). Therefore, it may infer that the deployment of hybrid reinforcement of PF and CF to control the shear cracks is ineffective.

Table 4-4 summarized the failure modes of all the beams. Most of the specimens failed by the diagonal tension failure with the exception of an additional feature observed in Beam OPC. At the low end of the critical diagonal crack in this beam, the crack propagation occurred horizontally along the bottom reinforcing bars and towards the support (shown in Figure 4-5 (a)). This led to a secondary splitting failure between the tension bars and concrete defined as “shear-tension” failure by ACI-ASCE Committee 426 [42]. Hence, the beam failed by a combination of diagonal-tension and shear-tension failure. This failure can be attributed to the high dowel action in reinforcing bars caused by an inadequate contribution of aggregate interlock of concrete [46].

As compared to the reference beams, the performance of diagonal tension failure in the fibre reinforced concrete beams was less brittle and sudden due to a gradual opening of the critical diagonal crack via the bridging action of fibres. At the critical cracks, the fibre pull-out mode was observed in the beams reinforced with SF (as shown in Figures 4-6 (a) and (b)) while fibre rupture was found in the PF reinforced concrete beams (as presented in Figure 4-6 (c)). This observation may imply a good bond strength of PF and GPC composites owing to the continuous embossing shape of the fibres.

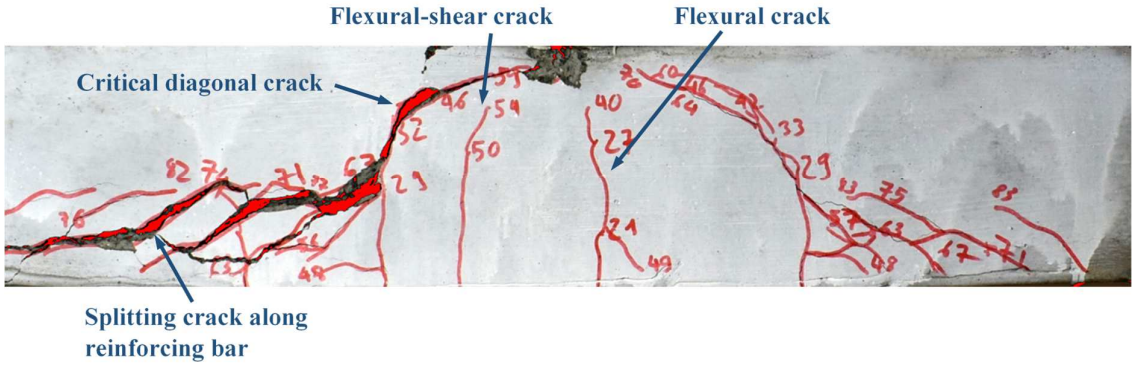

(a) OPC

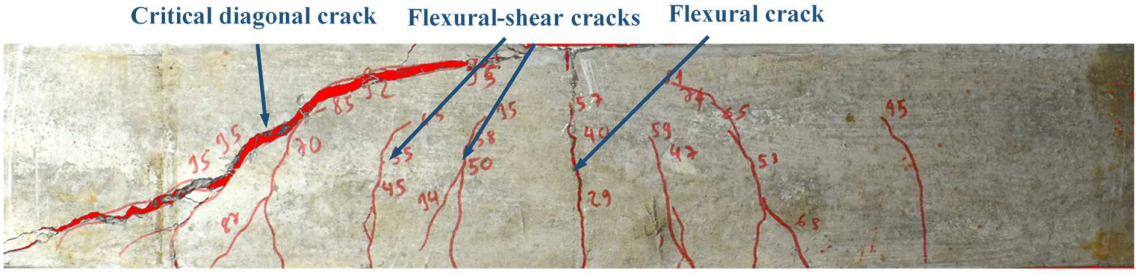

(b) OPC-0.5SF

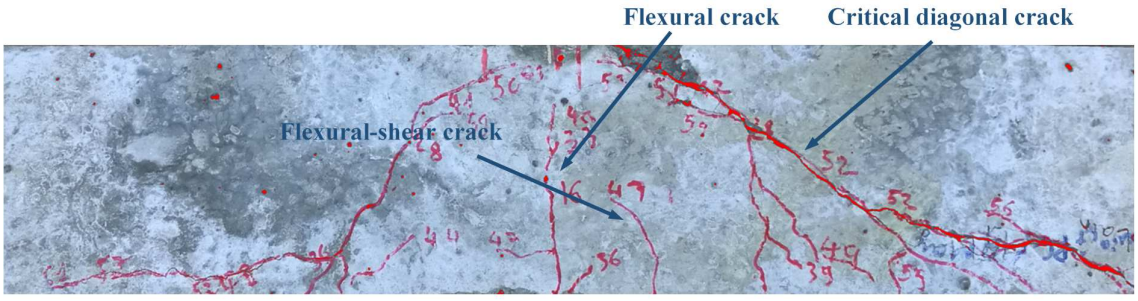

(c) GPC1

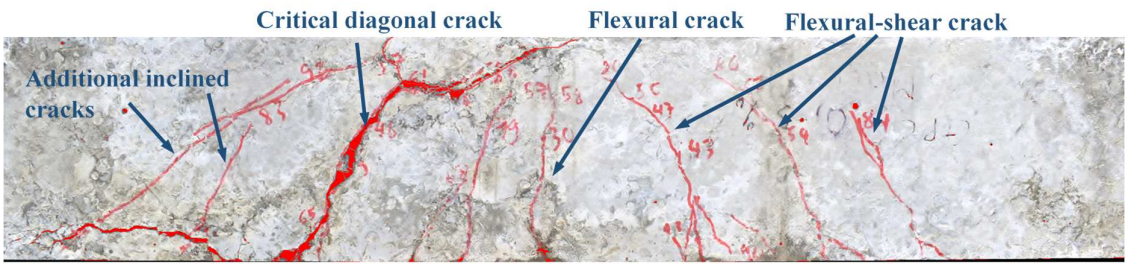

(d) GPC-0.5SF

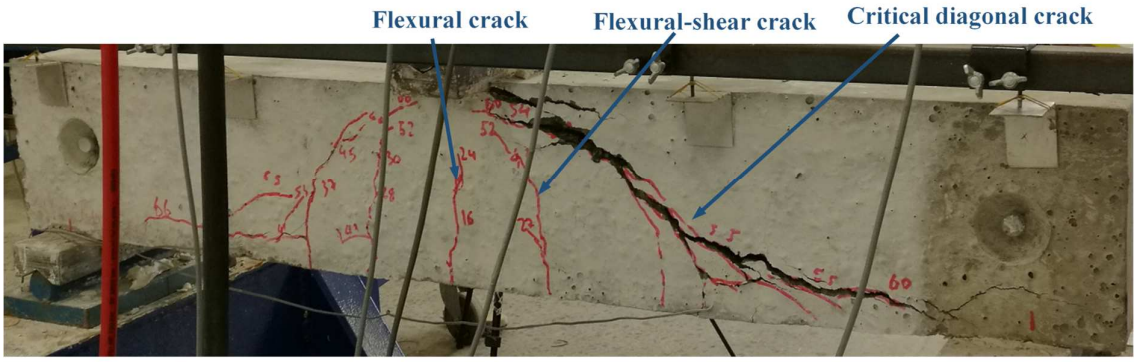

(e) GPC-0.5PF

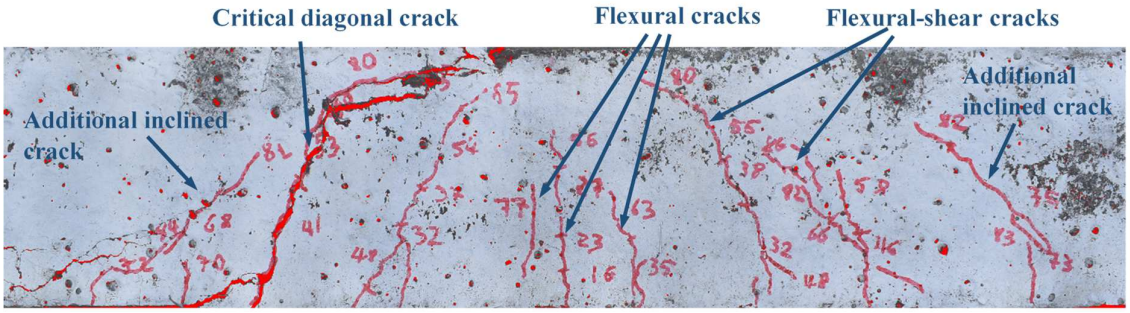

(f) GPC-0.3SF-0.2PVF

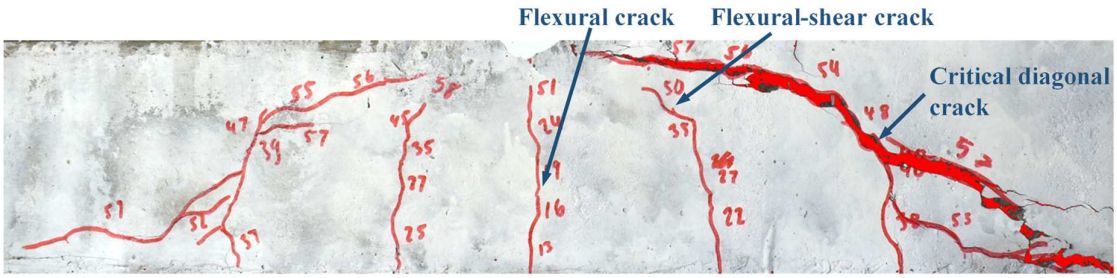

(g) GPC-0.3PF-0.2CF

Figure 4-5. Typical cracking pattern of tested beams

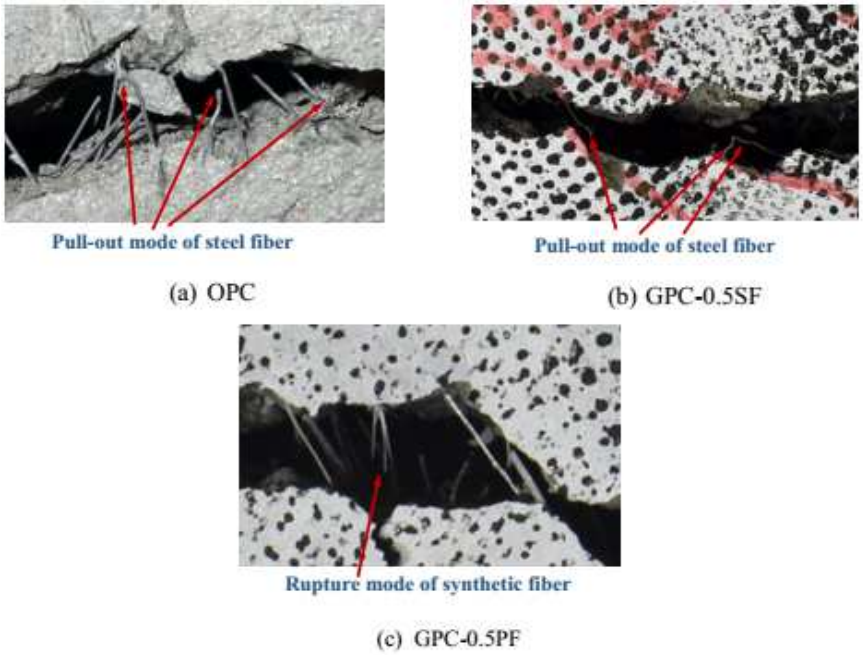

(a) OPC

(b) GPC-0.5SF

(c) GPC-0.5PF

Figure 4-6. Failure modes of fibres at the critical diagonal crack

Table 4-4. Summary of the experimental results

Beam	f_c' *(Mpa)*	V_u *(kN)*	$\frac{V_u}{bd\sqrt{f_c'}}$	δ_p *(mm)*	δ_u *(mm)*	μ	Failure mode
OPC	66.0	42	0.205	9.7	10.4	1.07	DT-ST
OPC-SF0.5	66.0	47.6	0.233	7.3	8.3	1.14	DT
GPC1	40.0	32.1	0.201	7.6	8.2	1.08	DT
GPC2	49.0	35.1	0.199	8.5	9.0	1.06	DT
GPC-SF0.25	34.8	31.7	0.213	5.5	6.0	1.09	DT
GPC-SF0.5	42.0	50.6	0.310	9.5	10.8	1.14	DT
GPC-SF1	51.0	53.5	0.297	8.2	9.4	1.15	DT
GPC-PF0.25	31.0	27.7	0.197	5.5	6.4	1.16	DT
GPC-PF0.5	36.0	40	0.265	9.4	10.1	1.07	DT
GPC-0.4SF-0.1PVF	31.7	37.3	0.213	6.1	6.9	1.13	DT
GPC-0.3SF-0.2PVF	33.7	43	0.213	7.5	8.8	1.17	DT

GPC-PF0.4-CF0.1	29.9	29.3	0.263	5.6	7.2	1.29	DT
GPC-PF0.3-CF0.2	28.7	28.7	0.294	5.4	8.3	1.54	DT

DT denotes diagonal tension while ST indicates shear tension

4.3.2. Load-deflection response and ductility

Figure 4-7 shows the applied load versus midspan deflection curves of all the tested beams. As can be seen from the figure, two distinct stages can be observed in the load-deflection response of the beams. The first stage of the curves was linear up to the existence of the initial flexural crack, which represents the uncracked behaviour of the beams. After the first crack occurred, the beam underwent the post-cracked behaviour. At this stage, the load-deflection curves behaved non-linear and exhibited a gradual reduction of stiffness until reaching the peak load.

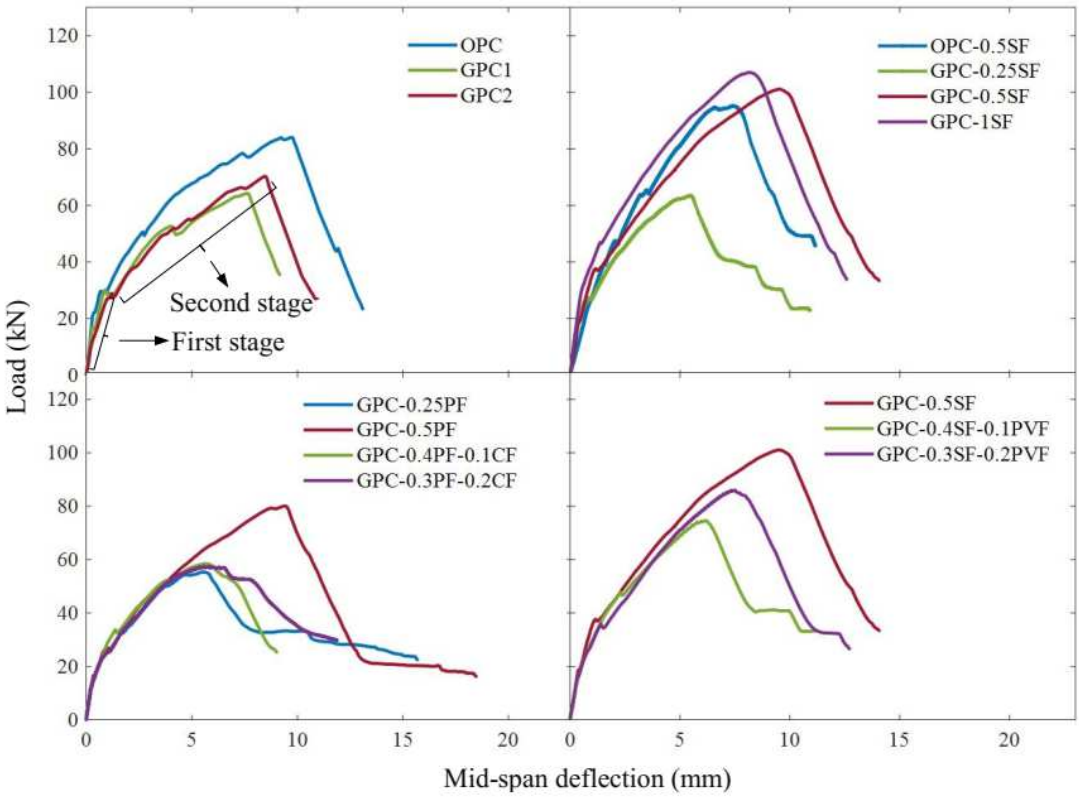

Figure 4-7. Load-deflection curves of the tested beams

In order to eliminate the variation of compressive strength, the measured shear forces were normalized as follows: $\frac{V}{\sqrt{f_c'}bd}$, where V= measured shear force (N), b = width of specimen

(mm), d = depth of specimen (mm), and f_c' = cylinder compressive strength of concrete (MPa). The normalized shear forces have been used in previous studies [35]. The normalized shear forces versus the deflection relationships of the beams are presented in Figure 4-8. Beams OPC and GPC1 exhibited a similar behaviour while Beam GPC2 yielded a significantly smaller initial stiffness and cracking resistance (Figure 4-8 (a)). This observation corroborates the same phenomenon reported in the previous study [1]. It is believed that the main reason is due to the high drying shrinkage (severe shrinkage cracking as shown in Figure 4-9) induced by the high slag content of Mixture 2. The uncracked stage of all the beams reinforced with fibres was identical to the plain one (Figure 4-8 (b)) due to a negligible contribution of fibres to an uncracked section [45]. However, the role of fibres became crucial at the post-cracked stage when their bridging action through macro-cracks was triggered. In particular, the SFRC beams and the ones reinforced with the combination of PF and CF exhibited a considerable enhancement of stiffness compared to the plain one. Moreover, the post-cracked stiffness of the beams increased with the volume fraction of steel fibres from 0.25% to 1%. The PFRC beams, by contrast, showed a marginal improvement in the post-cracked stiffness which may be attributed to the low elastic modulus of PF. Based on those observations, it can be deduced that the presence of high modulus fibres can improve the post-cracked stiffness of GPC beams reinforced with BFRP bars.

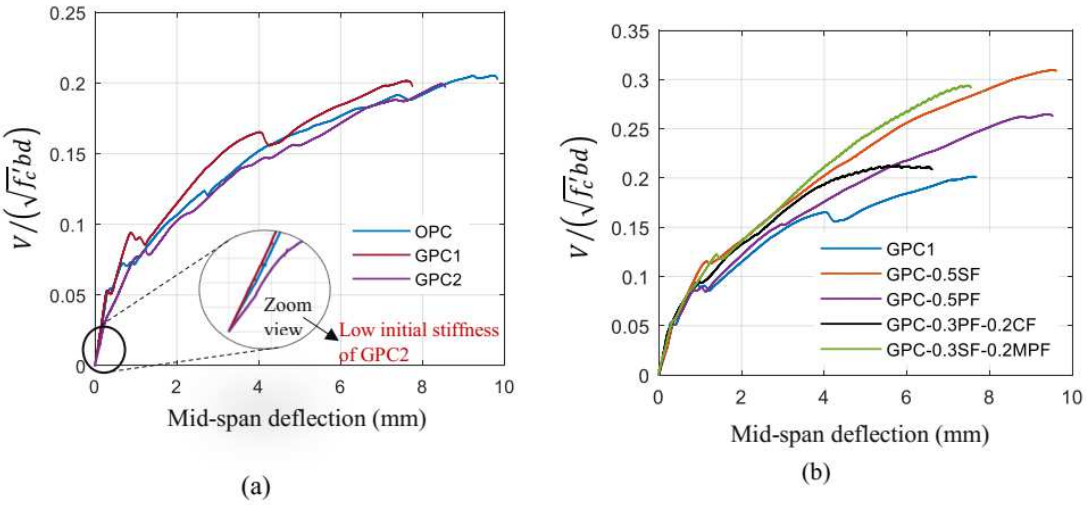

Figure 4-8. Normalized shear forces vs mid-span deflection

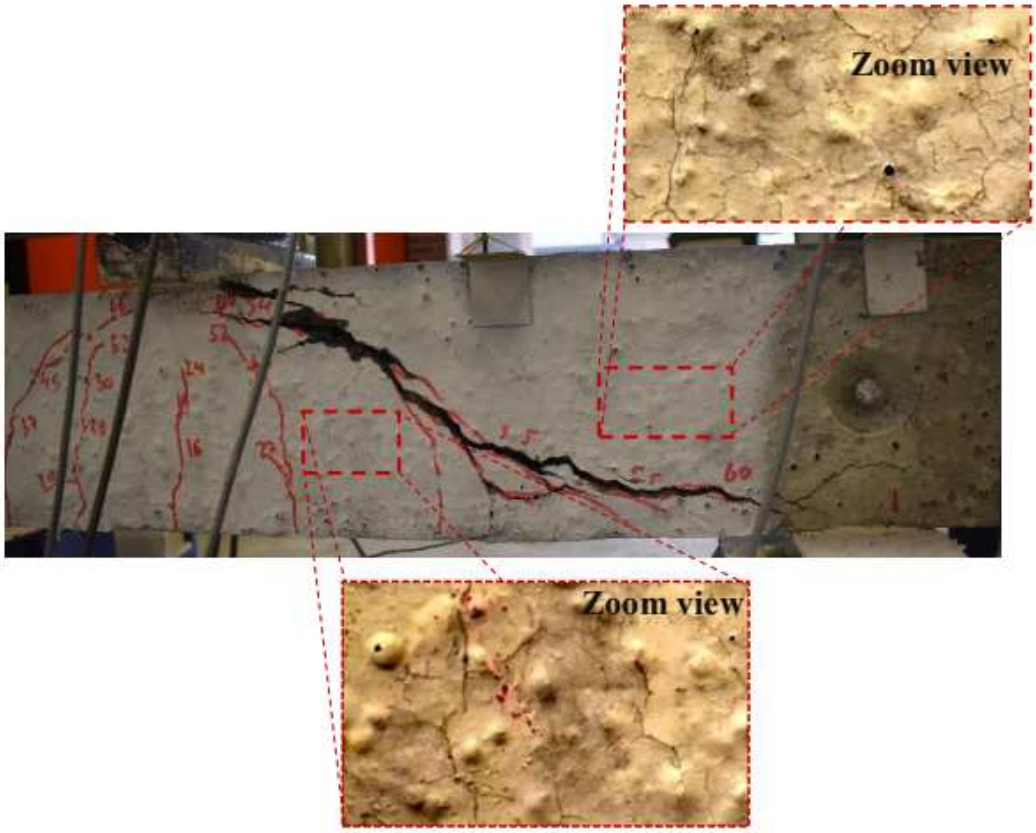

Figure 4-9. The shrinkage cracks of Beam GPC2

Since all the beams did not experience a clear yield load before failure, the ductility index μ of the beams was determined as the ratio of the ultimate deflection δ_u at the decreased load of 85% of peak load to the peak deflection δ_p at peak load instead of yield point [25]. As shown in Table 4-4, Beam GPC-PF0.3-CF0.2 demonstrated the highest ductility with an improvement up to 41% compared to the plain beam GPC1. Meanwhile, the fibre hybridization of SF and PVF showed a slight enhancement in ductility of the beams (8%) which was similar to the beams added with PF or SF. This marginal influence can be attributed to the insufficient content of fibres which is unable to shift the brittle diagonal-tension (DT) failure mode. Nevertheless, the exceptionally high fracture toughness of carbon fibre reinforced concrete [47] helped Beam-PF0.3-CF0.2 resist the crack growth and thus improved the ductility significantly.

4.3.3. Contribution of fibre on shear resistance

The effect of different types and volume fractions of fibre reinforcements on the normalized shear strength of the tested beams is presented in Figure 4-10. It can be noticed that an increase

of volume fraction up to 0.5% resulted in an increase in shear strength of the SF reinforced GPC beams. Particularly, the maximum increase in the shear strength by 56% was obtained at 0.5% SF. The efficiency of SF, however, was declined when a higher volume fraction was used, i.e. 1% of SF. This phenomenon corroborates a similar observation reported in the previous study [1] and indicated a smaller optimal volume fraction of SF (at 0.5-0.75%) for GPC compared to the corresponding value of conventional OPC at 2.5% [48]. This can be attributed to the low concrete slump and poor workability in the GPC mixture with a high content of GGBFS [36]. Furthermore, the fibre dispersion might be affected by high viscosity of sodium silicate solution and then lead to a reduction in the optimal volume fraction of fibres. Since there has been no study in literature investigating the effect of viscosity of sodium silicate on the workability and fibre distribution in the GPC mixture, it is suggested that further studies relating to those problems should be conducted.

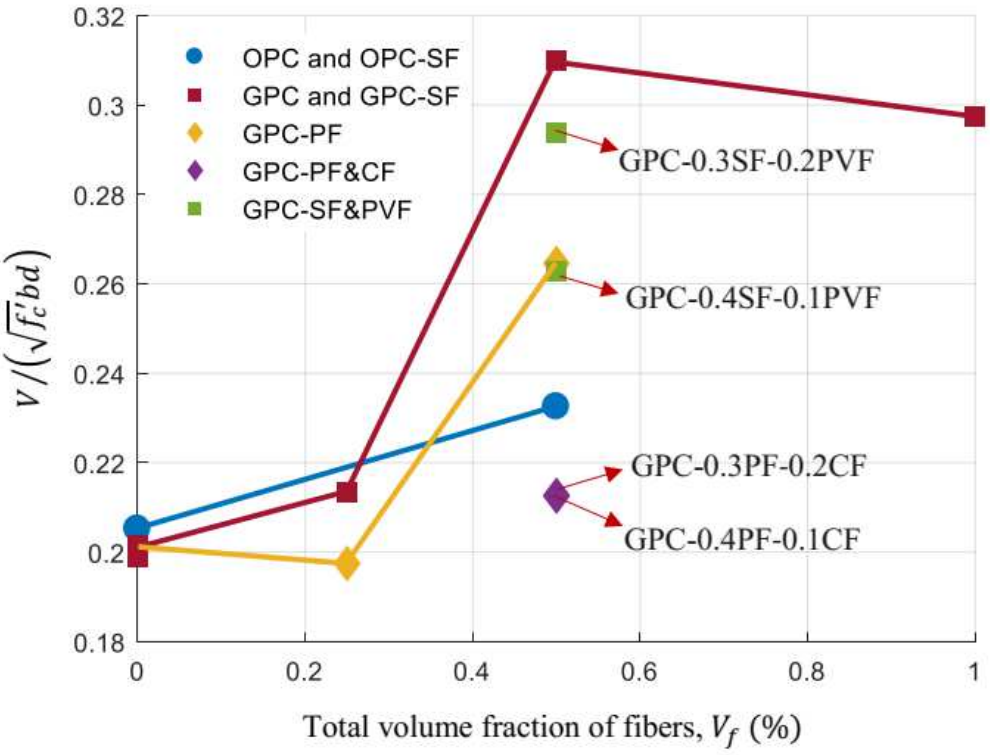

Figure 4-10. Effect of fibre on normalized shear strength of the beams

With the same volume fraction of SF, Beam OPC-0.5SF showed a less enhancement (increase by 14% compared to the plain OPC beam) in the shear strength than Beam GPC-0.5SF (increase by 56% compared to the plain GPC beam). This finding is attributed to the better interfacial bond strength of SF and geopolymer mortar [44, 49] leading to a better bridging

action at the diagonal crack. Meanwhile, PF is less efficient than SF due to its low elastic modulus and less effective number of fibres bridging the cracks. Since the size of PFs was bigger than SFs, with the same volume fraction, there were fewer PFs than SFs added to the beams. As a result, it is recommended that the volume fraction of PF should be higher than that of SF to obtain a similar outcome. In particular, the beam reinforced with 0.5% PF showed a significant increase in shear strength by 33% while the corresponding enhancement of GPC-0.5SF was 56%. In terms of fibre hybridization, the addition of CF did not improve the shear strength of the beams. As can be seen from Figure 4-10, Beams GPC-0.3PF-0.2CF and GPC-0.4PF-0.1CF exhibited a marginal increase by 7%. On the other hand, the hybrid reinforcement of SF and PVF showed a good fibre synergy. With a ratio of 0.3% SF and 0.2% PVF, the enhancement in the shear strength of Beam GPC-0.3SF-0.2PVF reached 47% which is about the same as Beam GPC-0.5SF.

In general, to obtain a good improvement in terms of shear strength with low fibre content, the addition of SF and PF and the hybrid fibre reinforcement of SF and PVF are suggested. In contrast, the combination of PF and CF is found ineffective to enhance the shear strength. The main reason is still questionable and requires further investigations.

4. 4. Prediction of shear strength of the beams reinforced with steel fibres and verification

In this section, the development of models to estimate the shear of FRC beams was conducted. Three models were proposed based on the current formulas for calculating the shear strength of SFRC beams using conventional steel bars [50-52]. Due to the low elastic modulus of FRP bars leading to a reduction of shear strength, some modifications to those current equations were carried out. Then the proposed models were verified with the test data from this study and literature.

4.4.1. Theoretical models for shear prediction of SFRC beams employing conventional longitudinal steel bars without stirrup

Numerous theoretical and experimental studies have been conducted to propose the model for shear strength of SFRC beams without stirrup since the 1980s [53]. One of the rational approaches was initially introduced by Mansur et al. [50] and then improved by Khuntia et al. [51]. The method was developed based on the equilibrium condition through a critical diagonal crack, as illustrated in Figure 4-11. Based on the figure, the ultimate shear strength of SFRC

beams is the sum of the shear contribution from concrete, V_c, and SF, V_{fs}, and expressed as the following equation [51]:

$$V_u = V_c + V_{fs} \tag{4-1}$$

The contribution of concrete to the shear resistance considering the aggregate interlock action (V_a), the resistance of compressed concrete (V_{cc}), and the dowel action of longitudinal bars (V_d) is estimated by the empirical equation of ACI building code [51]

$$V_c = \left(0.167\sqrt{f_c'} + 17\frac{\rho_s V d}{M}\right) bd \leq \left(0.29\sqrt{f_c'}\right) bd \tag{4-2}$$

where f_c' is the compressive strength of concrete (MPa), ρ_s is the longitudinal reinforcement ratio, $\frac{V}{M}$, is the ratio of external shear to moment at the critical section considered as the end of diagonal crack (shown in Figure 4-11), and b(mm) and d(mm) are the width and effective depth of beams, respectively. In the case of shear span ratio $\frac{a}{d} \geq 2$, Khuntia et al. [51] assumed that the angle of the critical diagonal crack would be taken as 45^0. Therefore, based on the location of the critical section, $\frac{V}{M}$ is equal to $\frac{1}{a-d}$ [50] and then Eq. (4-2) is rewritten as:

$$V_c = \left(0.167\sqrt{f_c'} + 17\rho_s \frac{d}{a-d}\right) bd \leq \left(0.29\sqrt{f_c'}\right) bd \tag{4-3}$$

The shear resistance of SF is contributed via the residual tensile stress, σ_p, acting through the diagonal tension crack. That stress may be assumed to be uniform along the crack, as shown in Figure 4-11. The effective shear depth, d_v, can be approximated as $0.9d$ (see Figure 4-11). By combining with the assumption of $\theta = 45^0$, the shear contribution from SF can be presented as:

$$V_{fs} = 0.9db\sigma_p \tag{4-4}$$

A simplified equation for determining the residual tensile stress, σ_p(MPa), in the case of pull-out mode is expressed as follows [54, 55]:

$$\sigma_p = 0.41\beta_{sh}\tau_b V_f \frac{l_f}{d_f} \tag{4-5}$$

where β_{sh} is the fibre shape factor or taken as 1 for hooked-end steel fibre, V_f is the volume fraction of fibre, l_f(mm) is the fibre length, d_f(mm) is the fibre diameter, and τ_b(MPa) is the interface bond strength between fibre and matrix. The interface bond strength between fibre and OPC, τ_b was suggested as $0.68\sqrt{f_c'}$ by Khuntia et al. [51]. This formula was adopted to calculate the shear strength of SFRC beams by a previous study [56] which achieved a good correlation between test data and prediction. Therefore, the interface bond strength $\tau_b = 0.68\sqrt{f_c'}$ is used for calculating the shear strength of the OPC beams. In terms of the GPC beams, the application of that formula may result in the considerable underestimate of residual tensile stress due to the superior bond strength of fibres and GPC matrix compared to that of OPC matrix [44, 49]. It is shown in Figure 4-12 that the equation proposed by Khuntia et al. [51] underestimates the interface bond strength of fibres and GPC matrix. Based on the experimental results of the previous pull-out tests [49], the fitting relationship of bond strength, τ_b, and $\sqrt{f_c'}$ can be taken as $1.21\sqrt{f_c'}$ in the case of GPC (see Figure 4-12).

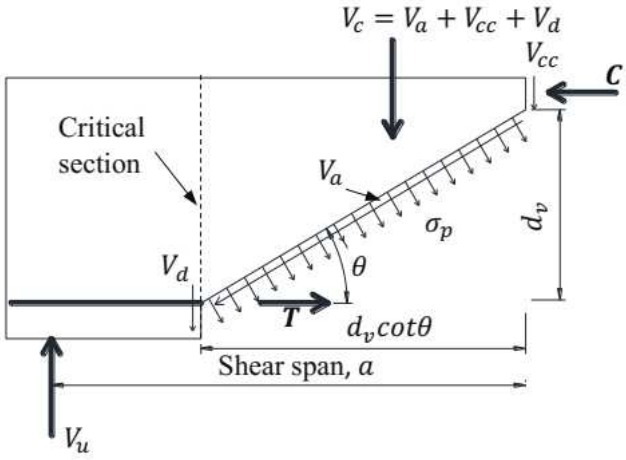

Figure 4-11. Visualization of the shear model for SFRC beams

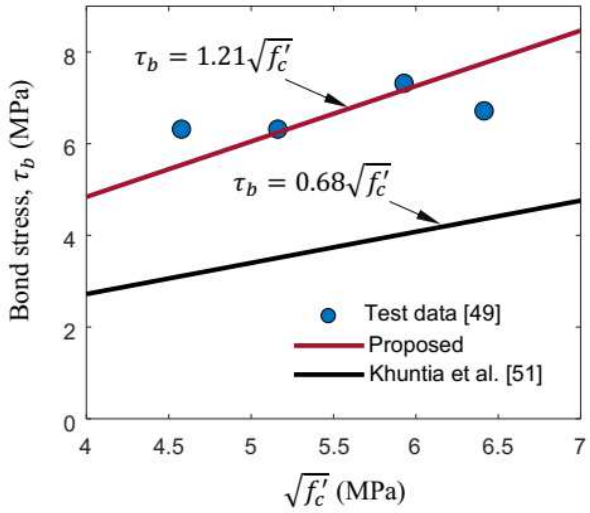

Figure 4-12. Relationship of bond strength τ_b and quantity $\sqrt{f_c'}$ for GPC

The aforementioned method based on the model of Khuntia et al. [51] is simple and convenient for calculating the shear strength of SFRC beams in practice. However, the comparison of the predicted values and test data of slender SFRC slender beams with shear span ratio $a/d \geq 2.5$ collected from the literature (Table 4-7 in the appendix) indicates an underestimation in the shear strength (see Figure 4-13 (a)). This can be attributed to a conservative assumption of 45^0 diagonal crack and empirical estimation of shear contribution from concrete from Eq. (4-3). Meanwhile, other studies proposed more accurate approaches such as the model based on plasticity theory [57], strain-based shear strength model [58], or modified compression field theory (MCFT) [59]. Currently, MCFT is one of the most comprehensive models to estimate the shear behavior of reinforced concrete elements and is adopted in CSA A23.3-04 (2004) design code [60]. Moreover, through applying MFCT some previous studies developed shear strength models considering the bridging effect of fibres at diagonal cracks [52, 56, 61] and achieved satisfactory results. In this chapter, a method based on MFCT suggested by Ding et al. [52] is simplified and used to predict the shear strength of the tested beams reinforced with SF. Based on MCFT [59], the shear resistance from concrete is calculated as follows:

$$V_c = \frac{0.4}{1 + 1500\varepsilon_x}\frac{1300}{1000 + s_{xe}}\sqrt{f_c'}bd_v \tag{4-6}$$

In Eq. (4-6), ε_x is the longitudinal strain at the mid-depth of the cross-section which is approximated by using Eq. (4-7) [62]:

$$\varepsilon_x = V_u \frac{\frac{M}{(Vd_v)} + 0.5\cot\theta}{2E_s A_s} \tag{4-7}$$

where θ is the orientation of diagonal crack (see Figure 4-11) computed based on Eq. (4-8), E_s(MPa) and A_s(mm^2) are elastic modulus and total cross-sectional area of longitudinal reinforcing bars, respectively, and the ratio of $\frac{M}{V}$ is the ratio of the external ultimate moment and shear force at the critical section as mentioned in Eq. (4-2):

$$\theta = (29^0 + 7000\varepsilon_x)\left(0.88 + \frac{s_{xe}}{2500}\right) \leq 75^0 \tag{4-8}$$

Based on the condition of moment equilibrium at the critical section, $\frac{M}{V}$ can be taken as $a - 0.9d\cot\theta$, and then the Eq. (4-7) is rewritten as follows:

$$\varepsilon_x = V_u \frac{a - 0.5d_v\cot\theta}{2E_s A_s d_v} \tag{4-9}$$

The cracking spacing parameter, s_{xe}, in Eqs. (4-6) and (4-8) is a function of the maximum aggregate size, a_g (mm), and computed by using Eq. (4-10) [23]:

$$s_{xe} = \frac{31.5d}{16 + a_g} \tag{4-10}$$

The shear contribution of fibre, V_{fs}, becomes a function of the orientation of diagonal crack, θ and determined as follows:

$$V_{fs} = d_v b \sigma_p \cot\theta \tag{4-11}$$

where the residual stress, σ_p, is computed by using Eq. (4-5). By combining Eqs. (4-11) and (4-6), the ultimate shear strength of SFRC beams is expressed as follows:

$$V_u = \left(\frac{0.4}{1 + 1500\varepsilon_x}\frac{1300}{1000 + s_{xe}}\sqrt{f_c'} + \sigma_p\cot\theta\right) b d_v \tag{4-12}$$

To solve Eq. (4-12), a Newton-Raphson iterative algorithm developed in Matlab programming language is adopted [63]. As can be seen from Figure 4-13 (b), the proposed model based on MCFT [64] shows a good correlation with the mean ratio of experimental values, V_u^{exp} and

estimation, V_u^{est} at 1.02 and standard deviation at 0.23. This indicates that MCFT is suitable for predicting the shear strength of conventional SFRC beams.

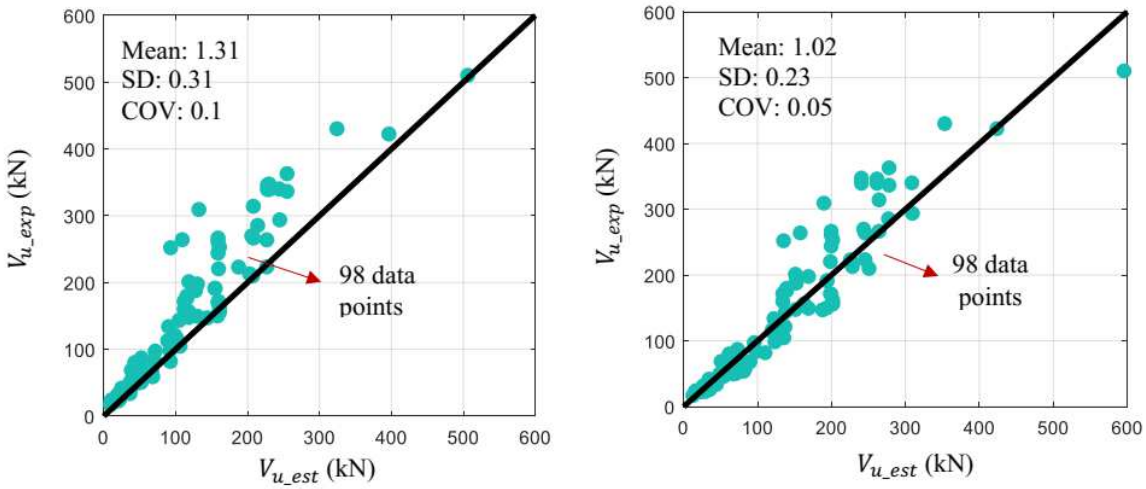

(a) Based on Khuntia et al. [51] (b) Based on MCFT [64]

Figure 4-13. Verification of shear strength prediction of SFRC beams

This section summarizes the theories for estimating the shear strength of SFRC and then based on those studies two models were proposed. The first model demonstrates a simple procedure and convenient for design but yields conservative estimations. The second model based on MCFT is more complicated but provides accurate predictions. However, the direct application of those models for the beams employing longitudinal FRP bars is questionable owing to the distinguished characteristics of the reinforcements. In particular, the beams using FRP bars exhibit lower shear stress at shear failure caused by the larger longitudinal strains compared to the conventional ones [23]. Therefore, the modifications for those models are necessary and are conducted in the next section for predicting the shear strength of tested beams using longitudinal BFRP bars.

4.4.2. Modified models for shear prediction of SFRC beams employing BFRP bars without stirrup

In this section, three modified models for estimating the shear capacity of the SFRC beams using BFRP bars for longitudinal reinforcement are proposed. The equations of three models for estimating the shear capacity of the tested beams are summarized in Table 4-5. In Models 1 and 2, the aforementioned method to determine the shear contribution of SF, V_f, by using

Eqs. (4-4) and (4-5) is adopted while the shear resistance of concrete is computed based on existing models of the concrete beams reinforced with FRP bars. By adopting ACI 440.1R-06 [6], the concrete shear capacity of Model 1 is calculated by using Eqs. (4-1.1)- (4-1.3) (see Table 4-5). The equation proposed by El-Sayed et al. [21] is employed in Model 2 to estimate shear resistance of concrete and presented in Eq. (4-2.1) (see Table 4-5). In that model, the depth reduction factor of equivalent rectangular stress block, β_1, for GPC is determined by using Eq. (4-2.3) proposed in a previous study [12]. Model 3 is developed based on MCFT following the same procedures for SFRC beams presented in the previous section. Due to the high strain effect of longitudinal FRP bars, instead of using Eq. (4-6) for calculating the concrete shear resistance, Houlet et al. [22] proposed an equation (Eq. (4-13)) for better shear strength prediction of the concrete beams reinforced with FRP bars. By combining Eqs. (4-13) and (4-11), the equation of ultimate shear strength, V_u, of longitudinal FRP bars reinforced concrete beams is derived and presented at Eq. (4-3.1) in Table 4-5. To verify the proposed models, the comparison between the estimated values and experimental results was conducted in the next section

$$V_c = \frac{0.3}{0.5 + (1000\varepsilon_x + 0.15)^{0.7}} \frac{1300}{1000 + s_{xe}} \sqrt{f_c'} bd \tag{13}$$

Table 4-5. Summary of proposed models for SFRC beam using longitudinal BFRP bars

Model	Equations for shear capacity models	
1	$V_c = \frac{2}{5}\sqrt{f_c'}bc$ [65]	(4-1.1)
	$c = kd$	(4-1.2)
	$k = \sqrt{2\rho_f n_f + \left(\rho_f n_f\right)^2} - \rho_f n_f$ where ρ_f is FRP reinforcement ratio and n_f is the modulus ratio $\frac{E_f}{E_c}$	(4-1.3)
	$E_c = 4700\sqrt{f_c'}$ in the case of OPC [66]	(4-1.4)
	$E_c = 3510\sqrt{f_c'}$ in the case of GPC [5]	(4-1.5)
	$V_f = 0.9db\sigma_p$	(4-1.6)
	$\sigma_p = 0.41\beta_{sh}\tau_b V_f \frac{l_f}{d_f}$	(4-1.7)
	$\tau_b = 0.68\sqrt{f_c'}$ in the case of OPC	(4-1.8)
	$\tau_b = 1.21\sqrt{f_c'}$ in the case of GPC	(4-1.9)

	$V_u = V_c + V_{fs}$	(4-1.10)
2	$V_c = \left(\frac{\rho_f E_f}{90\beta}\right)^3 \left(\frac{\sqrt{f_c'}bd}{6}\right)$	(4-2.1)
	where β depth reduction factor of equivalent rectangular stress block [21]	
	$\beta = 0.85 - 0.05\frac{f_c' - 28}{7} \geq 0.65$ in the case of OPC [66]	(4-2.2)
	$\beta = -0.00254 f_c' + 0.8675 \geq 0.7$ in the case of GPC [12]	(4-2.3)
	$V_u = V_c + V_{fs}$ where V_{fs} is computed similarly as Eqs. (4-1.4)-(4-1.7)	(4-2.4)
3	$V_u = \left(\frac{0.3}{0.5 + (1000\varepsilon_x + 0.15)^{0.7}} \frac{1300}{1000 + s_{xe}} \sqrt{f_c'} + \sigma_p \cot\theta\right) b d_v$	(4-3.1)
	where σ_p is determined by using Eqs. (4-1.5)-(4-1.7)	
	$\theta = (29^0 + 7000\varepsilon_x)\left(0.88 + \frac{s_{xe}}{2500}\right) \leq 75^0$	(4-3.2)
	$s_{xe} = \frac{31.5d}{16 + a_g}$	(4-3.3)
	$\varepsilon_x = V_u \frac{a - 0.5 d_v \cot\theta}{2 E_f A_f d_v}$	(4-3.4)

4.4.3. Verification of predicted and experimental results

The comparison of the estimated values and experimental results is summarized in Table 4-6 and visualized in Figure 4-14. In the table, V_u^1, V_u^2, and V_u^3 refer to the predicted shear capacity determined by Model 1, 2, and 3, respectively, while V_u^{exp} refers to the ultimate shear force obtained from the tests. As can be seen from Table 4-6, Model 1 exhibits the most considerable underestimation with the mean ratio of experimental to predicted values equal to 1.75. This can be attributed that Eq. (4-1.1) recommended by ACI 440.1R-06 [65], which provides a highly conservative estimation for concrete shear resistance. It can be noticed from Figure 4-14 that in the case of the plain beams, the estimated values by using that equation can be approximately 3 times lower than the tested results. Model 2 gives a more reasonable but rather conservative prediction with the mean ratio of experimental to predicted values at 1.5. When there are the presence and contribution of SF, the influence of concrete shear resistance on the ultimate shear capacity of the beam is likely to be less dominant. Hence, those models seem to provide better predictions with a high volume fraction of SF. Model 3 demonstrates the best correlation with the mean ratio of V_u^{exp}/V_u^{est} at 1.14 and the standard deviation of 0.17. This indicates the

proposed MCFT is appropriate to be used for calculating the shear strength of the steel fibre reinforced OPC and GPC beams employing the longitudinal BFRP bars. Nevertheless, the model shows an underestimation of shear capacity in the case of the plain beams such as Beam OPC, GPC1, and GPC2. The main reason may be due to the conservative calculation of longitudinal strain at the mid-depth of the cross-section. It is noted that the estimated values, ε_x^3 of Beams OPC, GPC1 and GPC2 are lower than the values obtained from strain gauges attached to the longitudinal bars. Therefore, it is suggested that there should be more studies investigating this phenomenon. In the case of Beam GPC-1SF, all three models exhibit an overestimation of shear strength. This is perhaps because of the overestimation of residual tensile stress, σ_p, by using Eq. (4-5). The equation was derived for OPC reinforced with the volume fraction of steel fibre varying from 0 to an optimal value at 2.5%. This range of volume fraction, however, may be unsuitable to be applied for GPC as mentioned previously in Section 4.3.3. As a result, the equation is suggested to be applied for GPC reinforced with a volume fraction of fibre less than 1%.

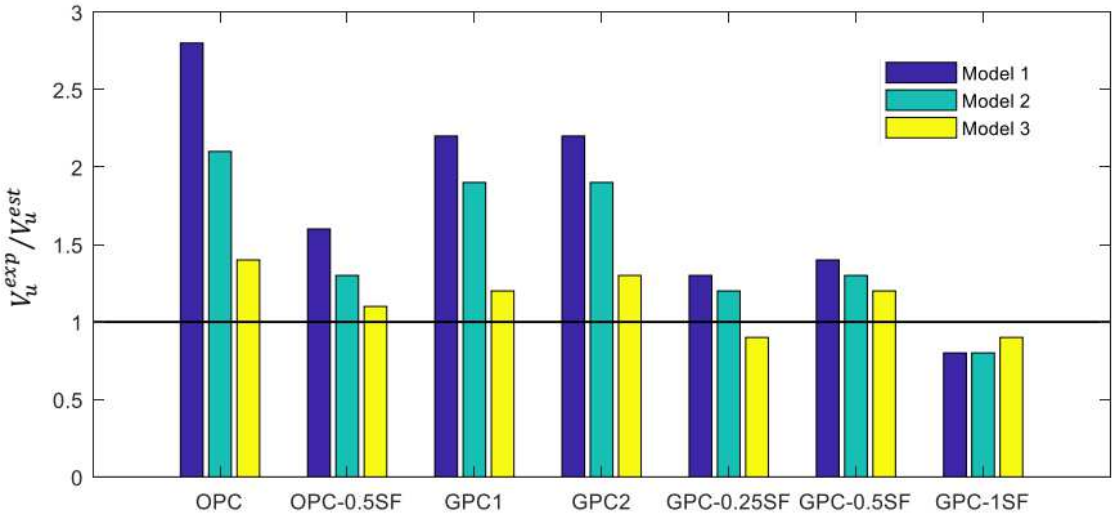

Figure 4-14. Correlation of experimental to estimated values

Table 4-6. Experimental results versus estimated values

Beam	V_u^{exp} (kN)	ε_x^{exp}	ε_x^3	V_u^1 (kN)	V_u^2 (kN)	V_u^3 (kN)	$\frac{V_u^{exp}}{V_u^1}$	$\frac{V_u^{exp}}{V_u^2}$	$\frac{V_u^{exp}}{V_u^3}$
OPC	42.0	0.0027	0.0020	15.0	19.8	30.7	2.79	2.12	1.37
OPC-0.5SF	47.6	0.0035	0.0028	30.6	35.4	42.5	1.56	1.34	1.12

GPC1	32.1	0.0024	0.0017	14.9	17.3	26.1	2.16	1.86	1.23
GPC2	35.1	0.0022	0.0018	15.7	18.1	27.9	2.23	1.94	1.26
GPC-0.25SF	31.7	0.0021	0.0022	24.3	26.9	33.8	1.30	1.18	0.94
GPC-0.5SF	50.6	0.0029	0.0029	37.2	39.6	43.7	1.36	1.28	1.16
GPC-1SF	53.5	0.0035	0.0041	64.6	66.9	58.5	0.83	0.80	0.91
Mean							1.75	1.50	1.14
STD							0.67	0.48	0.17
COV							0.45	0.23	0.03

4. 5. Conclusion

The shear response of the fibres reinforced OPC and GPC employing longitudinal BFRP bars is investigated. Based on the experimental and analytical results, the following conclusion can be drawn:

- The general shear behavior of the plain OPC and GPC beams is similar. Beam GPC2 shows a lower initial stiffness due to severe drying shrinkage cracks caused by the presence of high slag content.
- The addition of the SF not only increases the shear capacity of the OPC and GPC beams but also enhances the cracking resistance and post-cracked stiffness. The better performance was observed in the SF reinforced GPC beams compared to the OPC counterparts due to a better bonding behavior of SF and GPC matrix. In particular, the normalized shear capacity of Beam GPC-0.5SF increased by 56% in comparison to the increment of OPC-0.5SF by 14%. However, the optimal volume fraction of SF for GPC seems to be lower than the conventional values of OPC. In this chapter, the addition of 1% SF indicated a less improvement in normalized shear strength as compared to GPC-0.5SF. Therefore, the effective volume fraction of SF less than 1% is recommended for improving the shear behavior of GPC beams.
- Despite less efficiency than SF, the addition of PF exhibited considerable improvement in the shear capacity of GPC beams. For example, the normalized shear strength of Beam GPC-0.5PF increased significantly by 33% as compared to the plain GPC beams. It is suggested that a higher volume fraction of PF should be adopted to achieve the desired enhancement equivalent to those obtained from SF.

- The fibre hybridization of SF and PVF demonstrates a good synergy with the ratio of 0.3SF and 0.2PVF. Take the Beam GPC-0.3SF-0.2PVF as an example, its normalized shear strength increased by 47% which is nearly the same improvement observed in Beam GPC-0.5SF.
- The hybrid fibre reinforcement of PF and CF is efficient to improve the ductility of the beams but inefficient to enhance the shear capacity.
- Three proposed model demonstrates the different level of accuracy when comparing with the experimental results. Model 1 employing the equations from ACI 440.1R-06 significantly underestimates the shear capacity of the tested beam, the results calculated by using Model 2 are also conservative but acceptable. On the other hand, Model 3 based on MCFT obtains a good agreement with the test data which indicates that MCFT can be applied for calculating shear strength of SFRC members using longitudinal FRP bars without stirrups. Finally, it is suggested that in the case of GPC, the models are suitable to be adopted with the fibre volume fraction up to 1%. With a higher content of fibre, the three models seem to overestimate the shear capacity of the GPC beams due to an overestimation of residual tensile stress by using Eq. (4-5) for GPC.

Based on these findings, it can be suggested that the addition of different kinds of fibres can be a feasible method to improve the shear performance of the concrete beams employing the longitudinal FRP bars. The combination of PF, GPC, and BFRP bars can be a viable solution to develop sustainable and durable structures. Nonetheless, further studies are needed to investigate this aspect. Moreover, more experimental works should be conducted to verify the proposed models presented in this chapter.

Notation

A_f = cross-sectional area of bottom longitudinal reinforcing FRP bars (mm^2)

A_s = cross-sectional area of bottom longitudinal reinforcing conventional steel bars (mm^2)

a = shear span of the beam (mm)

a_g = maximum aggregate size (mm)

b = breadth of rectangular section of beam (mm)

d = effective depth of concrete section (mm)

d_v = shear effective depth of concrete section (mm)

d_f = fibre diameter (mm)

E_c = elastic modulus of concrete (MPa)

E_f = elastic modulus of FRP bars (MPa)

E_s = elastic modulus of steel bars (MPa)

f_c' = concrete cylinder compressive strength (MPa)

M = external moment at a critical section (N.m or kN.m)

n_f = the modular ratio of FRP and concrete

s_{xe} = cracking spacing parameters

V_a = shear contribution of aggregate interlock

V_c = shear resistance of concrete (N or kN)

V_{cc} = shear resistance of compressed concrete

V_d = shear contribution of dowel action

V_{fs} = shear contribution from fibres (N or kN)

V_u = ultimate shear force of the beams (N or kN)

V_u^{exp} = measured shear force of the tested beams (N or kN)

V_u^{est} = predicted shear force (N or kN)

V_u^1 = predicted shear force by using model 1 (N or kN)

V_u^2 = predicted shear force by using model 2 (N or kN)

V_u^3 = predicted shear force by using model 3 (N or kN)

V_f = volume fraction of fibre

β_{sh} = the fibre shape factor

β = depth reduction factor of equivalent rectangular stress block

δ_p = deflection at peak load (mm)

δ_u = ultimate deflection at 85% of peak load (mm)

ε_x = longitudinal strain at the mid-depth of a critical section

θ = orientation of inclined cracks

μ = ductility index

ρ_s = steel reinforcement ratio

ρ_f = FRP reinforcement ratio

σ_p = residual tensile stress (MPa)

τ_b = bond strength of a single fibre embedded in concrete (MPa)

Appendix

Table 4-7. Database of slender SFRC beams

Ref	Fibre type	b (mm)	d (mm)	$\frac{a}{d}$	ρ_s (%)	f_{xy} (MPa)	V_f (%)	l_f (mm)	d_f (mm)	f_c' (Mpa)	a_g (mm)	V_u^{exp} (kN)
Mansur et al. [50]	hooked - end	150	197	2.8	1.34	462	0.50	30	0.5	29.1	20	52.60
		150	197	3.6	1.34	462	0.50	30	0.5	29.1	20	44.92
		150	197	2.8	1.34	462	0.75	30	0.5	29.9	20	59.99
		150	197	2.8	2.00	462	0.75	30	0.5	29.9	20	65.01
		150	197	2.8	1.34	462	0.75	30	0.5	20.6	20	45.21
		150	197	2.8	2.00	462	0.75	30	0.5	20.6	20	59.99
		150	197	2.8	1.34	462	0.75	30	0.5	33.4	20	75.06
		150	197	2.8	2.00	462	0.75	30	0.5	33.4	20	85.99
Narayanan and Darwish [67]	hooked-end	85	130	2.5	2.00	530	0.25	30	0.3	52.5	20	29.50
		85	130	3.0	2.00	530	0.25	30	0.3	52.5	20	30.61
		85	130	2.5	2.00	530	0.25	30	0.3	33.9	20	22.87
		85	130	3.0	2.00	530	0.25	30	0.3	33.9	20	21.44
		85	130	3.0	2.00	530	0.50	30	0.3	52.5	20	35.69
		85	130	3.0	2.00	530	1.00	30	0.3	60.8	20	40.44
		85	130	3.0	2.00	530	0.50	30	0.3	36.0	20	21.77
		85	130	3.0	2.00	530	1.00	30	0.3	35.2	20	32.82
		85	130	2.5	2.00	530	0.50	30	0.3	52.5	20	40.77
		85	130	3.5	2.00	530	0.50	30	0.3	47.4	20	28.84

Table 4-7. Database of slender SFRC beams (continued)

Ref	Fibre type	b (mm)	d (mm)	$\frac{a}{d}$	ρ_s (%)	f_{xy} (MPa)	V_f (%)	l_f (mm)	d_f (mm)	f_c' (Mpa)	a_g (mm)	V_u^{exp} (kN)
Narayanan and Darwish [67]	hooked-end	85	130	2.5	2.00	530	1.00	30	0.3	57.1	20	48.84
		85	130	3.5	2.00	530	1.00	30	0.3	61.1	20	32.82
		85	128	3.0	3.69	530	0.50	30	0.3	47.4	20	32.20
		85	126	3.1	5.72	530	0.50	30	0.3	47.4	20	38.02
		85	128	3.0	3.69	530	0.50	30	0.3	36.0	20	24.37
		85	126	3.1	5.72	530	0.50	30	0.3	36.0	20	24.95
		85	128	3.0	3.69	530	1.00	30	0.3	61.1	20	47.55
		85	126	3.1	5.72	530	1.00	30	0.3	61.1	20	53.55
		85	126	3.1	5.72	530	1.50	30	0.3	57.0	20	51.94
		85	126	3.1	5.72	530	2.00	30	0.3	47.5	20	52.80
		85	128	3.0	3.69	530	1.50	30	0.3	57.0	20	48.52
Lim et al. [68]	hooked-end	152	221	2.5	1.20	445	0.50	30	0.5	34.0	10	58.11
		152	221	2.5	2.40	445	1.00	30	0.5	34.0	10	82.64
		152	221	3.5	2.40	445	1.00	30	0.5	34.0	10	67.18
		152	221	2.5	2.40	445	0.50	30	0.5	34.0	10	63.82
		152	221	3.5	2.40	445	0.50	30	0.5	34.0	10	49.38
Ashour et al. [69]	hooked-end	125	204	4.0	2.84	460	0.50	60	0.8	95.4	10	57.89
		125	204	4.0	2.84	460	1.00	60	0.8	97.5	10	80.84
		125	201	4.0	4.58	470	1.00	60	0.8	93.8	10	97.49

Table 4-7. Database of slender SFRC beams (continued)

Ref	Fibre type	b (mm)	d (mm)	$\frac{a}{d}$	ρ_s (%)	f_{xy} (MPa)	V_f (%)	l_f (mm)	d_f (mm)	f_c' (Mpa)	a_g (mm)	V_u^{exp} (kN)
Li et al. [70]	hooked-end	127	204	3.0	2.20	450	1.00	30	0.5	22.7	10	79.02
		64	102	3.0	2.20	450	1.00	30	0.5	22.7	10	20.63
		64	102	3.0	1.10	450	1.00	30	0.5	22.7	10	15.86
		127	204	3.0	2.20	450	1.00	30	0.5	26.0	10	79.02
		64	102	3.0	2.20	450	1.00	30	0.5	26.0	10	23.17
Imam et al. [71]	hooked-end	200	300	2.5	1.87	550	0.75	60	0.8	110.0	10	268.80
		200	300	2.5	3.08	550	0.75	60	0.8	110.0	10	284.40
		200	300	3.5	3.08	550	0.75	60	0.8	111.5	10	208.80
		200	300	4.5	3.08	550	0.75	60	0.8	110.8	10	211.80
Kwak et al. [72]	hooked-end	125	212	3.0	1.52	442	0.50	50	0.8	30.8	19	67.58
Cucchiara et al. [73]	hooked-end	150	219	2.8	1.90	610	1.00	30	0.5	40.9	10	96.25
		150	219	2.8	1.90	610	2.00	30	0.5	43.2	10	103.48
Noghabai [74]	hooked-end	200	180	3.3	4.50	500	0.50	60	0.7	68.9	16	251.01
		200	180	3.3	4.50	500	0.75	60	0.7	68.9	16	262.96
		200	235	2.8	4.30	500	1.00	30	0.6	68.9	16	308.20
		200	410	2.9	3.00	590	0.50	60	0.7	68.9	16	265.45
		200	410	2.9	3.00	590	0.50	60	0.7	68.9	16	313.10
		200	410	2.9	3.00	590	0.75	60	0.7	68.4	16	339.09
		200	410	2.9	3.00	590	0.75	60	0.7	68.9	16	292.68

Table 4-7. Database of slender SFRC beams (continued)

Ref	Fibre type	b (mm)	d (mm)	$\frac{a}{d}$	ρ_s (%)	f_{xy} (MPa)	V_f (%)	l_f (mm)	d_f (mm)	f_c' (Mpa)	a_g (mm)	V_u^{exp} (kN)
Noghabai [74]	hooked-end	300	570	3.0	2.90	590	0.75	60	0.7	68.4	16	509.13
Based on database of Dinh Hai et al. [43]	hooked-end	200	260	3.5	3.60	500	0.51	60	0.9	43.7	10	120.31
		200	260	3.5	3.60	500	0.76	60	0.9	48.3	10	155.40
		200	262	2.5	1.20	500	0.76	60	0.9	38.7	10	107.57
		200	260	2.5	1.80	500	0.76	60	0.9	38.7	10	142.33
		200	260	4.0	1.80	500	0.76	60	0.9	40.3	10	115.54
		200	260	3.5	2.80	500	0.50	60	0.9	37.7	10	111.75
		200	410	3.3	3.10	500	0.50	60	0.9	37.7	10	146.01
		200	460	3.4	2.80	500	0.50	60	0.9	37.7	10	169.46
		200	460	3.4	2.80	500	0.50	60	0.9	37.7	10	265.50
		200	460	3.4	2.80	500	0.50	60	0.9	37.7	10	259.85
		200	460	3.4	2.80	500	0.50	60	0.9	37.7	10	242.90
		200	260	3.5	2.80	500	0.50	60	0.9	38.8	10	132.80
		200	460	3.4	2.40	500	0.50	60	0.9	38.8	10	149.00
		200	540	3.5	2.70	500	0.50	60	0.9	38.8	10	222.00
		200	460	3.4	2.80	500	0.50	60	0.9	38.8	10	154.73
		200	460	3.4	2.80	500	0.50	60	0.9	38.8	10	160.46
		200	460	3.4	2.80	500	0.50	60	0.9	38.8	10	252.15
Dinh Hai et al. [43]	hooked-end	152	381	3.4	2.00	410	0.75	30	0.6	44.8	14	170.55

Table 4-7. Database of slender SFRC beams (continued)

Ref	Fibre type	b (mm)	d (mm)	$\frac{a}{d}$	ρ_s (%)	f_{xy} (MPa)	V_f (%)	l_f (mm)	d_f (mm)	f_c' (Mpa)	a_g (mm)	V_u^{exp} (kN)
Dinh Hai et al. [43]	hooked-end	152	381	3.4	2.00	410	0.75	30	0.6	44.8	14	158.92
		152	381	3.5	2.00	410	1.00	30	0.6	38.1	10	175.16
		152	381	3.5	2.00	410	1.00	30	0.6	38.1	10	178.73
		152	381	3.5	2.70	410	1.00	30	0.6	38.1	10	200.18
		152	381	3.5	2.70	410	1.00	30	0.6	38.1	10	146.56
		152	381	3.4	2.70	410	1.50	30	0.6	31.0	10	148.32
		152	381	3.4	2.70	410	1.50	30	0.6	31.0	10	196.69
		152	381	3.4	2.70	410	1.50	30	0.6	44.9	10	190.15
		152	381	3.4	2.70	410	1.50	30	0.6	44.9	10	190.15
		152	381	3.4	2.70	410	1.00	60	0.8	49.2	10	170.61
		152	381	3.4	2.70	410	1.00	60	0.8	49.2	10	219.35
		152	381	3.4	2.00	410	0.75	30	0.4	43.3	10	190.54
		152	381	3.4	2.00	410	0.75	30	0.4	43.3	10	186.73
		203	610	3.5	2.10	410	0.75	30	0.6	50.8	10	361.86
		203	610	3.5	2.10	410	0.75	30	0.6	50.8	10	335.38
		203	610	3.5	2.10	410	0.75	60	0.8	28.7	10	344.96
		203	610	3.5	2.10	410	0.75	60	0.8	28.7	10	338.33
		203	610	3.5	1.60	410	0.75	30	0.6	42.3	10	338.26
		203	610	3.5	1.60	410	0.75	30	0.6	42.3	10	346.31
		203	610	3.5	1.60	410	0.75	60	0.8	29.6	10	262.75
		203	610	3.5	1.60	410	0.75	60	0.8	29.6	10	222.32
		203	610	3.5	2.10	410	1.50	30	0.6	44.4	10	429.06
		203	610	3.5	2.10	410	1.50	60	0.8	42.8	10	421.26

References

[1] Tran TT, Pham TM, Hao H. Experimental and analytical investigation on flexural behaviour of ambient cured geopolymer concrete beams reinforced with steel fibers. Eng Struct. 2019;200:109707.

[2] Khan MZN, Shaikh FUA, Hao Y, Hao H. Synthesis of high strength ambient cured geopolymer composite by using low calcium fly ash. Constr Build Mater. 2016;125:809-20.

[3] Sarker PK. Bond strength of reinforcing steel embedded in fly ash-based geopolymer concrete. Mater Struct. 2010;44:1021-30.

[4] Bakharev T. Resistance of geopolymer materials to acid attack. Cem Concr Res. 2005;35:658-70.

[5] Nath P, Sarker PK. Flexural strength and elastic modulus of ambient-cured blended low-calcium fly ash geopolymer concrete. Constr Build Mater. 2017;130:22-31.

[6] Sumajouw DMJ, Hardjito D, Wallah SE, Rangan BV. Fly ash-based geopolymer concrete: study of slender reinforced columns. J Mater Sci. 2006;42:3124-30.

[7] Sumajouw MDJ, Rangan BV. Low-Calcium Fly Ash-Based Geopolymer Concrete: Reinforced Beams and Columns, Research Report GC. Perth(Australia): Curtin University of Technology; 2006.

[8] Sarker PK. Analysis of geopolymer concrete columns. Mater Struct. 2008;42:715-24.

[9] Ngo TT, Tran TT, Pham TM, Hao H. Performance of geopolymer concrete in non-corrosive dry joint type using CFRP bolts under cyclic loading. 2019;Under review.

[10] Pan Z, Sanjayan JG, Rangan BV. Fracture properties of geopolymer paste and concrete. Mag Concr Res. 2011;63:763-71.

[11] Albitar M, Mohamed Ali MS, Visintin P. Experimental study on fly ash and lead smelter slag-based geopolymer concrete columns. Constr Build Mater. 2017;141:104-12.

[12] Tran TT, Pham TM, Hao H. Rectangular Stress-block Parameters for Fly-ash and Slag Based Geopolymer Concrete. Structures. 2019;19:143-55.

[13] Lu Z-H, Li H, Li W, Zhao Y-G, Dong W. An empirical model for the shear strength of corroded reinforced concrete beam. Constr Build Mater. 2018;188:1234-48.

[14] Lu Z-H, Li H, Li W, Zhao Y-G, Tang Z, Sun Z. Shear behavior degradation and failure pattern of reinforced concrete beam with chloride-induced stirrup corrosion. Adv Struct Eng. 2019;22:2998-3010.

[15] Le TD, Pham TM, Hao H, Yuan C. Performance of precast segmental concrete beams posttensioned with carbon fiber-reinforced polymer (CFRP) tendons. Compos Struct. 2019;208:56-69.

[16] Maranan GB, Manalo AC, Karunasena W, Benmokrane B. Pullout behaviour of GFRP bars with anchor head in geopolymer concrete. Compos Struct. 2015;132:1113-21.

[17] Sim J, Park C, Moon DY. Characteristics of basalt fiber as a strengthening material for concrete structures. Compos Part B: Eng. 2005;36:504-12.

[18] Monaldo E, Nerilli F, Vairo G. Basalt-based fiber-reinforced materials and structural applications in civil engineering. Compos Struct. 2019;214:246-63.

[19] Yost JR, Gross Shawn P, Dinehart David W. Shear Strength of Normal Strength Concrete Beams Reinforced with Deformed GFRP Bars. J Compos Constr. 2001;5:268-75.

[20] Tureyen AK, Frosch RJ. Shear Tests of FRP-Reinforced Concrete Beams without Stirrups. ACI Struct J. 2002;99.

[21] El-Sayed AK, El-Salakawy EF, Benmokrane B. Shear Strength of FRP-Reinforced Concrete Beams without Transverse Reinforcement. ACI Struct J. 2006;103.

[22] Hoult NA, Sherwood EG, Bentz EC, Collins MP. Does the Use of FRP Reinforcement Change the One-Way Shear Behavior of Reinforced Concrete Slabs? J Compos Constr. 2008;12:125-33.

[23] Bentz Evan C, Massam L, Collins Michael P. Shear Strength of Large Concrete Members with FRP Reinforcement. J Compos Constr. 2010;14:637-46.

[24] Maranan GB, Manalo AC, Benmokrane B, Karunasena W, Mendis P. Shear Behavior of Geopolymer Concrete Beams Reinforced with Glass Fiber-Reinforced Polymer Bars. ACI Struct J. 2017;114.

[25] Maranan GB, Manalo AC, Benmokrane B, Karunasena W, Mendis P, Nguyen TQ. Shear behaviour of geopolymer-concrete beams transversely reinforced with continuous rectangular GFRP composite spirals. Compos Struct. 2018;187:454-65.

[26] Visintin P, Mohamed Ali MS, Albitar M, Lucas W. Shear behaviour of geopolymer concrete beams without stirrups. Constr Build Mater. 2017;148:10-21.

[27] Ngo TT, Pham TM, Hao H. Effects of steel fibres and prestress levels on behaviour of newly proposed exterior dry joints using SFRC and CFRP bolts. Eng Struct. 2020;205:110083.

[28] Ng TS, Amin A, Foster SJ. The behaviour of steel-fibre-reinforced geopolymer concrete beams in shear. Mag Concr Res. 2013;65:308-18.

[29] Yin S, Tuladhar R, Shi F, Combe M, Collister T, Sivakugan N. Use of macro plastic fibres in concrete: A review. Constr Build Mater. 2015;93:180-8.

[30] Altoubat S, Yazdanbakhsh A, Rieder K-A. Shear Behavior of Macro-Synthetic Fiber-Reinforced Concrete Beams without Stirrups. ACI Mater J. 2009;106:381-9.

[31] Ortiz Navas F, Navarro-Gregori J, Leiva Herdocia G, Serna P, Cuenca E. An experimental study on the shear behaviour of reinforced concrete beams with macro-synthetic fibres. Constr Build Mater. 2018;169:888-99.

[32] Kang S-T, Choi J-I, Koh K-T, Lee KS, Lee BY. Hybrid effects of steel fiber and microfiber on the tensile behavior of ultra-high performance concrete. Compos Struct. 2016;145:37-42.

[33] Al-Majidi MH, Lampropoulos A, Cundy AB. Tensile properties of a novel fibre reinforced geopolymer composite with enhanced strain hardening characteristics. Compos Struct. 2017;168:402-27.

[34] Banthia N, Gupta R. Hybrid fiber reinforced concrete (HyFRC): fiber synergy in high strength matrices. Mater Struct. 2004;37:707-16.

[35] Sahoo DR, Maran K, Kumar A. Effect of steel and synthetic fibers on shear strength of RC beams without shear stirrups. Constr Build Mater. 2015;83:150-8.

[36] Nath P, Sarker PK. Effect of GGBFS on setting, workability and early strength properties of fly ash geopolymer concrete cured in ambient condition. Constr Build Mater. 2014;66:163-71.

[37] Ltd JGMVNMTDC. http://www.gmvchina.com/en/infos.asp?id=327. 2019.

[38] Ltd BP. https://bosfa.com/products/dramix-5d-4d-3d/. 2019.

[39] Ltd BP. https://barchip.com/product/. 2019.

[40] Ltd KC. https://www.kuraray.com/products/vinylon. 2019.

[41] LTD BMGP. https://beyondmaterials.com.au/product/chopped-carbon-fibre-3-50-mm/. 2019.

[42] 426 A-AC. The Shear Strength of Reinforced Concrete Members. ACI Journal Proceedings. 1973;70.

[43] Dinh Hai H, Parra-Montesinos Gustavo J, Wight James K. Shear Strength Model for Steel Fiber Reinforced Concrete Beams without Stirrup Reinforcement. J Struct Eng. 2011;137:1039-51.

[44] Bhutta A, Farooq M, Zanotti C, Banthia N. Pull-out behavior of different fibers in geopolymer mortars: effects of alkaline solution concentration and curing. Mater Struct. 2017;50:80.

[45] Bentur A, Mindess S. Fibre reinforced cementitious composites: CRC Press; 2006.

[46] El-Sayed AK, El-Salakawy EF, Benmokrane B. Shear Capacity of High-Strength Concrete Beams Reinforced with Fiber-Reinforced Polymer Bars. ACI Struct J. 2006;103.

[47] Banthia N, Sheng J. Fracture toughness of micro-fiber reinforced cement composites. Cem Concr Compos. 1996;18:251-69.

[48] Yazıcı Ş, İnan G, Tabak V. Effect of aspect ratio and volume fraction of steel fiber on the mechanical properties of SFRC. Constr Build Mater. 2007;21:1250-3.

[49] Bhutta A, Farooq M, Banthia N. Matrix hybridization using waste fuel ash and slag in alkali-activated composites and its influence on maturity of fiber-matrix bond. J Cleaner Prod. 2018;177:857-67.

[50] Mansur MA, Ong KCG, Paramasivam P. Shear Strength of Fibrous Concrete Beams Without Stirrups. J Struct Eng. 1986;112:2066-79.

[51] Khuntia M, Stojadinovic B, Goel S. Shear Strength of Normal and High-Strength Fiber Reinforced Concrete Beams without Stirrups. ACI Struct J. 1999;96:282-9.

[52] Ding Y, Zhang F, Torgal F, Zhang Y. Shear behaviour of steel fibre reinforced self-consolidating concrete beams based on the modified compression field theory. Compos Struct. 2012;94:2440-9.

[53] Slater E, Moni M, Alam MS. Predicting the shear strength of steel fiber reinforced concrete beams. Constr Build Mater. 2012;26:423-36.

[54] Swamy RN, Jones R, Chiam ATP. Influence of Steel fibers on the Shear Resistance of Lightweight Concrete I-Beams. ACI Struct J. 1993;90.

[55] Lim TY, Paramasivam P, Lee SL. Analytical Model for Tensile Behavior of Steel-Fiber Concrete. Materials Journal. 1987;84:286-98.

[56] Zhang F, Ding Y, Xu J, Zhang Y, Zhu W, Shi Y. Shear strength prediction for steel fiber reinforced concrete beams without stirrups. Eng Struct. 2016;127:101-16.

[57] Spinella N, Colajanni P, Recupero A. Simple Plastic Model for Shear Critical SFRC Beams. J Struct Eng. 2010;136:390-400.

[58] Choi K-K, Park H-G, Wight JK. Shear Strength of Steel Fiber-Reinforced Concrete Beams without Web Reinforcement. ACI Struct J. 2007;104.

[59] Bentz EC, Vecchio FJ, Collins MP. Simplified Modified Compression Field Theory for Calculating Shear Strength of Reinforced Concrete Elements. ACI Struct J. 2006;103.

[60] A23.3 CC. Design of concrete structures (CSA A23.3-04). Mississauga, Ont.: Canadian Standards Association; 2004.

[61] Kim KS, Lee DH, Hwang J-H, Kuchma DA. Shear behavior model for steel fiber-reinforced concrete members without transverse reinforcements. Compos Part B: Eng. 2012;43:2324-34.

[62] Collins MP, Mitchell D, Adebar P, Vecchio FJ. A General Shear Design Method. ACI Struct J. 1996;93.

[63] MathWorks. https://au.mathworks.com/help/optim/ug/fsolve.html. 2019.

[64] Bentz EC, Collins MP. Development of the 2004 Canadian Standards Association (CSA) A23. 3 shear provisions for reinforced concrete. Can J Civ Eng. 2006;33:521-34.

[65] Committee ACI. 440.1R-06: Guide for the Design and Construction of Structural Concrete Reinforced with FRP Bars. Technical Documents.

[66] 318 AC. Building Code Requirements for Structural Concrete (ACI 318-11). 2011.

[67] Narayanan R, Darwish IYS. Use of Steel Fibers as Shear Reinforcement. ACI Struct J. 1987;84.

[68] Lim TY, Paramasivam P, Lee SL. Shear and moment capacity of reinforced steel-fibre-concrete beams. Mag Concr Res. 1987;39:148-60.

[69] Ashour SA, Hasanain GS, Wafa FF. Shear Behavior of High-Strength Fiber Reinforced Concrete Beams. ACI Struct J. 1992;89:176-84.

[70] Li VC, Ward R, Hmaza AM. Steel and Synthetic Fibers as Shear Reinforcement. ACI Mater J. 1992;89:499-508.

[71] Imam M, Vandewalle L, Mortelmans F, Van Gemert D. Shear domain of fibre-reinforced high-strength concrete beams. Eng Struct. 1997;19:738-47.

[72] Kwak Y-K, Eberhard MO, Kim W-S, Kim J. Shear Strength of Steel Fiber-Reinforced Concrete Beams without Stirrups. ACI Struct J. 2002;99.

[73] Cucchiara C, La Mendola L, Papia M. Effectiveness of stirrups and steel fibres as shear reinforcement. Cem Concr Compos. 2004;26:777-86.

[74] Noghabai K. Beams of Fibrous Concrete in Shear and Bending: Experiment and Model. J Struct Eng. 2000;126:243-51.

Chapter 5. Effect of Fibre on Flexural Failure of Ambient-Cured Geopolymer Concrete Beams under Impact Loading

Abstract[4]

Increased number of studies of the performances of geopolymer concrete (GPC) structures reinforced with fibre reinforced polymer (FRP) under static loadings have been reported recently, aiming at developing an alternative of the traditional constructions with ordinary Portland concrete (OPC) and steel reinforcement because GPC is a sustainable construction material and FRP is corrosion resistant. Study of the dynamic performance of GPC structures reinforced with FRP is, however, very limited. This study experimentally investigates the impact response of ambient cured GPC beams reinforced with different types of fibres and basalt fibre reinforced polymer (BFRP) bars. Four GPC beams reinforced with steel fibres or synthetic fibres and two control beams made of GPC and OPC without fibre reinforcement were cast and cured under ambient conditions. The volume fraction of fibres varied from 0 to 0.5% were used in concrete mix and BFRP bars and stirrups were used for longitudinal and transverse reinforcements respectively. All the beams were tested under drop-weight impact and after impact tests, the damaged beams were monotonically loaded under three-point bending tests to obtain the residual strength. The experimental results demonstrate that the presence of fibres reduced damages in the crushing zone and mitigated the concrete cover spalling at the bottom of the beams. Also, increasing the volume fraction of fibres shifted the crack patterns and failure modes of the beams from shear-flexure to flexural dominance. However, adding fibres had insignificant effects on the peak impact force, reaction forces, and mid-span displacement. The findings from the residual strength tests indicate that the beams with higher fibre dosage which failed in flexural dominance mode under impact loading have smaller residual strength, different from the expected performance observed in the fibre reinforced concrete beams under static load. Discussions are provided to explain these observations.

[4] This chapter was extracted from the paper submitted in Engineering Structures, but the tittle of the chapter and subsections were modified to follow the flow of the thesis. The full bibliographic citation of the paper is as follows: Tran TT, Pham TM, Huang Z, Chen W, Hao H, Elchalakani M. Impact response of fibre reinforced geopolymer concrete beams with BFRP bars and stirrups. Eng Struct. 2021;231:111785.

5. 1. Introduction

Since the production of Portland cement is energy-intensive and releases an enormous amount of carbon dioxide and other pollutants into the atmosphere, sustainable materials such as geopolymer concrete (GPC) have been received a lot of research attention in recent decades. In recent years, GPC can be synthesized under ambient conditions with satisfactory compressive strength [1] and hence it becomes possible to apply this material in the large-scale cast-in-situ structures. Previous studies show several superior mechanical characteristics of GPC in comparison with ordinary Portland concrete (OPC) including high bonding strength with reinforcing steel bars [2], better fire endurance [3], and better resistance to an acidic environment [4]. Despite those excellent properties, GPC shows lower resistance to cracking than OPC due to the much lower fracture energy [5]. To deal with this problem, a GPC composite reinforced with hybrid steel and synthetic fibres have been developed and demonstrated good mechanical properties in terms of ductility, post-peak behaviour in flexural tests, and toughness [6]. The inclusion of fibres also improves significantly the performance of GPC composite under dynamic splitting tension and compression [7, 8]. Therefore, the fibre reinforced GPC composite is a promising sustainable solution for structures subjected to extreme loads, namely impact and blast.

Meanwhile, a majority of the previous studies were conducted to investigate the response of ambient-cured GPC beams and columns under quasi-static loading conditions [9-14]. From those studies, it was reported that the behaviour of the ambient-cured GPC structures is generally similar to that of OPC ones with comparable performance. Therefore, the design procedures which are developed for OPC structures can be adopted to estimate the strength of GPC ones. However, due to the intrinsically brittle characteristic of a highly cross-link framework of geopolymeric matrix [5], the ambient-cured GPC structures also exhibit several adverse effects such as lower cracking load and more brittle failure when comparing with OPC ones [1]. Such differences result in smaller stress block parameters of ambient-cured GPC structures than those recommended in current codes for OPC structures [14]. As a result, the rectangular stress-block parameters given in concrete standards for OPC were modified to yield a better strength prediction of ambient-cured GPC columns [15]. To overcome the brittleness problem of GPC material, recent investigations indicate that the addition of fibres can significantly improve the ductility of ambient-cured GPC structures [1, 16]. Due to the superior interface bond strength between fibres and matrix [17], the bridging effect of fibre is likely to

be more effective in enhancing the flexural and shear capacities of the ambient-cured GPC beams than those of OPC counterparts [1, 18]. These previous studies have shown that fibres reinforced ambient-cured GPC structures have a great potential to replace the conventional OPC structures which are not environmentally friendly.

During the service life, concrete structures may suffer from impact loading caused by vehicle collisions or falling objects. Several studies investigating the structural behaviour of conventional reinforced concrete beams indicate significant differences between the quasi-static and impact response [19-21]. For example, under impact loading, cracks caused by negative bending moment are observed on the top of the simply supported beams which are not possible for simply-supported beam subjected to a static load. Cotsovos [22] attributed this phenomenon to the effective response length of the beams which is reduced because of the high loading rate. Such a reduction of the effective length was explained by traveling of plastic hinges from the mid-span of the beam to the stationary point [23]. Consequently, only a portion of the beam is accelerated at the early stage of the impact process if the plastic hinges do not reach the supports [23]. Furthermore, failure of the beams subjected to impact load is also distinguishable from those under static loading with respect to the failure mechanism [24, 25]. It was reported that the beams may fail in shear or even punching shear when subjected to impact load, although their static shear capacities are designed to be four times higher than the flexural ones that the beams would fail in a pure flexural manner under static loading [21].

Owing to the profound differences between the impact and static responses, there were several design suggestions for the concrete beams subjected to impact loading. Pham and Hao [26] suggested that the use of FRP sheets can improve significantly the stiffness and impact resistance of the beams. Another method is to modify concrete by adding materials that can absorb energy. It is recommended that the inclusion of rubbers can not only reduce the peak impact force but also improve the energy absorption of the concrete beams [25]. Also, fibre reinforcement has been adopted to enhance the impact behaviour of conventional concrete beams. Ulzurrun and Zanuy [27] indicated that the presence of 1% steel fibre dosage can shift the failure modes of the beams without stirrups from shear to flexure, thereby yielding a better impact performance. The combination of steel fibres and stirrups also leads to the improved impact behaviour of the ultra-high-performance fibre reinforced concrete (UHPFRC) beams through reducing the peak and residual displacements and the energy dissipating capacity [28]. From the aforementioned review, it can be seen that beams under static and dynamic loads

behave differently, but there has been no study in the literature that investigates the impact response of ambient-cured GPC beams reinforced with fibres yet.

In this chapter, four GPC beams reinforced with different types of fibres including steel fibres and synthetic fibres, and two control beams (GPC and OPC) without fibres were tested under drop-weight impacts. The volume fraction of fibres varied from 0 to 0.5% which is low dosages for easy mixing due to the poor workability of GPC mixtures [1]. To mitigate the corrosion problems, fibre reinforced polymer (FRP) material has been used to replace conventional steel material for yielding more durable reinforced concrete structures [29, 30]. In terms of the impact response, it was demonstrated that concrete structures using FRP reinforcements could yield comparable performance when compared with those adopting conventional steel reinforcements [31, 32]. Therefore, basalt fibre reinforced polymer (BFRP) bars were used for both longitudinal reinforcements and transverse stirrups. After completion of the drop-weight tests, all the cracked beams were subjected to quasi-static three-point bending tests to determine their residual capacities. Based on the experimental results, the effect of fibres on the impact responses and residual performance of the GPC beams is discussed and explained. From those discussions, some recommendations are provided to give better understandings and designs for fibre reinforced GPC beams subjected to impact loads.

5. 2. Experimental scheme

5.2.1. Test specimens and material property

A total of four fibre reinforced GPC beams and two control specimens including GPC and OPC beam without fibres were designed with the following configuration: width (b) of 150 mm, depth (h) of 200 mm, and length of 1250 mm. Two 10-mm diameter BFRP bars ($A_f = 157\ mm^2$) corresponding to reinforcement ratio, $\rho_f = 0.63\%$, were employed for the bottom and top longitudinal reinforcements. The reinforcement ratio adopted in this study is much higher than the balanced ratio (0.26%) estimated according to ACI 440.1R-06 [33]. It indicates that the beams were over-reinforced and failure due to rupture of the bars was not expected. The transverse reinforcements were 10-mm diameter BFRP stirrups with the spacing as illustrated in Figure 5-1. The static shear capacity and the flexural strength of control beams designed based on ACI 440.1R-06 [33] were 131 kN and 64 kN respectively. Therefore, the beams were expected to fail in the flexural mode under static load. The Young's modulus, E_f, tensile strength, f_{fu}, and elongation at break, ε_{fu}, of the BFRP reinforcements were 55 GPa,

1100~1200 MPa, and 2%, respectively. More detailed properties of BFRP reinforcing bars can be found in the previous studies [18, 34]. In addition, strain gauges were bonded to the BFRP stirrups and longitudinal bars to monitor their strain during testing. The location of strain gauges attached to the stirrup was decided based on the assumed 45^{o} inclined shear cracks induced from impacted areas (Figure 5-1).

Table 5-1 shows the classification of the beams with the employment of various kinds of fibres and volume fraction and the two control beams without fibre. The tensile strengths of the synthetic Vinyl Polypropylene fibres (PF) and hooked-end steel fibres (SF) were 640 MPa and 1345 MPa while the elastic moduli were 12 GPa and 210 GPa, respectively [35, 36]. The geometry of two different types of fibres is shown in Figure 5-2 and also summarized in Table5-1. To achieve a workable mixture, the fibre volume fraction should not exceed 0.5 % owing to the poor workability of GPC [37].

The mixtures of GPC and OPC aiming to 40 MPa in compressive strength are shown in Tables 5-2 and 5-3. The chemical composition of the fly ash and ground granulated blast furnace slag (GGBFS) can be referred from the previous study because they came from the same supplier [1]. All the beams and cylinders with the dimension of 100 mm x 200 mm were cast based on the procedure in the previous study [1], then covered by a plastic sheet and left in the ambient lab condition until testing dates. All the cylinders were tested based on the ASTM C39/C39M-18 [38] at the same testing dates of the beams. As can be seen from Table 5-1, the compressive strength of different batches varied from 40 to 44 MPa, which indicates the consistency of the mixture and specimen fabrication.

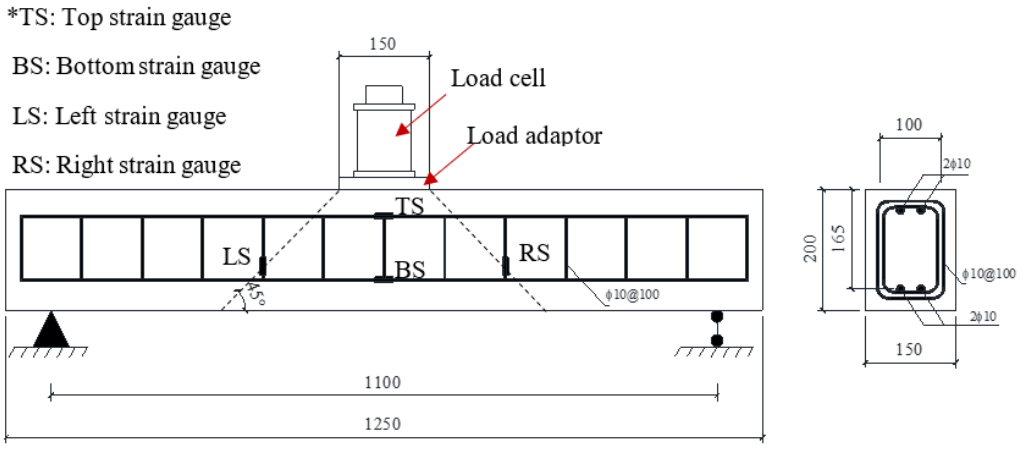

Figure 5-1. Specimen Configuration (unit: mm)

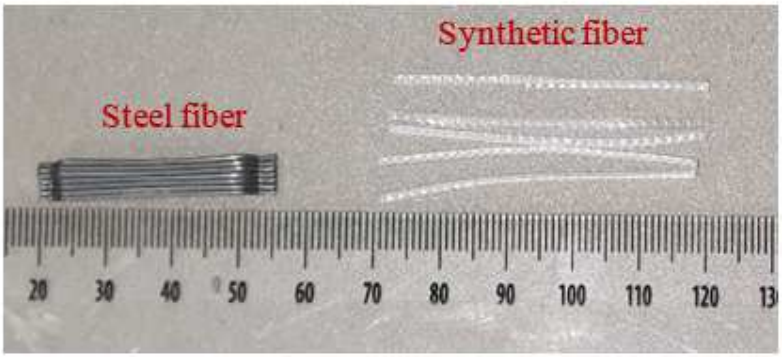

Figure 5-2. Steel and synthetic fibres used in the study

Table 5-1. Fibre volume fraction and compressive strength of all the beams

Beam	Steel			Synthetic			f_c'
	V_f(%)	l_f(mm)	d_f(mm)	V_f(%)	l_f(mm)	d_f(mm)	(MPa)
OPC	-	-	-	-	-	-	44.0
GPC	-	-	-	-	-	-	44.0
GPC-0.25SF	0.25	35	0.55	-	-	-	43.9
GPC-0.5SF	0.5	35	0.55	-	-	-	41.4
GPC-0.25PF	-	-	-	0.25	48	0.85	40.3
GPC-0.5PF	-	-	-	0.5	48	0.85	42.3

V_f: volume fraction of fibre, l_f: fibre length, d_f: fibre diameter

- Not applicable

Table 5-2. Mix proportion of GPC (kg/m^3)

FA	GGBFS	Aggregates		NaOH	Na_2SiO_3
		Crushed stone	Sand	Solution	solution
360	40	1196	360	59.4	173.7

Table 5-3. Mix proportion of OPC (kg/m^3)

Water	Cement	Aggregates		Superplasticizer
		Crushed stone	Sand	
204	408	863	876	2.04

5.2.2. Testing procedure

The drop-weight test system described in the previous study [26] was adopted here, as shown in Figure 5-3. The hemi-spherical drop hammer made of a solid steel cylinder with a mass of 208 kg and a striking surface of 50 mm in radius was dropped freely from the height of 2 m onto the mid-span of the beams. At the mid-span, a combination system of a load cell and a steel load adaptor (150x150x20 mm with the total weight of 22 kg) was fixed on top of the beam to measure the impact load. The boundary condition was a simply supported beam with an effective span of 1100 mm. Two load cells were fixed on the top and bottom at the each end of the beam to record the negative and positive reaction forces. To monitor the failure and deflection process of the beams, a high-speed camera setting to capture 20,000 frames per second was used. The tracking points were attached to the surface of the beams and the drop hammer to track the displacement of the beams and the residual velocity of the drop hammer. Signals from the load cells and strain gauges were captured at the frequency of 50 kHz by a computerized data acquisition system. More details about the impact test setup and the instrumentations can be found in reference [26]. After the completion of the drop-weight tests, all the cracked beams were subjected to monotonic quasi-static loads under the three-point static bending test to determine the residual capacity and the load-deflection response. The description of the test setup is illustrated in Figure 5-4.

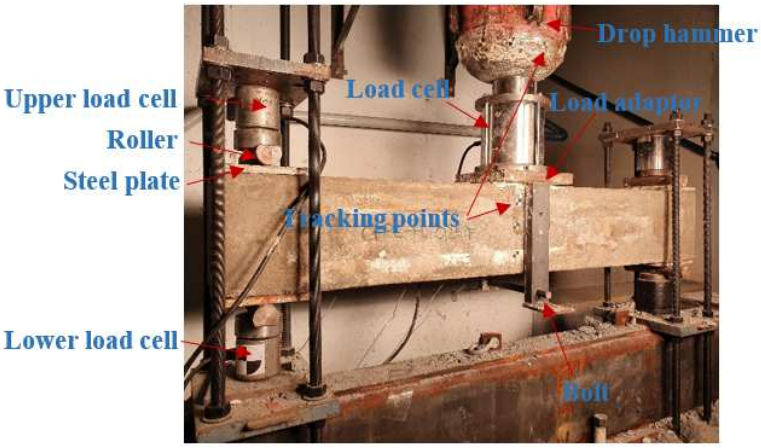

Figure 5-3. Drop-weight test system

Figure 5-4. Three-point load test of residual capacity

5. 3. Impact test results and discussion

In this section, the dynamic behaviour of all the tested beams including crack patterns, failure modes, and time histories of impact and reaction forces, displacement, and strain of reinforcing bars is discussed. The effect of fibres on the enhancements of the impact resistance capacities of the GPC beams is also examined.

5.3.1. Crack pattern

Based on the videos recorded in the tests, the impact response can be described in four main phases as shown in Figure 5-5. Phase 1 commenced when the drop hammer collided with the beam and then the midspan displacement of the beam increased up to the first peak. This phase had lasted until the drop hammer hit the beam for the second time. Phase 2 was the duration from the beginning of the second impact to the moment when the beam reached the maximum midspan deflection. Afterward, the duration when the beam bounced from the peak deflection to the maximum displacement recovery at the instant when the impact force reduced to zero was considered as Phase 3 and the subsequent free vibration was considered as Phase 4.

The propagation of primary cracks in the control OPC beam as presented in Figure 5-6a occurred mainly in the first and second phases, and after that, no new crack was observed. The propagation of primary cracks occurred mainly in the first and second phases. Therefore, the high-speed camera images of crack patterns of the beams at the end of Phase 1 and Phase 2 are presented in Figures 5-6b and c. The numbers near the cracks in the images (Figures 6b and c) represent the time (ms) when cracks develop to the marked position in the images. Both the control beams GPC and OPC exhibited quite similar cracking pattern (Figures 6b and c). At

Phase 1, a vertical flexural crack initiated and then widened at the midspan of the beams at 0.5 ms and then was followed by the formation of further flexural cracks (close to the supports) after 1 ms. Horizontal cracks close to the soffit of the beam resulting from the reflected tensile wave under the loading area [39] were also observed at 1 ms. At 2 ms of the collision process, the flexural crack at the midspan of the beam propagated vertically upward close to the top of the beam. Subsequently, the flexural cracks close to the supports propagate diagonally toward the impacted area at 4 ms. After Phase 1, the existing cracks widened significantly due to the second impact event and there was no formation of new cracks in the subsequent phases. It is worth noting that there was no obvious separation between the drop hammer and the beams between impact one and impact two. The beams also suffered severe concrete crushing at the end of the inclined cracks near the impacted area at 8 ms which was considered as shear compression failure (as shown in Figure 5-6c). Moreover, concrete crushing at the top surface of the midspan due to the flexural global response was observed when the beam reached the peak deformation. The reflected tensile stress wave from the second impulse caused the unconfined concrete at the bottom spalling off (see Figure 5-6c). In general, the crack propagation of the control beams was a combination of the vertical flexural and inclined shear cracks resulted from the global response and horizontal cracks near the bottom of the beam caused by the transmission of the stress waves.

For the fibre reinforced beams, it is worth noting that the addition of fibres prevented the formation of horizontal cracks and also the spalling of concrete at the beam soffit caused by the reflected local stress waves (see Figure 5-6c). As a result, it can be deduced that the bridging effect of fibres effectively impedes the local cracks from emerging and propagating. Furthermore, the presence of fibres changed the crack pattern of the GPC beams in the first phase from shear to a flexural pattern. In particular, Beam GPC-0.5PF demonstrated fewer inclined cracks compared to the control beams. This tendency is more obvious in the case of the beam reinforced with 0.5% SF, where no inclined crack was observed (Figure 5-6c). Generally, when the volume fraction of fibre increases, the number of shear cracks of the beams reduces and the crack pattern shifts from being governed by the combination of shear and flexure to flexure. The same phenomenon was also found in concrete structures reinforced with fibres which were reported in the previous studies [28, 40]. This can be attributed to the fact that the fibres enhance the shear resistance more effectively than the flexural resistance [41]. Consequently, the dominance of flexural response mode was observed with the flexural cracks on the GPC beams reinforced with high fibre dosage. The addition of PFs had a similar effect

but was slightly less effective to reduce the shear cracks than SFs due to their inferior stiffness and less effective number of fibres bridging the cracks [18], but it also mitigated the concrete spalling damage as shown in the figure.

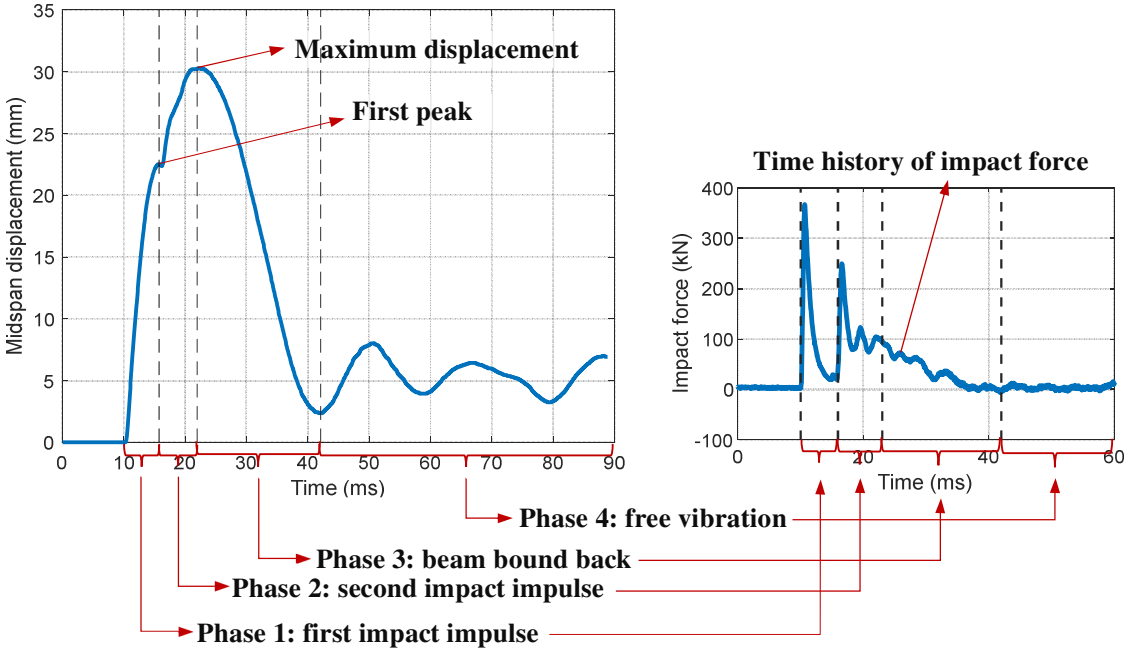

Figure 5-5. Impact response phase classifications (Beam GPC used for illustration)

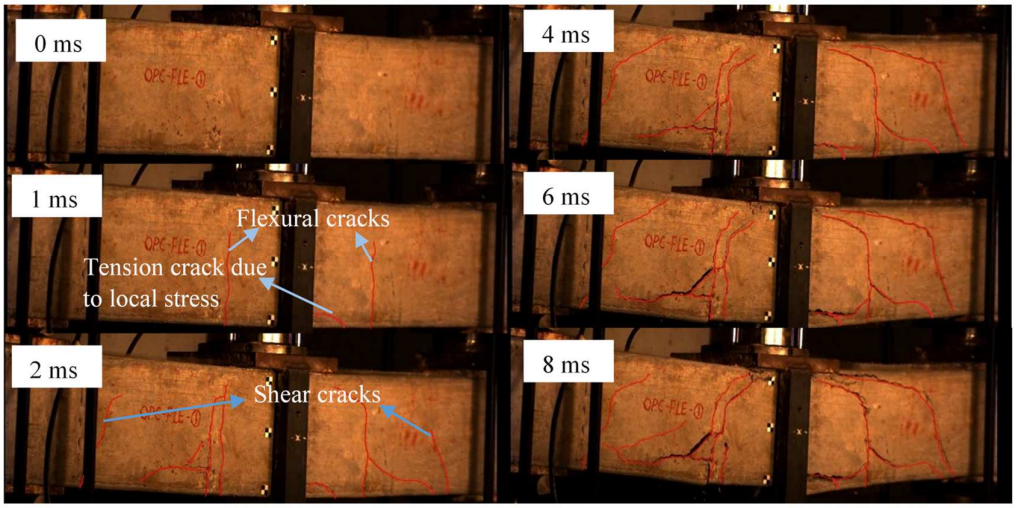

(a) Crack propagation in control beam OPC

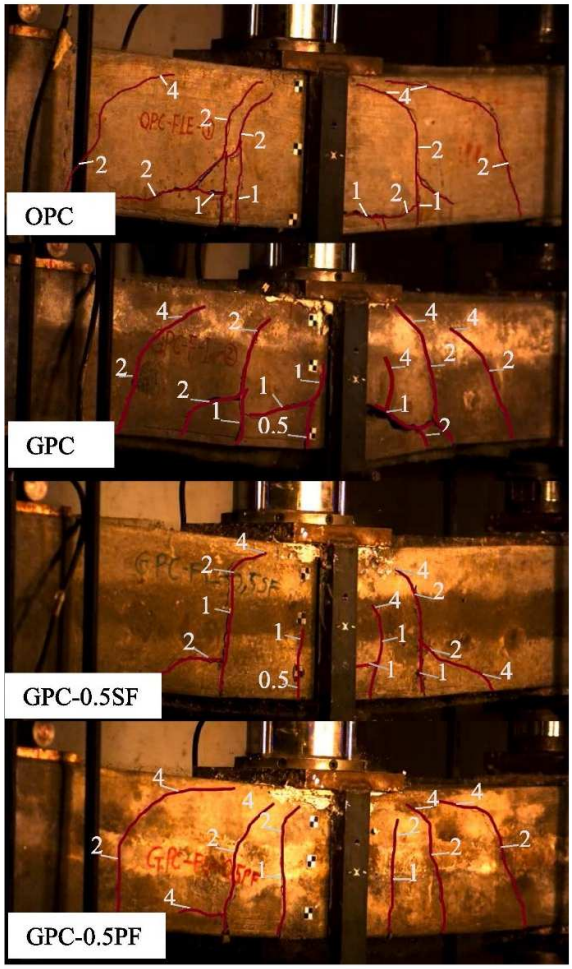

(b) Crack patterns of beams at end Phase 1 (t=5ms)

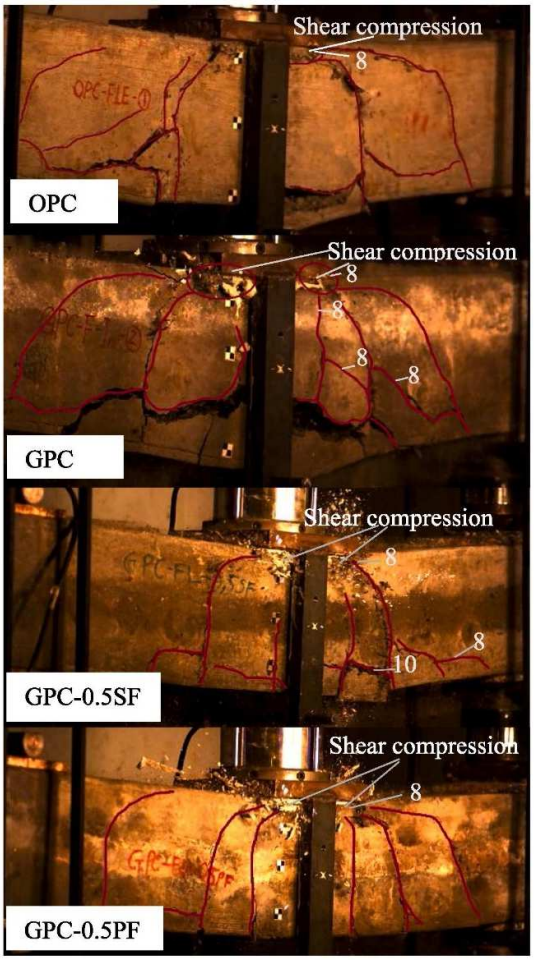

(c) Crack patterns of beams at end Phase 2 (t=13ms)

Note: The number in the figures indicates the time instant (in millisecond) when cracks appeared.

Figure 5-6. Cracks patterns of impacted beams in Phases 1 and 2

5.3.2. Failure modes

Figure 5-7 illustrates the typical final failure patterns of the tested beams. Both the control beams show relatively similar failure pattern of a combined flexural failure at midspan section with the concrete crushing at the top surface (denoted as type I) and shear failure with diagonal tension shear failure with the critical crack close to the supports (denoted as type II) and shear compression (denoted as type III). Type I, Type II, and Type III are typical flexural and shear

failure modes of slender beams (shear span to effective depth ratio greater than 2.5) under static loading which are detailed in previous studies [42, 43]. It should be noted that the reinforcement ratio adopted in this study (0.63%) was 2.5 times higher than the designed balanced ratio according to ACI-440.1R-06 (0.26%). Therefore, concrete crushing at the top surface governed the flexural failure (Type I) while no rupture of the bottom bars was observed. As can be seen from Figures 5-7a and b, the transmission of local stress waves also caused the spalling of concrete cover along the bottom reinforcing bars (denoted as Type IV). It is worth noting that the GPC beam experienced more severe local damages with a larger spalling area of concrete cover as compared to OPC specimen. This difference may be due to the brittleness of GPC material. Mindess et al. [44] conducted some drop-weight tests to investigate the impact resistance of plain high strength concrete and normal concrete beams with a notch. Mindess et al. [44] suggested that high strength concrete was more sensitive to the notch and might require less fracture energy at a high strain rate than normal concrete even though the first one had much higher compressive strength than the later one. As a result, the high strength concrete specimens had a lower impact strength than normal concrete ones. As reported in the literature, GPC exhibited very brittle behaviour and low fracture energy [5]. The brittleness of GPC explains the difference between the control GPC and OPC beams. GPC is more sensitive to the existing cracks formed in Phase 1 and thus requires less fracture energy to spall concrete cover than OPC. However, the effect of high strain rate on the fracture energy of GPC has not been unveiled in the literature and thus further studies are deemed necessary.

Due to the crack bridging effect, the presence of fibres helps mitigating or even preventing the spalling of concrete cover of the GPC beams caused by reflected tensile stress wave. This results in the exclusion of the failure type IV in those beams (see Figures 5-7c-f). The addition of fibres also reduced the damage in the crushing zone of Type I and Type III owing to the enhancement of ductility and toughness [1]. Furthermore, it is also worth noting that the increase of fibre dosage changes the dominant failure mode from shear to flexure. It can be seen from Figure 5-7d, when the volume fraction of SF increased to 0.5%, the beam failed mainly by flexure (Type I) without diagonal shear cracks. However, it can be seen that the damage at flexural cracks of Beam GPC-0.5SF was severer than that of Beam GPC-0.25SF, indicating increasing the volume fraction of SFs might result in more prominent flexural failure. The damages of Beam-0.5SF were local at a crack probably due to the deficiency of fibre distribution in the section illustrated in Figure 5-17. Moreover, mitigating the shear damage also resulted in the damage concentrated to the flexural failure, hence led to larger

flexural cracks. The shift of failure modes can be attributed to the better enhancement of shear strength than flexural capacity as explained previously. The improvement of shear behaviour by using the PF was also observed in Beam GPC-0.5PF (Figure 5-7f), but less pronounced than SF. The main reason is because of the low elastic modulus and less effective number of fibres for bridging the cracks.

The failure modes of the tested beams can be generalized into three types as shown in Figure 5-8. Based on the figure and the previous discussion, it can be recommended that (1) adding fibres either PF or SF prevents the GPC beams from severe spalling of the unconfined concrete in the beam soffit, caused by local stress wave propagation; (2) addition of PF or SF can reduce damage in crushing zone; (3) an increase of fibre content can shift the failure mode of the GPC beams from shear to flexure dominant failure.

(a) Beam OPC

(b) Beam GPC

(c) Beam GPC-0.25SF

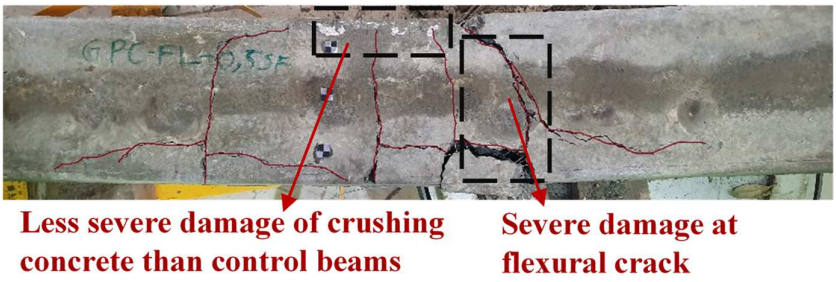

(d) Beam GPC-0.5SF

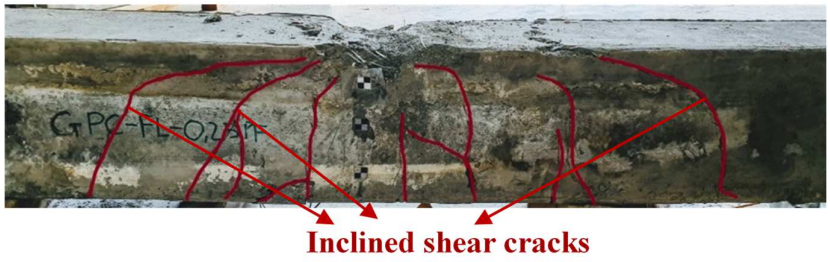

(e) Beam GPC-0.25PF

(f) Beam GPC-0.5PF

Figure 5-7. Failure patterns of the tested beams

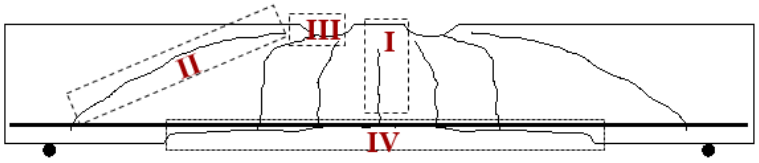

(a) Failure pattern of two control beams

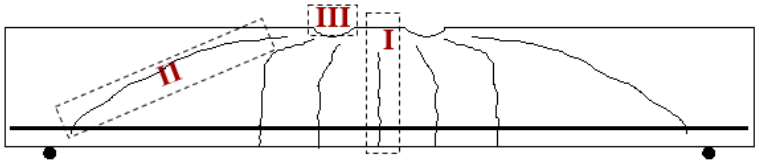

(b) Failure pattern of GPC beams with PF and 0.25%SF

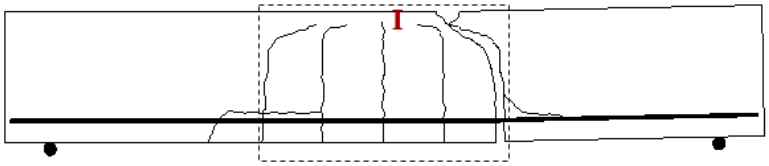

(c) Failure pattern of Beam GPC-0.5SF

I: Flexural failure
II: Diagonal tension shear failure
III: Shear compression
IV: Spalling concrete cover

Figure 5-8. Summary of failure patterns

5.3.3. Impact force and reaction force

The time histories of impact and reaction forces of all the tested GPC beams during the first 50 ms are plotted in Figure 5-9. The analysis of impact and reaction forces is divided into two main phases which are denoted in Figure 5-9. The determination of those phases is the same as those described previously in Section 5.3.1. The details of the maximum impact force, reaction forces, and displacement are summarized in Table 5-4.

From Figure 5-9a, it can be observed that Phase 1 response of the control beam GPC commenced at the instant of the initial collision between the beam and drop hammer which resulted in the increase of impact force to the peak value at 367 kN within about 1 ms. Subsequently, the impact force decreased sharply to about 20 kN after approximately 5 ms. After Phase 1, the second phase started at the moment when the impact force increased again and reached the second peak at roughly 248 kN due to the second impact between the drop hammer and the beam. Afterward, the impact force continued exhibiting two further peaks with smaller values (about 121 kN and 104 kN). The ending of the second phase occurred at about 13 ms after the initial collision. During Phase 3, the impact force decreased gradually to zero

at 30 ms thereafter no impact force was transmitted. Moreover, it can be noted the responses of impact force are almost similar between the Beam GPC and OPC, thereby suggesting that the interaction of GPC structures with drop weight is similar to that of OPC counterparts.

The time history response of the GPC beams reinforced with fibres was closely analogous to the control one. It can be noted that the addition of fibres reduced slightly the first peak load, (P_{ud}^{1}) and the second peak, (P_{ud}^{2}) compared to the control beam. This minor variance corroborates the findings of the previous studies [27, 45]. This can be attributed to the fact that the impact force is not prominently influenced by the global stiffness of the beams if there is no significant difference in the failure modes [46]. Through the numerical simulations, a previous study demonstrated that changing the flexural and shear stiffness of the beams does not affect the impact force [46]. On the other hand, the peak of impact force is sensitive to the contact stiffness between the projectile and the beam [47]. As shown in Table 5-1, the beams reinforced with the fibres have slightly smaller compressive strength than the control beam, indicating a lower hardness of the contact surface. This may be the reason for the minor reduction in the peak impact force of the beam reinforced with fibres.

Meanwhile, the experimental results have shown that the negative reaction forces were observed before their positive counterparts. This phenomenon was consistent with the results of the previous study [26] and might be due to the surface Rayleigh wave as presented in the previous duty [21]. The general response of the reaction force among the GPC beams is almost analogous. The content of fibres has no significant influence on the peak reaction force of the tested beams. For instance, the biggest difference of maximum reaction force, R_{ud}, among the GPC beams (GPC-0.25SF and GPC-0.5SF) is only 2%. This indicates that the inclusion of fibres does not considerably affect the reaction force. The same phenomenon was also found in a previous study investigating the effect of shear reinforcement on the dynamic behaviour of the reinforced OPC beams [48]. In that study, it was demonstrated that if the beams are reinforced with a sufficient shear reinforcement ratio, the dynamic reaction force was governed by the flexural stiffness [46]. This explanation is applicable for the beams presented in this chapter since the addition of fibres with the low volume fraction from 0% to 0.5% did not considerably improve the flexural stiffness of the beams. As a result, the reaction forces of these beams were relatively similar. To clarify this phenomenon, it is suggested that further investigations should be conducted.

The time lag between the impact force and the reaction force was observed and presented in this chapter (see Figure 5-10a). The measured time lag of all the tested beams ranged between 0.32 ms and 0.4 ms as summarized in Table 5-4. Given the distance from the midspan to the support of 0.55 m, the stress wave velocity of the tested beams is estimated from 1370-1725 m/s and illustrated in Figure 5-10b. Meanwhile, the velocity of the longitudinal stress wave of GPC calculated by $c = \sqrt{E/\rho}$ is 3223 m/s. It is evident that the stress wave velocity measured from the experiment is smaller than the theoretical estimation. This phenomenon is consistent with the findings of the previous studies [22, 26]. A recent study suggested that the measured stress wave velocity from the time lag between the impact and reaction force should be the velocity of R-wave [25]. The R-wave velocities traveling in OPC which were reported in the study of Rhazi et al. [49] varying from 1900 m/s to 2350 m/s whereas those of GPC have not been reported in the literature. It should be noted that the theoretical stress wave velocities of GPC should be smaller than those of OPC due to the lower elastic modulus [1]. Therefore, it can be inferred that the R-wave velocities of GPC are lower than those of OPC, which means the theoretical R-wave velocities of GPC may be close to the experimental values presented in this chapter. However, other factors such as pre-damage and cracks during the impact process that deteriorate the continuity of medium, wave dispersion, and the inaccuracy in estimating the time for stress wave transferring from the load cell to adapter would also affect the above wave velocity estimations [26]. It can be seen from Figure 5-10b, the beams reinforced with fibres exhibit slightly higher stress wave velocities compared to the control beam. This can be explained by the fact that the presence of fibres prevents the formation of shrinkage cracks of GPC matrix and microcracks occurring during stress wave propagation through the beams, and thereby increasing the velocity of stress wave propagation.

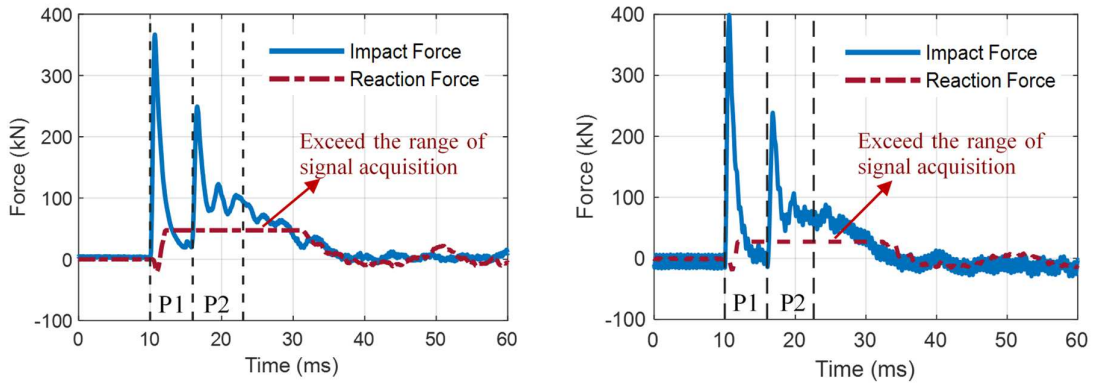

(a) GPC (b) OPC

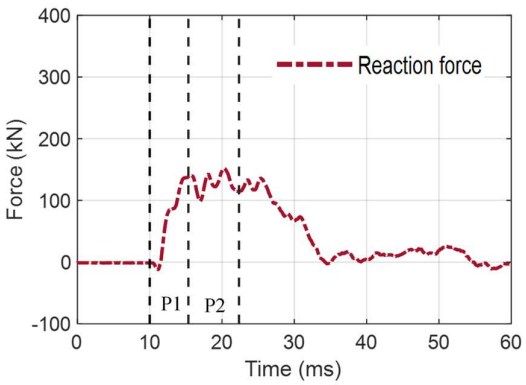

(c) GPC-0.25SF

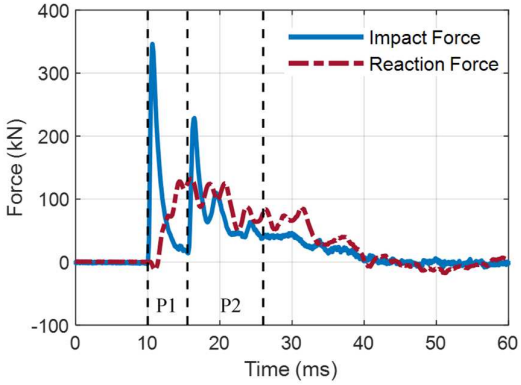

(d) GPC-0.5SF

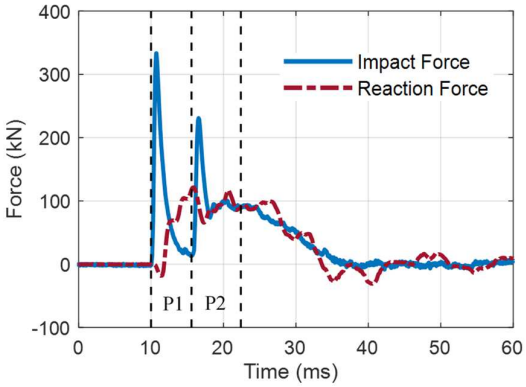

(e) GPC-0.25PF

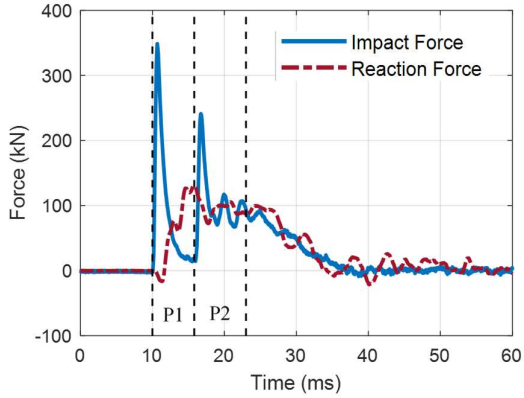

(f) GPC-0.5PF

Figure 5-9. Time history of impact force and reaction forces

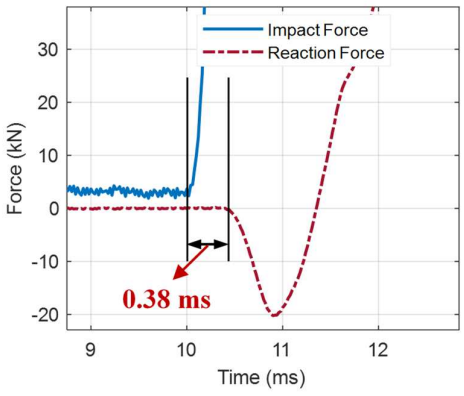

(a)

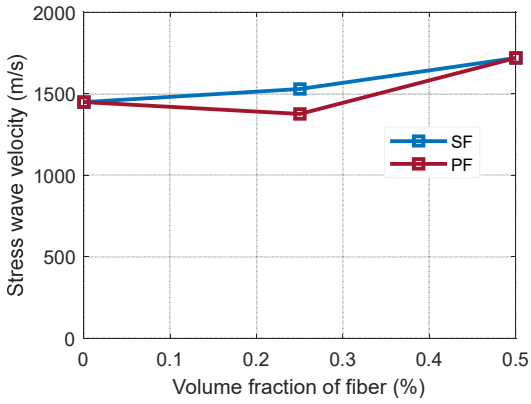

(b)

Figure 5-10. (a) Time lag in the control beam GPC and (b) the effect of fibre dosage on stress wave velocity

Table 5-4. Experimental results of impact tests

Beam	v_i (m/s)	v_r (m/s)	Time lag (ms)	P_{ud}^1 (kN)	R_{ud} (kN)	P_{ud}^2 (kN)	δ_{pd} (mm)	δ_{rd} (mm)
GPC	6.26	-2.1	0.38	362.6	-	245.1	30.3	6.9
OPC	6.26	-2.0	-	399.1	-	237.4	31.0	9.1
GPC-0.25SF	6.26	-2.3	0.36	-	129.3	-	30.8	6.4
GPC-0.5SF	6.26	-1.1	0.32	345.7	132.4	227.7	32.0	12.1
GPC-0.25PF	6. 26	-2.5	0.40	332.5	121.9	231.0	33.3	7.4
GPC-0.5PF	6.26	-2.3	0.32	348.7	130.1	241.1	32.1	7.8

- Data lost due to equipment malfunction

P_{ud}^1 and P_{ud}^2: peaks of the first and second impact force, and R_{ud}: peak of reaction force

δ_{pd} and δ_{rd}: maximum and residual displacement

v_i: initial velocity of drop-hammer at collision moment, v_r: residual velocity of drop hammer when beam rebounds

5.3.4. Midspan displacement and strain of reinforcing bars

The time histories of midspan displacement of all the GPC beams are plotted in Figure 5-11. The displacement response during Phase 1 and Phase 2 of all the beams were quite similar. It is worth noting that the addition of fibres might be ineffective to reduce the maximum displacements of the beams. A similar phenomenon was observed in the previous study by Jin et al. [45]. In that study, the midspan deflection of the beams reinforced with a large number of stirrups behaved similarly until reaching the peak value, irrespective of the fibre dosage. Lee et al. [28] also reported that the effect of fibres on the maximum response of displacement became less pronounced when the beam was reinforced with 0.64% transverse reinforcement. Such a phenomenon happens because the presence of the stirrup changes the failure mode of the beam from shear dominance to flexural dominance. Therefore, the maximum displacement of the beam may be dominated by the flexural stiffness which is not significantly improved by using a low volume fraction of fibres (from 0% to 0.5%). In this chpater, the behaviour of the GPC beams was primarily governed by the flexural response owing to the heavy shear reinforcement ratio and thus the effect of low fibre content on the maximum displacement response becomes minor.

The residual displacement of the beam after Phase 2 can be considered as an indicator of the level of the damages [50]. It can be seen that the addition of PF up to 0.5% or using 0.25% SF

influenced insignificantly the residual displacement, which implies that Beams GPC, GPC-0.25PF, GPC-0.5PF, and GPC-0.25SF had the same level of damage caused by impact loads. As discussed in Sections 5.3.1 and 5.3.2, the use of PF up to 0.5% or 0.25% SF mitigated the concrete crushing and spalling damage while the damages caused by the general failure pattern such as diagonal tension cracks were only slightly affected. Meanwhile, the beam incorporated 0.5% SFs had different failure mode with severer damages in a local flexural crack as discussed above. Such damages can reduce the stiffness of the beam and consequently yielded the large residual displacement.

It is interesting to note that there is a trend that the damping ratio of the beams increased with the fibre dosage. Figure 5-11 shows that the free vibration of the beams reinforced with PF/SFs exhibited a damped sinusoidal wave with very low frequency and stopped very quickly after two cycles or even one cycle if volume fraction of fibre increased to 0.5%. Meanwhile, the control one was able to maintain free vibration for more than 3 cycles. To explain this phenomenon, it is necessary to understand the mechanism of energy dissipation in the damping behaviour of reinforced concrete beams. In the cracked stage, the beam energy used for the vibratory motion is dissipated due to two main mechanisms: (1) viscous damping of the uncracked concrete in the compressive zone and (2) the friction between the reinforcing bars and cracked concrete in the tension zone [51]. The presence of fibres in the concrete matrix can introduce more interfaces and transition zones, which result in energy loss by internal friction during vibration [52]. This may enhance the energy dissipation through the first mechanism, thereby increasing the damping ratio of the beams with fibre reinforcement. However, the experimental results in the previous studies indicated that the addition of SF and PF with volume fraction up to 0.5% has an insignificant effect on the damping of concrete material [52, 53], this is different from those observed in this chapter. Since a similar ratio and configuration of longitudinal reinforcements were adopted for all the beams, the energy loss caused by the friction between the longitudinal reinforcing bars and cracked concrete should be similar for all the beams. Therefore, the observed faster free vibration attenuation was caused by the friction between the fibres and concrete matrix at the interfaces of macro-cracks which formed during Phase 1 and Phase 2 of the impact process. Consequently, the increase of fibre content increases the energy dissipation, thus increases the damping ratio as observed in the fibre reinforced beams.

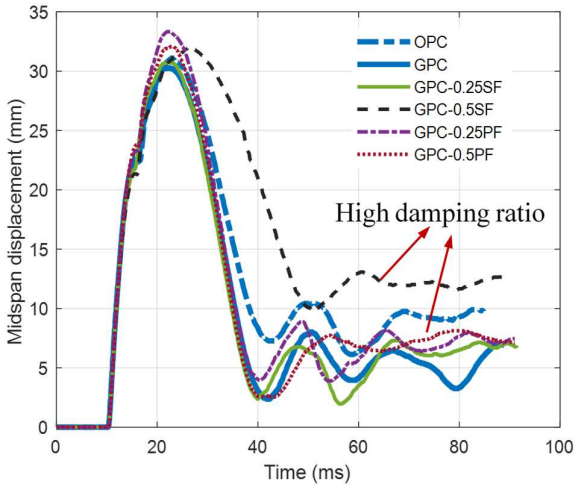

Figure 5-11. Time history of midspan displacement in the impact tests

The strain of top reinforcing BFRP bars is displayed in Figure 5-12a. It can be seen from the figure, the top reinforcing bars were initially compressive with small values and then the strain increased up to the first positive peak, at the end of phase 1. During the second phase, the strain of top reinforcing bars decreased significantly until reaching the lowest negative values when the beams reached maximum displacements. Subsequently, the strain rebounded to positive values and then stabilized at positive residual values, which means the top bars were in tension. It is interesting to note that the strain of top reinforcing bars at some moments was positive (the bars in tension) while the beams deflected downward, indicating that the top layer of the beams should be in compression, instead of tension. The top reinforcement bar in tension implies the depth of the neutral axis might be smaller than the distance from the top compressive layer of concrete to the centroid of the top reinforcing bars at those moments.

To clarify that phenomenon, the curves of neutral axis depth with the respondent curvature (φ) to ultimate curvature φ_{ult} ratios are calculated and illustrated in Figure 5-13a. Figure 5-13b exhibits the curves of strains in top reinforcing bars vs curvature ratios. The detailed sectional analysis method (SAM), which was proposed to estimate the flexural displacement of GPC beams reinforced with fibres in the previous study [1], was adopted to derive those curves. It should be noted that the method was developed for analysing the GPC beams under static loading. It is still, however, valid to use the method for evaluating the response of reinforcing bars in the impacted beams. As shown in the figures, in the fully cracked section the depth of the neutral axis (~27 mm) reduces significantly to the values which are smaller than the distance from the top reinforcing bars to the top layer of the beams (35 mm). This means the

entire reinforcement cage, including the top reinforcing bars are in tension and their strain has positive values (tension). After the section is fully cracked, the neutral depth becomes stable and increases slightly at the ultimate state. The addition of fibres seems to increase the depth of the neutral axis, thereby reducing the tension strain of top reinforcing bars.

Based on those theoretical estimations, it can be seen that the strain response of the top reinforcing bars in the case of the GPC beams during the first impact impulse is similar to the strain behaviour of the static cases. The first positive peak of strain in the case of the impacted GPC Beam was corresponding to the first peak of displacement (see Figure 5-12b), at which the section was fully cracked and the neutral axis was above the top bars. This explains why the top reinforcing bars at that moment were in tension (positive strain). The inclusion of fibres also reduced the first peaks of positive strain, which is explained previously due to the increase of neutral depth. Furthermore, it can be seen that after the second impulse occurred, the strain of the top reinforcing bars changed considerably from the high positive to the large negative values. This means that there was a significant shift in the location of the neutral axis during the second phase. Such a phenomenon is distinguishable from the static behaviour of the GPC beams using the BFRP bars, at which the position of the neutral axis remains nearly constant after the section is fully cracked. This can be attributed to the fact that the first impact pulse caused considerable crushing damage to the top concrete cover, and hence be not able to carry any stress. For that reason, when the beam bent further by the second impact impulse, the extreme compression layer shifted to a lower location near the top reinforcing bars and the reinforcing cage was resisting the impact load (as illustrated in Figure 5-14). Consequently, the top reinforcing bars in the control Beam GPC were compressed with the lowest negative value of 0.36%. Finally, the subsequent peaks of the strain in the top reinforcing bars were corresponding to the peaks of midspan displacement during the free vibration of the beams (as shown in Figure 5-12b).

In the cases of the beams reinforced with steel fibres, it can be noted that the peak negative strain in the top reinforcing bars was significantly lower as compared to the control beam. This can stem from the ability to maintain integrity in the top concrete layers of fibre reinforced GPC. For example, as can be seen from Figure 5-7c and d, the top concrete cover of GPC beams reinforced with steel fibres was still intact. Therefore, the extreme compression layer remains close to the top surface of the beams and the location of the neutral axis might not move downward significantly. This results in the top reinforcing bars of GPC beams reinforced with fibres being less compressed than those of the control counterpart. Due to the severe

damage caused by impact loading, the top concrete near the top reinforcing bars suffered severe crushing damage and the compression zone moved downward, causing this region always in the compression state during the free vibration phase. Accordingly, only positive values of strain were recorded in the tests.

The values obtained from the strain gauge attached in stirrups show the unsymmetrical behaviour of the GPC beams reinforced with the fibres, which may result from the inhomogeneous fibre distribution. The plateau in the response of Beams GPC-0.25SF, GPC-0.5PF, and GPC-0.5SF obtained from the right strain gauges was caused by the excess of the range of signal acquisition system. It is worth noting that the maximum strain of stirrups in both sides of the beams can reach 0.8% which is two times higher than the design value of FRP shear reinforcement suggested according to ACI-440.1R-06 [33]. This may indicate the beams under impact loading experienced larger shear cracks than those subjected to static conditions. Finally, due to the malfunction of the acquisition system, the data of strain gauges attached in bottom bars could not be captured.

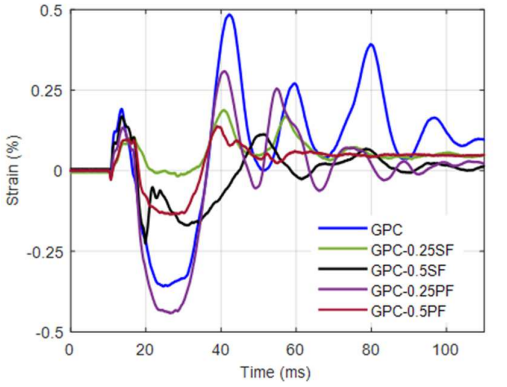

(a)

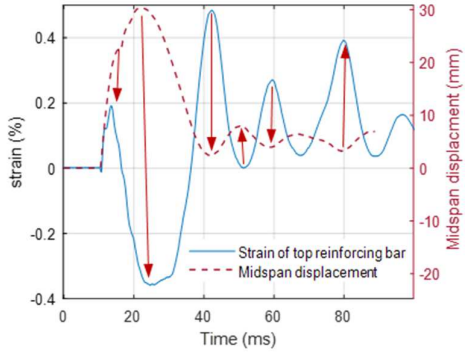

(b)

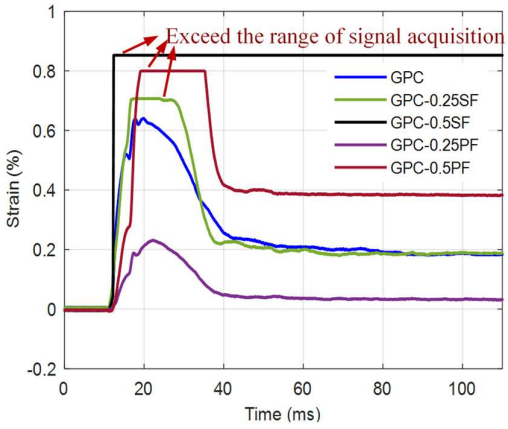

(c)

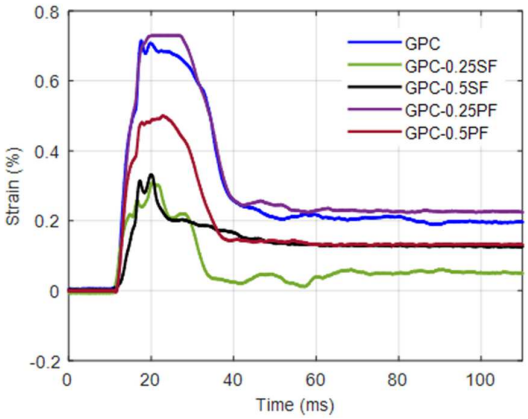

(d)

Note: the strain of Beam OPC and bottom reinforcing bars of GPC beams was not recorded due to malfunction

Figure 5-12. Strains of reinforcing bars: (a) Top strain gauge (TG); (b) Relation between peaks of displacement and top strain gauge in Beam GPC; (c) Right strain gauge (RG); (d) Left strain gauge (LG)

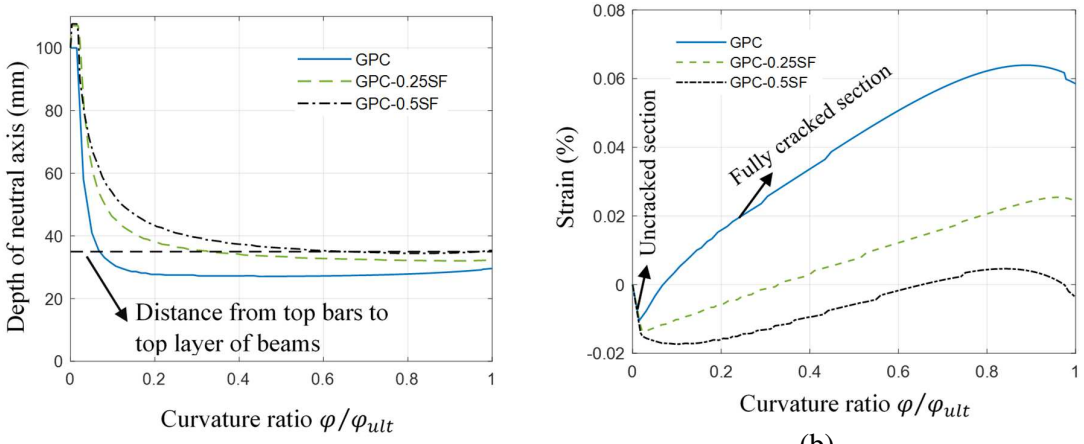

Figure 5-13. (a) Depth of neutral axis and (b) strain of top reinforcing bars vs curvature ratio

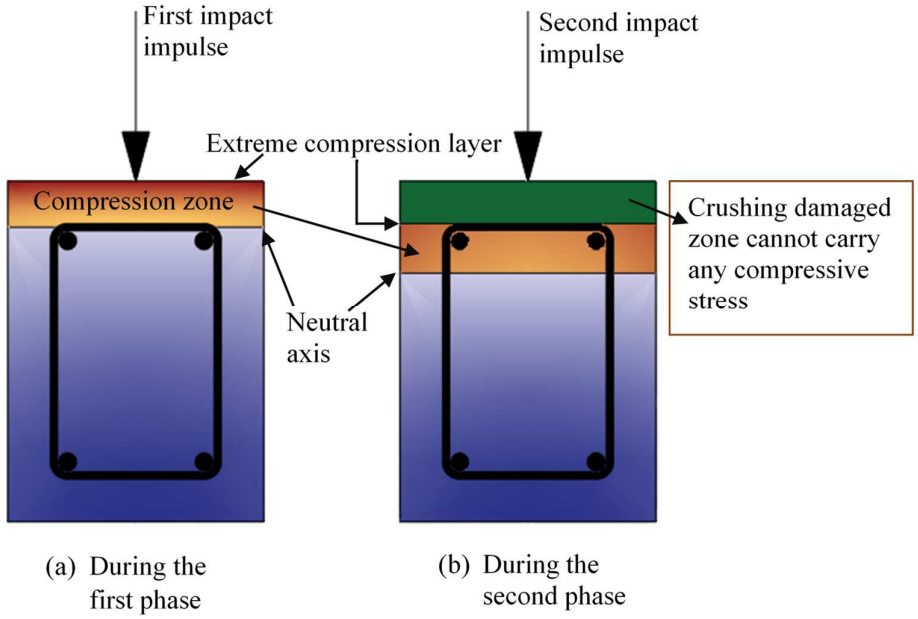

Figure 5-14. The assumed relocation of neutral axis after the second impact happens in the control GPC beam

5.3.5. Loops of impact force vs displacement

One of the critical parameters when investigating the impact response of the beams is the energy imparted in the beams. The imparted energy can be determined based on the variation between the initial and residual kinetic energy of the drop hammer, equating to $\frac{1}{2}M(V_i^2 - V_r^2)$ (M is the mass of drop hammer, v_i and v_r are the initial and residual impact velocity of drop hammer which were estimated by using the image processing technique. The analysing software was provided by Photron company.) [25]. According to the energy conservation principle, the imparted energy also equates to work done by impact force on the drop hammer. Moreover, it can be seen from the loops of impact force vs midspan displacement (as shown in Figure 5-15), there was no separation between the drop hammer and the beams during the impact process from initial to residual configuration. Therefore, it is reasonable to use the integration of the enclosed area under the loop of impact force vs midspan displacement for determining the external work done on the beam.

The imparted energy is transferred into the beams in the forms of the kinetic energy of the beams, the beam deformation, fracture energy, and the indentation effect. In the previous studies, there was an effort to determine the deformation energy of the beams by using the loops of reaction vs midspan displacement [28, 54]. It should be noted that those studies assumed the total reaction of both supports was equivalent to bending force by considering the distributed inertial force as the concentrated load at midspan of the beams. However, it can be noted that when the impact force reached the first peak with the midspan displacement of the beam at 5 mm (see Figure 5-15), the reaction force had been not activated yet and thereby resulting in zero estimated value of deformation energy up to that moment. This is due to the local response of the beams occurring before the global stiffness is activated [23]. Therefore, the static assumption that total reaction is equivalent to bending force may be unsuitable to calculate the deformation energy of the beams under impact loading since the energy consumption during the first phase deformation is not included. Nevertheless, the study in this chapter still adopted the loops of reaction force and mid-span displacement to calculate the deformation energy of the beams because of lacking reasonable methods reported in the literature. The reaction force was measured only from the right-side support. Therefore, it is assumed that the reaction forces of two supports behave symmetrically and thus the total reaction force can be taken as double of the measured reaction force.

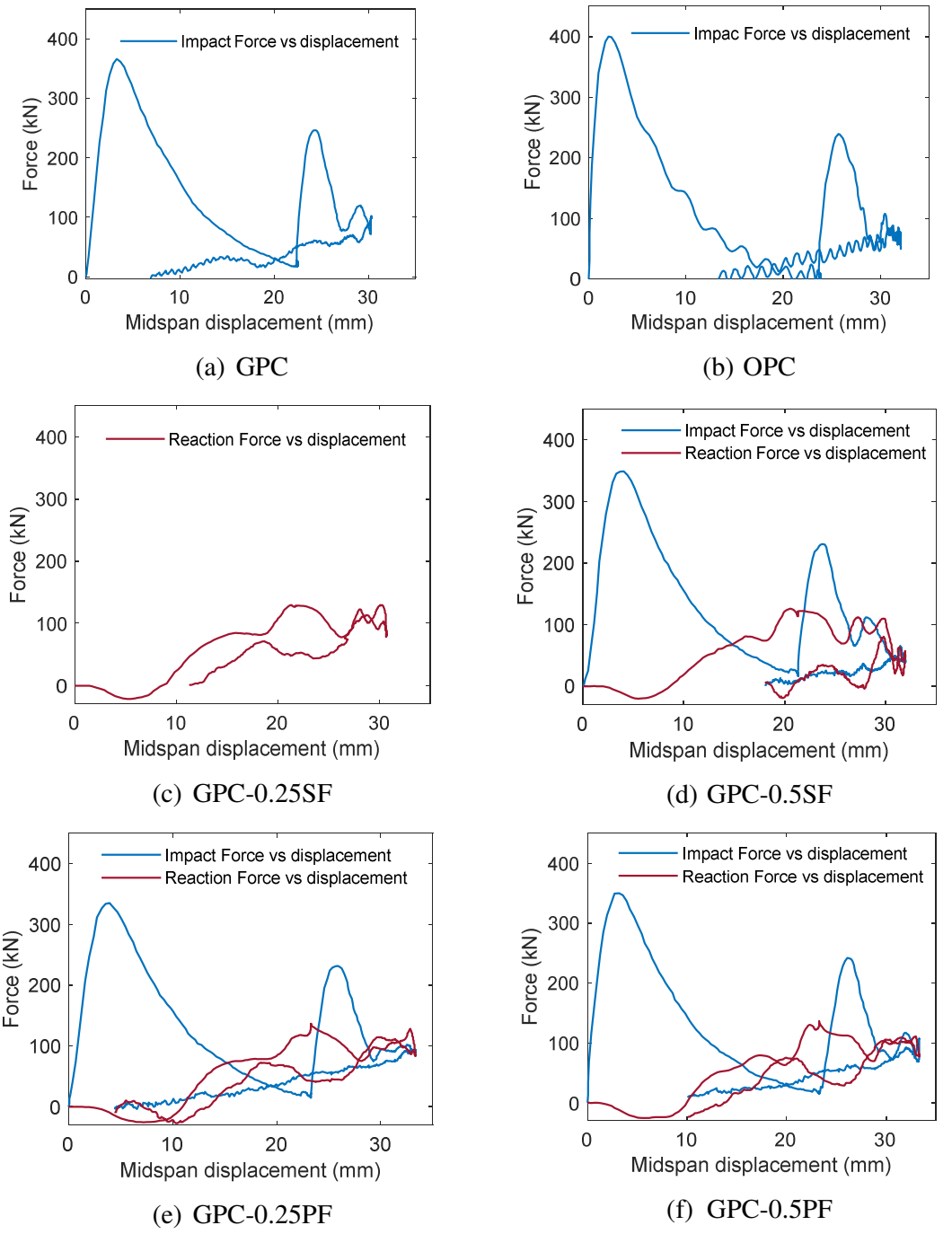

Figure 5-15. Impact force/ reaction force vs midspan displacement loops of the tested beams (no data from some tested cases are available owing to equipment malfunction)

The estimated values of the imparted energy, the work done by impact force, and beam deformation energy are illustrated in Figure 5-16. It can be seen that the calculation of imparted energy and the work done by impact force is remarkably similar, which means that the energy conservation law is satisfied. This demonstrates that both the methods are reasonable to

determine the energy transferred into the beams during the impact process. As shown, energy consumption associated with global beam deformation is only a portion of the total energy imparted to the beam. Other sources that consume energy include stress wave propagation and localized material damage and kinetic energy associated with beam vibrations. As shown, when the beam was reinforced with 0.5% steel fibres, localized damage was effectively mitigated, therefore most imparted energy to the beam converted to global beam deformation.

In general, the variation of fibre content had little effect on the imparted energy of the beams (shown in Figure 5-16). This can be attributed to the insignificant influence of low volume fraction of fibres on the dynamic response of the beams as mention previously. A slightly larger imparted energy was observed in the Beam GPC-0.5SF since it experienced high residual displacement due to severe flexural damage possibly caused by poor distribution of fibre on the local section as discussed above. In general, it can be seen from the figure that the deformation energy of the tested beams made up approximately one-third of the imparted energy (except for Beam GPC-0.5SF), which is smaller than the value (0.6) of the beams without stirrup reported by Kishi et al. [54]. Such variance can be properly explained by the fact that the beams presented in this chapter are strong enough to maintain the longer vibration of the beam and therefore much more energy is expensed for the kinetic movement rather than flexural deformation and fracture of the beams.

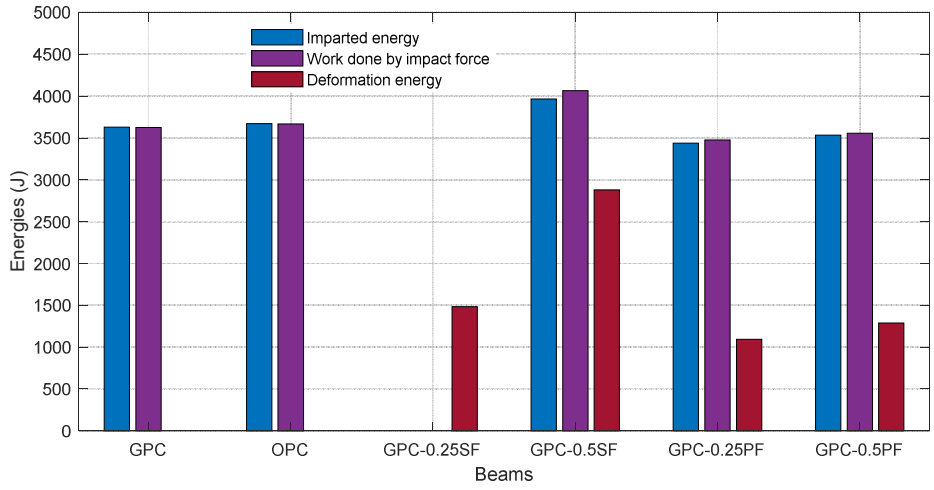

Note: Due to loss of data of impact and reaction forces, some energies of Beams GPC, OPC, and GPC-0.25SF could not be calculated

Figure 5-16. Estimated energies of the tested beams

5. 4. Residual performance of the impacted beams

After conducting the drop-weight tests, all the cracked beams were subjected to monotonic static loads under three-point bending tests to obtain the residual strength. The failure patterns of the beams under the residual strength tests are shown in Figure 5-17. Under the quasi-static loading condition, all the tested beams failed by flexure as the designed shear capacity is much higher than the flexural one. In the case of the control OPC beam, concrete crushing at the loading point caused the failure whereas the GPC beam demonstrated a severe rupture at the bottom reinforcing bars. This can be attributed to the substantial loss of bottom concrete cover which results in the high concentration of tension stress on the bottom bars. After the bars had ruptured, the tension force transferred to the concrete at the end of GPC beam. This led to concrete spalling and anchorage failure at the end of the beam (as seen in Figure 5-17). The inclusion of fibre maintains the integrity of the bottom concrete, and hence all the beams reinforced with fibres except the Beam GPC-0.5SF failed in the same manner as the control beam OPC. Meanwhile, the GPC beam reinforced with 0.5% SF formed a hinge at the existing flexural crack in the early loading stages which led to premature failure. It can be seen from Figures 5-7d and 5-8c, the crack extended almost to the top of the beam after the impact test, which means concrete in that heavily cracked section was almost unable to carry further internal forces. By taking a close observation of the hinge section, it can be noted that there were very few fibres distributed in this section (see Figure 5-17). This might be the reason for the severe local damage with a single dominant crack and high residual displacement of the beams under impact loads, and thereby reduce the residual capacity. Such a phenomenon indicates the complication of impact response and thus it is suggested that further investigation should be conducted to clarify this issue.

Figure 5-18 shows the load vs. midspan displacement curves of all the beams from the residual strength tests. The data of the similar GPC beam without fibre reinforcement subjected to static three-point bending loads was obtained from the previous study [34] for comparison, hereafter named as the static beam. The static GPC beam has the same dimensions and design of reinforcing bars as the control GPC beam of this study. The static GPC beam was also reported to fail by flexural mode with top concrete crushing and no rupture of BFRP bars. Detailed information of the beam can be found in the previous study [34]. From the figure, it can be seen that all the cracked beams behaved nonlinearly from the beginning until reaching the ultimate load. Moreover, the cracked beams exhibited the higher displacements at the service

load compared to the static beam. The benchmark for the service load of these beams is taken as 60% of the ultimate load of the static beam [55]. Figure 5-18 also shows that the cracked beams show relatively similar after-cracking stiffness to that of the static GPC beams while the initial stiffness of the cracked beams was significantly lower than that of the reference static GPC beams. This phenomenon explains the observation that the cracked beams exhibited larger displacement at the service load compared to the reference static GPC beam. Meanwhile, Figure 5-19a shows the effect of fibre on the service displacement of the beams. Due to the bridging ability of fibres to transfer the tensile force and delay the opening of the cracks, the service displacements of fibre reinforced beams reduced significantly by 20% for Beam GPC-0.5PF and 28% for Beam GPC-0.25SF with respect to the control beam GPC. In contrast, the beam reinforced with 0.5% of steel fibres exhibited a very low stiffness and residual capacity contrary to the others. This can be attributed to the defect of the beam related to the poor fibre distribution at the hinge section (as mentioned previously). In general, the inclusion of fibres helped improve the stiffness of the impact-damaged beams at which the SFs seem to be more effective than PFs owing to the higher elastic modulus.

The effect of fibres on the residual capacity of the beams is illustrated in Figure 5-19b. It is interesting to note that increasing the fibre dosage to 0.25% enhanced the residual capacity of the beam whereas increasing further volume fraction of fibre to 0.5% led to less effective improvement. For example, the residual capacity of Beam GPC-0.25PF was 22% higher than that of the control beam GPC while Beam GPC-0.5PF exhibited only 13% improvement. Furthermore, it can be seen that the beams reinforced with SF show poorer performances in terms of residual strength than the PF reinforced specimens. Such a phenomenon is opposite to the trend of the beams tested under quasi-static loading in which the increase of fibre dosage up to 1% for SF or 2% for PF can increase the ultimate flexural strength [1, 56]. The explanation for this phenomenon may be related to the crack and failure patterns of the beams under impact loading. Based on the observations in Sections 5.3.1 and 5.3.2, it is apparent that the impact response and damage of the beams containing more fibres were more dominated by flexure than shear response mode due to the better shear enhancement of fibre reinforcement. Therefore, those beams suffered more severe damage caused by flexural mode compared to the beams using less fibre content, resulting in smaller residual flexural capacity. This implies the addition of high fibre dosage can be effective to achieve the sufficient shear strength of the beam under impact loading but may not be effective in enhancing the flexural capacity. To clarify the phenomenon, it is suggested that further investigations need to be conducted.

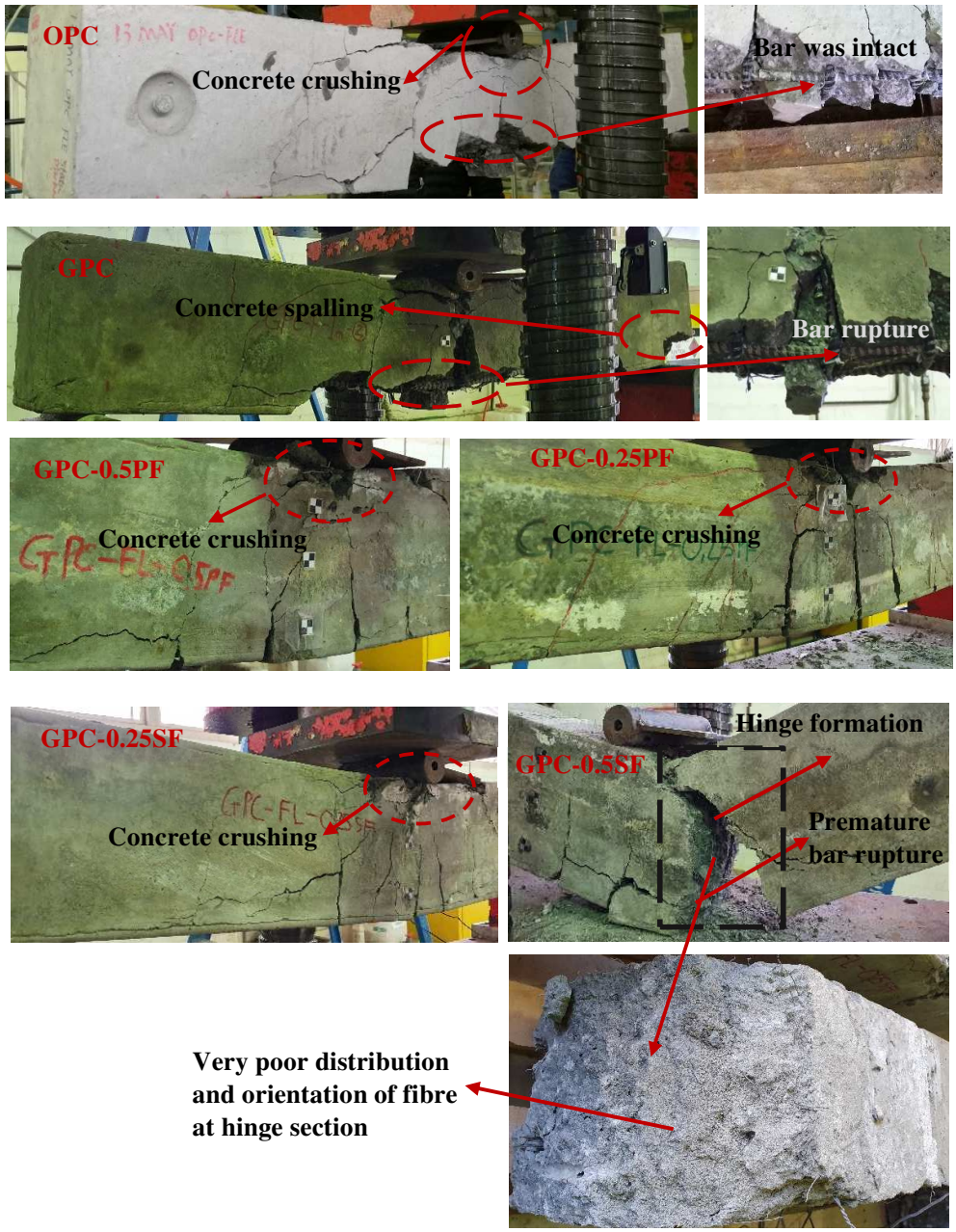

Figure 5-17. Failure patterns of the beams under residual strength tests

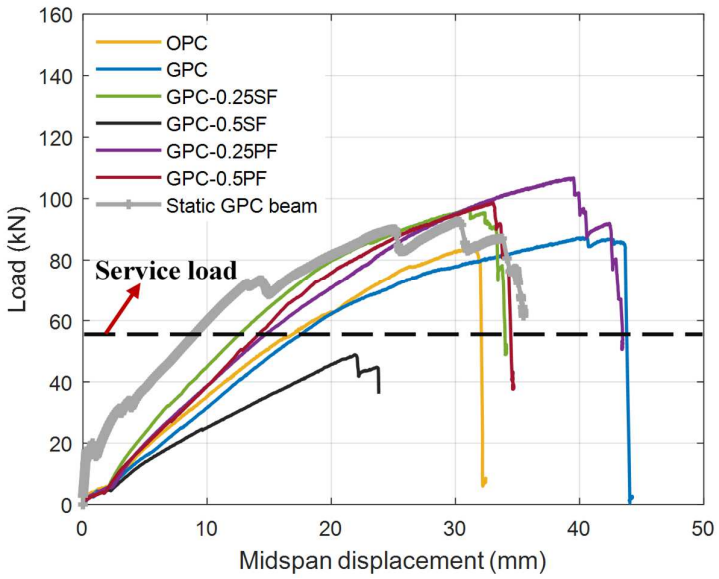

Figure 5-18. Load-displacement curves of the tested beams from residual strength tests

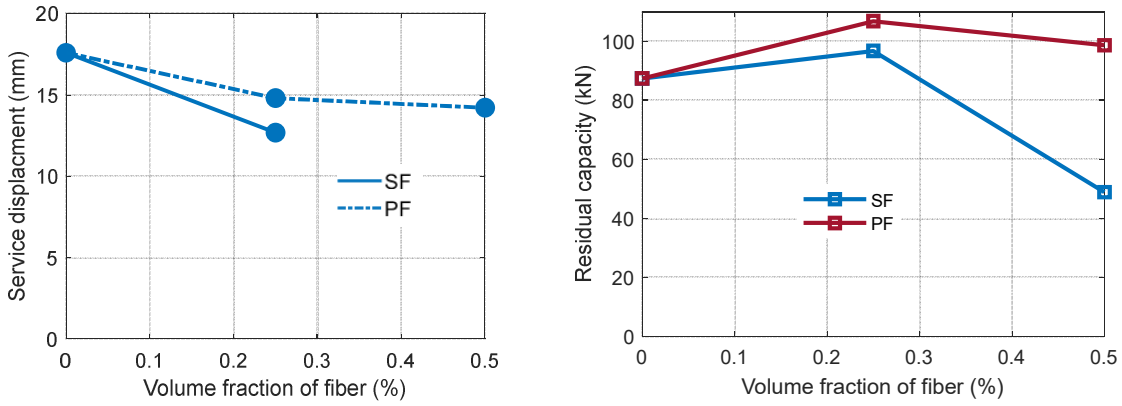

(a) (b)

Note: The service displacement of Beam GPC-0.5SF is not presented since the beam failed prematurely

Figure 5-19. (a) Effect of fibre on service displacement and (b) residual capacity

5. 5. Conclusion

This chapter investigates the impact response of the fibre reinforced GPC beams with BFRP bars for longitudinal and transverse reinforcements. The GPC beam exhibits quite similar behavior to OPC except a severe spalling of concrete cover at beam soffit due to

extreme brittleness of GPC. The inclusion of fibres improves significantly the impact and residual performance of the GPC beams. The main findings can be summarized as follows:

1. Due to the brittle characteristics, the control beam GPC exhibited more severe spalling concrete cover at beam soffit caused by the local stress wave propagation than the corresponding OPC beam.
2. The inclusion of fibres mitigated the spalling damage of concrete cover and also reduced the damage of concrete crushing in the impacted area.
3. Increasing the fibre dosage may change the crack and failure patterns from shear to flexure dominance. The phenomenon became more apparent in the case of SF than PF.
4. In general, the dynamic response of the beams, including the reaction forces, midspan displacement, and energy absorption is not strongly influenced by the presence of fibres due to the existence of sufficient stirrup reinforcement.
5. The damping ratio of the beams increased with the fibre dosage.
6. All the cracked beams failed by flexure under residual loading capacity test as expected. The inclusion of the fibre shifted the failure pattern of GPC beams from the bar rupture to the top concrete crushing.
7. The addition of fibres enhanced the stiffness of the damaged beams which resulted in a decrease of service displacement by 28% compared to the GPC beam without fibre.
8. The residual strength of the beams reinforced with 0.25% PF, 0.5% PF, and 0.25%SF increased by 22%, 13%, and 10% in comparison with the control GPC beam.

Finally, the response of the beams made of GPC under impact loading is quite similar to the OPC counterparts while the fibre reinforcement improves significantly the performance of the beams by reducing the crack and spalling damages and enhance the residual capacity. Therefore, it can be seen that GPC reinforced with fibres has a great potential to be applied in constructions to resist impact loads. Furthermore, the study also indicated that the usage of BFRP bars for longitudinal and transverse reinforcement could be an effective solution for durable structures. Despite being a critical parameter, the influence of longitudinal and transverse BFRP reinforcement ratios has not been investigated yet. Hence, further investigations about this issue should be conducted.

References

[1] Tran TT, Pham TM, Hao H. Experimental and analytical investigation on flexural behaviour of ambient cured geopolymer concrete beams reinforced with steel fibers. Eng Struct. 2019;200:109707.

[2] Sarker PK. Bond strength of reinforcing steel embedded in fly ash-based geopolymer concrete. Mater Struct. 2010;44:1021-30.

[3] Pan Z, Sanjayan JG. Stress–strain behaviour and abrupt loss of stiffness of geopolymer at elevated temperatures. Cem Concr Compos. 2010;32:657-64.

[4] Ariffin MAM, Bhutta MAR, Hussin MW, Mohd Tahir M, Aziah N. Sulfuric acid resistance of blended ash geopolymer concrete. Constr Build Mater. 2013;43:80-6.

[5] Pan Z, Sanjayan JG, Rangan BV. Fracture properties of geopolymer paste and concrete. Mag Concr Res. 2011;63:763-71.

[6] Khan MZN, Hao Y, Hao H, Shaikh FUA. Mechanical properties of ambient cured high strength hybrid steel and synthetic fibers reinforced geopolymer composites. Cem Concr Compos. 2018;85:133-52.

[7] Khan MZN, Hao Y, Hao H, Shaikh FUA. Experimental evaluation of quasi-static and dynamic compressive properties of ambient-cured high-strength plain and fiber reinforced geopolymer composites. Constr Build Mater. 2018;166:482-99.

[8] Khan MZN, Hao Y, Hao H, Shaikh FuA. Mechanical properties and behaviour of high-strength plain and hybrid-fiber reinforced geopolymer composites under dynamic splitting tension. Cem Concr Compos. 2019;104:103343.

[9] Maranan GB, Manalo AC, Benmokrane B, Karunasena W, Mendis P. Evaluation of the flexural strength and serviceability of geopolymer concrete beams reinforced with glass-fibre-reinforced polymer (GFRP) bars. Eng Struct. 2015;101:529-41.

[10] Un CH, Sanjayan JG, San Nicolas R, van Deventer JSJ. Predictions of long-term deflection of geopolymer concrete beams. Constr Build Mater. 2015;94:10-9.

[11] Nguyen KT, Ahn N, Le TA, Lee K. Theoretical and experimental study on mechanical properties and flexural strength of fly ash-geopolymer concrete. Constr Build Mater. 2016;106:65-77.

[12] Visintin P, Mohamed Ali MS, Albitar M, Lucas W. Shear behaviour of geopolymer concrete beams without stirrups. Constr Build Mater. 2017;148:10-21.

[13] Maranan GB, Manalo AC, Benmokrane B, Karunasena W, Mendis P, Nguyen TQ. Shear behaviour of geopolymer-concrete beams transversely reinforced with continuous rectangular GFRP composite spirals. Compos Struct. 2018;187:454-65.

[14] Dong M, Elchalakani M, Karrech A, Pham TM, Yang B. Glass fibre-reinforced polymer circular alkali-activated fly ash/slag concrete members under combined loading. Eng Struct. 2019;199:109598.

[15] Tran TT, Pham TM, Hao H. Rectangular Stress-block Parameters for Fly-ash and Slag Based Geopolymer Concrete. Structures. 2019;19:143-55.

[16] Farhan NA, Sheikh MN, Hadi MNS. Behaviour of Ambient Cured Steel Fibre Reinforced Geopolymer Concrete Columns Under Axial and Flexural Loads. Structures. 2018;15:184-95.

[17] Bhutta A, Farooq M, Zanotti C, Banthia N. Pull-out behavior of different fibers in geopolymer mortars: effects of alkaline solution concentration and curing. Mater Struct. 2017;50:80.

[18] Tran TT, Pham TM, Hao H. Effect of hybrid fibers on shear behaviour of geopolymer concrete beams reinforced by basalt fiber reinforced polymer (BFRP) bars without stirrups. Compos Struct. 2020;243:112236.

[19] Cotsovos DM, Stathopoulos ND, Zeris CA. Behavior of RC Beams Subjected to High Rates of Concentrated Loading. J Struct Eng. 2008;134:1839-51.

[20] Saatci S, Vecchio FJ. Effects of Shear Mechanisms on Impact Behavior of Reinforced Concrete Beams. ACI Struct J. 2009;106:78-86.

[21] Pham TM, Hao H. Behavior of fiber-reinforced polymer-strengthened reinforced concrete beams under static and impact loads. Int J Prot Struct. 2017;8:3-24.

[22] Cotsovos DM. A simplified approach for assessing the load-carrying capacity of reinforced concrete beams under concentrated load applied at high rates. International Journal of Impact Engineering. 2010;37:907-17.

[23] Pham TM, Hao H. Plastic hinges and inertia forces in RC beams under impact loads. International Journal of Impact Engineering. 2017;103:1-11.

[24] Zhao D-B, Yi W-J, Kunnath Sashi K. Shear Mechanisms in Reinforced Concrete Beams under Impact Loading. J Struct Eng. 2017;143:04017089.

[25] Pham TM, Chen W, Elchalakani M, Karrech A, Hao H. Experimental investigation on lightweight rubberized concrete beams strengthened with BFRP sheets subjected to impact loads. Eng Struct. 2020;205:110095.

[26] Pham TM, Hao H. Impact Behavior of FRP-Strengthened RC Beams without Stirrups. J Compos Constr. 2016;20.

[27] Ulzurrun GSD, Zanuy C. Enhancement of impact performance of reinforced concrete beams without stirrups by adding steel fibers. Constr Build Mater. 2017;145:166-82.

[28] Lee J-Y, Yuan T, Shin H-O, Yoon Y-S. Strategic use of steel fibers and stirrups on enhancing impact resistance of ultra-high-performance fiber-reinforced concrete beams. Cem Concr Compos. 2020;107:103499.

[29] Ngo TT, Pham TM, Hao H. Ductile and dry exterior joints using CFRP bolts for moment-resisting frames. Structures. 2020;28:668-84.

[30] Ngo TT, Pham TM, Hao H. Effects of steel fibres and prestress levels on behaviour of newly proposed exterior dry joints using SFRC and CFRP bolts. Eng Struct. 2020;205:110083.

[31] Sadraie H, Khaloo A, Soltani H. Dynamic performance of concrete slabs reinforced with steel and GFRP bars under impact loading. Eng Struct. 2019;191:62-81.

[32] Soltani H, Khaloo A, Sadraie H. Dynamic performance enhancement of RC slabs by steel fibers vs. externally bonded GFRP sheets under impact loading. Eng Struct. 2020;213:110539.

[33] Committee ACI. 440.1R-06: Guide for the Design and Construction of Structural Concrete Reinforced with FRP Bars. Technical Documents.

[34] Huang Z, Chen W, Hao H, Chen Z, Pham TM, Tran TT, Elchalakani M. Flexural Behaviour of Ambient Cured Geopolymer Concrete Beams Reinforced with BFRP Bars under Static and Impact Loads. 2020;Under review.

[35] Ltd BP. https://barchip.com/product/. 2019.

[36] Ltd BP. https://bosfa.com/products/dramix-5d-4d-3d/. 2019.

[37] Nath P, Sarker PK. Effect of GGBFS on setting, workability and early strength properties of fly ash geopolymer concrete cured in ambient condition. Constr Build Mater. 2014;66:163-71.

[38] ASTM I. ASTM C39/C39M-18 Standard Test Method for Compressive Strength of Cylindrical Concrete Specimens. West Conshohocken, PA.2018.

[39] Fujikake K, Li B, Soeun S. Impact Response of Reinforced Concrete Beam and Its Analytical Evaluation. J Struct Eng. 2009;135:938-50.

[40] Ngo TT, Pham TM, Hao H. Effects of different fibre types in monolithic and dry joints using GFRP bolts and reinforcements under impact loading. 2020;Under review.

[41] Folino P, Ripani M, Xargay H, Rocca N. Comprehensive analysis of Fiber Reinforced Concrete beams with conventional reinforcement. Eng Struct. 2020;202:109862.

[42] 426 A-AC. The Shear Strength of Reinforced Concrete Members. ACI Journal Proceedings. 1973;70.

[43] Wight JK, MacGregor JG. Reinforced concrete : mechanics and design. 6th ed. Boston: Pearson; 2012.

[44] Mindess S, Banthia N, Yan C. The fracture toughness of concrete under impact loading. Cem Concr Res. 1987;17:231-41.

[45] Jin L, Zhang R, Dou G, Xu J, Du X. Experimental and numerical study of reinforced concrete beams with steel fibers subjected to impact loading. Int J Damage Mech. 2018;27:1058-83.

[46] Pham TM, Hao H. Influence of global stiffness and equivalent model on prediction of impact response of RC beams. International Journal of Impact Engineering. 2018;113:88-97.

[47] Pham TM, Hao Y, Hao H. Sensitivity of impact behaviour of RC beams to contact stiffness. International Journal of Impact Engineering. 2018;112:155-64.

[48] Ožbolt J, Sharma A. Numerical simulation of reinforced concrete beams with different shear reinforcements under dynamic impact loads. International Journal of Impact Engineering. 2011;38:940-50.

[49] Rhazi J, Hassaim M, Ballivy G, Hunaidi O. Effects of concrete non-homogeneity on Rayleigh waves dispersion. Mag Concr Res. 2002;54:193-201.

[50] Saleh Z, Sheikh MN, Remennikov A, Basu A. Overload damage mechanisms of GFRP-RC beams subjected to high-intensity low-velocity impact loads. Compos Struct. 2020;233:111578.

[51] Franchetti P, Modena C, Feng MQ. Nonlinear Damping Identification in Precast Prestressed Reinforced Concrete Beams. Computer-Aided Civil and Infrastructure Engineering. 2009;24:577-92.

[52] Giner VT, Baeza FJ, Ivorra S, Zornoza E, Galao Ó. Effect of steel and carbon fiber additions on the dynamic properties of concrete containing silica fume. Mater Des. 2012;34:332-9.

[53] Noushini A, Samali B, Vessalas K. Effect of polyvinyl alcohol (PVA) fibre on dynamic and material properties of fibre reinforced concrete. Constr Build Mater. 2013;49:374-83.

[54] Kishi N, Mikami H, Matsuoka KG, Ando T. Impact behavior of shear-failure-type RC beams without shear rebar. International Journal of Impact Engineering. 2002;27:955-68.

[55] Bischoff PH. Rational model for calculating deflection of reinforced concrete beams and slabs. Can J Civ Eng. 2007;34:992-1002.

[56] Yang J-M, Min K-H, Shin H-O, Yoon Y-S. Effect of steel and synthetic fibers on flexural behavior of high-strength concrete beams reinforced with FRP bars. Compos Part B: Eng. 2012;43:1077-86.

Chapter 6. Effect of Fibres on Shear Failure of Ambient-Cured Geopolymer Concrete Beams under Impact Loading

Abstract[5]

This chapter investigates the shear capacity of fibre reinforced geopolymer concrete (GPC) beams subjected to impact loads. For easy examination of the shear capacities, GPC beams, as well as two reference beams made of Ordinary Portland Concrete (OPC), without stirrups were prepared and subjected to the drop-weight impact tests with different contact conditions (direct contact and rubber pad contact). In the case of the beams under direct contact, the failure mode was observed to be a purely diagonal shear failure. The change in concrete material from OPC to GPC showed a marginal effect on the impact response of the beams. Adding fibres into the GPC matrix improved considerably the post-failure behaviour of the beams. The beams reinforced with fibres exhibited not only less concrete spalling and fragmentation but also much higher reaction forces and the second impulse of the impact force. However, the fibre reinforcement seemed to have only a minor effect on the local and contact stiffness of the beams and thus the first impulse of impact force of all the beams was quite similar. The fast Fourier transform (FFT) analysis showed that the adoption of rubber pad contact reduced the highest dominated frequency of impact force from 2.5 kHz to 0.5 kHz. Using rubber pad contact led to the change in the failure pattern of the beams from the purely diagonal shear to the flexure-shear combined failure. The methods used for estimating the imparted and absorbed energy were compared and evaluated. The analysis results demonstrated that the method based on the impact force vs displacement yielded inaccurate results when the inclination angle between drop hammer and the beams increased. Therefore, the study suggests that the variation in the kinetic energy of drop hammer should be used to calculate the imparted energy to the impacted beam.

[5] This chapter was extracted from the paper submitted in International Journal of Impact Engineering, but the tittle of the chapter and subsections were modified to follow the flow of the thesis. The full bibliographic citation of the paper is as follows:
Tran TT, Pham TM, Huang Z, Chen W, Hao H, Elchalakani M. Effect of Fibre Reinforcements on Shear Capacity of Geopolymer Concrete Beams subjected to Impact Loads. 2020; Under Review.

6.1. Introduction

Geopolymer concrete (GPC) is an emerging building material that has great potential to replace Ordinary Portland concrete (OPC) due to the sustainability issue in the production process of Portland cement. The main advantages of GPC over OPC are that the manufacturing process of GPC involves the chemical reaction between aluminosilicate sources and alkali activators, thereby reducing the total CO2 emission [1]. Moreover, recent studies demonstrated that GPC can be synthesized in ambient cured condition with satisfactory compressive strengths (ranging from 40 to 70 MPa) [2, 3]. Apart from sustainable problems, corrosion of steel bars causes critical issues related to the durability of structures. The issues can be potentially solved by using the basalt fibre reinforced polymer (BFRP) bars which have excellent mechanical properties and are cost-efficiency [3]. Therefore, recent studies at Curtin University in Australia have investigated the performance of GPC structures reinforced with BFRP bars. The research project has been conducted in two stages. In the first stage, the improvement of fibre reinforcement in the flexural and shear behaviour of GPC beams subjected to static loading conditions was demonstrated [2, 3]. The second stage focuses on studying the effect of fibre reinforcement on the impact behaviour of GPC beams. The previous study investigated the effectiveness of using fibres to enhance the flexural performance of GPC beams reinforced with longitudinal BFRP bars and stirrups under impact loading [4]. The study presented in this chapter investigates the shear capacity of the fibre reinforced GPC beams subjected to impact loads by drop-weight tests of beams without stirrups.

Due to the intrinsically brittle characteristic of geopolymeric matrix [5], the ambient-cured GPC structures exhibit several adverse aspects of structural performance like poorer cracking resistance and explosive concrete crushing in compression zone when comparing with OPC counterparts [2, 6]. Such problems can be overcome by incorporating fibres into the GPC since fibres can increase the fracture toughness, ductility, and residual tensile strength of the brittle matrix [7]. Particularly, the inclusion of fibres helps not only improve the static flexural strength and ductility of the GPC beams [2] but also enhance significantly the static shear capacity of the GPC beams [3]. Interestingly, the fibres have superior bond strength with GPC compared to OPC [8, 9] and consequently are more effective to improve the static performance of GPC structures [3]. Such differences between GPC and OPC require better understandings and some modifications in current models of OPC structures for application to the design analysis of GPC counterparts. Therefore, studies have been carried out and several models have

been developed to calculate the static capacity of GPC columns [10], the static deflection response [2], and the static shear strength of fibre reinforced GPC beams [3]. These studies have shown that fibres reinforced ambient-cured GPC structures have great potential to be adopted in structural elements subjected to static loading conditions.

There has been no study investigating the effect of fibre reinforcements on the impact response of GPC structures until now. Previous studies have shown that the behaviour of concrete structures under impact loading is distinguishable from that under static loading. For example, because of the presence of inertial force, simply-supported beams subjected to a concentrated impact load at the mid-span exhibit cracks on the top surface of the beams caused by negative bending moment [11, 12]. This phenomenon would not occur in simply-supported beams under static loading conditions. The failure mode of the beams under impact loading could be governed by the shear-dominance mechanism even though the static flexural capacity was designed four times higher than shear strength [13]. Increasing the impact velocity makes the shear-dominance phenomenon become more pronounced and thus leads to a change of the shear failure mode from diagonal tension to punching shear failure [14]. With the impact velocity over 7 m/s, the failure pattern of the beams is dominated by the formation of shear-plug near the loading point (i.e. 45-degree diagonal shear cracks propagating toward impacted point) [15-17]. This phenomenon was explained due to the local response of the beams based on the theory of plastic hinge traveling to supports [18]. If the impact force reaches the first peak in a very short duration, the plastic hinge might not have enough time to arrive at the supports. As a result, only a portion of the beam within stationary points is accelerated, which results in the local damages such as shear-plug cracks near the impact point. Furthermore, some previous studies indicated that the first impulse of impact force was not influenced by the boundary condition and global stiffness [19, 20] but strongly affected by the contact stiffness [21] of the structure under impact. For this reason, the variation in the drop-hammer geometry or contact interlayers can lead to very different impact force profiles and thus the beams' impact response [22]. Through the aforementioned review, it is apparent that dynamic phenomena of reinforced concrete beams under impact loading is complicated and unable to be unveiled based on the static theory. Therefore, it is essential to conduct an experimental study to investigate the impact response of GPC beams.

In the study of this chapter, the shear behaviour of GPC beams reinforced with different types of fibres under impact loading conditions was investigated via the drop-weight tests. There were two control GPC and OPC beams without fibres and four GPC beams with fibre

reinforcement. Two commercial fibre types, namely hooked-end steel fibre (SF) and Vinyl Polypropylene synthetic fibre (PF) were adopted. The low fibre dosage varying from 0% to 0.5% was considered. Due to the corrosive issues of steel bars, basalt fibre reinforced polymer (BFRP) bars were used for longitudinal reinforcement. For better examining the shear capacity of the fibre reinforcement, no stirrup was provided. Finally, two other GPC and OPC beams without fibre reinforcement were tested under different contact conditions by placing a rubber pad on top of the load cell. Based on experimental results, the effect of different kinds of fibres and contact conditions on the impact response of the tested beams was discussed.

6.2. Experimental Procedure

6.2.1. Specimen configuration and test setup

A total of 7 GPC beams and 2 OPC beams with longitudinal BFRP bars (Young's modulus of 55 GPa, tensile strength of 1100-1200 MPa, and breaking elongation of 2%) [23] were fabricated and tested under the drop-weight impact. The dimension of all the beams and the detailed description of reinforcement are presented in Figure 6-1. The beams were 1250 mm long with a rectangular cross-section (width of 150 mm and depth of 200 mm). Two 16-mm diameter BFRP bars were adopted for longitudinal reinforcements with a corresponding ratio of 1.6%. Two strain gauges (LS and RS as shown in Figure 6-1) were placed on the longitudinal reinforcing bars at locations where shear cracks are expected to occur for measuring tension strain. To ensure the accuracy of fabricating the BFRP cages, only three stirrups with 4 mm in diameter were placed at the middle and two supports of the beam. These stirrups were used to properly align the reinforcement cage in a desirable position while they would not affect the shear response because they were placed out of the shear flow zone. The designed beams had the static flexural capacities twice higher than the corresponding static shear strength. As expected, the beams failed in diagonal shear failure under static three-point bending tests [3].

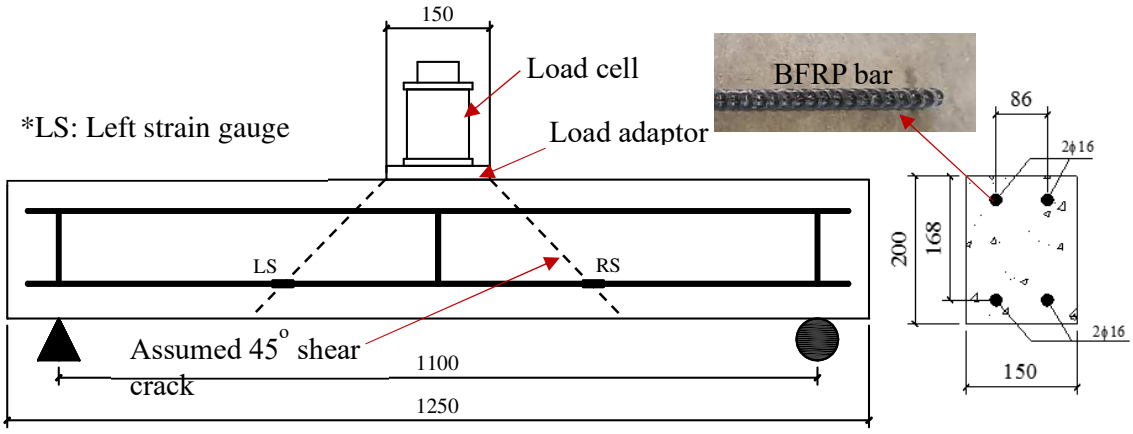

Figure 6-1. Illustration of beam dimension, reinforcement and test configuration

The impact tests were conducted using the instrumented drop-weight test system [16] as shown in Figure 6-2. The beams were simply supported on steel rollers with an effective span of 1100 mm. To prevent uplifting, the pre-load of 40 kN was applied to the supports by tightening the bolts. Therefore, two load cells were placed on the upper and lower rollers at the left-side support to measure the upward (bottom load cell) and downward reaction force (top load cell). At the mid-span, a combination system of a steel load adaptor and load cell (150x150x20 mm with a total weight of 22 kg) was fixed on the top surface of the beam by using fast-cured plaster. The projectile was a hemi-spherical drop-hammer made of a solid steel cylinder with a mass of 208.8 kg and a flat striking surface. The detailed description of the drop hammer can be found in the previous studies [16]. The drop-hammer was placed in a guided tube and dropped freely from 2 m height onto the midspan of the beams. The data of impact force, reaction forces, and the strain was captured by a computerized data acquisition system with a frequency of 50 kHz. Moreover, a high-speed camera with a frequency of 20,000 frames per second was employed to record the failure process of the tested beams.

Two different contact conditions of impact were considered and presented in this chapter. In the first scenario, the projectile collided directly with the top surface of the load cell. In the second condition five layers of rubber pad with a total thickness of 15 mm were placed on top of the load cell (see Figure 6-2b). Such a change in the contact condition would lead to distinguished impact responses of the beams (as presented in Section 6.3).

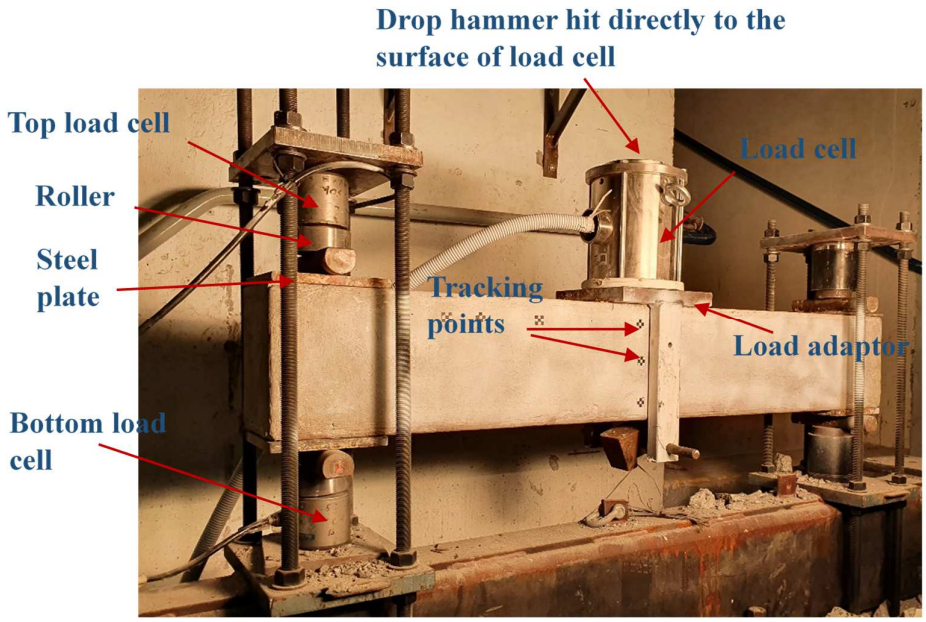

(a) Direct contact

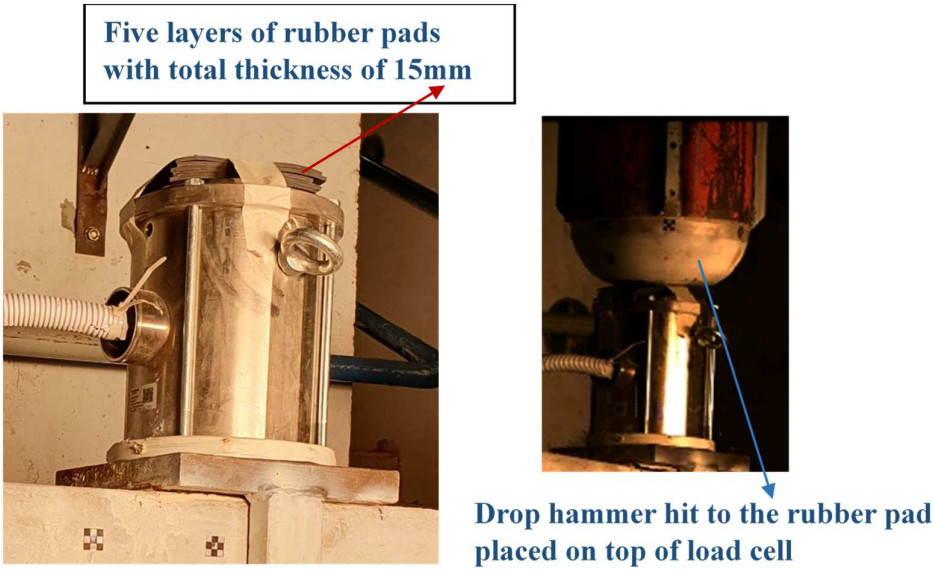

(b) Rubber pad contact

Figure 6-2. Test setup

6.2.2. Specimen classification and material properties

Six beams including two control OPC and GPC beams and four GPC beams reinforced with different types of fibres were cast and tested under direct contact condition (DC). Two other GPC and OPC beams without fibre reinforcement were fabricated and subjected to drop-weight

tests with a rubber-pad contact. The beam classification and compressive strength of concrete material are presented in Table 6-1. Two kinds of fibre reinforcement namely macro hooked-end steel fibre (SF) and macro Vinyl Polypropylene synthetic fibre (PF) were adopted. The volume fraction of fibres considered in this chapter was low ranging from 0% to 0.5% because of the poor workability of the GPC mixture [3]. The properties of macro hooked-end steel fibre (SF) [24] and macro Vinyl Polypropylene synthetic fibre (PF) [25] are provided in Table 6-2 and the actual fibres are shown in Figure 6-3. The designed mixture of GPC is given in Table 6-3. The detailed properties of materials and the casting procedures of GPC beams can be found in the previous study [2]. After casting, all the specimens were cured under the ambient lab condition until testing days.

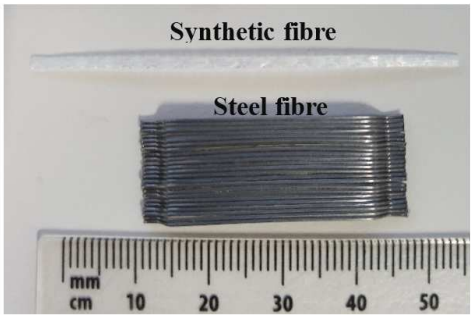

Figure 6-3. Synthetic and steel fibres

Table 6-1. Beam classification and compressive strength

Beams	Impact contact	Fibre volume fraction (%)		$f_c'(MPa)$
		Steel	Synthetic	
OPC-NoF-DC*	DC	-	-	66
GPC-NoF-DC*	DC	-	-	50
GPC-0.25SF	DC	0.25	-	55
GPC-0.5SF	DC	0.5	-	47
GPC-0.25PF	DC	-	0.25	49

GPC-0.5PF	DC	-	0.5	51
OPC-NoF-RP*	RP	-	-	66
GPC-NoF-RP*	RP	-	-	52

*DC: direct contact, *RP: rubber-pad contact

- Not applicable

Table 6-2. Fibre properties

	Fibre shape	Length (mm)	Diameter (μm)	Density (g/cm^3)	Modulus (GPa)	Tensile strength (MPa)
Steel	Hooked-end	35	550	7.8	210	1345
Synthetic	Embossing	48	-	0.9	12	640

-Not applicable

Table 6-3. Mix proportion of GPC (kg/m^3)

Materials	Quantity (kg/m^3)
FA	300
GGBFS	100
Crushed stone	1100
Sand	630
NaOH solution	69
Na_2SiO_3 solution	172

*FA: Fly ash, * GGBFS: Ground granulated blast furnace slag

6.3. Experimental results and discussion

6.3.1. Crack patterns and failure modes

The crack propagation and failure mode of the tested beams under impact load are presented in three subsections. The first subsection compares the cracking behaviour and failure pattern of two control OPC and GPC beams without fibres (Beam OPC-NoF-DC and GPC-NoF-DC). Meanwhile, the effect of different kinds of fibres on the cracking development is discussed in the second subsection. The final subsection examines the influence of different contact conditions on the cracking and failure mode of the beams.

a. General response of the control beams

The cracking behaviour in Beam OPC-NoF-DC at five instants t_1 to t_5 are shown in Figure 6-4a to Figure 6-4e while the final crack and failure pattern are displayed in Figure 6-4f. The corresponding time instants in the impact force vs mid-span displacement curve are indicated in Figure 6-4g. At t_1 = 0.25 ms when the impact force reached the peak, two cracks caused by negative bending moment were initiated at top of the beam while the flexural crack caused by positive bending moment emerged at the bottom of mid-span as shown in Figure 6-4a. The formation of cracks at the top surface of the beam was due to the high inertial force resulting in the negative bending moment in those areas as also observed in the previous studies [16, 18]. Subsequently, the diagonal shear crack close to supports was formed and propagated toward the impacted area at t_2 = 0.5 ms (Figure 6-4b). At this moment, the cracks at the top of the beam caused by negative bending were closed due to the global deformation of the beam. Therefore, after that moment, those cracks could not be easily observed. All the shear and flexural cracks of the beam were fully developed at t_4 = 1.5 ms and then no new crack was formed (Figure 6-4d). The first impulse ended at about t_3 = 1 ms. At the moment t_5 = 4 ms when the second impact occurred, the critical diagonal crack widened substantially which led to a diagonal tension failure of the beam (as shown in Figure 6-4e). After that, the effect of aggregate interlock became insignificant, resulting in high dowel action in the longitudinal bottom reinforcing bars [3]. Consequently, the longitudinal rebars suffered severe splitting damages and the anchorage failure as shown in Figure 6-4f. The spalling concrete at the top of the beam near the impact area and the bottom of the beam close to support (see Figure 6-4f) was observed in the beam. In general, the main response of the beam lasted from t_1 to t_4 (the

duration was about 1.5 ms) which means the first impulse was the primary contributor to the diagonal tension failure of the beam. The subsequent impacts further enhanced the failure and caused reinforcement bar splitting due to dowel action and concrete spalling.

The progressive cracking behaviour and failure pattern of Beam GPC-NoF-DC are shown in Figure 6-5. It can be seen that the main response of the GPC beam in the period from t_1 = 0.25 ms to t_4 = 1.5 ms was almost identical to Beam OPC-NoF-DC (as can be seen from Figure 6-5a to Figure 6-5d). The GPC beam also had the same diagonal tension failure compared to the OPC counterpart (see Figure 6-5e). The minor variance occurred in the post-failure behaviour where the GPC beam suffered more spalling concrete damages and concrete fragmentations caused by tension stress but less severe bar splitting than the OPC specimen. This is due to the more brittle characteristic and lower fracture energy of GPC [2, 26]. However, the overall behaviour of the GPC beam was quite similar to the OPC beam which implies that GPC has great potential to be applied in constructions, replacing concrete structures to resist impact loads.

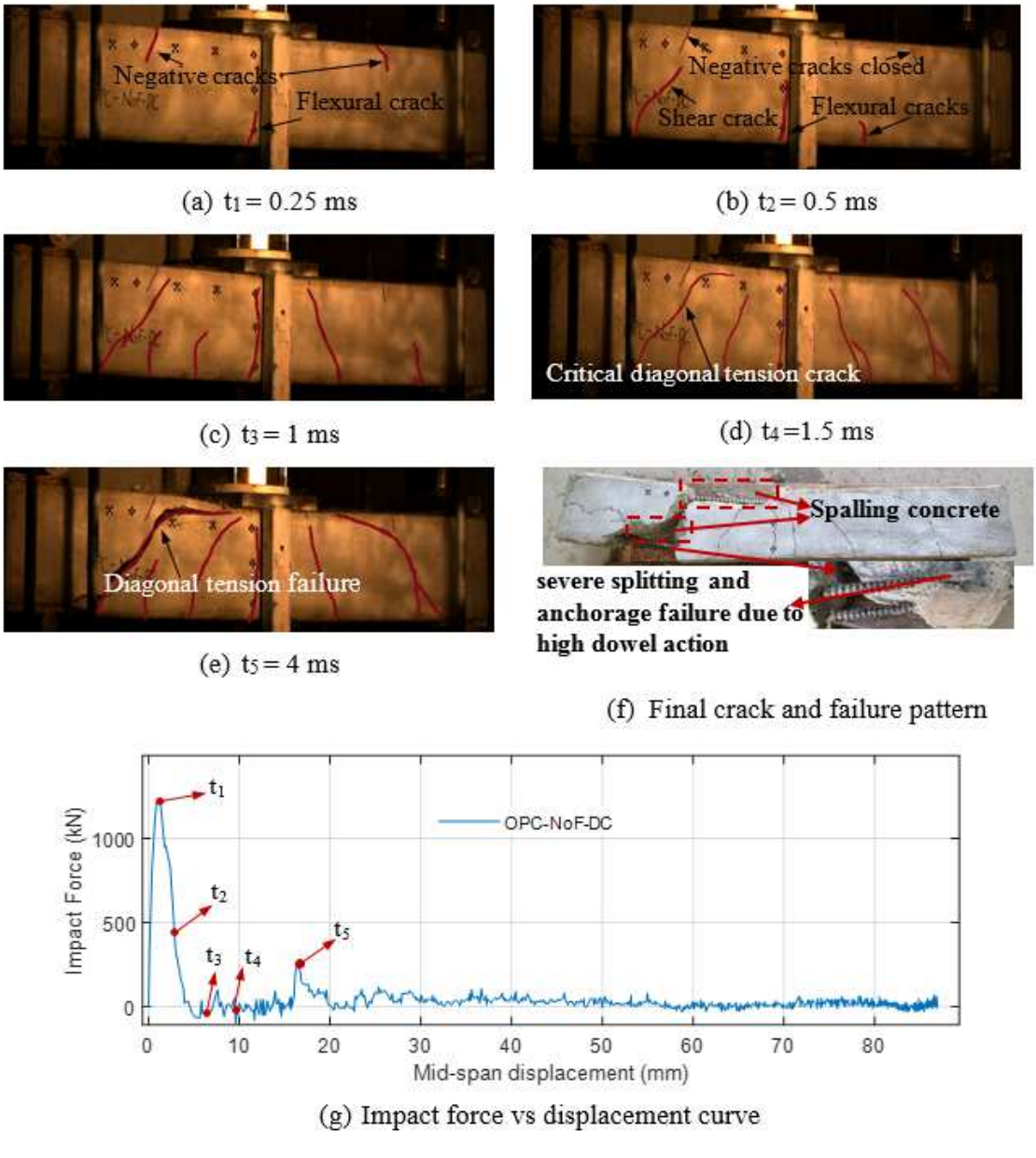

Figure 6-4. The crack propagation and failure pattern of Beam OPC-NoF-DC

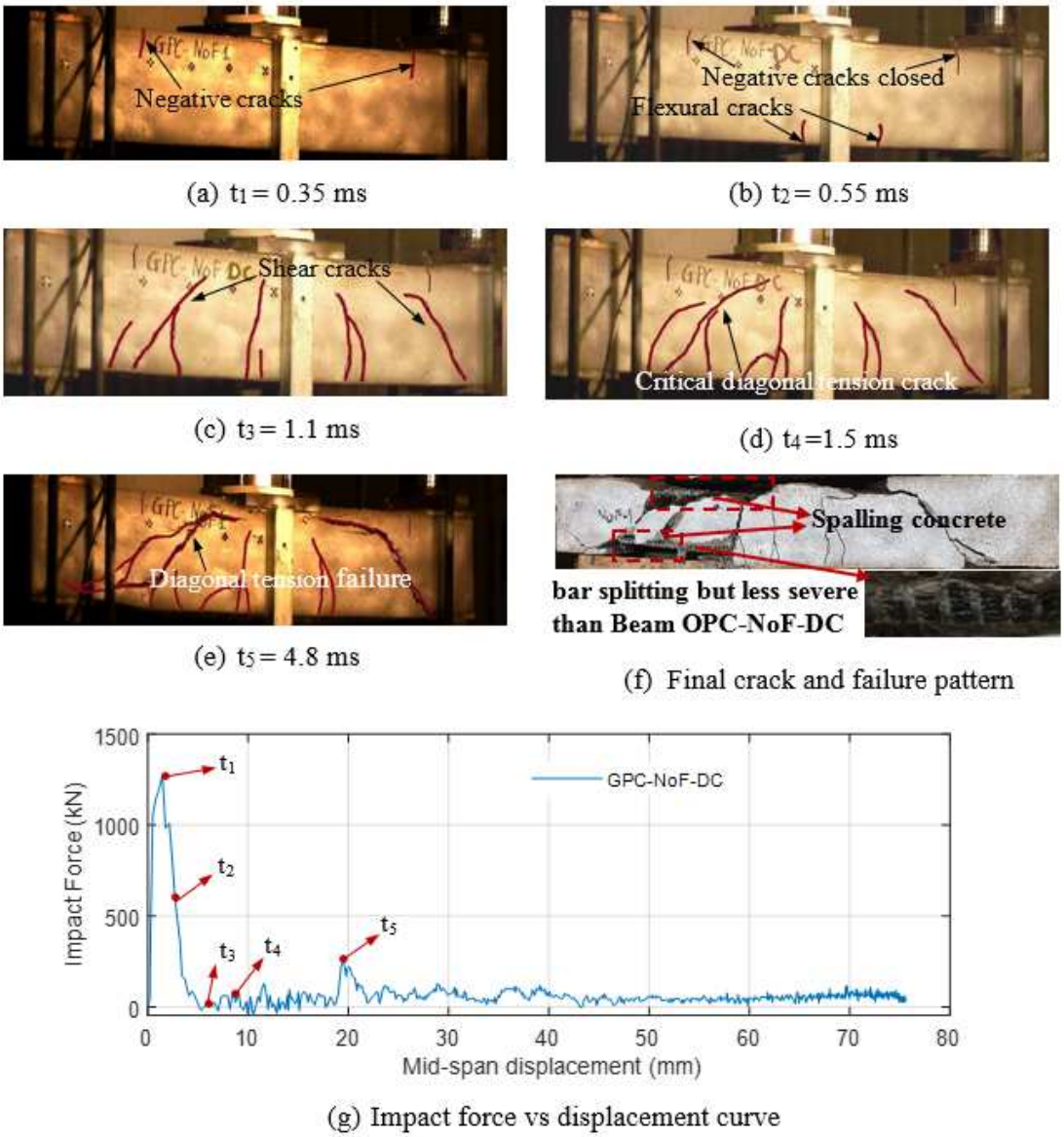

Figure 6-5. The crack propagation and failure pattern of Beam GPC-NoF-DC

b. Effect of fibres on cracking behaviour and failure pattern

The cracking behaviour and failure patterns of the GPC beam reinforced with SF and PF are shown in Figures 6-6 and 6-7. In general, the fibre reinforcement with the volume fraction up to 0.5% was unable to change the failure mode of the tested beams. The results presented in this chapter are consistent with the previous study that using 0.5% fibre could not change the diagonal tension failure mode of the beams [27]. However, due to the bridging effect of fibres, the concrete spalling and fragmentation damage were substantially reduced as shown in Beam GPC-0.5SF and Beam GPC-0.5PF in Figure 6-6f and Figure 6-7f as compared to Beam GPC-

NoF-DC. Furthermore, there was no opening of cracks caused by negative bending moment observed in Beam GPC-0.5SF. This can be explained by the fact that the bridging effect of SFs was effective to mitigate the opening of those cracks. In contrast, because of very low stiffness (12 GPa), the presence of PFs was not unable to prevent the opening of negative cracks.

It is also quite interesting to notice that the beam reinforced with PFs exhibited a narrower critical diagonal crack than the specimen using SFs. This can be attributed to the better bonding behaviour between PF and concrete matrix. It can be seen from Figure 6-8 that the pull-out failure occurred with SFs while the PFs experienced the rupture failure owing to its better bonds to the concrete matrix and relatively low tensile strength. Such a better bonding has resulted from a longer fibre length. Moreover, due to the better bridging effect at the critical crack, Beam GPC-0.5PF also demonstrated less severe damages caused by dowel action. From those observations, it can be suggested that the SFs are effective to delay the opening of cracks caused by negative bending at the early stage of the impact, but the PFs are more effective to control the excessively large cracks in the post-failure stage.

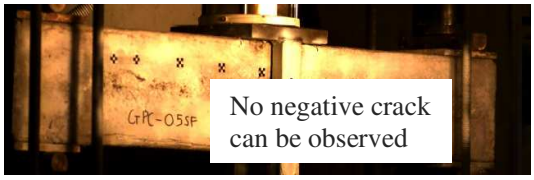

(a) $t_1 = 0.35$ ms

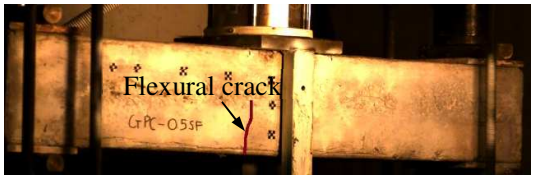

(b) $t_2 = 0.55$ ms

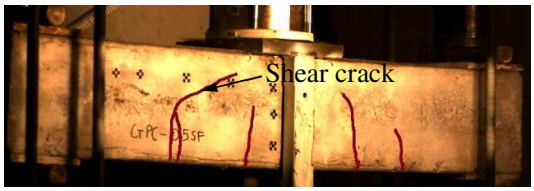

(c) $t_3 = 1.1$ ms

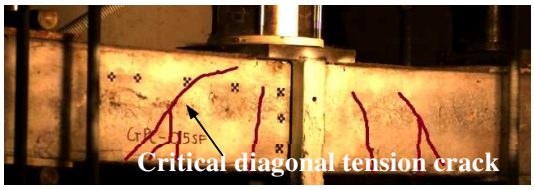

(d) $t_4 = 1.5$ ms

(e) $t_5 = 3.6$ ms

(f) Final crack and failure pattern

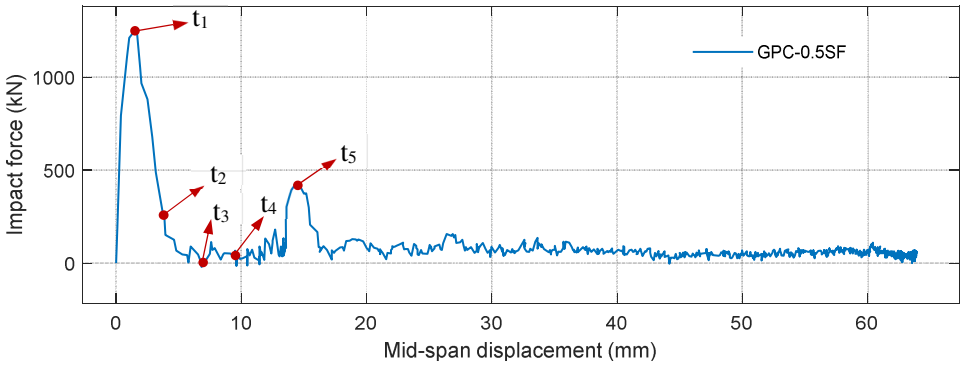

(g) Impact force vs displacement curve

Figure 6-6. The crack propagation and failure pattern of Beam GPC-0.5SF

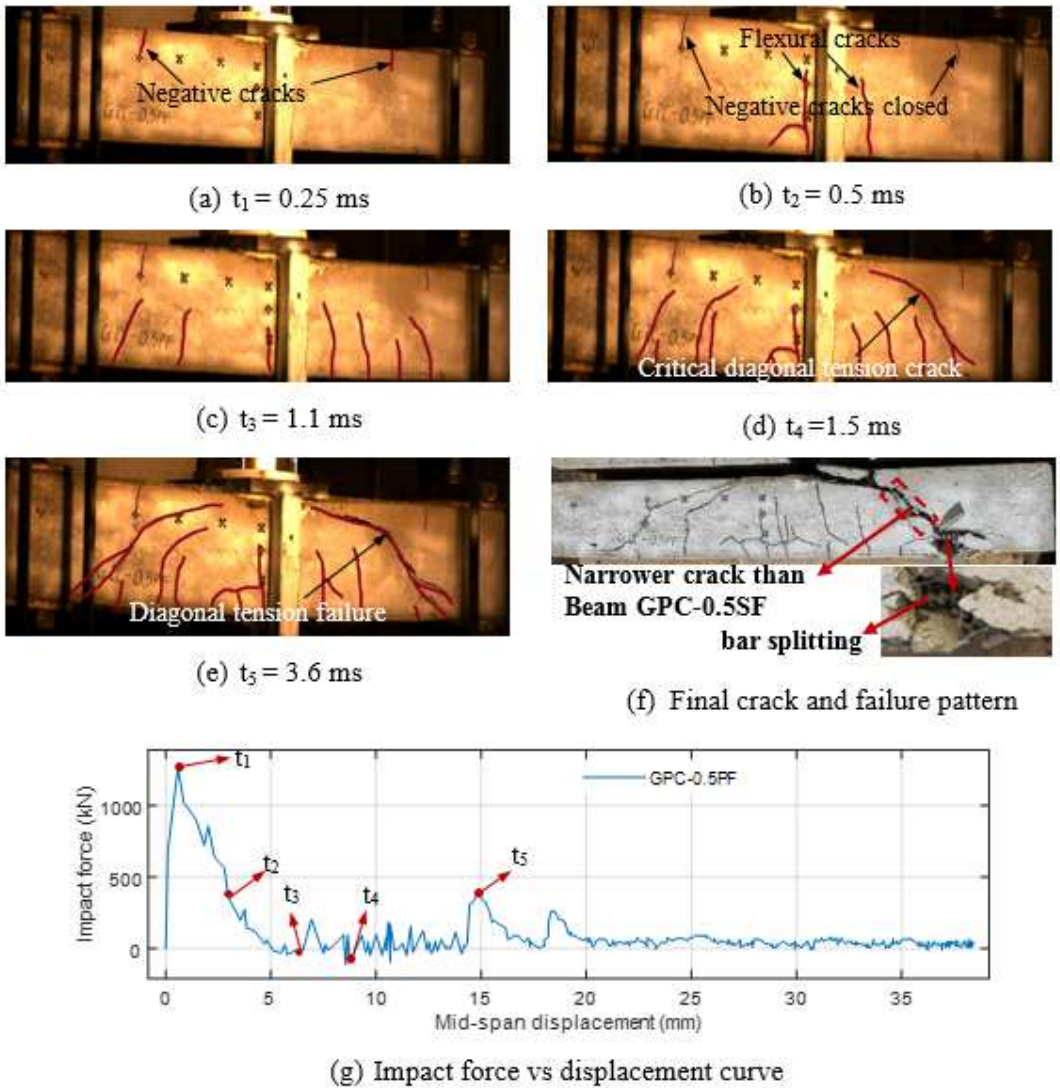

(a) $t_1 = 0.25$ ms

(b) $t_2 = 0.5$ ms

(c) $t_3 = 1.1$ ms

(d) $t_4 = 1.5$ ms

(e) $t_5 = 3.6$ ms

(f) Final crack and failure pattern

(g) Impact force vs displacement curve

Figure 6-7. The crack propagation and failure pattern of Beam GPC-0.5PF

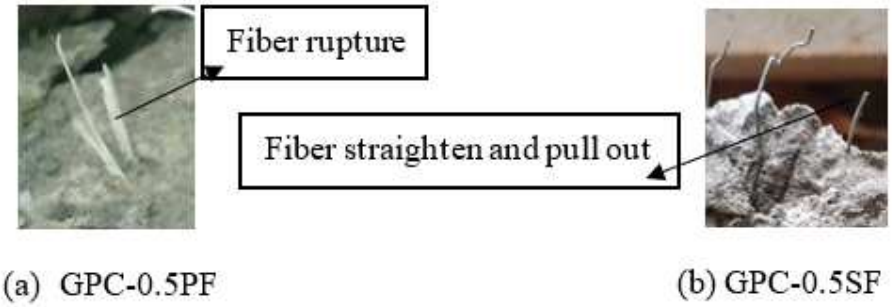

Figure 6-8. The pull-out behaviour of fibre reinforced GPC beams

c. Effect of different contact conditions on cracking behaviour and failure pattern

Changing the contact condition of impact leads to the different contact stiffness which strongly influences the impact behaviour of the beam [21]. It is worth noticing that there was a distinction in the progressive cracking and failure pattern of the beam using rubber-pad contact (see Figure 6-9a to Figure 6-9f) and the specimen applying direct contact (see Figure 6-5a to Figure 6-5f). Firstly, the progressive failure happened more slowly and there was no formation of cracks caused by the negative bending moment observed in Beam GPC-NoF-RP. This can be explained by the fact that when using rubber pad layers, the contact stiffness of the impact area decreased, thereby reducing significantly the impact force (as shown in Figure 6-9g). Consequently, the inertial force decreased considerably, which resulted in a smaller negative bending moment. If the negative bending moment is small, the tensile stress in concrete is smaller than its tensile strength and thus the cracks on top of the beam are not formed. Moreover, it can be noted that the cracking behaviour and failure pattern of the beam using rubber pad layers were dominated by a combination of flexure and shear failure mode. For example, despite exhibiting shear cracks, the beam also demonstrated severe concrete crushing on the top of the beam along with the rupture at the longitudinal reinforcing bars (see Figure 6-9f) caused by the flexural response. This could be attributed to the use of the rubber pad layers which reduced the impact force but elongated the impact duration [22]. It can be seen from the impact force vs mid-span displacement curve of Beam GPC-NoF-DC (Figure 6-5g), the first impulse ended in 1 ms with a peak of 1278 kN. Due to such a high impact force occurring in a short duration, the beam only experienced a small, namely 5 mm deformation, before failing by diagonal shear. Meanwhile, the first impact impulse of Beam GPC-NoF-RP lasted until 4 ms with a considerably smaller peak of 278 kN. Hence, more flexural deformation of the beam involved in the impact response compared to the specimen using direct contact and

the beam damage mode changed from the shear dominance to combined shear and flexure mode. The two considered contact conditions represent the two rather extreme impact conditions in reality, i.e, direct stiff contact and soft contact. Actual impact conditions in practice are likely to have the contact stiffness falling between these two scenarios as upper and lower bounds.

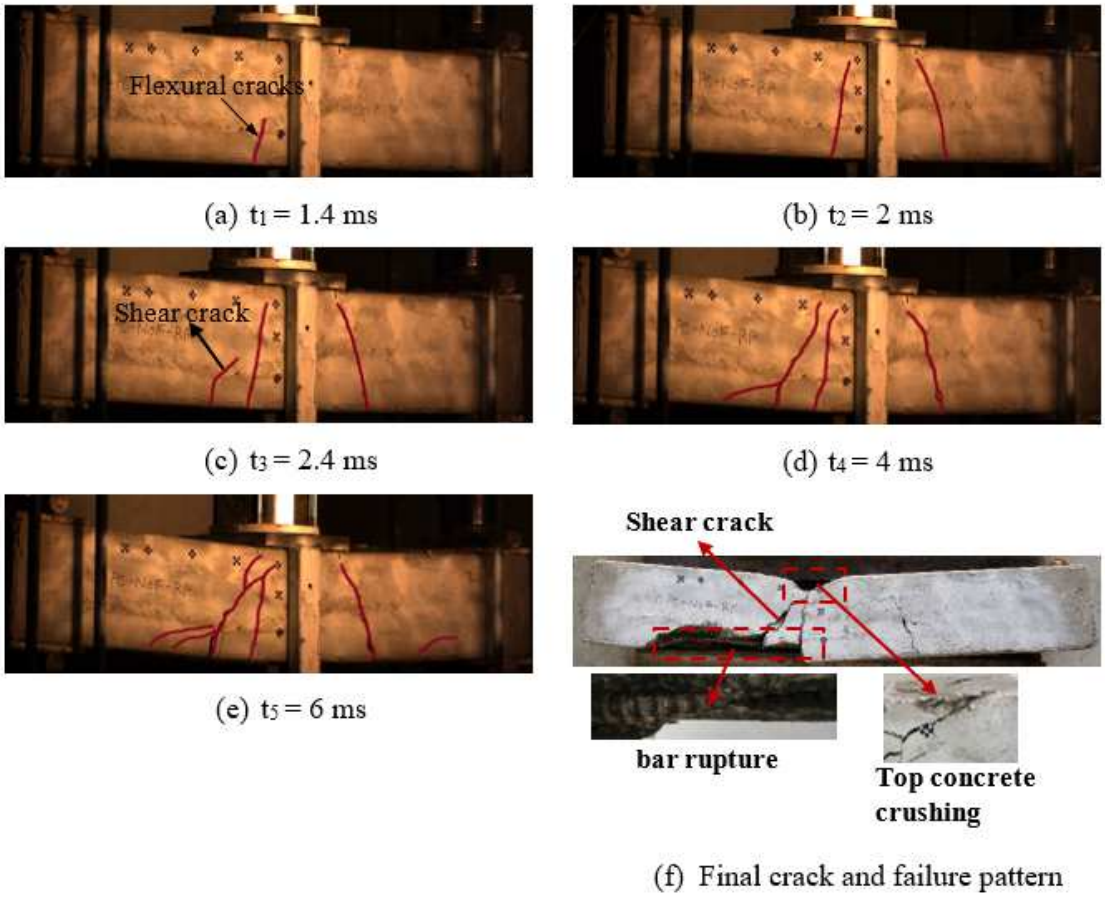

Figure 6-9. The crack propagation and failure pattern of Beam GPC-NoF-RP

6.3.2. Dynamic forces

In this section, the effect of fibres and contact conditions on the dynamic forces including impact forces and reaction force was investigated. The Fast Fourier Transformation (FFT) was also adopted to examine how the rubber pad contact affected the dominated frequency of impact forces. The experimental results of the drop-weight tests are presented in Table 6-4.

a. General response of the control beams

The time histories of the impact force and reaction force of two control Beams OPC-NoF-DC and GPC-NoF-DC are presented in Figures 6-10a and b while the comparisons of the forces from the two beams are illustrated in Figures 6-10c and d. To clarify the influence of fibres on the impact response of the beams, the previous study classified the impact force of the beams into four phases [28]. In this chapter, the profile of the impact force is classified into two phases and exhibited in Figure 6-10c. Phase 1 with duration of 1.5 ms included the first impulse of the impact force is taken from the initial impact to the instant when the diagonal tension cracks of the beams were entirely developed (equivalent to t_4 as defined in Section 6.3.1). Meanwhile, Phase 2 describing the following response of the impact force after Phase 1 corresponds to the post-failure period of the beam. It can be seen that the impact force of Beam OPC-NoF-DC reached the first peak in short duration (0.25 ms) and then decreased to zero at 0.8 ms, which implies a separation between the drop-hammer and the beam. After that, the impact force increased to the second peak due to the second collision of the drop-hammer and the beam. The second impulse also lasted for 1 ms and the impact force subsequently reduced to a small value close to zeros at 7-8 ms. The reaction force was initiated slightly behind the action of the impact force, starting with a negative value before increasing up to the positive values. Such a phenomenon was also observed in the previous studies [12, 13] and explained due to the arrival of Rayleigh waves [12].

It can be noted that the impact force of GPC and OPC beams were similar with the first peaks of 1278 kN and 1253 kN and the second peaks of 237 kN and 263 kN, respectively. Additionally, there was no significant difference in the reaction force of Beams GPC-NoF-DC and OPC-NoF-DC in the initial stage either. The reaction force of both the beams achieved the peak at approximately 2 ms with the value of 89 kN and 81 kN for GPC and OPC, respectively. After 20 ms, the reaction force of the two beams became divergent as shown in Figure 6-10d. It is because of the difference in the post-failure behaviour where Beam OPC-NoF-DC experienced a higher dowel action, resulting in the anchorage failure at the end of the

longitudinal reinforcing bars (see Figure 6-4f). At the moment of anchorage failure, the bar detached from the concrete matrix which led to the upward movement of the beam end. Therefore, the reaction force of Beam OPC-NoF-DC decreased suddenly to the negative value of 40 kN. Meanwhile, the damage of the reinforcing bar due to dowel action in GPC beam was less severe. The damage occurred mainly due to concrete fragmentation and spalling. However, in general, changing material from OPC to GPC with comparable compressive strength did not show noticeable variation in the main response of the dynamic forces of the beams.

Table 6-4. Experimental results of impact tests

Beam	V_0 (m/s)	V_r (m/s)	P_{ud}^1 (kN)	R_{ud} (kN)	P_{ud}^2 (kN)	δ_{pd} (mm)	δ_{rd} (mm)
OPC-NoF-DC	6.33	-1.1	1253	81	237	86.9	52.9
GPC-NoF-DC	6.30	-0.3	1278	89	263	75.2	24.8
GPC-0.25SF	6.38	-0.4	1357	117	419	47.8	27.1
GPC-0.5SF	6.20	-0.0	1253	121	419	63.9	48.5
GPC-0.25PF	6.23	-1.0	1200	100	445	55.8	21.0
GPC-0.5PF	6.22	-1.3	1304	120	445	38.1	9.9
OPC-NoF-RP	6.24	-0.7	281	127	149	42.3	35.6
GPC-NoF-RP	6.18	-0.5	267	129	164	64.3	37.6

P_{ud}^1 and P_{ud}^2: peaks of the first and second impact force, and R_{ud}: peak of reaction force

δ_{pd} and δ_{rd}: maximum and residual displacement

V_0 and V_r: initial impact and residual velocity of drop hammer

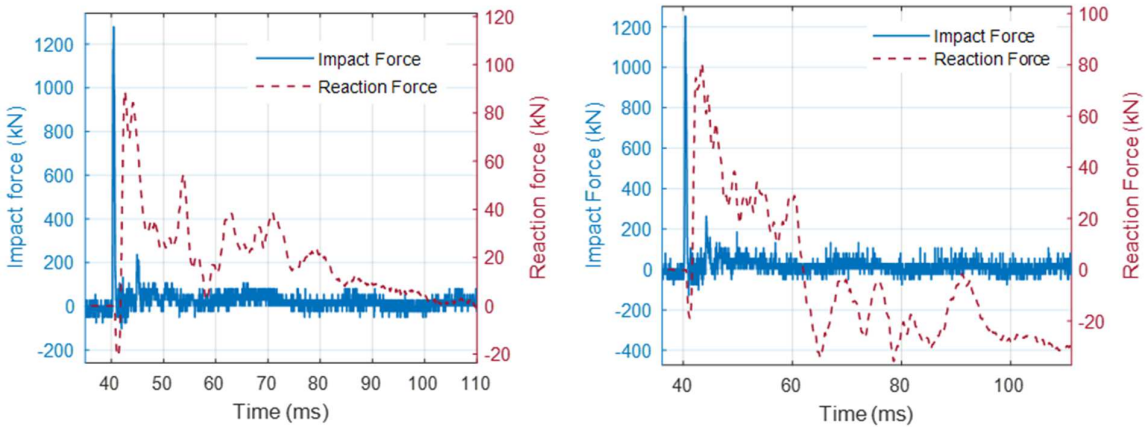

(a) (b)

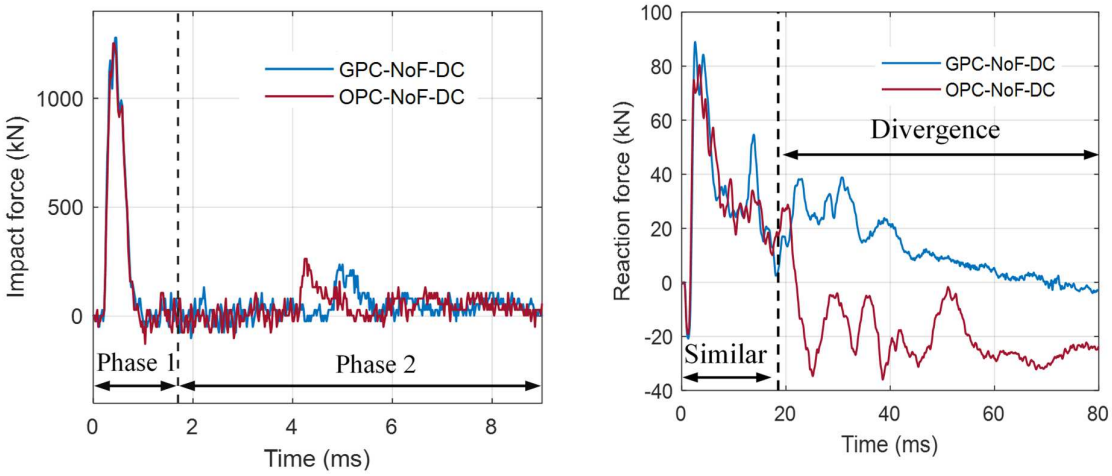

Figure 6-10. Impact and reaction force profile of Beam GPC-NoF-DC (a) and Beam OPC-NoF-DC (b); the comparison of impact force (c) and reaction force (d)

b. Effect of fibres on the dynamic forces

The impact force response of the fibre reinforced GPC beams is presented in Figure 6-11. It is worth noting that the inclusion of fibre had a marginal effect on impact force in Phase 1 but strongly influenced that in Phase 2 (see Figure 6-11c). Particularly, the beams using the fibre reinforcement only exhibited a minor change in the first peaks of impact force (the highest increase of 6% when using 0.25% fibres) whereas there was an obvious trend that incorporation of fibre increased the second peaks by 87%. To explain this phenomenon, a brief discussion of the influence of global stiffness on the impact response of the reinforced concrete beams was conducted in a previous study. By using the numerical simulation method, Pham and Hao [20] demonstrated that if the first impact impulse occurs in a short duration, the beams only respond locally and the global stiffness does not affect the response of the beam in that duration. As expected, the duration of the first impulse observed in the tested beams presented in this chapter is short, i.e., 0.8 ms which is comparable to that in [20]. This means that the impact response was governed by the local stiffness of the beam in the early stage. Therefore, it can be inferred that the presence of fibre did not influence considerably the local stiffness. However, Phase 2 of the impact force was influenced significantly by the global stiffness of the beam [20]. The incorporation of the fibres improved significantly the shear stiffness of the beam and hence increased the second peak of the impact force. In contrast, such a significant increase in the peaks of the second impulse might not necessarily happen in the beams dominated by flexural

stiffness as discussed in the previous investigation [28]. This is because fibres are more effective to enhance the shear strength than the flexural capacity [29]. Moreover, fibre reinforcement also reduced the damage intensity caused by the first impact force in Phase 1, therefore the beam stiffness was not substantially degraded as compared to that of the non-fibre reinforced beams, which therefore also resulted in a larger second peak impact force.

Interestingly, as can be seen from Figure 6-11b, the GPC beams reinforced with PFs experienced the third peak and their magnitudes increased with the volume fraction of fibres (184 kN and 315 kN in the cases of 0.25% PF and 0.5% PF, respectively). This can be attributed to the better bonding of PFs with concrete matrix which resulted in more residual strength after the beam damage in Phase 1. Meanwhile, the SF reinforced GPC beams cannot carry more force (no third peak observed) due to the pull-out failure of fibres after the critical diagonal cracks opened widely. It can be seen from Figure 6-8, SFs mainly exhibited pull-out failure while the rupture failure was primarily observed in PFs. From those observations, it can be concluded that the impact force in Phase 2 was strongly influenced by the inclusion of fibres, in which PFs performed better than SFs. The main reason for the less efficient enhancement of SFs can be attributed to the pull-out failure resulted from the shorter fibre length.

Furthermore, the presence of fibres can increase slightly the reaction forces (as shown in Figure 6-12). In terms of the beams using PFs, the peak reaction forces increased by 12% to 35% with the increasing volume fraction from 0.25% to 0.5%. This can be attributed to the fact that the reaction force is affected by global stiffness [20] which is improved through the addition of fibres. Meanwhile, the beam using 0.25% SFs demonstrated a similar increase of the reaction force as the beam with 0.5% SFs (see Figure 6-12a), and the increase in the peak reaction force is about 34%. These results indicate that SF reinforcement is effective in enhancing the beam stiffness which affects the reaction force, but increasing the SF dosage from 0.25% to 0.5% has a minimum effect. The reason why increasing the SF dosage does not affect the beam impact response is not clear. Further investigation is therefore needed.

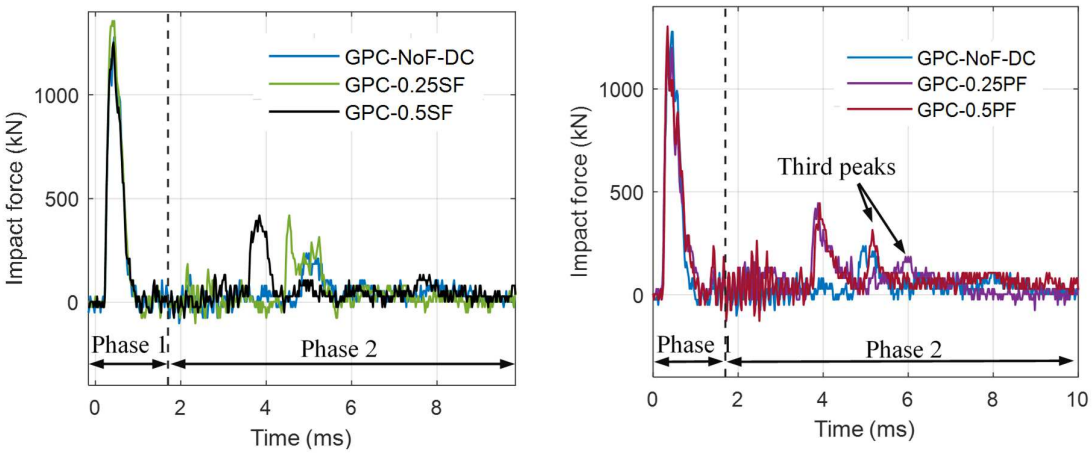

(a) (b)

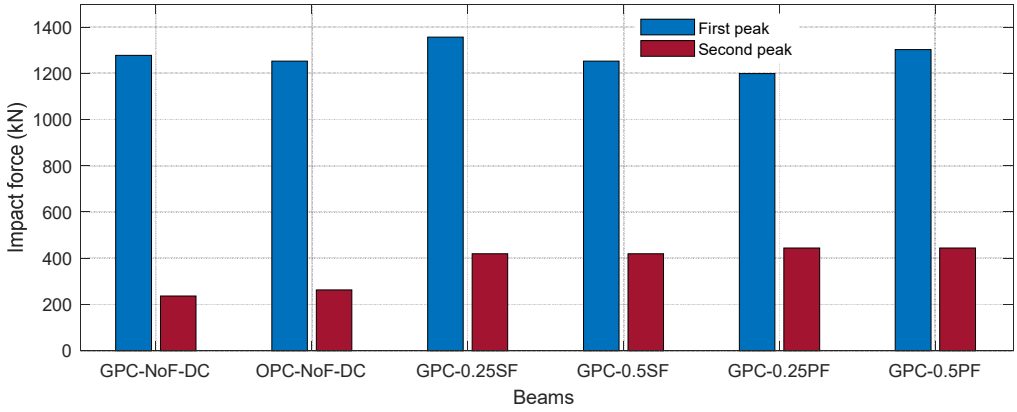

(c) Peaks of impact force

Figure 6-11. Impact force of beams with SFs (a) and beams with PFs (b); comparing peaks of impact force (c)

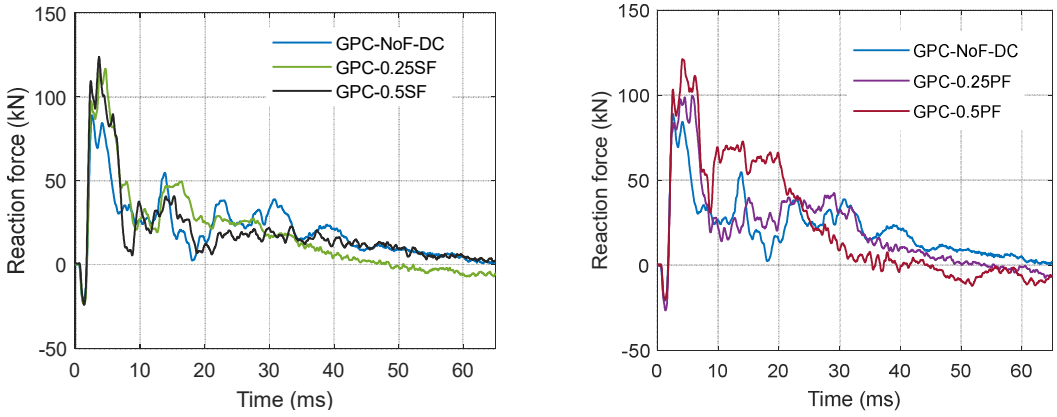

(a) (b)

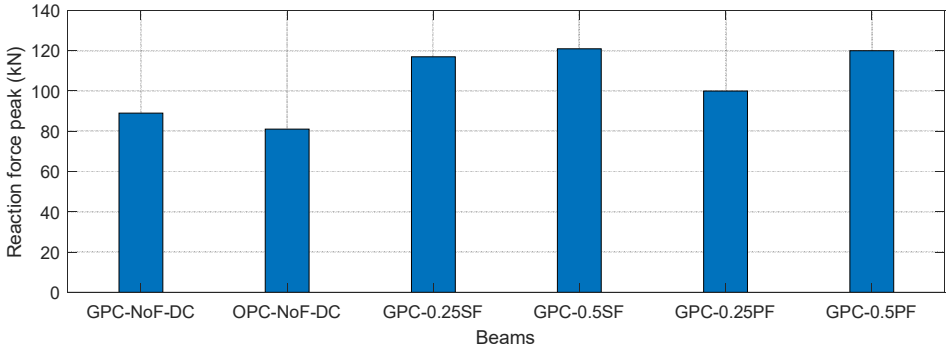

(c)

Figure 6-12. Reaction force profile of beams with SFs (a) and beams with PFs (b); comparing peaks of reaction force (c)

c. Effect of different contact conditions on the dynamic forces

The impact force profile was demonstrated to be heavily dependent on the contact stiffness between the drop-hammer and beam [21]. The variation of the contact stiffness in impact tests may result from different usage of interlayers such as metal plates and rubber pads [22], or change of contact quality by using plaster [21]. Previous studies consistently concluded that a decrease in the contact stiffness led to a reduction in the peak of impact force but prolonged the duration [21, 22]. In this chapter, the first peak amplitude of the impact force of the beams adopting rubber pads was only a quarter of that recorded in the direct contact case but the duration (4 ms) was five times longer (see Figures 6-13a and c). This can be attributed to the considerably lower contact stiffness when using rubber pads. Moreover, the loading frequency is also one of the critical parameters when evaluating the impact response of structures. Therefore, the Fast Fourier Transform (FFT) technique was employed to transfer the time-domain plots of the impact force into the frequency domain (see Figures 6-13b and d). As can be seen from those figures, the frequency band of impact force with direct drop-weight contact is a lot wider up to 2.5 kHz, while the impact force acting on beams with rubber pads exhibited a narrower bandwidth of frequency, i.e., 0-0.5 kHz. This can be explained by the fact that the large portion of impact energy caused by high-frequency waves was filtered out by the rubber deformation.

The difference in the reaction forces of the beams with different kinds of contact conditions is plotted in Figure 6-14. It can be noted that there was no negative reaction force observed in the early stage of the beams adopting the rubber pad contact. Similar findings were reported in the previous numerical investigation [22]. It is believed that since the major portion of the impact

energy was transferred into the deformation of rubber pads, the energy converted into surface Rayleigh wave might be relatively small, thereby leading to the negligible negative reaction force. Furthermore, it is worth noticing that the peaks of reaction forces increased significantly by 50% when changing from direct contact to rubber pad contact. This can be attributed to the difference in impact force when changing the contact condition. In cases of the beams using the direct contact condition, the first impulse of impact force happened in a very short duration (0.8 ms) with a very high peak (~ 1250 kN). In the period of the first impulse, the impact force was resisted mainly by inertia force and the reaction force was not activated [18]. Therefore, the maximum shear force during the first impulse was equal to half of the first peak of impact force [16]. If the maximum shear force was higher than the dynamic shear capacity it led to the very early shear failure of the beam as observed in Section 6.3.1. During this period, the contribution of the reaction force to resisting the impact load was minimum. The contribution of reaction force to the resistance of the impact became significant after the first impulse, but at a smaller amplitude because the subsequent impact force amplitude was smaller. Moreover, intensifying the damage in the beam, e.g., friction at the shear cracks induced by the first impulse would also contribute to resisting the subsequent impact, hence led to smaller reaction force. In contrast, the impact force of beams with the rubber pad contact was a lot smaller (~266 kN) and duration longer (4 ms). As a result, during the first impulse, the inertia force was substantially smaller, and the beams overcame the early shear failure and subsequently experienced flexural failure due to the second impulse. The impact force was mainly resisted by the reaction force. Therefore, the recorded reaction force was even higher than that recorded on the beam subjected to direct impact although the impact force amplitude was lower.

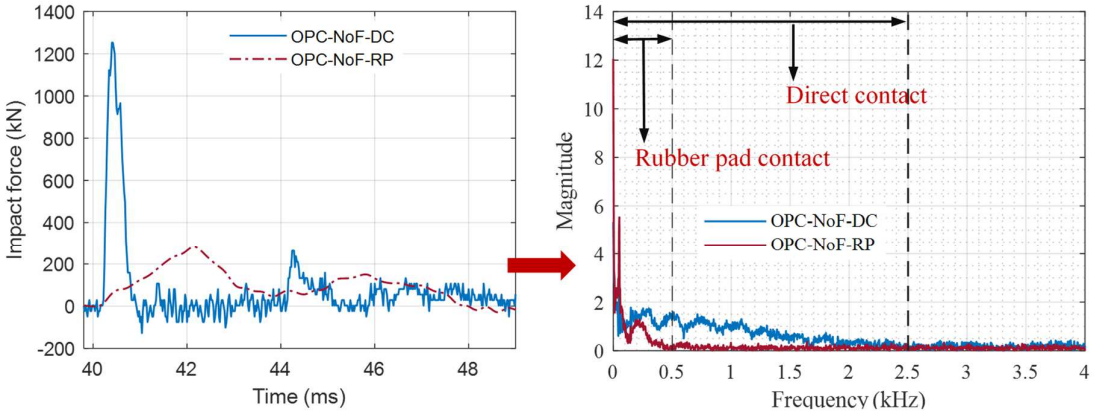

(a) Time-domain of impact force of OPC beams

(b) Frequency-domain of impact force of OPC beams

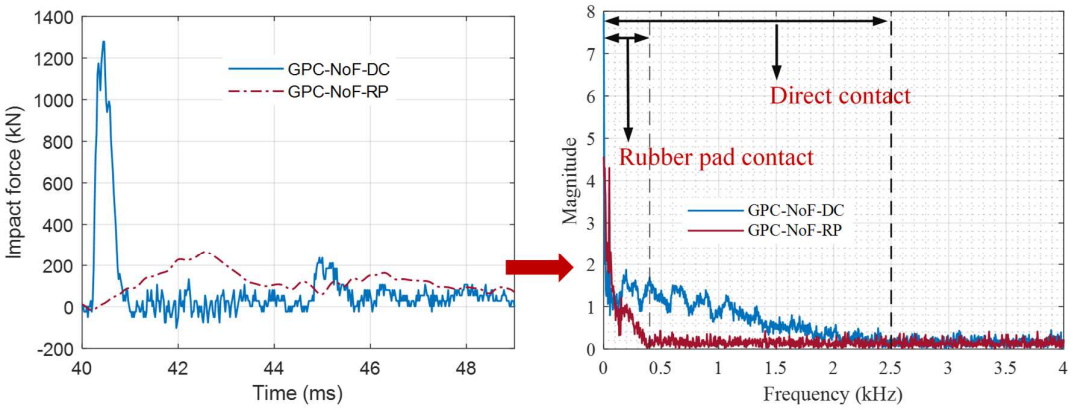

(c) Time-domain of impact force of GPC beams

(d) Frequency-domain of impact force of GPC beams

Figure 6-13. Comparison of impact force profiles and their FFT spectrums of beams with different contact conditions

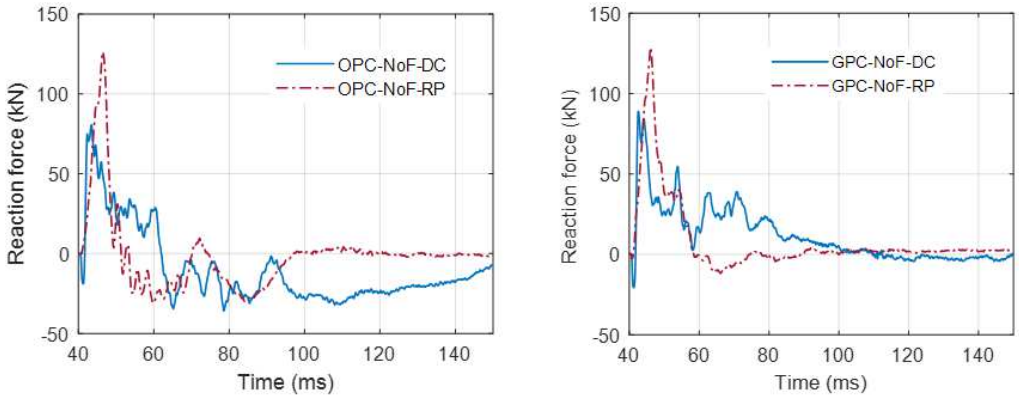

(a) OPC beams

(b) GPC beams

Figure 6-14. Comparison of reaction forces of beams with different contact conditions

6.3.3. Displacement response and estimated energy

d. Displacement response

The time history of mid-span displacement derived from the image processing is presented in Figure 6-15a while the maximum and residual displacement are illustrated in Figure 6-15b. It can be seen that all the beams exhibited a negligible oscillation in the free vibration phase. This was due to severe damages caused by diagonal tension failure in the transient state response. It should be noted that the beams failed by diagonal tension cracks at the early stage (t_4 = 1.4 ms as discussed in section 6.3.1) when the displacement reached roughly 9 mm. Therefore, the

maximum and residual displacements of the beams are associated with post-failure behaviour such as dowel action and concrete spalling. For example, the control GPC beam suffered a smaller maximum and residual displacement than the OPC specimen. It was because the GPC beam experienced less dowel action failure and hence maintained the good integrity of reinforcing bars.

It is worth noting that the inclusion of fibres can reduce considerably the maximum displacement of the beams. Reinforcing the beam with the volume fraction of 0.25% and 0.5% of PFs decreased the maximum displacement by 26% and 50% as compared to the reference beam. Meanwhile, reinforcing the beam with 0.25% SF is more effective compared to 0.25% PF reinforcement, however, further increasing the SF volume to 0.5% shows insignificant improvement. A similar phenomenon was also recorded in the previous study where the GPC beam using 0.5% volumes fraction of SFs exhibit no enhancement in the impact performance compared to the beam reinforced with 0.25% fibres [8]. Such an issue is believed to be related to the pre-mature pull-out failure due to the poor bonding of SFs. The fibre length of SFs used in the study presented this chapter may not be sufficient to bridge the large cracks formed in impact incidents. Nonetheless, it is suggested that there should be further investigations to clarify this observation.

Moreover, the residual displacement of the beams can be reduced by the addition of PFs. Adoption of 0.5% PF decreased the residual displacement of the control GPC beam by 58%. Nevertheless, the incorporation of SFs is unable to reduce the residual displacement. It should be noted that the residual performance of the beams is primarily dependant on the recovery of the elastic deformation of reinforcing FRP bars. If the FRP bars maintain the integrity after the transient state, more deformation of the beam can be recovered and less residual displacement exists. As discussed in Section 6.3.1, all the beams using SFs experienced severe damages to reinforcing bars such as rupture and splitting failure (see Figure 15-6f). This is the reason why those beams suffered large residual displacement. On the other hand, with better bonding, PFs reduce excessive opening of diagonal cracks, thereby mitigating the dowel action failure of the reinforcing bars.

The displacement response of the beams corresponding to the two contact conditions is plotted in Figure 6-16. It can be seen that the beams using rubber pad contact exhibited a smaller displacement than those impacted directly. This is inconsistent with the findings of a previous study [22] where the displacement of the beams with rubber pad layers in the impact area was

larger compared to the specimens using steel plate contact. Since the top surface of the load cell was made of steel, it is reasonable to consider the steel plate contact of the previous study to be equivalent to the direct contact condition of the study presented in this chapter. That previous study explained that the higher portion of the impact energy was transferred to the beams using rubber pad interlayers due to the longer contact duration. It should be noted that the explanation might be valid when the response of beams under both direct contact and rubber contact conditions is governed by the same flexural mode, i.e, bending deformation only and no shear failure occurs. In the study of this chapter, the tested beams using direct contact failed abruptly in shear failure mode after undergoing the first impulse. This means that the overall stiffness of the beams reduced sharply, and hence subsequent impulses caused large displacements. The adoption of rubber pad contact decreased significantly the impact force which led to less severe damages of the beams in Phase 1. Consequently, the beams could maintain the integrity of the overall stiffness, and thus the displacement was smaller.

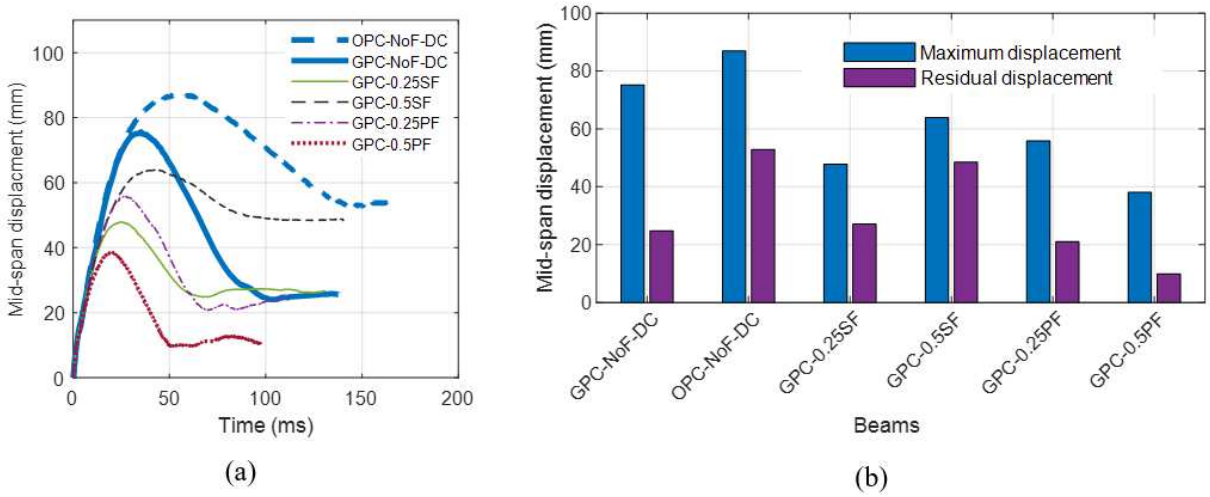

Figure 6-15. Time histories of mid-span displacement of the tested beams (a); maximum and residual mid-span displacement of the tested beams (b)

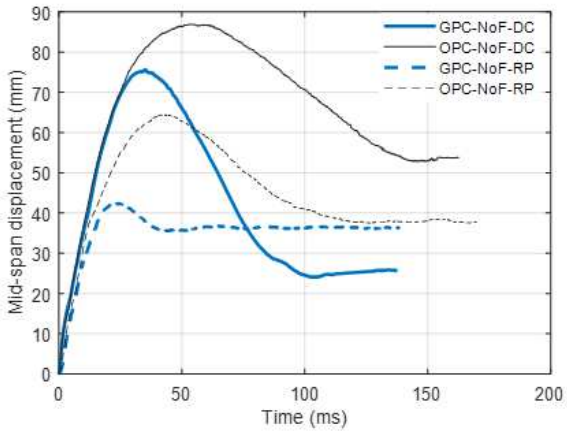

Figure 6-16. Time histories of mid-span displacement of beams using different kinds of contact conditions

e. Estimating forms of energy

One of the critical aspects of the structural performance under impact loads is the ability to absorb impact energy. In the literature, total energy transferred into the beams can be calculated by integrating areas under the impact force vs. displacement curve [14]. However, this method might be inappropriate if the separation between the drop-hammer and the beam occurs during the transient stage [12]. An alternative method is to use the variation of the kinetic energy of the drop hammer to estimate the energy transferred into the beams [12]. The transferred energy is converted mainly in the forms of deformation energy, fracture energy, and kinetic energy of the beams [4, 12]. There have been some previous studies calculating the portion of energy transforming into the deformation and fracture of the beams based on the area under the reaction force vs displacement curve [30, 31]. Even though those methods were adopted in the previous studies and provided reasonable results, the quasi-static assumptions of the methods might be unreasonable if the impact force happens in a short duration and vanishes before the beam deflection reaches the maximum values [12]. Therefore, in this section, those methods were examined based on the analysis results and some suggestions for using the methods were recommended.

If the energy loss during collision is assumed to be negligible, the equation of energy imparted into the beams at a certain time, *t* can be expressed as

$$\frac{1}{2}M(V_0^2 - V(t)^2) = W(t) \tag{6-1}$$

where M is the mass of drop hammer, V_0 is the initial impact velocity of drop hammer at the first collision, and $V(t)$ is the impact velocity of drop hammer at a certain moment, t after the first collision. The velocity, $V(t)$, of drop hammer was obtained by taking the tangent slopes of the time history of displacement curve of the drop hammer. $W(t)$ is external work done by impact force at time t which can be estimated by integrating the area under impact force vs displacement curve of the beam. In the case of the beam using the rubber pad contact, the energy stored in forms of the deformation and fracture of rubber (E_{rub}) need to be considered as presented in Eq. (6-2):

$$\frac{1}{2}M(V_0^2 - V(t)^2) - E_{rub} = W(t) \tag{6-2}$$

Eqs. (6-1) and (6-2) demonstrated that the energy imparted into the beams can be determined by two methods: Method 1 adopted the time history of drop hammer velocity while Method 2 used the impact force vs displacement curves.

Furthermore, a portion of imparted energy is absorbed mainly in forms of deformation and fracture of the beams and the other is dissipated in forms of the kinetic energy of the beam. Therefore, by assuming that the energy loss during beam vibration is small, the energy-balanced equation of the beam can be written as follows:

$$\frac{1}{2}M(V_0^2 - V(t)^2) = E_a(t) + E_k(t) \tag{6-3}$$

At a certain moment t, $E_k(t)$ is the kinetic energy of the beam while $E_a(t)$ is the absorbed energy of the beam caused by deformation and fracture. Meanwhile, other forms of energy consumption owing to indentation or energy loss due to damping and friction were not considered in this chapter. To calculate the portion of energy absorbed in forms of deformation and fracture, the previous studies employed the concept of the true bending load placed at midspan of the beam as expressed below [31, 32]:

$$P_b(t) = P_t(t) - P_i(t) = R_1 + R_2 \tag{6-4}$$

The free body diagram to derive the Eq. (6-4) is illustrated in Figure 6-17. In Eq. (6-4), $P_t(t)$ is the impact force measured from the load cell at time t, $P_i(t)$ is the concentrated load equivalent to the distributed inertial load (see Figure 6-17), $P_b(t)$ is the true bending load,

R_1 and R_2 are the reaction force at two support (see Figure 6-17). It is assumed that the absorbed energy in forms of beam deformation and fracture is caused by the true bending force $P_b(t)$. Therefore, the absorbed energy $E_a(t)$ is equivalent to the work done by the true bending force $P_b(t)$ on the displacement of the beams. The value of true bending force $P_b(t)$ equals to the total reaction force of both supports (as shown in Eq. 6-4). As a result, the absorbed energy $E_a(t)$ can be estimated simply by integrating the area under the total reaction force vs mid-span displacement curve [30, 31]. Since the study presented in this chapter only measured the reaction force at the right support, the total reaction force can be taken as the double of the measured reaction force by assuming that the response of the beam is symmetrical.

Figure 6-18 shows the total reaction force vs midspan displacement and the shaded area represents the total absorbed energy E_a. It should be noted that in the early stage, due to local response the displacement of the beam reached approximately 3 mm while the reaction force was still not activated yet (see Figure 6-18). After that, owing to the effect of R-wave, the reaction force was initiated with a negative value and then reached the first positive values at 10 mm of displacement. Therefore, only the shaded area of the reaction force vs displacement is used for estimating the absorbed energy of the beam (as shown in Figure 6-18) whereas a portion of the deformation energy caused by the displacement from 0 to 10 mm cannot be taken into account. Such issues surely lead to inaccuracy in estimating the actual absorbed energy of the beams by this approach. However, because of lacking the appropriate methods, in this chapter, the positive reaction force vs displacement is still used to estimate the absorbed energy of the beams $E_a(t)$. It is acknowledged that the energy consumption due to local damage and stress wave propagation in the initial impacting stage is not included in this approach of absorbed energy estimation.

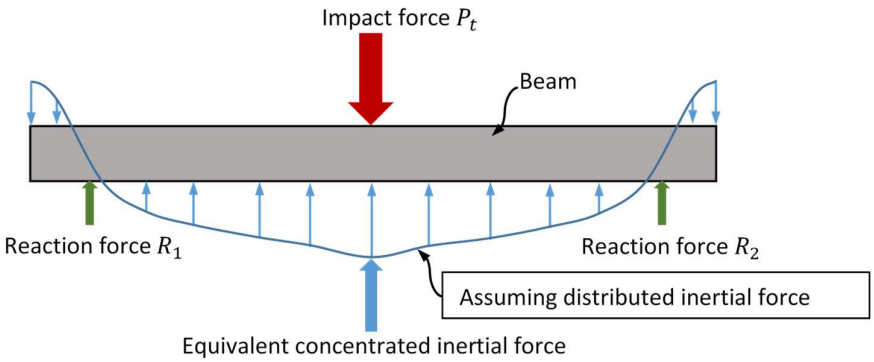

Figure 6-17. Equilibrium diagram to determine the true bending load

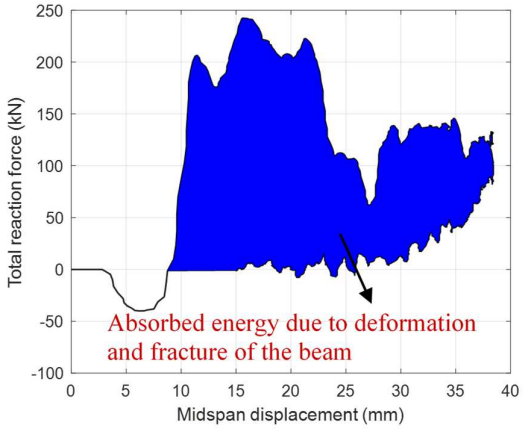

Figure 6-18. Reaction force vs mid-span displacement of Beam GPC-0.5PF

The velocity profile of the drop hammer is presented in Figure 6-19a. It can be seen that due to the short duration of the first impulse, the velocity of drop hammer decreased sharply in the early stage in the cases of the beams using direct contact compared to the beam employing rubber pad contact. The velocity of drop hammer reduced to zero at the moment when the beams reached the maximum displacement, which means that the whole of the kinetic energy of drop hammer transferred into the beam at that moment. After that, the velocity of drop hammers increased with the negative values implying a reversed movement (upward direction) because of the beams bouncing back to the initial position. The maximum negative value of rebound velocity of the drop hammer is considered as its residual velocity V_r (as presented in Table 6-4). After reaching the residual velocity, the drop hammer was separated from the beams and the beam experienced free vibration, which means that there was no more impact energy transferred into the beam. Therefore, the total imparted energy E_i of the beams can be simply calculated by the residual velocity of the drop hammer as follows [12]:

$$E_i = \frac{1}{2} M(V_0^2 - V_r^2) \tag{6-5}$$

Based on the time history of the drop hammer velocity, the time history of energy imparted into the beam is plotted in Figures 6-19b to d. It can be seen from the figures after reaching the maximum value, the energy imparted into the beams decreased slightly and subsequently remained at a constant value which represents the total imparted energy E_i (shown in Eq. (6-5)). The slight reduction in the energy is due to the fact that one portion of energy from the beam is reversed back to the drop hammer in the form of residual velocity. Meanwhile, the

work done by impact force estimated by Method 2 (impact force vs displacement curve) differed significantly from the imparted energy calculated by Method 1 (conservation of kinetic energy) in cases of the beams using direct contact (see Figures 6-19b and c). Interestingly, the total work done of Beam OPC-NoF-DC determined by integrating the impact force vs displacement curve was much higher than the total imparted energy (see Figure 6-19c). This implies that using the impact force vs displacement curve to estimate the energy imparted into the beams might not be reasonable in the case of the study presented in this chapter.

The aforementioned issue can be due to several reasons: (1) after the beam exhibits severe diagonal tension damage, it approximately splits into two asymmetrical halves (see Figure 6-20a). As a result, the displacement at the midspan tracking point measured from the camera does not appropriately represent the midspan displacement of the entire beam. Accordingly, using the displacement at the midspan tracking point in calculating the work done will over predict the actual imparted energy. (2) After several separations, the drop hammer collided with the beam in the diagonal direction. This results in the fact that the actual impact force acting on the beam did not exactly align with the measured displacement in the vertical direction (see Figure 6-20a). Due to the unsymmetrical failure of diagonal tension mode, the angle of impact force and displacement vector became large (see Figure 6-20a at t = 20 ms). In physical meaning, if the force is being exerted at an angle θ to the displacement direction, the work done should be calculated as $W = Fdcos(\theta)$ (F is the force, d is the induced displacement). Therefore, the measured impact force and displacement in the vertical direction in the test could not be used to calculate the actual work done by impact force on the beam. In the case of the beam using rubber pad contact, the drop hammer moved with the beam in the vertical direction during the impact process (see Figure 6-20b). Also, the beam was not intensively damaged and split into several parts but almost maintained the initial configuration as compared to OPC-NoF-DC (see Figure 6-20b). Therefore, the measured displacement at midspan can be used to represent the deformation of the entire beam. Because of those reasons, using Method 2 to calculate of work done by the impact force of Beam GPC-NoF-RP still yielded reasonable results as shown in Figure 6-19d. According to Eq. (6-2), the difference in the calculations of two methods represented the energy absorbed by the fracture of rubber pads, which is approximately 14% of total input kinetic energy. Generally, this chapter suggests that the energy imparted into the beams is better calculated using the variation in the kinetic energy of drop hammer (Method 1) due to two reasons: (1) when the beam exhibits severe damage, the actual midspan displacement of entire beam is difficult to be accurately measured; and (2)

after the occurrence of large deformation the measured vertical impact force does not align with the primary beam deformation direction, resulting in inaccurate estimation of work done by the impact force on the beam. Further explanations indicating that the energies derived based on the force-displacement curve might be not accurate can be found in the study of Pham et al. [12].

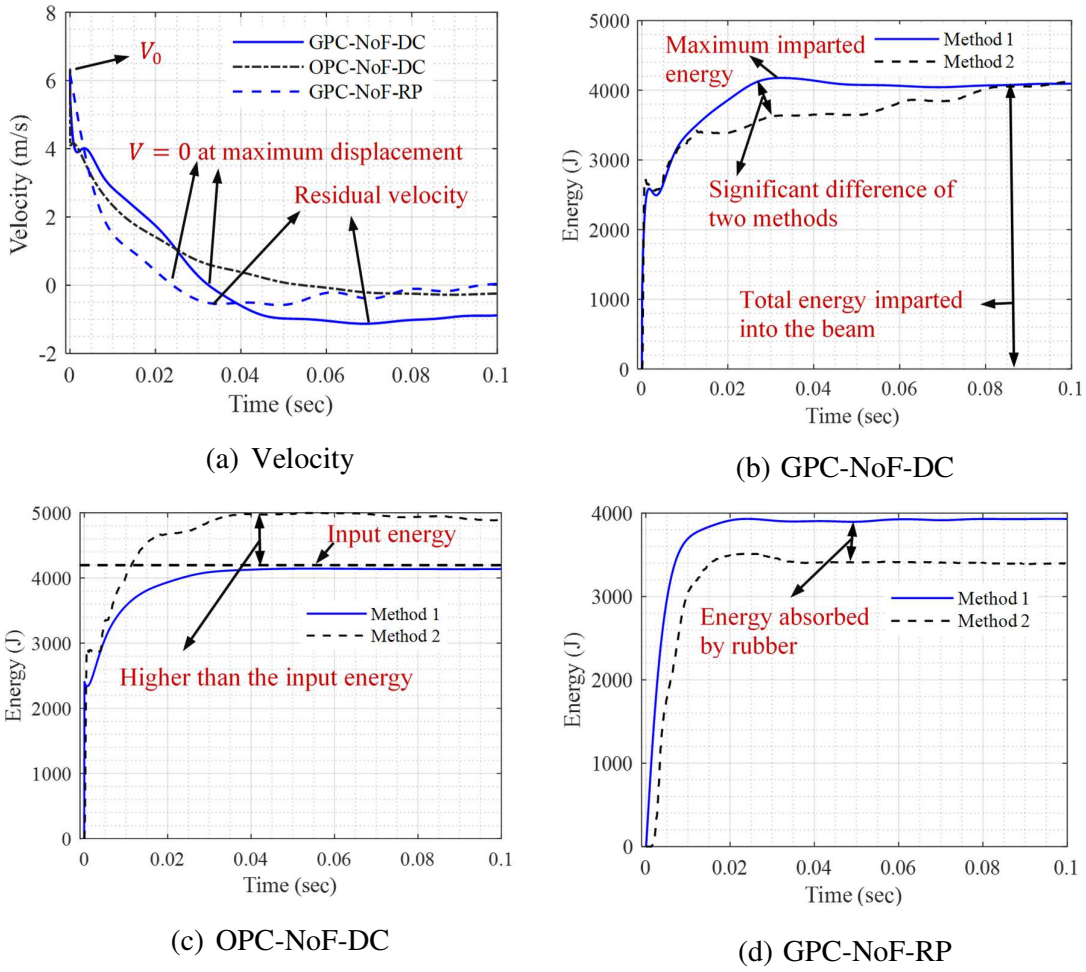

(a) Velocity

(b) GPC-NoF-DC

(c) OPC-NoF-DC

(d) GPC-NoF-RP

Figure 6-19. Velocity of drop hammer (a); Estimated imparted energy of the tested beams (b-d)

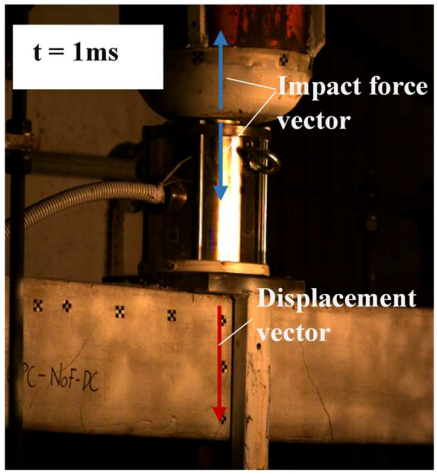

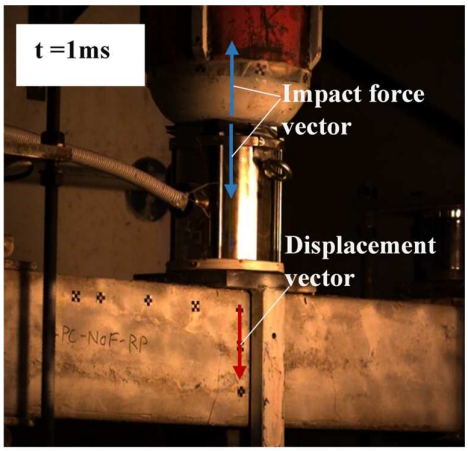

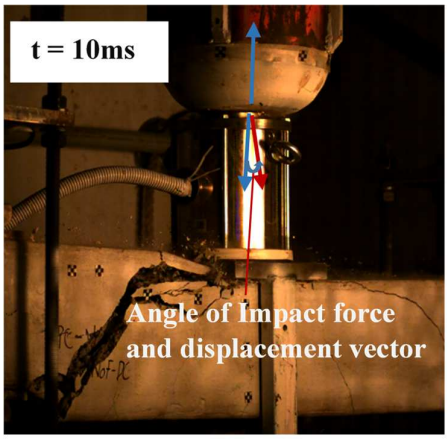

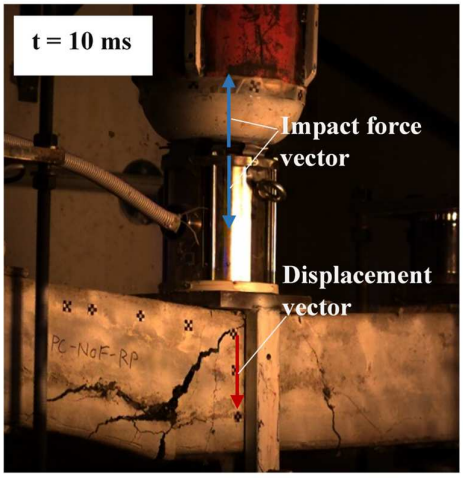

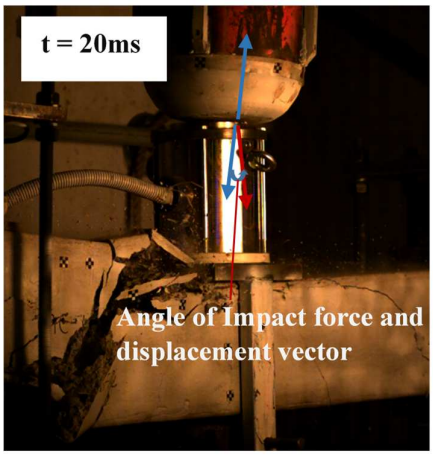

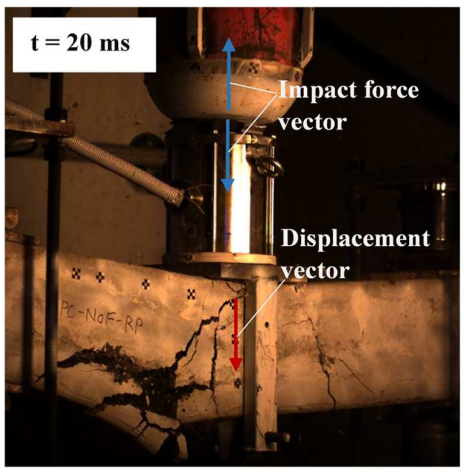

(a) OPC-NoF-DC (b) GPC-NoF-RP

Figure 6-20. The collision process of drop hammer and the beams

The total imparted energy E_i and the absorbed energy E_a of the tested beams are presented in Figure 6-21. From the figure, it can be seen that the presence of fibre exhibited a marginal effect on the total imparted and absorbed energies of the beams. This can be attributed to the fact that the inclusion of fibres could not change the failure mode of the beams presented in this chapter. All the beams failed in the same diagonal tension mode and thereby had similar total imparted and absorbed energy. The same phenomenon was observed in the previous investigation on the flexural behaviour of the fibre reinforced GPC beams using BFRP stirrups under impact loading [4]. All the beams of that study failed in the same flexural manner and exhibited similar total absorbed energy. The total absorbed energy in that study was recorded as 30% of the total imparted energy. Meanwhile, in this chapter, the total absorbed energy ranges between 90-99% of the total imparted energy. This is because the beams presented in this chapter were not reinforced with shear reinforcement and thus suffered much more severe damages. From those observations, the total absorbed energy of the beam under impact loading is strongly dependent on the failure mode and damage level of the beams. It is worth noting that even though the method of determining the energy absorption relies on some assumptions and the true bending load, the calculated energy absorption and the imparted energy agree very well. Also, due to these assumptions, the energy absorptions of Beams GPC-0.5SF and GPC-0.5PF are even slightly higher than the corresponding imparted energy. Therefore, the proposed two methods to estimate the imparted energy and absorbed energy should be used with caution and more studies on this issue are deemed necessary.

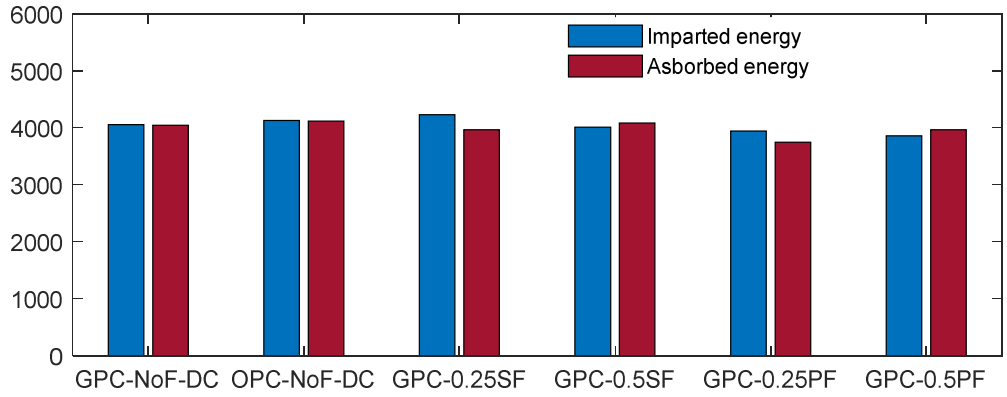

Figure 6-21. Estimated energy of the tested beams

6.4. Conclusion

This chapter investigated the shear behaviour of the fibre reinforced GPC beams without stirrups under impact loading. The GPC beams exhibited almost similar impact performance to the corresponding OPC beams. The incorporation of fibres considerably improved the impact response of the GPC beams in terms of the maximum and residual displacement, reaction force, and also mitigated the negative and spalling cracks. The effect of different contact conditions on impact response was also investigated and discussed. The key outcomes can be summarized as follows:

1. The control GPC and OPC beams exhibited similar cracking and diagonal tension failure in the early stage (from t_1 = 0 ms to t_4 = 1.4 ms). The differences occurred in the post-failure stage where the GPC beam suffered more severe concrete spalling and fragmentation, but less dowel action compared to the OPC beam.
2. The inclusion of fibres did not change the failure mode of the beams but improved the post-failure performance. SFs were more effective to prevent the opening of small cracks caused by negative bending moment but less efficient to bridge the large diagonal cracks compared to PFs. This can be attributed to the premature pull-out failure of SFs due to insufficient bond length.
3. In terms of the dynamic forces, the first impulse of impact force was independent of the presence of fibres while the second peaks increased significantly by 87% owing to fibre reinforcements. The addition of fibre also resulted in larger reaction force.
4. The presence of fibres reduced significantly the maximum displacement (50% for Beam GPC-0.5PF) and residual displacement (58% for Beam GPC-0.5PF). PFs were demonstrated to be more effective to improve the displacement performance than SFs.
5. The effect of fibres on the total absorbed energy of the tested beams was minor but it is indicated that the ratio of total absorbed and imparted energy is strongly dependent on the failure mode.
6. The failure mode and cracking pattern were influenced by contact conditions. The adoption of rubber-pad contact changed the failure mode of the beams from purely diagonal shear to flexure-shear combined failure.
7. The peaks of the impact force decreased by four times while the duration increased by five times when using rubber pad contact compared to direct contact. The bandwidth of

impact force frequency also changed from 0-2.5 kHz for direct contact to 0-0.5 kHz for rubber-pad contact.

8. The reaction force of the tested beams using rubber-pad contact increased by 50% while the midspan displacement was reduced significantly as compared with the beam subjected to direct impact.

Finally, the fibre reinforcement demonstrated a good enhancement in the shear behaviour of GPC beams subjected to impact loading. It was observed that the pull-out failure could lead to less effectiveness of fibre reinforcements on the structural performance under impact loading. Therefore, the length and shape of fibres as key parameters should be carefully considered when designing the structure subjected to impact loads. The contact condition affects significantly the impact response of the beams and thus needs to be taken into consideration when analysing the impact behaviour of structures.

References

[1] Khan MZN, Shaikh FUA, Hao Y, Hao H. Synthesis of high strength ambient cured geopolymer composite by using low calcium fly ash. Constr Build Mater. 2016;125:809-20.

[2] Tran TT, Pham TM, Hao H. Experimental and analytical investigation on flexural behaviour of ambient cured geopolymer concrete beams reinforced with steel fibers. Eng Struct. 2019;200:109707.

[3] Tran TT, Pham TM, Hao H. Effect of hybrid fibers on shear behaviour of geopolymer concrete beams reinforced by basalt fiber reinforced polymer (BFRP) bars without stirrups. Compos Struct. 2020;243:112236.

[4] Huang Z, Chen W, Hao H, Chen Z, Pham TM, Tran TT, Elchalakani M. Shear Behaviour of Ambient Cured Geopolymer Concrete Beams Reinforced with BFRP Bars under Static and Impact Loads. 2020;Under review.

[5] Pan Z, Sanjayan JG, Rangan BV. Fracture properties of geopolymer paste and concrete. Mag Concr Res. 2011;63:763-71.

[6] Yost JR, Radlinska A, Ernst S, Salera M, Martignetti NJ. Structural behavior of alkali activated fly ash concrete. Part 2: structural testing and experimental findings. Mater Struct. 2012;46:449-62.

[7] Khan MZN, Hao Y, Hao H, Shaikh FUA. Mechanical properties of ambient cured high strength hybrid steel and synthetic fibers reinforced geopolymer composites. Cem Concr Compos. 2018;85:133-52.

[8] Bhutta A, Farooq M, Zanotti C, Banthia N. Pull-out behavior of different fibers in geopolymer mortars: effects of alkaline solution concentration and curing. Mater Struct. 2017;50:80.

[9] Bhutta A, Farooq M, Banthia N. Matrix hybridization using waste fuel ash and slag in alkali-activated composites and its influence on maturity of fiber-matrix bond. J Cleaner Prod. 2018;177:857-67.

[10] Tran TT, Pham TM, Hao H. Rectangular Stress-block Parameters for Fly-ash and Slag Based Geopolymer Concrete. Structures. 2019;19:143-55.

[11] Cotsovos DM, Stathopoulos ND, Zeris CA. Behavior of RC Beams Subjected to High Rates of Concentrated Loading. J Struct Eng. 2008;134:1839-51.

[12] Pham TM, Chen W, Elchalakani M, Karrech A, Hao H. Experimental investigation on lightweight rubberized concrete beams strengthened with BFRP sheets subjected to impact loads. Eng Struct. 2020;205:110095.

[13] Pham TM, Hao H. Behavior of fiber-reinforced polymer-strengthened reinforced concrete beams under static and impact loads. International Journal of Protective Structures. 2017;8:3-24.

[14] Fu Y, Yu X, Dong X, Zhou F, Ning J, Li P, Zheng Y. Investigating the failure behaviors of RC beams without stirrups under impact loading. Int J Impact Eng. 2020;137:103432.

[15] Saatci S, Vecchio FJ. Effects of Shear Mechanisms on Impact Behavior of Reinforced Concrete Beams. ACI Struct J. 2009;106:78-86.

[16] Pham TM, Hao H. Impact Behavior of FRP-Strengthened RC Beams without Stirrups. J Compos Constr. 2016;20.

[17] Zhao D-B, Yi W-J, Kunnath Sashi K. Shear Mechanisms in Reinforced Concrete Beams under Impact Loading. J Struct Eng. 2017;143:04017089.

[18] Pham TM, Hao H. Plastic hinges and inertia forces in RC beams under impact loads. Int J Impact Eng. 2017;103:1-11.

[19] Pham TM, Hao H. Effect of the plastic hinge and boundary conditions on the impact behavior of reinforced concrete beams. Int J Impact Eng. 2017;102:74-85.

[20] Pham TM, Hao H. Influence of global stiffness and equivalent model on prediction of impact response of RC beams. Int J Impact Eng. 2018;113:88-97.

[21] Pham TM, Hao Y, Hao H. Sensitivity of impact behaviour of RC beams to contact stiffness. Int J Impact Eng. 2018;112:155-64.

[22] Li H, Chen W, Hao H. Influence of drop weight geometry and interlayer on impact behavior of RC beams. Int J Impact Eng. 2019;131:222-37.

[23] Ltd JGMVNMTDC. http://www.gmvchina.com/en/infos.asp?id=327. 2019.

[24] Ltd BP. https://bosfa.com/products/dramix-5d-4d-3d/. 2019.

[25] Ltd BP. https://barchip.com/product/. 2019.

[26] Nath P, Sarker PK. Fracture properties of GGBFS-blended fly ash geopolymer concrete cured in ambient temperature. Mater Struct. 2016;50.

[27] Ulzurrun GSD, Zanuy C. Enhancement of impact performance of reinforced concrete beams without stirrups by adding steel fibers. Constr Build Mater. 2017;145:166-82.

[28] Tran TT, Pham TM, Huang Z, Chen W, Hao H, Elchalakani M. Impact Response of Fibre Reinforced Geopolymer Concrete Beams with BFRP Bars and Stirrups. 2020;Under review.

[29] Folino P, Ripani M, Xargay H, Rocca N. Comprehensive analysis of Fiber Reinforced Concrete beams with conventional reinforcement. Eng Struct. 2020;202:109862.

[30] Kishi N, Mikami H, Matsuoka KG, Ando T. Impact behavior of shear-failure-type RC beams without shear rebar. Int J Impact Eng. 2002;27:955-68.

[31] Lee J-Y, Yuan T, Shin H-O, Yoon Y-S. Strategic use of steel fibers and stirrups on enhancing impact resistance of ultra-high-performance fiber-reinforced concrete beams. Cem Concr Compos. 2020;107:103499.

[32] Soleimani SM, Banthia N. A Novel Drop Weight Impact Setup for Testing Reinforced Concrete Beams. Experimental Techniques. 2014;38:72-9.

Chapter 7. Conclusion and Future Work

7.1. Main findings

In this dissertation, the structural response of ambient-cured GPC beams with different types of fibre reinforcements (steel, synthetic, and hybridization fibre) subjected to static and impact loads is experimentally and analytically investigated. The effects of different kinds of contact conditions on the impact response of the GPC beams are also studied. The direct contact between the projectile and the load cell represents the hard contact and the contact of the projectile and rubber-pad layers is considered as the soft contact. Based on the experimental results, the analytical solutions are proposed to predict the flexural and shear capacity of fibre reinforced GPC beams subjected to static loads. To evaluate the imparted and absorbed energy of the GPC beams under impact load, the methods based on the velocity profiles of projectile and load-displacement curves are derived. The major findings of this dissertation are summarized as follows:

- Due to the difference in the compressive stress-strain relationship, the ambient-cured GPC structures had smaller stress-block parameters. Therefore, using the current rectangular stress block parameters in the available code provisions intended for OPC over predicted the capacity of ambient-cured GPC members (as presented in Chapter 2). The new sets of stress-block parameters proposed in this study provide a closer prediction of the capacity of ambient-cured GPC structures.
- Chapter 3 investigated the static flexural behaviour of the ambient-cured GPC beams. To synthesize the ambient-cured GPC with high compressive strength (60 to 70 MPa), the high slag content was adopted in the mixture. Therefore, severe dry shrinkage cracks occurred in the ambient-cured GPC beams. This phenomenon led to the poor cracking resistance and low post-cracked stiffness observed in those beams when comparing with the corresponding OPC specimens. The ambient-cured GPC beams also exhibited brittle failure due to explosive crushing concrete in the compression zone compared to progressive compression failure observed in the OPC beams. However, fibre inclusion helped overcome those issues. Through using SF reinforcement, the cracking resistance of the beams was improved, the stiffness in the post-cracked stage increased by decreasing the service deflection by 21%. Meanwhile, the flexural capacity increased by 40% and the ductility increased by 49%. The recommended volume fraction of fibres for the GPC beams was found at 0.75% whereas the optimal fiber dosage of OPC

structures is commonly recommended as 2%. This can be attributed to the poor workability performance of GPC compared to OPC with the same compressive strength. Despite the aforementioned adverse aspects, GPC showed superior bonding behavior between the concrete matrix and fibre. This leads to a shorter critical fibre length selected in designing the fibre reinforced GPC beams. The analytical investigation indicated that the use of the available design procedure intended for OPC in predicting load-deflection response of fibre reinforced GPC beam cannot yield reliable results when the volume fraction of fibre was higher than 0.75%.

- The shear performance of fibre reinforced GPC beams under static loads without using transverse reinforcement was presented in Chapter 4. It was found that the general shear response of the control (no fibre) OPC and GPC beams was quite similar. The incorporation of fibre enhanced the cracking resistance, post-cracked stiffness, and the shear capacity of the beams. Due to better bonding of GPC matrix and fibre, the fibre reinforcements seemed to be more effective in improving the shear capacity of the GPC beams than the OPC counterparts. The most effective dosage of fibre reinforcements was approximately 0.5% SF while an increase of fibre dosage up to 1% did not show more improvement in the shear strength of the beams. Due to the lower modulus, PF was less effective in improving the shear capacity of the beams compared to SF. However, this issue can be solved by increasing the volume fraction of PF. The use of fiber hybridization demonstrated a good synergy with the combination of 0.3%SF and 0.2% PVF whereas the hybrid fibre reinforcement of PF and CF was inefficient to improve the shear response of the beams. To design the shear capacity of the GPC beams, the models suggested in ACI 440.1R-06 were too conservative to predict the shear strength of the beams. Meanwhile, the model based on modified compression field theory (MCFT) obtained a good correlation with test data. This recommends that MCFT can be used for estimating the shear strength of fibre reinforced GPC beams.

- Chapter 5 examined the flexural failure of fibre reinforced GPC beams under impact load through the drop-weight test system and static residual capacity of the beams. It is demonstrated that the ambient-cured GPC beams had approximately identical performance compared to the corresponding OPC counterparts except a more severe spalling of concrete cover at beam soffit due to local stress wave propagation. It should be noted that the crack and failure pattern of the beams under impact load with impact velocity at 6.26 m/s was a combination of flexural and shear modes even though the

static shear capacity of those beams were designed to be two times higher than static flexural strength. However, the addition of fibres could shift the crack and failure patterns from shear to flexure dominance. By increasing the fibre dosage of SF up to 0.5%, the beam failed only by flexural modes. The presence of fibres also led to reducing crushing damage on the top of the beams and therefore resulted in the improvement in the stiffness and residual strength of impacted beams. Meanwhile, the fibre reinforcement did not influence significantly the dynamic response of the beams, including the reaction forces, midspan displacement, and energy absorption due to the existence of sufficient transverse reinforcements. Finally, the damping ratio of the beams increased with the volume fraction of fibres.

- The shear behaviour of the fibre reinforced GPC beams without stirrups under impact loading was presented in Chapter 6. The control GPC beams showed almost identical cracking and diagonal tension failure as the corresponding OPC specimens. The fibre reinforcement did not change the failure mode of the beams but significantly improved the post-failure response. The presence of fibres not only reduced considerably the maximum and residual displacement but also increased reaction force, and mitigated the spalling cracks. It was found that the first impulse of impact force did not depend on the inclusion of fibre. In contrast, the second peaks of impact force increased significantly with the presence of fibres. It is found that SFs were less effective in bridging the large diagonal cracks compared to PFs since SFs had an insufficient bond length to prevent premature pull-out failure. Furthermore, the influence of different contact conditions on the dynamic response of the beams under impact load was also investigated. It is demonstrated that the impact force peaks decreased by four times while the duration of impulse was prolonged by five times when changing from direct to rubber pad contact. This phenomenon led to a change in the cracking pattern and failure mode of the beams using rubber pad contact from purely diagonal shear to flexure-shear combined mode.

In general, the key results of this dissertation are visualized in Figures 7-1 and 7-2 while the recommendations for designing fibre reinforced GPC beams are summarized in Figure 7-3. Due to the disadvantages including brittle failure and low cracking resistance, GPC beams should be reinforced with fibres to improve ductility and load capacity. Under static loads, both commercial synthetic and steel fibres (presented in this dissertation) are good options for enhancing the structural performance of GPC. However, under impact loads,

the steel fibres are less effective than the synthetic fibres in bridging large cracks due to shorter fibre length, which means that longer fibres should be adopted in future work. Finally, it is recommended that the design procedure of GPC beams without or with fibre reinforcement can be developed based on the theory of conventional reinforced OPC beams with appropriate modifications.

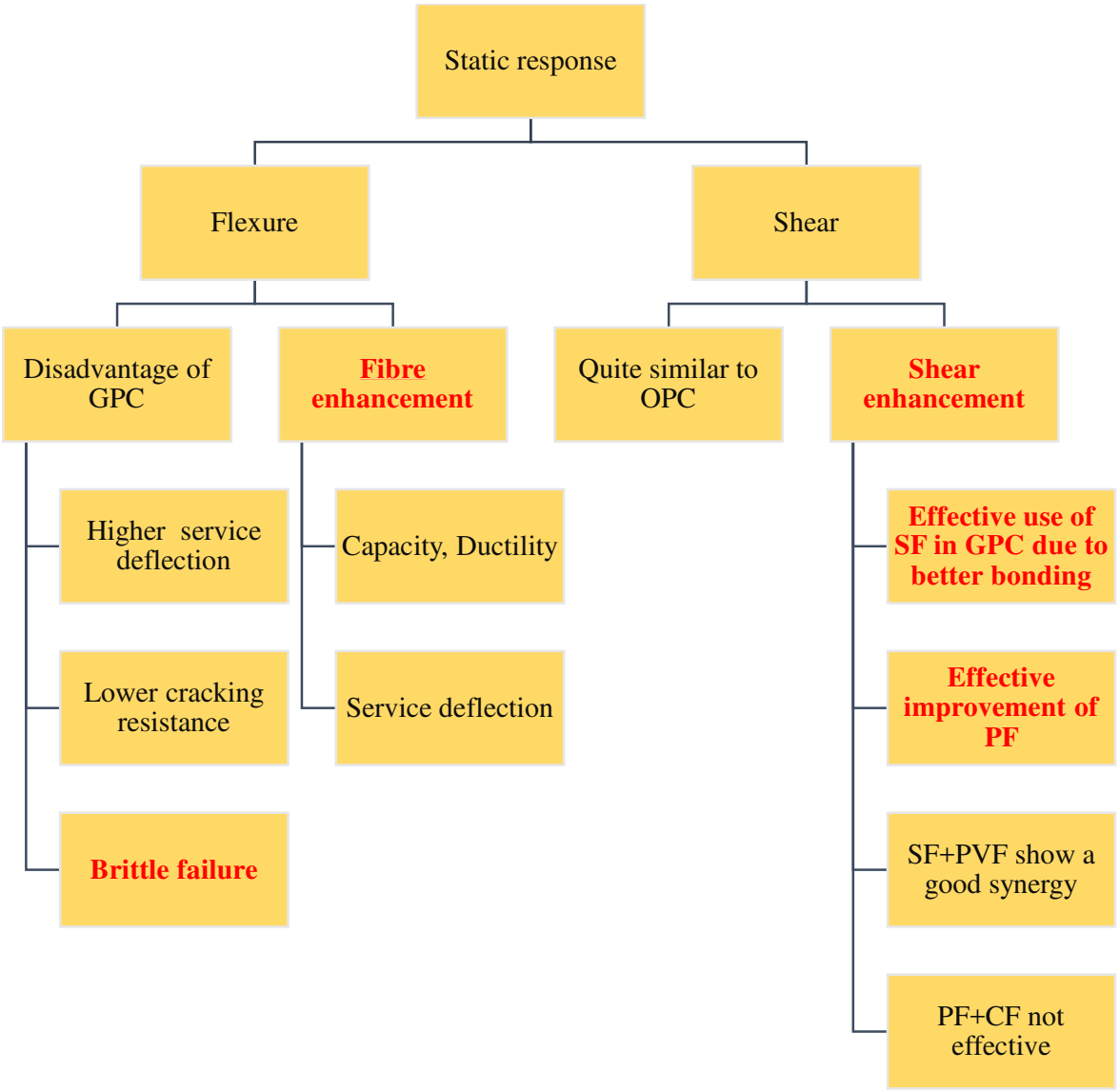

Figure 7-1. Visualization of key findings in static response

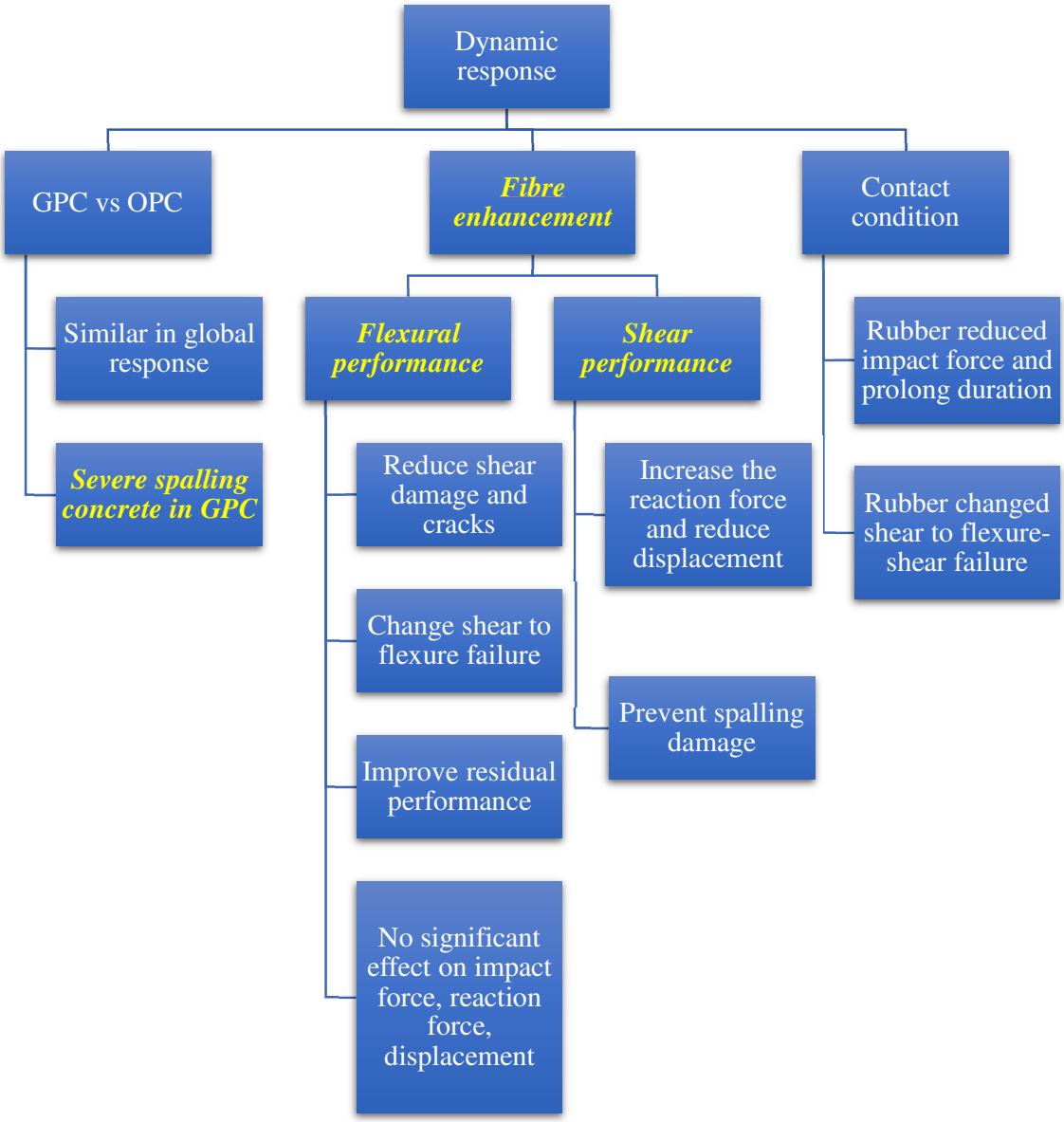

Figure 7-2. Visualization of key findings in impact response

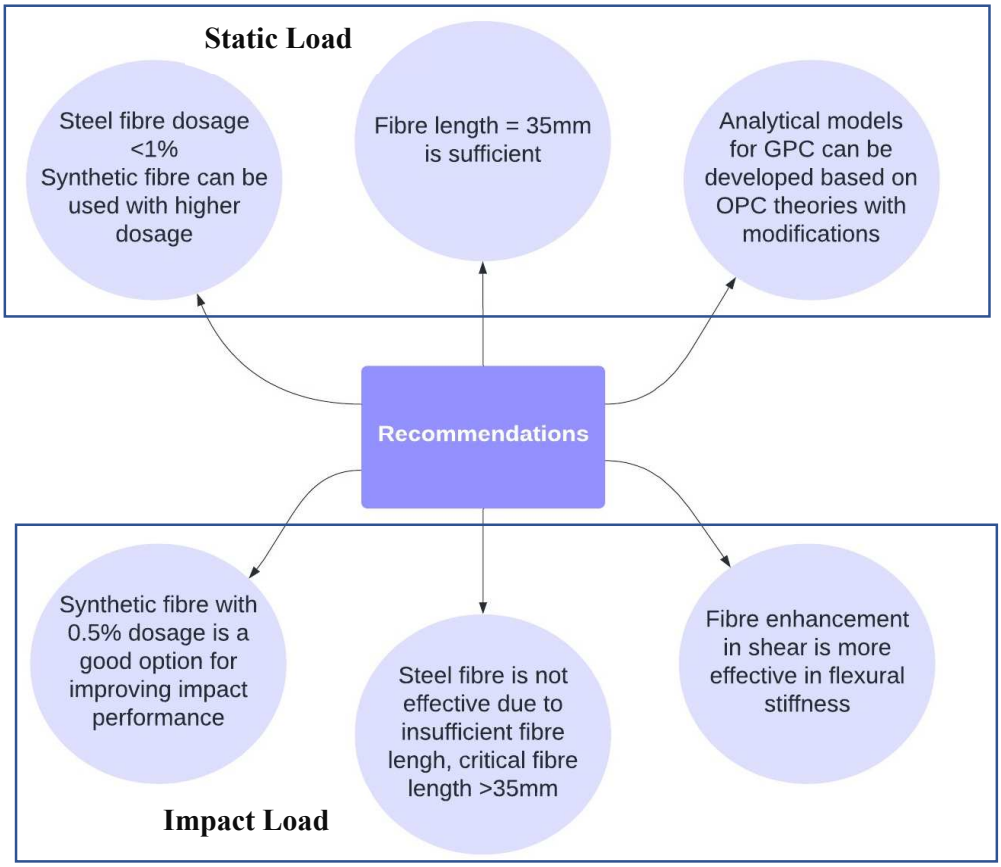

Figure 7-3. Recommendations for designing GPC beams reinforced with fibres

7.2. Recommendations for future work

- The fibre reinforcement used in Chapter 3 was SFs which can cause a durable issue related to fibre corrosion. Therefore, it is suggested a replacement of SFs with PFs and the structural investigation of the GPC beams reinforced with PFs under static loads is necessary.
- In Chapter 4, the contribution of fibre to the shear strength of beams without stirrups was investigated. However, in practice, the fibre can be used for replacing a part of transverse reinforcement to achieve a cost-effective design. Hence, the study can be extended to investigate the performance of fibre reinforced GPC beams with stirrups. Furthermore, the effects of other parameters such as shear span ratio, size of specimens, different types of longitudinal bars (CFRP or GFRP) were not considered, which means that further investigations are deemed necessary.
- In Chapters 5 and 6 the experimental investigations were limited with impact velocity at 6.26 m/s. It should be noted that the loading rate significantly affects the dynamic

response of the concrete beams and thus the effect of loading rate can be investigated in future work.

- The analytical solutions to design GPC beams under impact load have not been considered in this thesis. Therefore, in the future, analytical procedures can be conducted to estimate the dynamic shear and flexural capacity of GPC beams.
- As mentioned in Chapter 6, the SFs were not effective in bridging large cracks due to insufficient bond strength with the concrete matrix. To overcome this problem, the longer SFs or different shapes of fibres such as spiral fibres can be used to provide a better bond strength and further investigations should be conducted in the future.

Appendix I

STATEMENTS OF CONTRIBUTION OF CO-AUTHORS

To whom it may concern,

I, Thanh Tung Tran, conducted experimental tests, analytical derivations, data processing & analysis, and wrote manuscripts of the papers titled as follows, which were revised and edited by the co-authors. They also provided insights on experimental preparation, data processing, and data analysis.

1. Rectangular Stress-block Parameters for Fly-ash and Slag Based Geopolymer Concrete

2. Experimental and analytical investigation on flexural behaviour of ambient cured geopolymer concrete beams reinforced with steel fibers

3. Effect of hybrid fibers on shear behaviour of geopolymer concrete beams reinforced by basalt fiber reinforced polymer (BFRP) bars without stirrups

4. Impact Response of Fibre Reinforced Geopolymer Concrete Beams with BFRP Bars and Stirrups

5. Effect of Fibre Reinforcements on Shear Capacity of Geopolymer Concrete Beams subjected to Impact Loads

()

I, as a co-author, endorse that this level of contribution by the candidate indicated above is appropriate

(Prof. Hong Hao)	()
(Dr. Thong M. Pham)	()
(Dr. Wensu Chen)	()
(Mr. Zhijie Huang)	()
(Mr. Tuan Ngo)	()
(Dr. Mohamed Elchalakani)	()

Appendix II

Copyright Clearance

Chapter 2, article: "*Rectangular Stress-block Parameters for Fly-ash and Slag Based Geopolymer Concrete*"

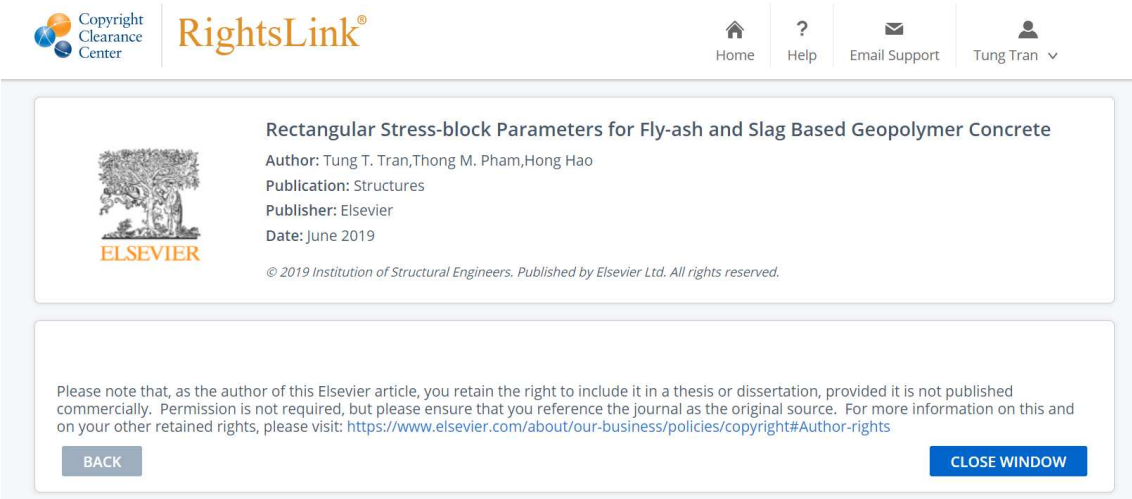

Chapter 3, article: "*Experimental and analytical investigation on flexural behaviour of ambient cured geopolymer concrete beams reinforced with steel fibers*"

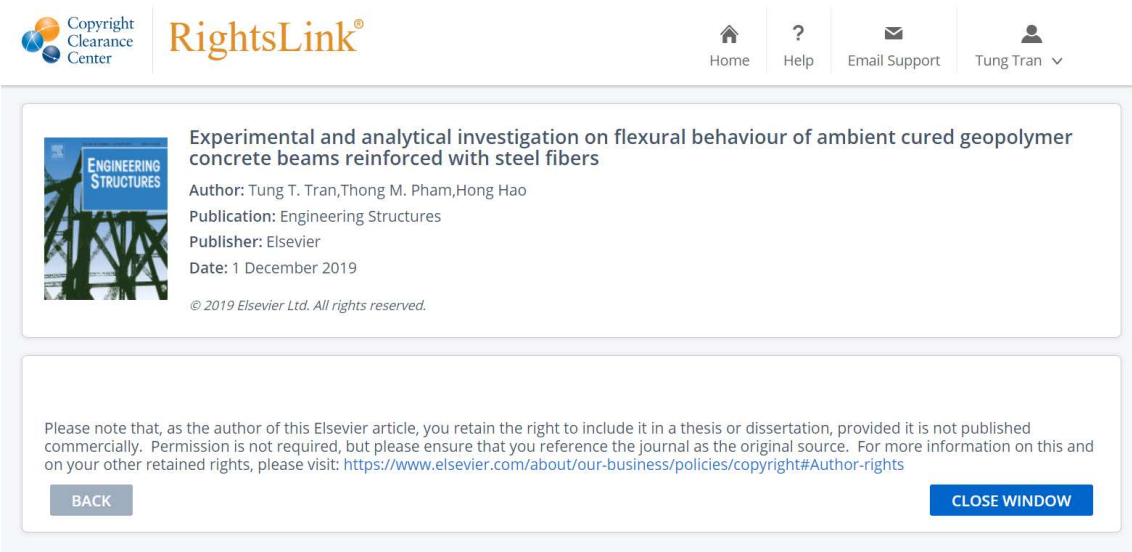

Chapter 4, article: "*Effect of hybrid fibers on shear behaviour of geopolymer concrete beams reinforced by basalt fiber reinforced polymer (BFRP) bars without stirrups*"

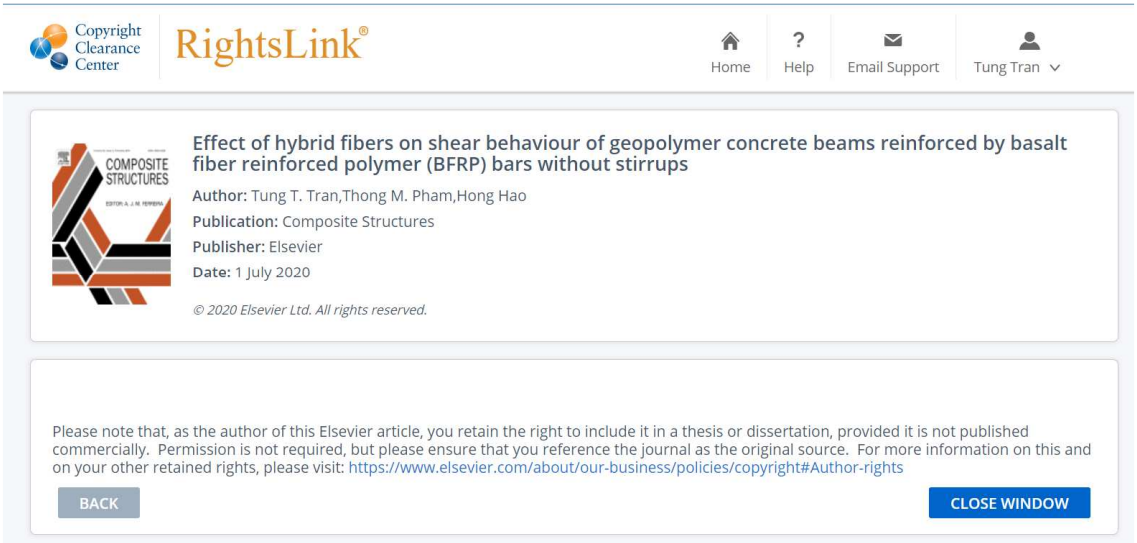

Chapter 5, article: *"Impact response of fibre reinforced geopolymer concrete beams with BFRP bars and stirrups"*